Ph.D. Thesis

Mechanical energy balance of frictional contacts; From surface to solid energy dissipation in contact dynamic instabilities.

Jointly awarded at the
Institut National des Sciences Appliquées of Lyon
École doctorale
Mécanique, Énergétique, Génie Civil, Acoustique (MEGA)
Spécialité: Mécanique

and at the
University of L'Aquila
Dottorato di ricerca in
Ingegneria Meccanica, Energetica e Gestionale

by

Jacopo BRUNETTI

On Decembre 4th, 2015

Ph.D. Committee:

Examiner/Reviewer:	A. AKAY	Professor	Bilkent University, Ankara
Examiner:	L. BAILLET	Professor	Université JF, Grenoble
Examiner/Tutor:	Y. BERTHIER	DR CNRS	INSA de Lyon
Examiner/Tutor:	W. D'AMBROGIO	Professor	University of L'Aquila
Examiner/Reviewer:	N. HOFFMANN	Professor	Hamburg University, Imperial College
Examiner/Tutor:	F. MASSI	Professor	University of Rome "La Sapienza"

Research laboratories:

LaMCoS - Laboratoire de Mécanique des Contacts et des Structures
UMR CNRS 5514 - INSA de Lyon
20, avenue Albert Einstein, 69621 Villeurbanne Cedex - France

DIIIE - Dipartimento di Ingegneria Industriale e dell'Informazione e di Economia
Università degli studi dell'Aquila
Via G. Gronchi, 18, 67100 L'Aquila (AQ) - Italy

SIGLE	ECOLE DOCTORALE	NOM ET COORDONNEES DU RESPONSABLE
CHIMIE	**CHIMIE DE LYON** **http://www.edchimie-lyon.fr** Sec : Renée EL MELHEM Bat Blaise Pascal 3ᵉ etage 04 72 43 80 46 Insa : R. GOURDON secretariat@edchimie-lyon.fr	M. Jean Marc LANCELIN Université de Lyon – Collège Doctoral Bât ESCPE 43 bd du 11 novembre 1918 69622 VILLEURBANNE Cedex Tél : 04.72.43 13 95 directeur@edchimie-lyon.fr
E.E.A.	**ELECTRONIQUE,** **ELECTROTECHNIQUE, AUTOMATIQUE** **http://edeea.ec-lyon.fr** Sec : M.C. HAVGOUDOUKIAN Ecole-doctorale.eea@ec-lyon.fr	M. Gérard SCORLETTI Ecole Centrale de Lyon 36 avenue Guy de Collongue 69134 ECULLY Tél : 04.72.18 60.97 Fax : 04 78 43 37 17 Gerard.scorletti@ec-lyon.fr
E2M2	**EVOLUTION, ECOSYSTEME,** **MICROBIOLOGIE, MODELISATION** **http://e2m2.universite-lyon.fr** Sec : Safia AIT CHALAL Bat Atrium- UCB Lyon 1 04.72.44.83.62 Insa : S. REVERCHON Safia.ait-chalal@univ-lyon1.fr	M. Fabrice CORDEY Laboratoire de Géologie de Lyon Université Claude Bernard Lyon 1 Bât Géode – Bureau 225 43 bd du 11 novembre 1918 69622 VILLEURBANNE Cédex Tél : 04.72.44.83.74 Sylvie.reverchon-pescheux@insa-lyon.fr fabrice.cordey@ univ-lyon1.fr
EDISS	**INTERDISCIPLINAIRE SCIENCES-** **SANTE** **http://www.ediss-lyon.fr** Sec : Safia AIT CHALAL Bat Atrium – UCB Lyon 1 04 72 44 83 62 Insa : Safia.ait-chalal@univ-lyon1.fr	Mme Emmanuelle CANET-SOULAS INSERM U1060, CarMeN lab, Univ. Lyon 1 Bâtiment IMBL 11 avenue Jean Capelle INSA de Lyon 696621 Villeurbanne Tél : 04.72.11.90.13 Emmanuelle.canet@univ-lyon1.fr
INFOMATHS	**INFORMATIQUE ET** **MATHEMATIQUES** **http://infomaths.univ-lyon1.fr** Sec :Renée EL MELHEM Bat Blaise Pascal 3ᵉ etage infomaths@univ-lyon1.fr	Mme Sylvie CALABRETTO LIRIS – INSA de Lyon Bat Blaise Pascal 7 avenue Jean Capelle 69622 VILLEURBANNE Cedex Tél : 04.72. 43. 80. 46 Fax 04 72 43 16 87 Sylvie.calabretto@insa-lyon.fr
Matériaux	**MATERIAUX DE LYON** **http://ed34.universite-lyon.fr** Sec : M. LABOUNE PM : 71.70 –Fax : 87.12 Bat. Direction 1ᵉʳ et. Ed.materiaux@insa-lyon.fr	M. Jean-Yves BUFFIERE INSA de Lyon MATEIS Bâtiment Saint Exupéry 7 avenue Jean Capelle 69621 VILLEURBANNE Cedex Tél : 04.72.43 71.70 Fax 04 72 43 85 28 Ed.materiaux@insa-lyon.fr
MEGA	**MECANIQUE, ENERGETIQUE, GENIE** **CIVIL, ACOUSTIQUE** **http://mega.universite-lyon.fr** Sec : M. LABOUNE PM : 71.70 –Fax : 87.12 Bat. Direction 1ᵉʳ et. mega@insa-lyon.fr	M. Philippe BOISSE INSA de Lyon Laboratoire LAMCOS Bâtiment Jacquard 25 bis avenue Jean Capelle 69621 VILLEURBANNE Cedex Tél : 04.72 .43.71.70 Fax : 04 72 43 72 37 Philippe.boisse@insa-lyon.fr
ScSo	**ScSo*** **http://recherche.univ-lyon2.fr/scso/** Sec : Viviane POLSINELLI Brigitte DUBOIS Insa : J.Y. TOUSSAINT viviane.polsinelli@univ-lyon2.fr	Mme Isabelle VON BUELTZINGLOEWEN Université Lyon 2 86 rue Pasteur 69365 LYON Cedex 07 Tél : 04.78.77.23.86 Fax : 04.37.28.04.48 isavonb@dbmail.com

*ScSo : Histoire, Géographie, Aménagement, Urbanisme, Archéologie, Science politique, Sociologie, Anthropologie

i

Acknowledgements

This thesis has been developed in the framework of collaboration between French and Italian academic institutions the INSA of Lyon, The University of L'Aquila and The University of Rome "La Sapienza", so the first thanks goes to the institutions that have supported my research and made it possible: the two doctoral schools (The doctoral school MEGA of the INSA of Lyon and the Doctoral School in Mechanical Engineering of the University of L'Aquila).

I would like to express my deepest gratitude to my Italian and French supervisors of this thesis the Professors Walter D'Ambrogio and Yves Berthier, whose scientific and personal support added considerably to my doctoral experience. A very special thanks goes to my co-supervisor Professor Francesco Massi, he provided me with direction, technical support and became more of a mentor and friend, than a professor.

I would like also to express my gratitude to the Professor Laurent Baillet for his collaboration and contribution to the research work. A sincere thanks goes also to the reviewers, Professors Adnan Akay and Norbert Hoffmann for their careful revision rich of comments and suggestions which allowed me to improve this work.

I am sincerely grateful to all the people and friends who made my working environment at LaMCoS laboratory, at the DIIIE department or somewhere else stimulating and pleasant. Among them Fangfang, Matthieu, Hung, Guillaume, Rudy, Jerome, Joe, Maria, Pierrick, Eymard, Komla, Serge, Sayed, Bogdan, Mirela, Marion, Ghassene, Livia, Marine, Jose, Alexandra, Aurelien, Mathieu, Ben, Eric, Patrizia, Antonio, Silvia and Mariano. A very special thanks to my italian family in France Davide, Manuel, Giovanna, Francesca, Gabriele, Ilaria, Maria and Peppe. As well, I will never forget the support of my friends in L'Aquila Marco, Alessandro and Marilisa.

The development of this thesis would have never been possible without the support and the encouragement of my family, words can not express how grateful I am to my parents Carla and Francesco and to my sisters Carmen and Elvira.

This acknowledgments would not be completed without my full gratitude to the most important person in my life, my best friend and beloved wife Claudia, who shared with me these years. I can honestly say that it was only her love and day by day support, that ultimately made it possible for me to see this project through to the end.

iii

Cotutele agreements

KEPERTORIO N° 7961
PROT. N° 5942
DEL 18/02/2013

ACCORD DE COOPERATION POUR LA MISE EN ŒUVRE D'UNE COTUTELLE DE THESE

L'INSA de LYON, représenté par le Professeur Daniel BARBIER, Directeur Adjoint de la Recherche, agissant en qualité et en vertu des pouvoirs qui lui sont conférés, d'une part
ET
L'Université de L'Aquila ayant son siège à L'Aquila (Italie), Via Giovanni Falcone 25, représentée par son Recteur Professeur Ferdinando di Orio, agissant en-qualité et en vertu des pouvoirs qui lui sont conférés d'autre part

Vu pour la partie française :
- L'arrêté du 6 janvier 2005 relatif à la procédure de cotutelle internationale de thèse (France);
- L'arrêté du 7 août 2006 relatif aux études doctorales (France);
- La convention cadre franco-italienne entre la Conférence des Présidents d'Université (CPU) et la Conferenza dei Rettori delle Università Italiane (CRUI) sur la reconnaissance des diplômes et validation des titres universitaires signée en date 18 janvier 1996;
- La convention cadre franco-italienne entre la Conférence des Présidents d'Université (CPU) e la Conferenza dei Rettori delle Università Italiane (CRUI) sur la co-tutelle de thèse signée le 13 février 1998;

Et

Pour la partie italienne :
- Vue la Loi n. 210 du 3 juillet 1998 art. 4 – doctorat de recherche ;
- Vu le D.M. 224/99 relatif aux normes en matière de doctorat de recherche ;
- Vu les D.M. 509/99 et 270/2004 relatifs aux normes en matière d'autonomie didactique des Universités ;
- Vu le Règlement de l'Université en matière de doctorat de recherche ;

désireux (désireuses) de contribuer à l'instauration et/ou au développement de la coopération scientifique entre équipes de recherche italiennes et étrangères en favorisant la mobilité des doctorants

sont convenu(e)s des dispositions suivantes

Titre I – Modalités administratives

Art. 1 –L'INSA de Lyon et L'Université de L'Aquila désignées ci-après "les établissements", décident dans le respect des lois et des règlements en vigueur dans chacun des pays et/ou établissements, d'organiser conjointement une cotutelle de thèse au bénéfice de l'étudiant désigné ci-après :
Prénom et nom : Jacopo BRUNETTI
spécialité : ingenieur Mecanique – Doctorat en Ingegneria Meccanica, Energetica e Gestionale
sujet de thèse : **Energy balance between frictional contact and material deformation, from surface to solid energy dissipation… towards wear and friction control.**

The coupling between the vibrations of mechanical systems and the behavior of frictional contact surfaces has been the subject of a large amount of works in several specific research

vi

domains and focalized on various applications: dynamic instabilities, friction induced vibrations and acoustic emission issues like "brake squeal", wear phenomena such as "fretting" or "false Brinelling", etc.... One of the research branches the most investigated lies in the field of non-linear dynamics and deals with the vibration damping by frictional contact. A more general approach accounting for the energy transfer between surface and solid dynamics is needed to identify the energy effectively dissipated at the contact and the energy introduced in the system by friction induced vibrations.

Works developed in non-linear dynamics apply mainly macroscopic approaches, focused in the quantification of the quantity of energy dissipated at the contact. The purpose of this thesis is to add the tribological local characterization of the phenomenon by finite element analyses that, thanks to the recent evolutions of the computational means, will allow for the investigation of the local dynamics the contact at the origin of the energy dissipation. The proposed approach will be focused to the characterization of damping in complex systems by the distinction between energy dissipated in the material (material damping) and energy dissipated at the contact by friction, which plays a key role in the understanding and controlling wear and friction behaviors.

To allow this distinction, a main attention will addressed to the energy balance between the energy effectively dissipated in the contact and the energy re-injected in the system that gives origin to friction induced vibrations. In fact, while the macroscopic dynamic response of the system is affected by the contact behavior (contact damping and stiffness), a correct characterization of the local behavior needs to account for the dynamic response of the system that, vice-versa, affects the contact itself. A correct analysis of the energy flows is as well a necessary boundary condition for the local physical phenomena at the contact.

The numerical analysis will be carried out in parallel to the development and exploitation of a test bench for the reproduction of the physical phenomena and the validation of the numerical results.

Finally a parametrical analysis will be developed to investigate the role of the key parameters such as normal load, vibration amplitude, system dynamics, etc. The innovative aspect, with respect to the parametrical analyses in the literature, is the focus on the local phenomena at the contact that are at the origin of the macroscopic effect of these parameters on the system response.

This thesis will be developed in the framework of collaboration between the research group in tribology at LaMCoS of the INSA of Lyon and the research group of dynamics at the "Università degli studi dell'Aquila".

Les principes et les modalités administratives et pédagogiques de cette cotutelle sont définis par le présent accord.

Art. 2 - La durée prévue pour la préparation de la thèse en cotutelle est de 3 ans, à partir de l'année scolaire 2012/2013.
En cas de nécessité, cette durée peut être prolongée en conformité avec la réglementation en vigueur dans les deux établissements.

Art. 3 - La préparation de la thèse s'effectue par périodes alternées, à peu près équivalentes, dans chacun des deux établissements partenaires. La durée de ces périodes sera déterminée de commun accord par les deux directeurs de thèse.

Art. 4 – L'étudiant Jacopo BRUNETTI
est tenu à s'inscrire régulièrement dans les deux établissements. L'étudiant paiera les droits d'inscriptions à l' INSA de Lyon et en sera dispensé près l' Université de L'Aquila.

Art. 5 –Pour les périodes d'études effectuées en France et pour la soutenance, le doctorant bénéficie de l'ensemble des dispositions de l'arrêté du 7 août 2006 susvisé, et de la charte des thèses de l'INSA de Lyon.

Art.6 –Lors de son inscription, le doctorant devra fournir les justificatifs relatifs à ses ressources, à sa couverture sociale ainsi qu'à son assurance relative aux accidents du travail, dans chacun des pays.

Titre II – Modalités pédagogiques

Art. 1 – Le travail de thèse de l'étudiant sera réalisé sous la supervision commune de deux directeurs de thèse :
-   Yves BERTHIER (Directeur de Recherche CNRS au Laboratoire de Mécanique des Contacts et des Structures), directeur de thèse à l' INSA de Lyon ;
-   Walter D 'AMBROGIO (Professeur du Département de Ingegneria Industriale e dell'Informazione ed Economia), directeur de thèse à l'Université de L'Aquila;

qui s'engagent à exercer pleinement la fonction de tuteurs de le candidat ainsi qu'à formuler chacun un avis écrit sur la thèse de Doctorat. L'avis favorable des deux Directeurs de Thèse est une condition nécessaire à l'admission à l'examen final.

Art. 2- La thèse donnera lieu à une soutenance unique, reconnue par les deux établissements concernés. La soutenance aura lieu à l'INSA de Lyon. Le jury de soutenance est composé sur la base d'une proportion équilibrée de membres de chaque établissement désignés conjointement par les établissements contractants et comprend, en outre, des personnalités extérieures à ces établissements.
Il comprendra au moins cinq membres et au maximum huit membres, dont, sauf dérogation, les deux directeurs de thèse.

Art. 3 - La thèse sera rédigée et discuté en Anglais. Elle comportera un résumé substantiel rédigé en français et un résumé substantiel rédigé en italien.

Art. 4 – En cas de rapport favorable du Jury, chacun des deux établissements s'engage à conférer le titre de docteur de recherche pour la même thèse.
L'Université de L'Aquila s'engage à conférer le grade de docteur de recherche en Ingegneria Meccanica, Energetica e Gestionale.
L'INSA de Lyon s'engage à conférer le grade de docteur de recherche en Mécanique.

Art. 5 - Lorsque le doctorant doit valider des formations complémentaires (scientifiques ou visant à son insertion professionnelle), les établissements (l'Ecole Doctorale MEGA pour l'INSA) préciseront les modalités de reconnaissance mutuelle de ces formations, en accord avec les directeurs de thèse et le doctorant.

Titre III – Conclusions

Art. 1 – L'étudiant est tenu de respecter les règlements et les usages de l'établissement d'accueil.

Art. 2 – Par l'intermédiaire de leurs directeurs de thèses respectifs, les établissements signataires s'engagent à se communiquer toutes les informations et la documentation utiles à l'organisation de la cotutelle de thèse faisant l'objet du présent accord.

Art. 3 – Les modalités de présentation, de dépôt et de reproduction de la thèse seront établies dans chaque pays dans le respect de la réglementation en vigueur.

La protection du sujet de thèse, ainsi que la publication, l'exploitation et la protection des résultats issus des travaux de recherche du doctorant dans les deux établissements signataires seront assujetties à la réglementation en vigueur et assurées conformément aux procédures spécifiques à chacun des pays impliqués dans la cotutelle.

Sur demande, les dispositions concernant la protection des droits de propriété intellectuelle pourront faire l'objet de protocoles ou de documents spécifiques.

Art. 4 – Le présent accord entre en vigueur à partir de la date de signature du représentant légal de chaque établissement signataire et le reste jusqu'à la fin de l'année universitaire au cours de laquelle la thèse ou les travaux seront soutenus.

Dans le cas où l'étudiant ne serait pas inscrit dans l'un et/ou l'autre des établissements signataires, ou bien renoncerait par écrit à poursuivre, ou bien n'est pas autorisé à poursuivre la préparation de son thèse en vertu de la décision de l'un au moins des deux directeurs de thèse, les deux établissements signataires mettront fin conjointement et sans délai, aux dispositions du présent accord.

Art. 5 – Le présent accord est rédigé en quatre exemplaires originaux, dont deux en italien et deux en française, faisant également foi.

Fait à Villeurbanne, le ___31 OCT. 2012___   Fait à L'Aquila, le ___1 5 FEB. 2013___

Pour le directeur de l'INSA de Lyon   Pour le Recteur de l'Université dell'Aquila
Professeur Daniel BARBIER   Professeur
Directeur Ádjoint de la Recherche

Le Responsable de l'Ecole Doctorale   Il Coordinatore del Dottorato di Ricerca
Philippe BOISSE   Roberto CIPOLLONE

Le Directeur du laboratoire
David DUREISSEIX

Co-directeur (s) de thèse   Co-directeur de thèse
Yves BERTHIER   Walter D'AMBROGIO

Le Doctorant
Jacopo BRUNETTI

CONVENZIONE PER UNA CO-TUTELA DI TESI DI DOTTORATO DI RICERCA

L'INSA di Lione rappresentata dal Professore Daniel BARBIER, Addetto alla Direzione della Ricerca, che opera in virtù dei poteri che gli sono conferiti, da una parte

e

L'Università degli Studi dell'Aquila con sede in L'Aquila (Italia), Via G. Falcone, 25 rappresentata dal Rettore Prof. Ferdinando di Orio, che opera in virtù dei poteri che gli sono conferiti, dall'altra parte

Visti, per la parte francese,
- La delibera del 6 gennaio 2005 relativo alla procedura internazionale per la cotutela di tesi (Francia);
- La delibera del 7 agosto 2006 relativo al dottorato (Francia);
- La convenzione franco-italiana tra la Conférence des Présidents d'Université (CPU) e la Conferenza dei Rettori delle Università Italiane (CRUI) sul riconoscimento dei diplomi e della validità dei titoli universitari siglata in data 18 gennaio 1996;
- La convenzione franco-italiana tra la Conférence des Présidents d'Université (CPU) e la Conferenza dei Rettori delle Università Italiane (CRUI) sulla cotutela di tesi siglata li 13 febraio 1998;

e

Per la parte italiana:
- VISTA la Legge 210 del 3 luglio 1998 art. 4 – dottorato di ricerca;
- VISTO il D.M. 224/99 recante norme in materia di dottorato di ricerca
- VISTI i DD.MM. 509/1999 e 270/2004 recanti norme concernenti l'autonomia didattica degli Atenei;
- VISTO il Regolamento di Ateneo in materia di dottorato di ricerca;

nell'intento di contribuire ad instaurare e/o sviluppare la cooperazione scientifica tra équipe di ricerca italiana e straniere attraverso la mobilità dei dottorandi

convengono e stipulano quanto segue

Parte prima – Modalità amministrative

Art. 1 – L'INSA di Lione e L'Università degli Studi dell'Aquila denominati qui di seguito "Istituzioni" concordano, nel rispetto delle leggi e dei regolamenti in vigore in ciascun Paese e/o Istituzione, di organizzare congiuntamente una co-tutela di tesi di dottorato a beneficio del dottorando sottoindicato:

nome e cognome: Jacopo BRUNETTI

iscritto al corso di Dottorato di Ricerca in Ingegneria Meccanica, Energetica e Gestionale presso l'Università dell'Aquila e in "Mecanique" presso l' "ecole doctoral MEGA".

Argomento della tesi: **Energy balance between frictional contact and material deformation, from surface to solid energy dissipation... towards wear and friction control.**

The coupling between the vibrations of mechanical systems and the behavior of frictional contact surfaces has been the subject of a large amount of works in several specific research domains and focalized on various applications: dynamic instabilities, friction induced

X

vibrations and acoustic emission issues like "brake squeal", wear phenomena such as "fretting" or " false Brinelling ", etc.... One of the research branches the most investigated lies in the field of non-linear dynamics and deals with the vibration damping by frictional contact. A more general approach accounting for the energy transfer between surface and solid dynamics is needed to identify the energy effectively dissipated at the contact and the energy introduced in the system by friction induced vibrations.

Works developed in non-linear dynamics apply mainly macroscopic approaches, focused in the quantification of the quantity of energy dissipated at the contact. The purpose of this thesis is to add the tribological local characterization of the phenomenon by finite element analyses that, thanks to the recent evolutions of the computational means, will allow for the investigation of the local dynamics the contact at the origin of the energy dissipation. The proposed approach will be focused to the characterization of damping in complex systems by the distinction between energy dissipated in the material (material damping) and energy dissipated at the contact by friction, which plays a key role in the understanding and controlling wear and friction behaviors.

To allow this distinction, a main attention will addressed to the energy balance between the energy effectively dissipated in the contact and the energy re-injected in the system that gives origin to friction induced vibrations. In fact, while the macroscopic dynamic response of the system is affected by the contact behavior (contact damping and stiffness), a correct characterization of the local behavior needs to account for the dynamic response of the system that, vice-versa, affects the contact itself. A correct analysis of the energy flows is as well a necessary boundary condition for the local physical phenomena at the contact.

The numerical analysis will be carried out in parallel to the development and exploitation of a test bench for the reproduction of the physical phenomena and the validation of the numerical results.

Finally a parametrical analysis will be developed to investigate the role of the key parameters such as normal load, vibration amplitude, system dynamics, etc. The innovative aspect, with respect to the parametrical analyses in the literature, is the focus on the local phenomena at the contact that are at the origin of the macroscopic effect of these parameters on the system response.

This thesis will be developed in the framework of collaboration between the research group in tribology at LaMCoS of the INSA of Lyon and the research group of dynamics at the "Università degli studi dell'Aquila".

I principi e le modalità amministrative e didattiche di tale co-tutela sono definiti dalla presente convenzione.

Art. 2 - La durata per la preparazione della tesi è di 3 anni, a partire dall'anno accademico 2012/2013.
In caso di necessità tale durata potrà essere prorogata in conformità con la regolamentazione vigente nelle due Istituzioni.

Art. 3 - La preparazione della tesi si effettuerà in periodi alterni, pressoché equivalenti, in ciascuna delle due Istituzioni. La durata di tali periodi sarà fissata in comune accordo dai due Direttori di tesi.

Art. 4 –Il dott Jacopo Brunetti sarà iscritto in entrambe le Istituzioni. Corrisponderà i regolari diritti di iscrizione all'INSA di Lione e ne sarà esonerato presso l' Università dell'Aquila.

Art. 5 - Per tutto il periodo di preparazione della tesi il dott. Jacopo Brunetti beneficerà di quanto disposto dalla delibera del 7 Agosto 2006 e della carta dei tesisti de l'INSA de Lyon.

Art.6 - Per la durata della sua iscrizione, il dottorando dovrà fornire i giustificativi relativamente alle sue risorse, alla sua copertura sanitaria così come alla sua assicurazione sugli incidenti di lavoro, in ognuno dei paesi.

Parte seconda – Modalità didattiche

Art. 1 – Il dott. Jacopo Brunetti preparerà la tesi sotto la direzione comune dei professori:
- Yves BERTHIER (Direttore di ricerca CNRS presso il Laboratorio di Meccanica dei Contatti e delle strutture), direttore di tesi all'INSA di Lione;
- Walter D'AMBROGIO (Docente presso il Dipartimento di Ingegneria Industriale e dell'Informazione e di Economia), direttore di tesi all'Università dell'Aquila;

che si impegnano ad esercitare pienamente la funzione di tutori del dottorando e si impegnano a valutarne, ciascuno con propria relazione scritta, la tesi di Dottorato.
Il giudizio positivo di entrambi i Direttori di Tesi è condizione necessaria per l'ammissione all'esame finale.

Art. 2 - La discussione della tesi, unica e riconosciuta dalle due istituzioni, avrà luogo presso l'INSA di Lione. La Commissione giudicatrice, nominata dai Rettori delle due Università, sarà composta da un numero pari di studiosi appartenenti alle due Istituzioni e designati congiuntamente da esse, oltre a membri esterni alle due Istituzioni. Essa dovrà essere composta da un minimo di cinque membri ed un massimo di otto, appartenenti ai settori scientifico-disciplinari del Dottorato, tra cui, a meno di deroghe, i due direttori di tesi.

Art. 3 – La tesi sarà redatta e discussa in inglese; un riassunto sostanziale sarà redatto in lingua francese ed un riassunto sostanziale sarà redatto in lingua italiana.

Art. 4 – Ognuna delle due Istituzioni si impegna a conferire il titolo di dottore di ricerca per la stessa tesi, in seguito ad una relazione favorevole della Commissione giudicatrice.
L'Università degli Studi dell'Aquila conferirà il titolo di dottore di ricerca in Ingegneria Meccanica, Energetica e Gestionale.
L'INSA di Lione conferirà il titolo di dottore di ricerca in Meccanica.

Art. 5 - Nel caso in cui il dottorando debba convalidare le formazioni complementari (scientifiche o mirate al suo inserimento professionale), le Istituzioni (l'Ecole Doctorale MEGA pour l'INSA) specificheranno le modalità di riconoscimento reciproco di queste formazioni, in accordo con i direttori di tesi ed il dottorando.

Parte terza – Conclusione

Art. 1 – Il dottorando dovrà rispettare i regolamenti e le consuetudini dell'Istituzione ospitante.

Art. 2 – Le Istituzioni contraenti, attraverso l'intermediazione dei rispettivi direttori di tesi, si impegnano a comunicarsi rispettivamente tutte le informazioni e la documentazione utile per l'organizzazione della co-tutela di tesi oggetto della presente convenzione.

xii

Art. 3 – Le modalità di presentazione, di deposito e riproduzione della tesi saranno effettuate in ogni paese secondo i regolamenti in vigore.

La protezione dell'oggetto della tesi, così come la pubblicazione, lo sfruttamento e la protezione dei risultati ottenuti con lo studio di ricerca del dottorando nelle Istituzioni contraenti saranno assoggettati alla normativa in vigore e assicurati conformemente alle procedure specifiche di ciascun Paese coinvolto nella co-tutela.

Qualora richiesto, le disposizioni relative alla protezione dei diritti di proprietà intellettuale potranno costituire oggetto di protocolli o documenti specifici.

Art. 4 – La presente convenzione entra in vigore dalla data di firma del rappresentante legale di ciascuna Istituzione contraente e sarà valida fino alla fine dell'anno accademico nel corso del quale la tesi o lo studio saranno discussi.

Nel caso in cui il dottorando non fosse iscritto in una e/o l'altra delle Istituzioni contraenti, oppure rinunciasse per iscritto a proseguire, oppure, in virtù della decisione di almeno uno dei due direttori di tesi, non fosse autorizzato a proseguire la preparazione della tesi in co-tutela, le Istituzioni contraenti porranno fine, congiuntamente e senza ritardo, alle disposizioni del presente accordo.

Art. 5 – La presente convenzione è redatta in quattro esemplari originali, di cui due in lingua italiana e due in lingua francese, aventi medesimo valore legale.

Villeurbanne, li ___31 OCT. 2012___   L'Aquila, li ___1 5 FEB. 2013___

Per il Direttore dell'INSA de Lyon   Per il Rettore dell'Università dell'Aquila
Professore Daniel BARBIER   Professore
Addetto alla Direzione della Ricerca

_____   _____

Il Direttore della Scuola di Dottorato   Il Coordinatore del Dottorato di Ricerca
Philippe BOISSE   Roberto CIPOLLONE

_____   _____

Il Direttore del laboratorio
David DUREISSEIX

_____

Co-direttori di tesi   Co-direttore di tesi
Yves BERTHIER   Walter D'AMBROGIO

_____   _____

Il Dottorando
Jacopo BRUNETTI

_____

Résumé substantiel

Bilan énergétique mécanique de contacts frottants en présence d'instabilités dynamiques de contact; de la dissipation surfacique à la dissipation volumique.

Introduction
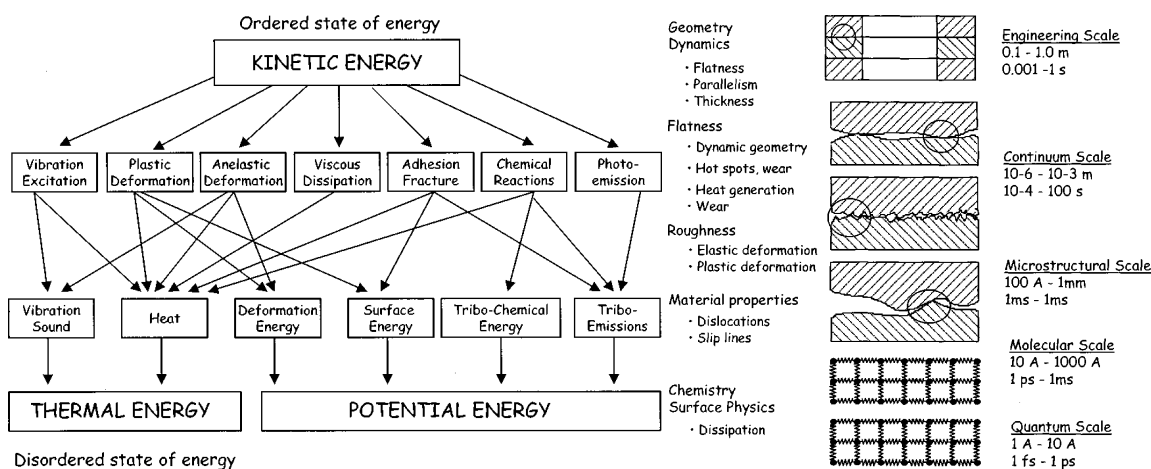
Chaque fois que se produit un mouvement relatif entre deux systèmes, avec une interface à contact sec, le contact frottant induit des vibrations. La dynamique locale au contact (ruptures et la génération d'ondes) se couple avec la dynamique du système, donnant origine à des vibrations et affectant le comportement frictionnel macroscopique du système.

Les déformations dues à la réponse dynamique du système affectent la répartition des contraintes de contact locales; inversement, la variation locale des contraintes et de statut (glissement, adhérence, séparation) du contact, les ondes générées par des ruptures locales, et les caractéristiques locales de contact (rigidité, amortissement, etc.) modifient la réponse dynamique du système.

Les soi-disant vibrations induites par frottement peuvent aboutir soit à un bruit acoustique de faible amplitude caractérisé par un large spectre de fréquence, qui est fonction des caractéristiques de surface (e.g. la rugosité) et de la dynamique des corps en contact; soit à un signal acoustique de large amplitude caractérisé par une excitation impulsive ou par un spectre harmonique.

Le dernier cas cité est caractéristique des instabilités dynamiques du système excités par les forces de contact. Les instabilités dynamiques de contact ont été l'objet de plusieurs études qui ont été porté sur des applications spécifiques comme le "squeak" des articulations mécaniques, le "squeaking" des prothèses de hanches ou le crissement de freins.

Bien que le comportement dynamique de systèmes mécaniques avec contacts frottants a largement été étudié dans la littérature au cours des dernières décennies, il manque toujours une pleine compréhension de la problématique. Les vibrations induites par le frottement, en fait, ne peuvent pas être réduites à un problème complexe de dynamique car elles impliquent aussi d'autres phénomènes autant complexes liés à la tribologie du contact. Jusqu'à présent, la nature multi-physique du probleème n'a pas été prise en compte, conduisant à considérer comme, imprévisibles, difficiles

(a) Une description de les chemins de l'énergie au cours de friction [AKA 02].

(b) Échelles de longueur et de temps associés à la friction et des exemples de différents phenomenes associé [AKA 02].

Figure 1: Transformation de l'énergie et les échelles des phénomènes.

ou indécelables la plupart des phénomènes liés à les vibrations induites par le frottement. Tenir compte de la réele complexité de la problématique n'est pas une tâche simple, en raison des différentes échelles spatiales et temporelles des phénomènes en jeu (Fig. 1(b)). Afin de développer une approche globale pour l'investigation des phénomènes multi-physiques, l'énergie pourrait être utilisée comme une caractéristique physique universelle du couplage (Fig. 1(a)). L'étude des flux d'énergie pourrait en fait donner de nouveaux éléments à la compréhension de l'interaction entre le comportement dynamique du système, la dynamique locale et le comportement tribologique de l'interface de contact.

Cette thèse se concentre sur l'étude des flux d'énergie mécanique impliqués dans les vibrations induites par frottement, afin de comprendre l'influence de la dynamique de contact sur la réponse du système et vice versa. Les flux d'énergie, provenant des surfaces en contact et dus aux vibrations induites par frottement, excitent la réponse dynamique du système et, vice versa, l'influence de la réponse dynamique du système sur la dissipation d'énergie locale à l'interface de contact, affecte les phénomènes tribologiques connexes. La distinction entre les différents termes d'énergie est ainsi utilisé pour identifier deux termes dissipatifs différents, i.e. la dissipation par amortissement matériel/système et la dissipation au contact. Ce travail vise à introduire une nouvelle perspective dans l'étude des vibrations induites par le frottement, en observant d'un point de vue énergétique le couplage entre le comportement local au contact et la dynamique globale.

Résultats

Dans cette thèse, les vibrations induite par le frottement ont été analysées en utilisant trois approches communes: l'approche par éléments finis pour étudier, par l'analyse des flux d'énergie, le couplage entre le contact et la dynamique du système; l'approche expérimentale pour valider les résultats numériques et observer l'influence des phénomènes pas encore inclus dans les modèles numériques; une approche avec une modèle à paramètres concentrés pour évaluer rapidement les effets des paramètres du système.

Comme une première étape, l'analyse des vibrations induites par frottement avec une approche énergétique se concentre principalement sur l'étude des vibrations instables, en raison de la forte interaction entre la dynamique locale et le contact. Une première application de cette approche générale est ici proposée pour résoudre le problème de la sélection entre les plusieurs modes instables récupérés par l'analyse des valeurs propres complexes d'un système frottant.

Le travail est organisé comme de suit:
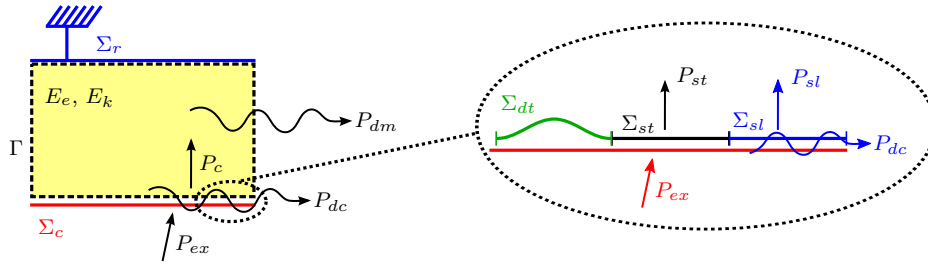
Figure 2: Schéma de bilan énergétique. E_e et E_k sont respectivement l'énergie potentielle élastique et l'énergie cinétique du corps élastique Γ, Σ_r est la partie du bord où une contrainte rigide est appliquée, Σ_c est la partie du bord où l'interaction de contact est définie. P_c est la puissance totalement échangé au contact, P_{ex} est la puissance absorbée par le système et P_{dm} est la puissance dissipée par l'amortissement matériau. Σ_{dt}, Σ_{sl} et Σ_{st} représentent respectivement le parties de la surface de contact Σ_c en conditions de détachement, de glissement et de adhérence. P_{sl} and P_{st} sont respectivement les puissances échangées en glissement et adhérence. P_{dc} est la puissance dissipée au contact.

La première partie donne un aperçu des problématiques liées à la dynamique de contact frottant dans la littérature (chapitre 1), incluant les travaux de recherche qui se focalisent sur l'analyse des énergies impliquées dans les vibrations induites par frottement. Ensuite, dans le chapitre 2 sont introduits les modèles, les outils numériques et l'équipement expérimental utilisé pour les études numériques et expérimentales présentées dans la thèse, et a été formulé un équilibre de l'énergie mécanique d'un système mécanique en contact frottant (Fig. 2).

Le chapitre 3 présente une étude numérique sur un modèle éléments finis 2D d'un dispositif expérimental (Fig. 3). Dans une approche classique, la stabilité
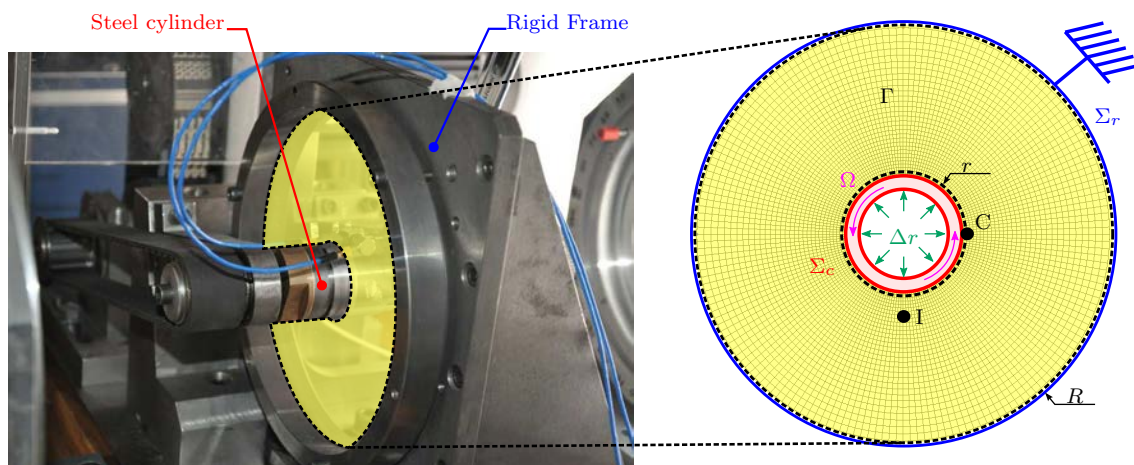
Figure 3: Dispositif expérimental "PhotoTrib" utilisé pour valider les résultats numériques (à gauche) et le modèle d'éléments finis du disque de polycarbonate (à droite).
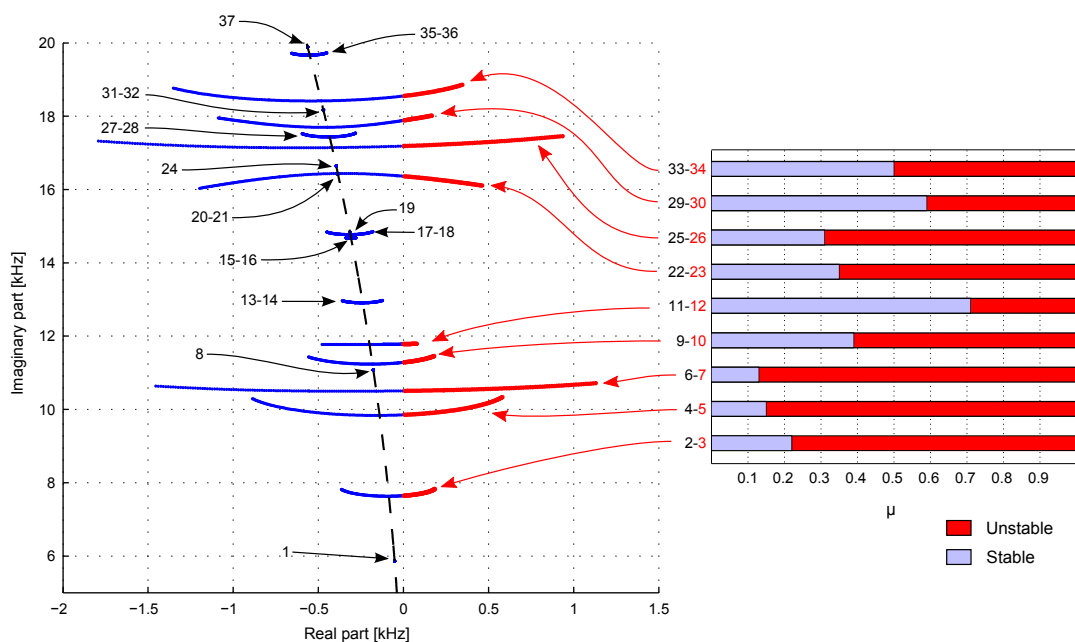
Figure 4: Locus plot des valeurs propres du système. Pour chaque valeur propre qui devient instable la valeur critique de le coefficient de frottement est rapporté dans le graph de stabilité.

(a) Comportement dans le temps (vitesse) du noeud interne I dans la direction circonférentielle et radiale

(b) Contraintes tangentielles et normales mesurées sur un noeud de contact.

(c) Puissances échangées et dissipée.

(d) Évolution de l'état de la surface de contact.

(e) Coefficient de frottement locale moyenne.

(f) Forces tangentielles et vitesse tangentielle d'un noeud de contact. Parties grises représentent les intervalles de temps où la Puissance nodale $\widetilde{P}_c < 0$.

Figure 5: Réponse du système en cas d'un coefficient de frottement $\mu = 0.3$ et une vitesse de rotation $\Omega = 100$ RPM

du système a été évaluée par une analyse linéaire des valeurs propres complexe en fonction du coefficient de frottement (Fig. 4); alors, la réponse du système en régime permanent a été évaluée par une analyse non linéaire transitoire (Fig. 5). Les quantités énergétiques impliquées dans les vibrations induites par frottement sont analysés au cours de la réponse transitoire (Fig. 5(c)), pour observer l'effet du coefficient de frottement local et des conditions aux limites (Fig. 5(d)) sur les différents termes du bilan énergétique.
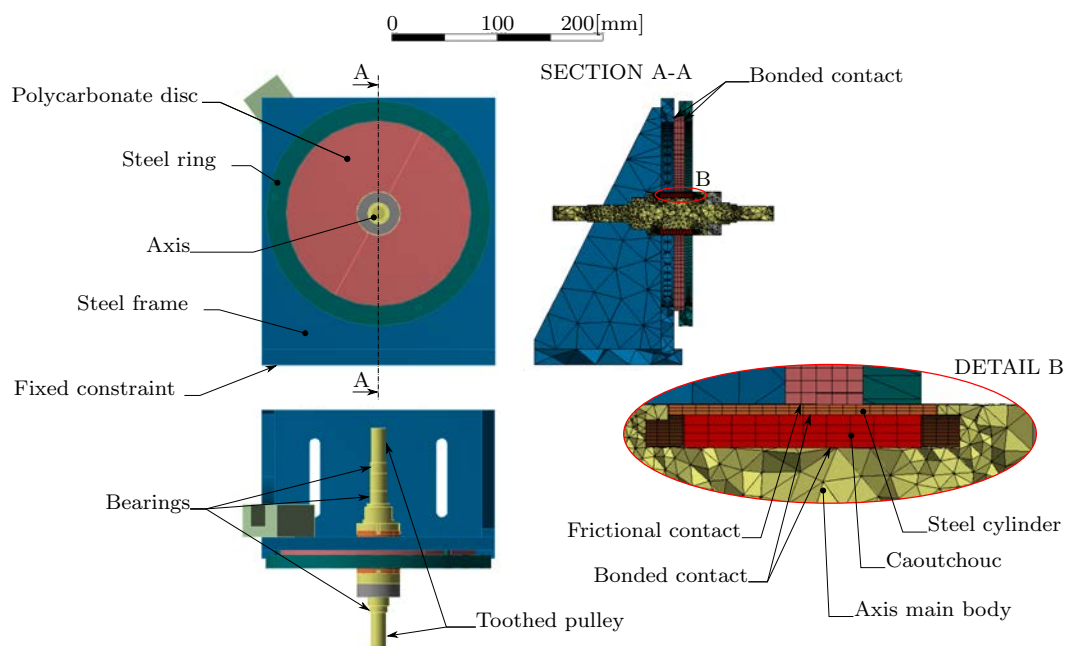
Figure 6: Modèle éléments finis 3D, conditions limites et contacts.

Dans le chapitre 4 est présentée une validation du comportement dynamique du modèle 2D, à travers la comparaison du modèle réduit 2D, avec un modèle éléments finis 3D qui reproduise l'ensemble de l'installation (Fig. 6). En outre, la comparaison des essais de crissement, réalisée sur le dispositif expérimental, avec les résultats numériques permet de confirmer que le modèle 2D est capable de reproduit les instabilités dynamiques du système réel (Fig. 7).

Dans la dernière partie de ce travail (chapitre 5) le bilan énergétique est appliqué pour résoudre un problème ouvert sur les instabilités dynamiques de contact, i.e. la prévisibilité réelle du régime permanent instable dans le cas d'un système caractérisé par plusieurs modes instables. Ici, l'approche de l'énergie est appliquée à un modèle de paramètres concentrés (Fig. 8). A partir des résultats de l'analyse des valeurs propres complexes, un nouvel indice d'instabilité a été défini via des considérations énergétiques. Le nouvel indice permet de comparer les différents modes instables et donne une mesure de la capacité de chaque mode à générer du crissement et à dominer la réponse transitoire.

Les principales contributions de ce travail sont résumées ci-après. Les vibrations

2D radial	2D circumferential	3D radial	3D circumferential	3D axial

2D mode 5 (9837 Hz)   3D mode 46 (5002 Hz)

2D mode 7 (10500 Hz)   3D mode 74 (7039 Hz)
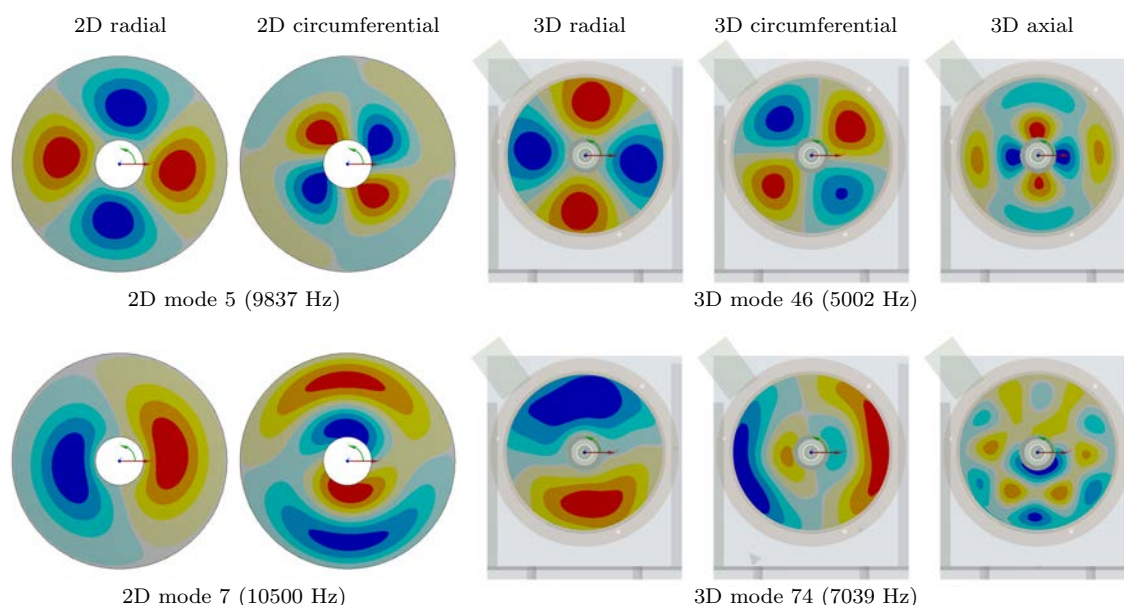
Figure 7: Comparaison de modes 3D et 2D.

induites par frottement ont été analysées numériquement sur un système 2D, qui reproduit le dispositif PhotoTrib développé au laboratoire de LaMCoS, et composé d'un corps élastique en contact frottant sur une surface rigide. Les résultats de l'analyse non linéaire transitoire ont confirmé les résultats de l'analyse des valeurs propres complexes sur la stabilité du système. La réponse transitoire est caractérisée par une réponse harmonique à la fréquence de l'un des modes instables dans le plan prédits par l'analyse des valeurs propres complexes (Fig. 9(a)). Les résultats mettent en évidence que même un système simple constitué par un corps déformable unique en contact frottant peut être instable.

Une formulation du bilan énergétique a été développée et analysée au cours de la réponse transitoire des vibrations induite par frottement aussi bien en conditions stables qu'instables. Elle montre que, pendant le contact frottant dans des conditions stables la plus grande partie de l'énergie est dissipée au contact, alors qu'une petite quantité d'énergie introduite dans le système produit une vibration qui est dissipée par l'amortissement matériau. En revanche, en cas de vibrations instables, l'augmentation exponentielle initiale de l'amplitude de vibration dépend de la différence entre l'énergie introduite par les vibrations induites par le frottement et les termes dissipatives (Fig. 5(c)); le cycle limite permanent est caractérisé par un équilibre entre l'énergie introduite dans le système par le contact et les termes dissipatifs. Cet équilibre énergétique permet une répartition de l'énergie introduite dans le système mécanique entre les deux termes dissipatifs.

Une analyse paramétrique a été développée pour étudier les effets, sur la réponse transitoire, des variations du coefficient de frottement et de la vitesse relative entre la surface rigide et le corps élastique. Les résultats ont mis en évidence l'influence de la distribution de la non-linéarité de contact sur l'excitation effective d'un mode

Figure 8: Modèle de paramètres concentrés.

instable, parmi les plusieurs modes instables via une analyse des valeurs propres complexes (Fig. 10). Les vibrations induites par frottement et le comportement dynamique local affectent le coefficient de frottement local moyen, qui montre une valeur maximale égale au coefficient de frottement imposé (Fig. 9(c)).

En outre, des comportements spécifiques ont été mis en évidence pour l'énergie mécanique et ses deux composants (l'énergie potentielle élastique et l'énergie cinétique), ainsi que pour la puissance échangée au contact et les termes dissipatifs de l'équilibre énergétique (Fig. 11 et 12). Des plages de transition des fluxes d'énergies ont été récupérées pour des gammes spécifiques des paramètres, correspondant à la transition du comportement local de contact.

La puissance, globale absorbée et dissipée par le système dans le cycle limite du régime permanent, est généralement différente de la puissance théorique absorbée pendant l'état stationnaire dans une condition de glissement uniforme (Fig. 12). La quantité de l'énergie absorbée par le système pendant le cycle limite, ainsi que la répartition entre les différents termes dissipatifs, dépend du comportement effectif du contact atteint au cours des vibrations instables (Fig. 10). En particulier, les vibrations induites par frottement modifient la capacité globale du système à absorber et dissiper l'énergie; une estimation de la puissance dissipée au contact, sans prendre en compte le comportement dynamique du système (flux d'énergie par les vibrations induites par frottement) peut conduire à des erreurs significatives dans la quantification de l'énergie dissipée au contact, ce qui affecte directement plusieurs phénomènes tribologiques.

La caractérisation dynamique 2D et 3D du dispositif PhotoTrib a permis une

(a) Fréquence principale des vibrations misurate pendant le limite cyclle.

(b) Amplitude de vibration tangentielle d'un noeud de contact au cours de cyclle limite.

(c) Coefficient de frottement moyen pendant le limite cyclle.

Figure 9: Réponse globale du système pendant le cycle limite pour valeurs différentes du coefficient de frottement et de la vitesse de rotation de la surface rigide interne.

(a) $\mu = 0.2$.

(b) $\mu = 0.3$.

(c) $\mu = 0.4$.

Figure 10: Effet de la vitesse de rotation Ω (RPM) et du coefficient de frottement μ sur la répartition de l'état de contact de la surface entière Σ_c pendant l'état stationnaire.

comparaison entre les résultats numériques du modèle 2D simplifié et les mesures expérimentales. Les mesures expérimentales de crissement montrent comment les mêmes modes instables sont reproduits soit expérimentalement soit numériquement, validant l'utilisation de la simulation 2D transitoires pour l'analyse des vibrations instables induites par le frottement sur le dispositif PhotoTrib (Fig. 13).

Les résultats d'une campagne expérimentale préliminaire permettent de distinguer parmi les principaux effets de la dissipation locale de l'énergie au contact sur la réponse dynamique du système. L'échauffement, généré par l'énergie dissipée au niveau du contact, produit une dilatation thermique réversible qui entraîne une augmentation du couple de freinage (Fig. 14). En outre, l'énergie dissipée au niveau du contact est également à l'origine de l'usure et des phénomènes physico-chimiques, avec la formation d'une couche de troisième-corps, qui produit une modification permanente des surfaces de contact, i.e. la modification permanente du couple de
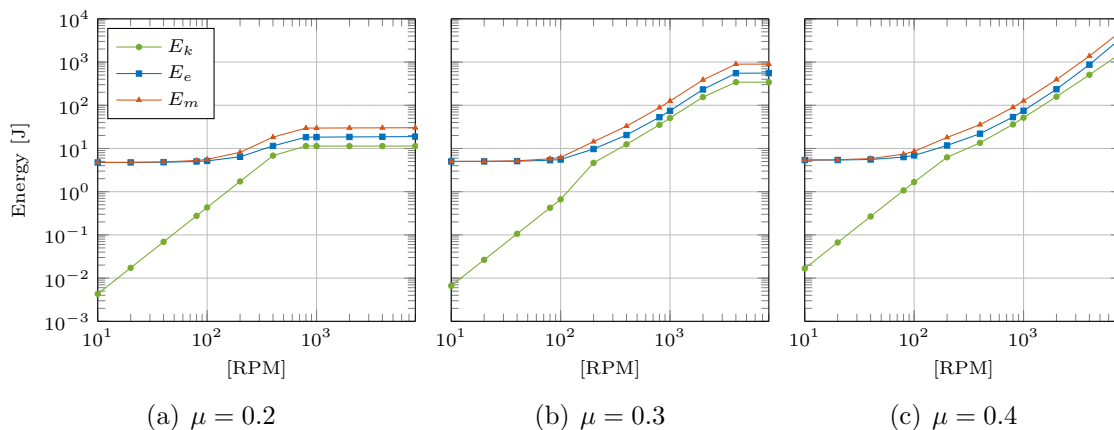
Figure 11: Répartition de l'énergie mécanique entre l'énergie élastique et cinétique Pendant le cycle de la limite, pour les différentes vitesses de rotation de la surface rigide.

freinage (Fig. 15).

Un modèle modulaire à parametrès concentrès avec des contacts frottants a été mis au point pour reproduire des vibrations induites par frottement (Fig. 8). L'utilisation d'un modèle réduit, combiné à une technique de solution linéaire par morceaux, permet une intégration rapide de la solution transitoire. Le modèle a été conçu avec une formulation modulaire, et chaque module dispose de degrés de liberté soit en contact soit en non contact avec des curseurs rigides; le but est la possible l'extension des dégrées de liberté du système et la présence de dégrées de liberté représentant soit l'interface de contact soit le système.

L'équilibre énergétique précédamment formulé a été utilisé sur le modèle à paramétres concentrés, pour approcher le problème de la surestimation d'instabilité, qui est caractéristique d'une analyse des valeurs propres complexes. Un nouvel indice d'instabilité (MAI) a été défini, par des considérations énergétiques, pour comparer les différents modes instables et pour sélectionner le mode qui devient effectivement instable pendant la réponse transitoire (Table 1).

L'indice d'absorption modale permet de quantifier l'attitude de chaque mode à échanger de l'énergie avec l'environnement extérieur. L'utilisation du nouvel indice énergétique sur le système à paramétres concentrés montre un bon accord entre la régime permanent (fréquence instable) et la valeur de l'indice MAI, calculé sur tous les modes instables du système.

L'indice MAI permet de définir une hiérarchie entre les divers modes instables du système et de mieux comprendre l'évolution de la réponse transitoire jusqu'au cycle limite du régime permanent. La coexistence de plusieurs fréquences modales dans la réponse transitoire a été associée à des valeurs similaires du MAI, i.e. la measure de la capacite de chaque mode à absorber l'énergie.

Le rôle de la perturbation initiale sur la sélection du mode instable dans la

(a) $\mu = 0.2$ (b) $\mu = 0.3$ (c) $\mu = 0.4$
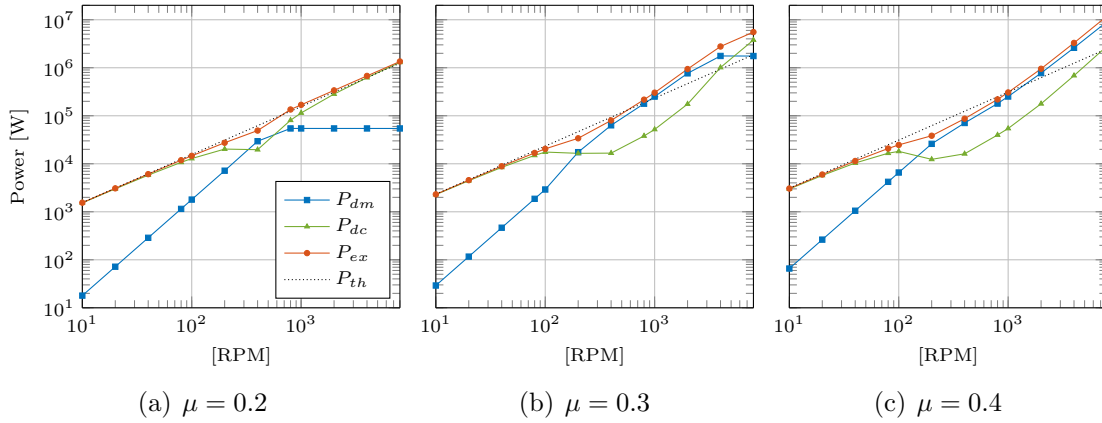
Figure 12: Décomposition de la puissance totale absorbée dans les deux termes dissipatives, pour les différentes vitesses de rotation de la surface rigide Ω (RPM).

réponse transitoire a été souligné. En général, l'excitation à large bande à l'interface de contact peut être supposée être à l'origine de la perturbation initiale de la dynamique du système. L'indice MAI tient en compte la forme de la perturbation initiale par la projection des vecteurs propres sur la position d'équilibre initiale.

Perspectives

Ce travail est axé sur l'équilibre de l'énergie mécanique pendant les vibrations de crissement, en ne considérant que la déformation élastique, la dissipation par l'amortissement et la dissipation de contact liées au déplacement relatif. Plusieurs autres aspects sont nécessaires d'être pris en compte, tels que les effets thermiques, les déformations plastiques locales et leurs effets sur la distribution des contraintes au niveau du contact. La puissance dissipée au contact pourrait être utilisée pour un couplage avec la méthode des éléments discrets (DEM), afin de distinguer la partie de la puissance mécanique réellement dissipée par l'éechauffement et la partie qui produit de modifications de surface locales: comme le détachement de matiére et l'évolution du troisième corps. Des développements ultérieurs de l'équilibre énergétique pourraient fournir des informations importantes vers une meilleure modélisation du coefficient de frottement local, en considérant l'effet des vibrations induites par frottement sur les phénomènes locales du contact.

    Une analyse thermomécanique complète des vibrations à haute fréquence induites par frottement serait intéressante, mais la différence des échelles temporelles entre la dynamique du système (1 ms) et les phénomènes thermiques globales (10 s) implique une pleine intégration directe difficile à mettre en œuvre. Néanmoins, l'utilisation combinée de l'analyse thermomécanique quasi-statique avec l'analyse des valeurs propres complexes et l'analyse transitoire non linéaire pourrait conduire à une meilleure compréhension de l'évolution des phénomènes de crissement sur un
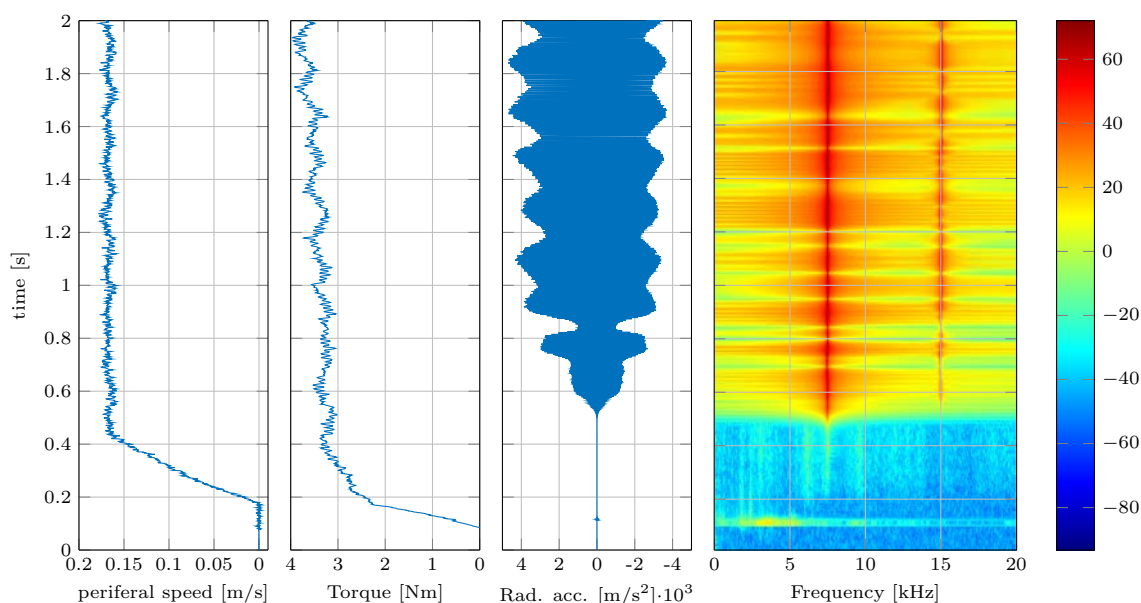
Figure 13: Réponse transitoire pour une vitesse de rotation $\Omega = 80\,\text{RPM}$ et une expansion radiale $\Delta r = 10\,\mu\text{m}$.
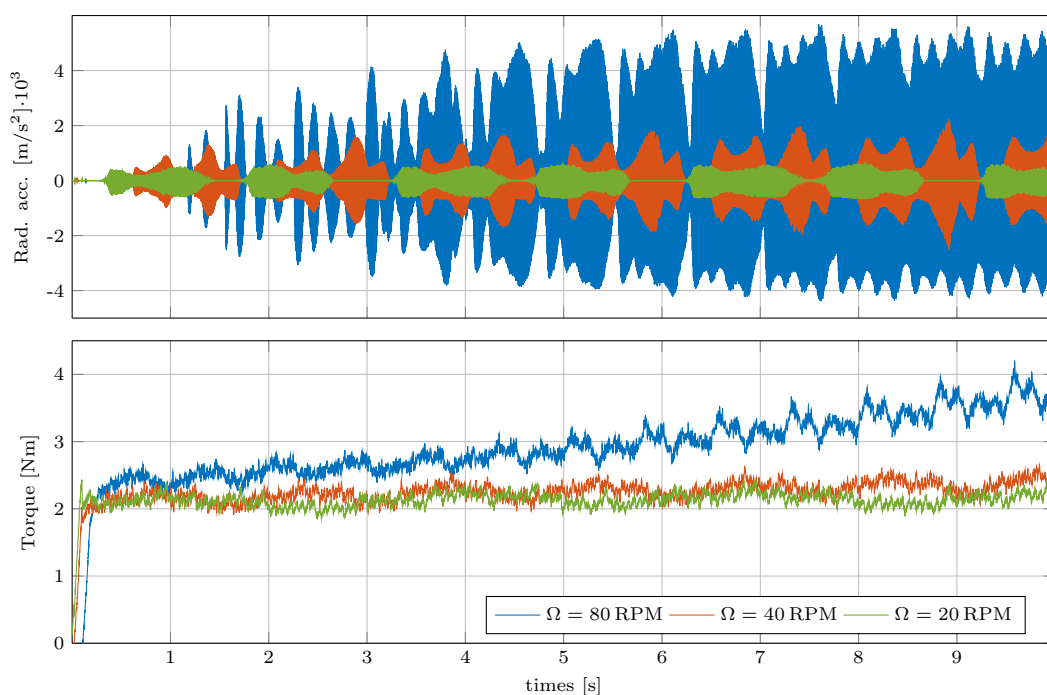
Figure 14: Réponse transitoire pour différentes valeurs de la vitesse de rotation ($\Omega = [20; 40; 80]\,\text{RPM}$). Réponse d'accélération dans la direction radiale (en haut) et le couple du moteur (en bas) en fonction du temps.
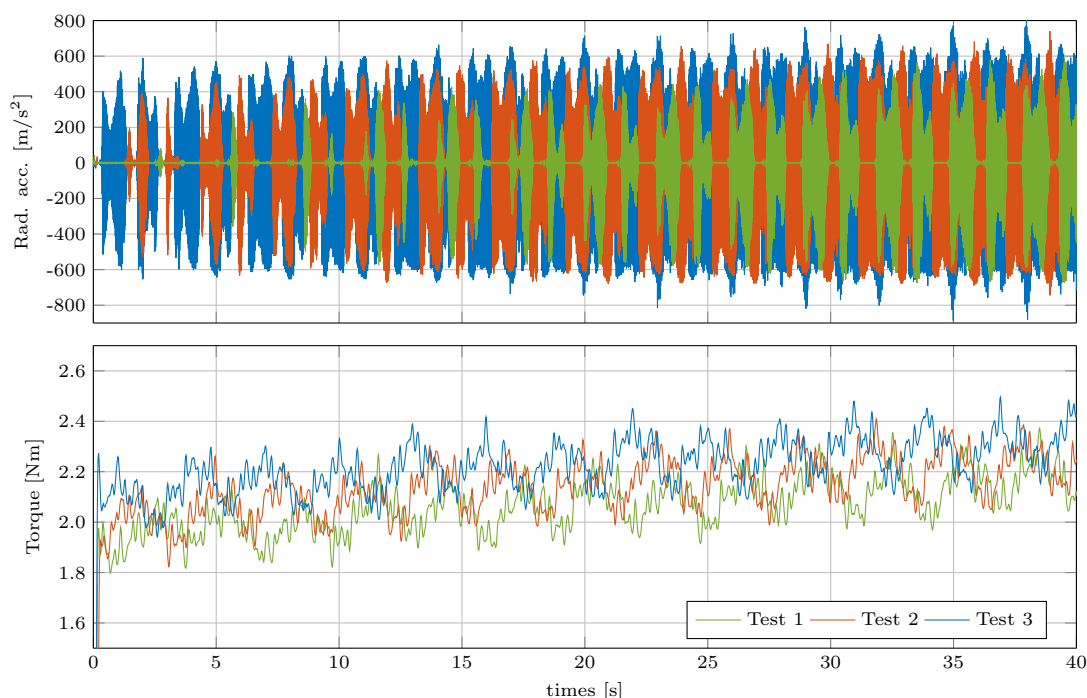
Figure 15: Réponses transitoires de trois essais consécutifs avec la même valeur de la vitesse de rotation ($\Omega = 20\,\mathrm{RPM}$). Réponse d'accélération dans la direction radiale (en haut) et le couple du moteur (en bas) en fonction du temps.

intervalle de temps de plusieurs secondes, qui caractérise généralement les épisodes de crissement.

La reproduction expérimentale des vibrations induite par frottement n'est toujours pas facile à gérer; en fait, l'interaction réelle de tous les phénomènes multiphysiques impliqués fait sa propre interprétation qui n'est pas évidente. L'étude numérique donne plusieurs éléments utiles pour améliorer la compréhension du comportement réel. L'observation directe du comportement local du contact est en fait impossible sans des modifications substantielles du système mécanique. Dans ce contexte, la tribologie numérique, combinée à l'analyse détaillée de la dynamique du contact, donne des informations utiles sur les phénomènes impliqués dans le contact.

Plusieurs aspects doivent d'avantage être étudiés d'un point de vue expérimentale sur le dispositif PhotoTrib:

- des analyses paramétriques ultérieures doit être effectuées pour distinguer les effets thermiques et les différentes modifications de surface;

- des observations de la surface de contact à travers le matériau en polycarbonate avec une caméra rapide peuvent donner des informations sur l'évolution de la couche de troisième corps;

		Friction coefficient μ						
		0.5	1.0	1.5	2.0	2.2	3.0	
Modes	1	$-1.36\mathrm{e}-03$	$-1.43\mathrm{e}-01$	$-6.87\mathrm{e}-01$	$-1.72\mathrm{e}+00$	$-2.30\mathrm{e}+00$	$-5.67\mathrm{e}+00$	χ_r [W]
	2	$-6.80\mathrm{e}-14$	$-7.69\mathrm{e}-12$	$-4.07\mathrm{e}-11$	$-1.16\mathrm{e}-10$	$-1.64\mathrm{e}-10$	$-5.39\mathrm{e}-10$	
	3	$-2.27\mathrm{e}+00$	$-5.62\mathrm{e}+00$	$-2.01\mathrm{e}+01$	$-3.68\mathrm{e}+02$	$-1.57\mathrm{e}+02$	$-1.37\mathrm{e}+02$	
	4	$-6.44\mathrm{e}-03$	$-9.83\mathrm{e}-01$	$-9.88\mathrm{e}+00$	$-5.42\mathrm{e}+01$	$+3.41\mathrm{e}+01$	$+7.03\mathrm{e}+01$	
	5	$-2.58\mathrm{e}-10$	$-6.72\mathrm{e}-10$	$-1.10\mathrm{e}-09$	$-1.66\mathrm{e}-09$	$-1.91\mathrm{e}-09$	$-3.05\mathrm{e}-09$	
	6	$-7.92\mathrm{e}-12$	$-7.23\mathrm{e}-11$	$+1.30\mathrm{e}-10$	$+3.76\mathrm{e}-10$	$+4.91\mathrm{e}-10$	$+1.05\mathrm{e}-09$	
$\mathrm{Re}(\lambda_4)$		-3.20	-3.11	-3.00	-1.03	$+1.29$	$+5.47$	Hz
$\mathrm{Re}(\lambda_6)$		-4.68	-0.91	$+1.24$	$+2.75$	$+3.32$	$+5.14$	
f_{lc}		$-$	$-$	219	$219-166$	166	166	Hz
mode_{lc}		$-$	$-$	6	$6-4$	4	4	

Table 1: Indice MAI χ_r rapporté à la partie réelle des valeurs propres complexes pour plusieurs valeurs du coefficient de frottement. Les cellules en gris clair correspondent aux modes couplés, les cellules en gris foncé correspondent aux modes instables. f_{lc}est la fréquence mesurée dans le cycle limite et mode_{lc} est le mode correspondant. Les valeurs bordés indiquént les modes prévus pour être instable par l'indice AMI χ et les modes ayant plus grande partie réelle des valeurs propres.

- une mesure locale de la dynamique de contact et de l'évolution de la température, par exemple avec un vibromètre laser et des thermocouples, fourniraient une mesure indirecte expérimentales de l'énergie effectivement introduit dans le disque de polycarbonate, et de l'énergie réellement dissipée au contact;

- les vibrations hors du plan devraient ainsi être mesurées afin d'estimer la dissipation d'énergie liée à la composante hors-plan des vibrations.

Le couplage de la présente analyse avec l'étude locale de la génération de la propagation d'onde au contact pourrait donner des informations utiles sur la façon dont la teneur en énergie à haute fréquence au contact (excitation ultrasonique lie à la propagation des ondes de surface dans le volume) est transféré vers la gamme de fréquence de vibration du système (dynamique d'ensemble du système). Des expériences avec une instrumentation acoustique près du contact pourraient ainsi valider cette approche.

L'indice d'absorption modale a été appliqué dans cette thèse, avec des résultats très prometteurs, sur un modèle à paramètres concentrés. Cette méthode est maintenant prête à être appliquée sur des systèmes plus réalistes. La prochaine étape sera l'extraction des matrices des vecteurs propres du CEA, effectuées sur le modèle éléments finis 2D du dispositif PhotoTrib, afin de calculer le MAI et vérifier que les fréquences de crissement obtenues par l'analyse transitoire et expérimentale correspond à celle prédite par le MAI. Une fois validée par les simulations par éléments finis et les expériences, l'approche présentée ici sera étendue à un système de freinage commerciale utilisant le CEA, via des modèles d'éléments finis complets.

Riassunto sostanziale

Bilancio energetico meccanico di un contatto con attrito; dalla dissipazione di superficie alla dissipazione di volume nelle instabilità dinamiche di contatto

Introduzione

Ogni volta che si genera un movimento relativo tra due sistemi con una interfaccia di contatto ad attrito secco, l'attrito induce delle vibrazioni nell'intero sistema meccanico. La dinamica locale al contatto (rotture e la generazione d'onde) si accoppia con la dinamica del sistema, dando origine a delle vibrazioni che modificano il comportamento di attrito macroscopico del sistema.

Le deformazioni dovute alla risposta dinamica del sistema modificano la distribuzione degli stress locali di contatto; al contrario, la variazione locale degli stress di contatto e dello stato di contatto (scorrimento, adesione, separazione), le onde generate dalle rotture locali, e le caratteristiche locali di contatto (rigidezza, smorzamento, etc.) modificano la risposta dinamica del sistema.

Le così dette vibrazioni indotte da attrito possono portare sia ad un rumore acustico di piccola ampiezza caratterizzato da un largo spettro di frequenze, che è funzione delle caratteristiche della superficie (e.g. la rugosità) e della dinamica dei corpi in contatto; sia a un segnale acustico di ampiezza elevata caratterizzato da una eccitazione impulsiva o da uno spettro armonico.

Quest'ultimo è caratteristico delle instabilità dinamiche del sistema eccitate dalle forze di contatto. Le instabilità dinamiche di contatto sono state l'oggetto di molti studi condotti su applicazioni specifiche come il "cigolio" dei giunti meccanici, lo "squeacking" delle protesi d'anca o lo "squeal" dei freni automobilistici.

Nonostante il comportamento dinamico dei sistemi meccanici con attrito secco sia stato largamente studiato nella letteratura degli ultimi decenni, manca ancora una piena comprensione della problematica. Le vibrazioni indotte da attrito, infatti, non possono essere ridotte ad un problema dinamico complesso in quanto coinvolgono altri fenomeni altrettanto complessi legati alla tribologia del contatto. Allo stato attuale, il non considerare la natura multi-fisica del problema porta a vedere come imprevedibili, difficili o inosservabili la maggior parte dei fenomeni legati alle vibrazioni indotte da attrito. Una piena presa in conto della reale complessità del

(a) Descrizione dei percorsi dell'energia durante l'attrito [AKA 02].

(b) Scale dimensionali e temporali associati all'attrito ed esempi dei diversi fenomeni associati [AKA 02].
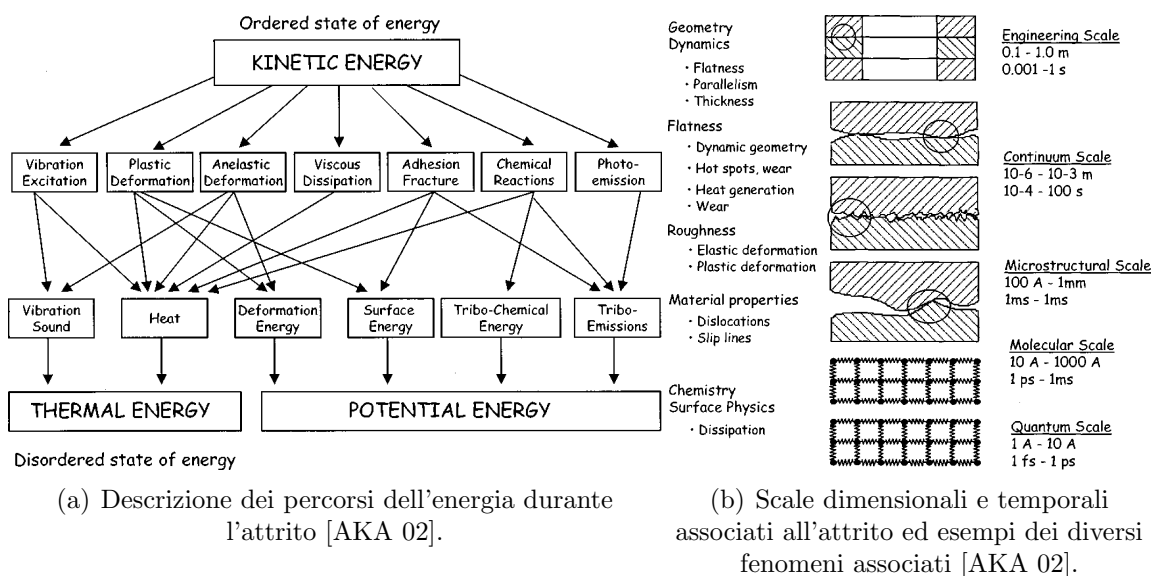
Figure 16: Trasformazione dell'energia e scale dei fenomeni.

problema non è banale a causa della differenza tra le scale spaziali e temporali dei fenomeni in gioco. Al fine di sviluppare un approccio complessivo allo studio dei fenomeno multi-fisico, l'energia potrebbe essere utilizzata come una caratteristica fisica universale di accoppiamento (Fig. 16(a)). Lo studio dei flussi d'energia potrebbe in fatti fornire dei nuovi elementi per la comprensione dell'interazione tra il comportamento dinamico del sistema, la dinamica locale ed il comportamento tribologico dell'interfaccia di contatto.

Questa tesi si concentra sullo studio dei flussi di energia meccanica coinvolta nelle vibrazioni indotte da attrito, allo scopo di comprendere l'influenza della dinamica del contatto sulla risposta del sistema e vice versa. I flussi di energia, provenienti dalla superficie in contatto e dovuti alle vibrazioni indotte da attrito, eccitano la risposta dinamica del sistema e vice versa, l'influenza della risposta dinamica del sistema sulla dissipazione di energia locale all'interfaccia di contatto influisce sui fenomeni tribologici ad essa connessi. La distinzione tra differenti termini energetici è stata quindi utilizzata per identificare i contributi dei due termini dissipativi, i.e. la dissipazione per smorzamento materiale e la dissipazione al contatto. Questo lavoro punta a introdurre una nuova prospettiva nello studio delle vibrazioni indotte da attrito, osservando da un punto di vista energetico l'accoppiamento tra il comportamento locale al contatto e la dinamica globale.

Risultati

In questa tesi le vibrazioni indotte da attrito sono state analizzate utilizzando tre approcci comuni: l'approccio ad elementi finiti, per studiare, attraverso l'analisi dei

flussi energetici l'accoppiamento tra il contatto e la dinamica del sistema; l'approccio sperimentale, per validare i risultati numerici e osservare l'influenza dei fenomeni non ancora inclusi nel modello numerico; l'approccio tramite un modello a parametri concentrati, per valutare rapidamente gli effetti dei parametri del sistema.

Come primo passo, l'analisi delle vibrazioni indotte da attrito con un approccio energetico si concentra principalmente sullo studio delle vibrazioni instabili, data la forte interazione tra la dinamica locale e la dinamica al contatto. Una prima applicazione di questo approccio generale è stata qui proposta per risolvere il problema della selezione tra i diversi modi instabili, determinati tramite una analisi agli autovalori complessi di un sistema con attrito secco.

Il lavoro é organizzato come segue:
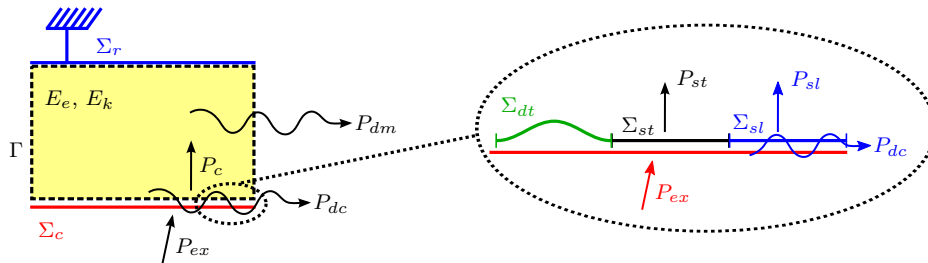
Figure 17: Schema di bilancio energetico. E_e e E_k sono rispettivamente l'energia potenziale elasitca e l'energia cinetica del corpo elastico Γ, Σ_rè la parte del bordo su cui è imposto un vincolo rigido, Σ_c è la parte del bordo in cui è stata definita l'interazione di contatto. P_c è la potenza totalmente scambiata al contatto, P_{ex} è la potenza assorbita dal sistema e P_{dm} è la potenza dissipata dallo smorzamento materiale. Σ_{dt}, Σ_{sl} e Σ_{st} rappresentano rispettivamente la parte della superficie in contatto Σ_c in condizioni di distacco, di scorrimento e di aderenza. P_{sl} e P_{st} sono rispettivamente le potenza scambiate in scorrimento ed aderenza. P_{dc} è la potenza dissipata al contatto.

La prima parte fornisce una panoramica dei problemi legati alla dinamica del contatto con attrito nella letteratura (capitolo 1), includendo i lavori di ricerca focalizzati sull'analisi delle energie coinvolte nelle vibrazioni indotte da attrito. Successivamente, nel capitolo 2 vengono introdotti i modelli numerici e sperimentali ed i metodi di analisi utilizzati negli studi numerici e sperimentali presentati nella tesi; infine, viene formulato un bilancio energetico meccanico per un sistema meccanico con attrito secco.

Il capitolo 3 presenta uno studio numerico su un modello agli elementi finiti 2D di un dispositivo sperimentale (Fig. 18). Con un approccio classico, la stabilità del sistema è stata valutata tramite un'analisi lineare agli autovalori complessi in funzione del coefficiente di attrito (Fig. 19); quindi, la risposta del sistema in regime permanente è stata calcolata tramite una analisi non lineare transitoria (Fig. 20). Le grandezze energetiche implicate nelle vibrazioni indotte da attrito sono state analizzate durante la risposta transitoria (Fig. 20(c)), per osservare l'effetto del
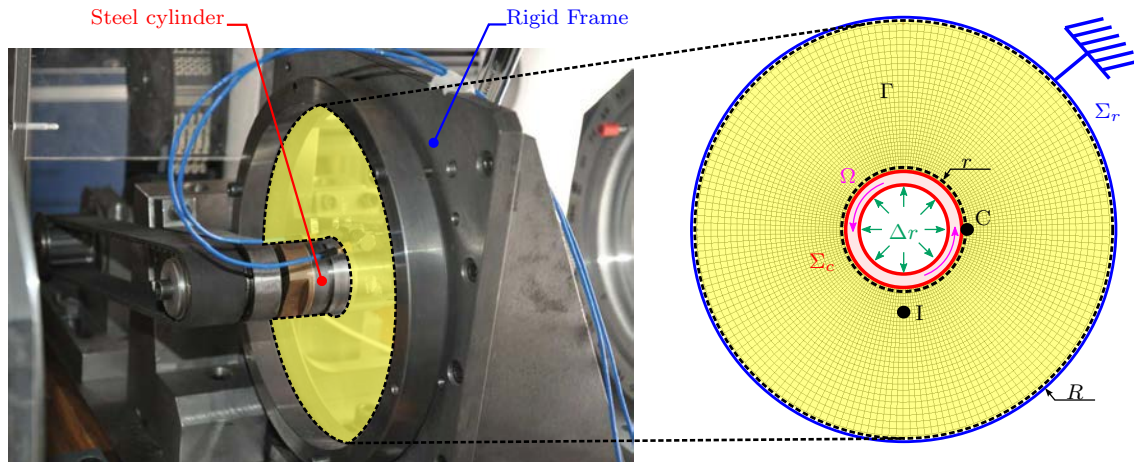
Figure 18: Dispositivo sperimentale "PhotoTrib" utilizzato per validare i risultati numerici (a sinistra) e il modello agli elementi finiti del disco in policarbonato (a destra).
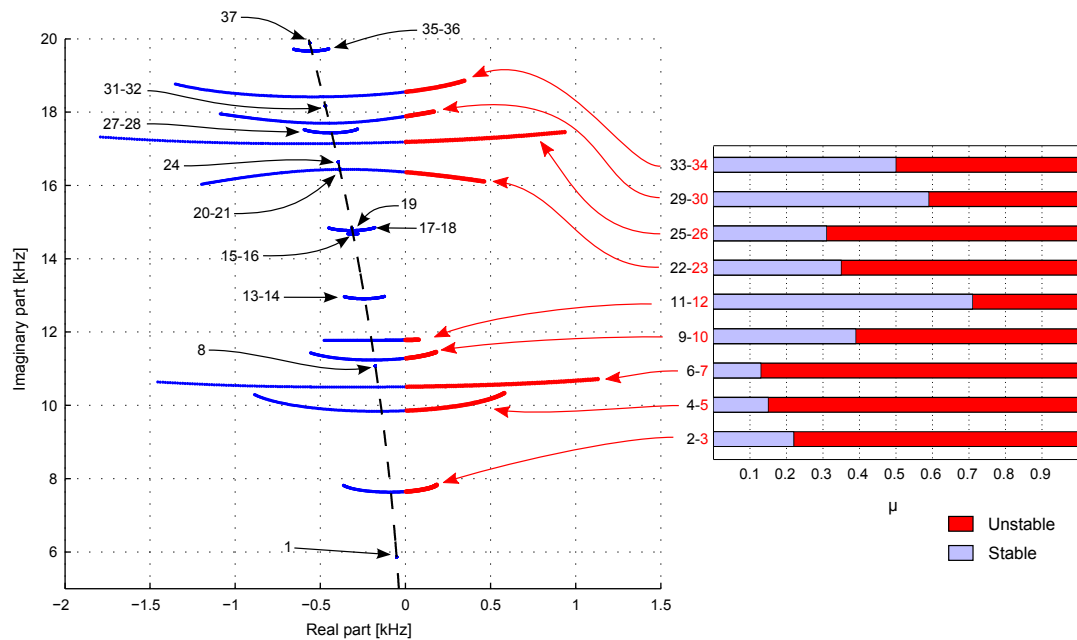
Figure 19: Grafico autovalori del sistema. Per ciascun autovalore che diventa instabile è ripostato il coefficiente di attrito critico nel grafico di stabilità.

(a) Risposta temporale (velocità) di un nodo interno I in direzione circonferenziale e radiale.

(b) Stress tangenziali e normali misurati su un nodo al contatto.

(c) Potenza scambiata e dissipata.

(d) Evoluzione delle condizioni di contatto.

(e) Coefficiente di attrito locale medio.

(f) Forza tangenziale e velocità tangenziale di un nodo al contatto. Parti grigie rappresentano gli intervalli di tempo in cui la potenza nodale $\widetilde{P}_c < 0$.

Figure 20: Risposta del sistema in caso di coefficiente di attrito $\mu = 0.3$ ed una velocità di rotazione $\Omega = 100$ RPM.

coefficiente di attrito locale e delle condizioni al contorno (Fig. 20(d)) sui differenti termini del bilancio energetico.
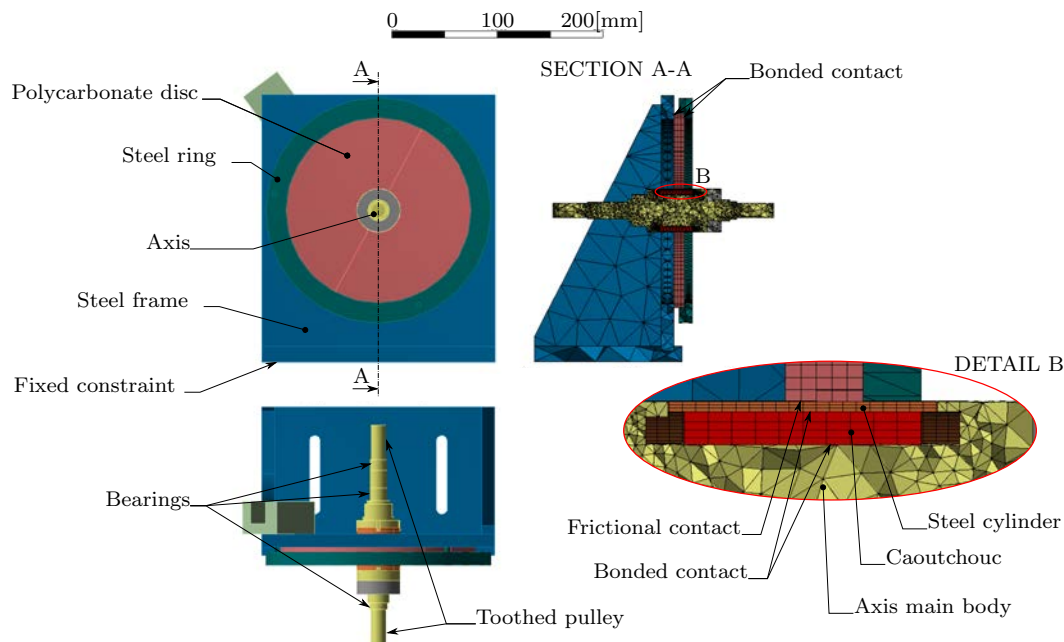
Figure 21: Modello agli elementi finiti 3D, condizioni al contorno e contatti.

Nel capitolo 4 è presentata una validazione del comportamento dinamico del modello 2D, tramite il confronto del modello ridotto 2D con un modello agli elementi finiti 3D che riproduce l'assieme del sistema meccanico (Fig. 21). Inoltre, il confronto dei test di squeal, realizzati sul dispositivo sperimentale, con i risultati numerici permette di confermare che il modello 2D è capace di riprodurre le instabilità dinamiche di contatto del sistema reale (Fig. 22).

Nell'ultima parte di questo lavoro (capitolo 5) il bilancio energetico è stato applicato allo studio di un problema aperto sulle instabilità dinamiche di contatto, i.e. la reale predicibilità del regime permanente instabile nel caso di un sistema caratterizzato da più modi instabili. In questo caso, l'approccio energetico è stato applicato ad un modello a parametri concentrati (Fig. 23). A partire dai risultati dell'analisi agli autovalori complessi, è stato definito un nuovo indice tramite delle considerazioni energetiche. Il nuovo indice permette di confrontare i diversi modi instabili e fornisce una misura della capacità di ciascun modo di generare squeal e di dominare la risposta transitoria.

I principali contributi originali di questo lavoro sono riassunti qui di seguito.

Le vibrazioni indotte da attrito sono state analizzate numericamente su un sistema 2D, che riproduce il dispositivo sperimentale PhotoTrib sviluppato al laboratorio LaMCoS, e composto da un corpo elastico in contatto con attrito su una superficie rigida. I risultati delle analisi non lineare transitorie hanno confermato i risultati dell'analisi agli autovalori complessi sulla stabilità del sistema. La risposta transito-

2D radial   2D circumferential   3D radial   3D circumferential   3D axial

2D mode 5 (9837 Hz)   3D mode 46 (5002 Hz)

2D mode 7 (10500 Hz)   3D mode 74 (7039 Hz)
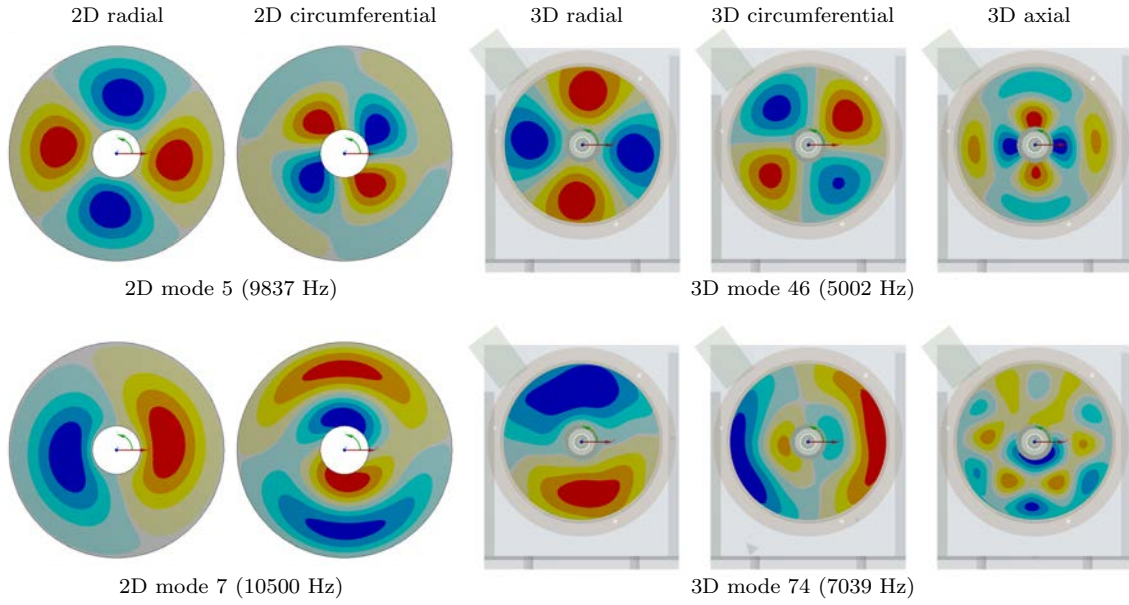
Figure 22: Confronto dei modi 3D e 2D.
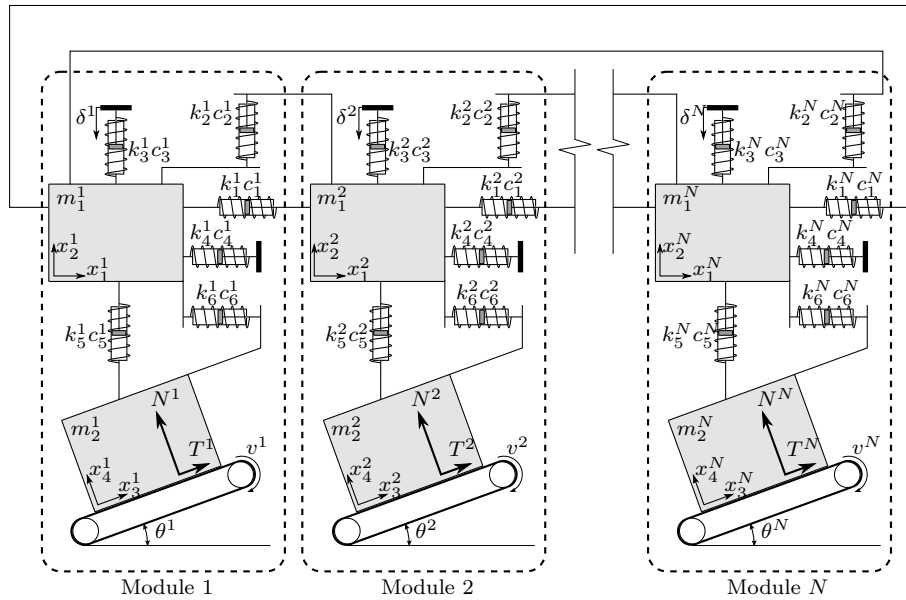
Figure 23: Modello modulare a parametri concentrati.

(a) Frequenze principali delle vibrazioni misurate durante il ciclo limite.

(b) Ampiezza della vibrazione tangenziale di un nodo al contatto durante il ciclo limite.

(c) Coefficiente di attrito medio durante il ciclo limite.
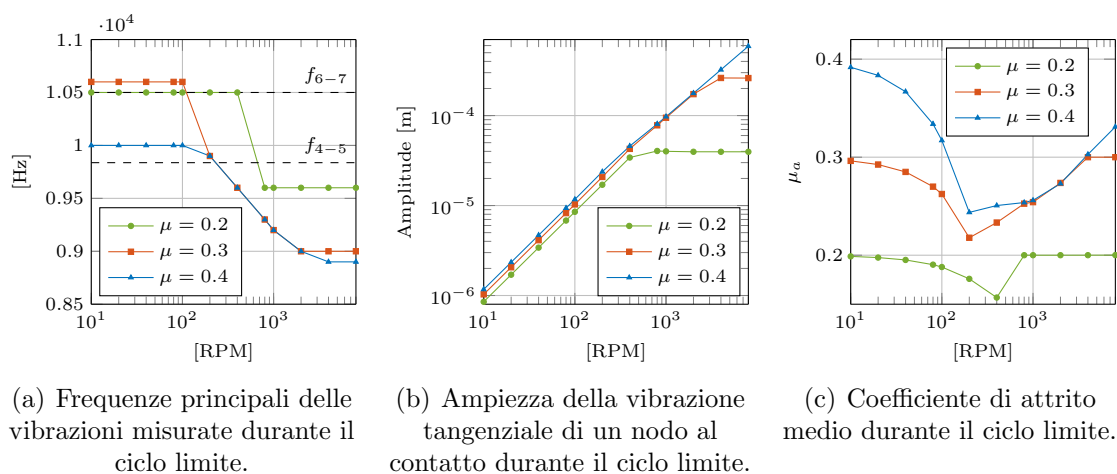
Figure 24: Risposta globale del sistema durante il ciclo limite per valori differenti del coefficiente di attrito e della velocità di rotazione della superficie rigida interna.

ria è caratterizzata da uno spettro armonico alla frequenza di uno dei modi instabili in piano predetti dall'analisi agli autovalori complessi (Fig. 24(a)). I risultati evidenziano che anche un sistema semplice costituito da un solo corpo deformabile in contatto con attrito può essere instabile.

È stata sviluppata una formulazione di un bilancio energetico e i termini di tale bilancio sono stati analizzati durante la risposta transitoria delle vibrazioni indotte da attrito sia in condizioni stabili che instabili. Queste analisi mostrano che durante il contatto con attrito in condizioni stabili, la parte più consistente dell'energia viene dissipata al contatto, mentre una piccola quantià d'energia che viene introdotta nel sistema produce delle vibrazioni e viene quindi dissipate dallo smorzamento materiale. Al contrario, in caso di vibrazioni instabili, l'aumento esponenziale iniziale dell'ampiezza di vibrazione dipende dalla differenza tra l'energia introdotta dalle vibrazioni indotte da attrito ed i termini dissipativi (Fig. 20(c)); il ciclo limite della condizione permanente è caratterizzato da un equilibrio tra l'energia introdotta nel sistema attraverso il contatto ed i termini dissipativi. Questo equilibrio energetico permette una ripartizione dell'energia introdotta nel sistema meccanico tra i due termini dissipativi.

Vengono riportati, inoltre, i risultati di un'analisi parametrica sviluppata per studiare gli effetti, sulla risposta transitoria, delle variazioni del coefficiente di attrito e della velocità relative tra la superficie rigida ed il corpo elastico. I risultati hanno messo in luce l'influenza della distribuzione delle nonlinearità di contatto sull'effettiva eccitazione di uno dei modi instabili, tra i diversi modi instabili individuati dall'analisi agli autovalori complessi (Fig. 25). Le vibrazioni indotte da attrito ed il comportamento dinamico locale influiscono sul coefficiente di attrito locale medio, che mostra un valore massimo uguale al coefficiente di attrito imposto (Fig. 24(c)).

Inoltre, sono stati messi in evidenza dei trend tipici per l'energia meccanica e

(a) $\mu = 0.2$.   (b) $\mu = 0.3$.   (c) $\mu = 0.4$.
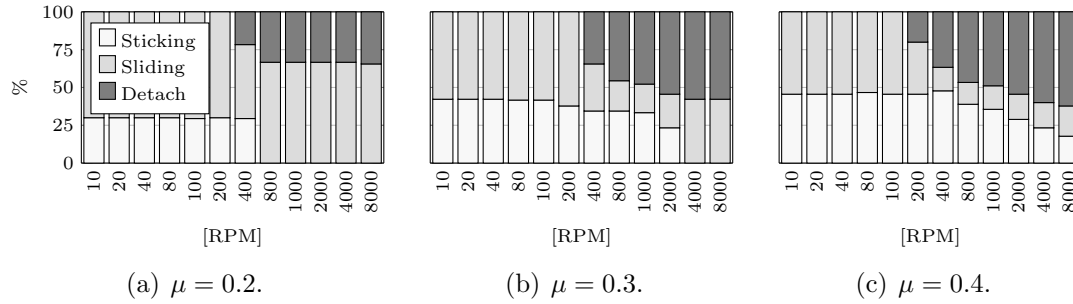
Figure 25: Effetto della velocità di rotazione Ω (RPM) e del coefficiente di attrito μ sulla ripartizione dello stato di contatto dell'intera superficie Σ_c durante le condizioni permanenti.

(a) $\mu = 0.2$ (b) $\mu = 0.3$ (c) $\mu = 0.4$
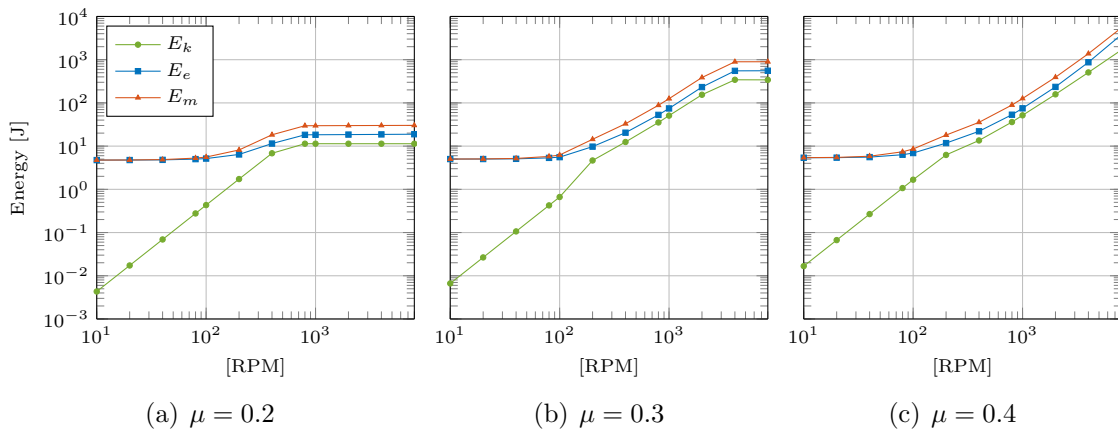
Figure 26: Suddivisione dell'energia meccanica in energia elastica ed energia cinetia durante il ciclo limite, per differenti velocità di rotazione della superificie rigida e diversi coefficienti di attrito.

le sue due componenti (l'energia potenziale elastica e l'energia cinetica), così come per la potenza scambiata ed i termini dissipativi del bilancio energetico (Fig. 26 e 27). Si possono tra l'altro individuare delle transizioni dei flussi di energia per dei range specifici dei parametri del sistema, che corrispondono alla transizione del comportamento locale del contatto.

La potenza globalmente assorbita e dissipata, dal sistema nel ciclo limite del regime permanente, è in generale diversa dalla potenza teorica assorbita durante lo stato stazionario in condizioni di scorrimento uniforme (Fig. 27). La quantità di energia assorbita dal sistema durante il ciclo limite, cosí come la ripartizione tra i diversi termini dissipativi, dipende dal comportamento effettivo del contato raggiunto durante le vibrazioni instabili (Fig. 25). In particolare, le vibrazioni indotte da attrito modificano la capacià complessiva del sistema di assorbire e di dissipare l'energia; una stima della potenza dissipata al contatto, senza tenere in conto il comportamento dinamico del sistema (flusso d'energia legato alle vibrazioni indotte da

(a) $\mu = 0.2$ (b) $\mu = 0.3$ (c) $\mu = 0.4$
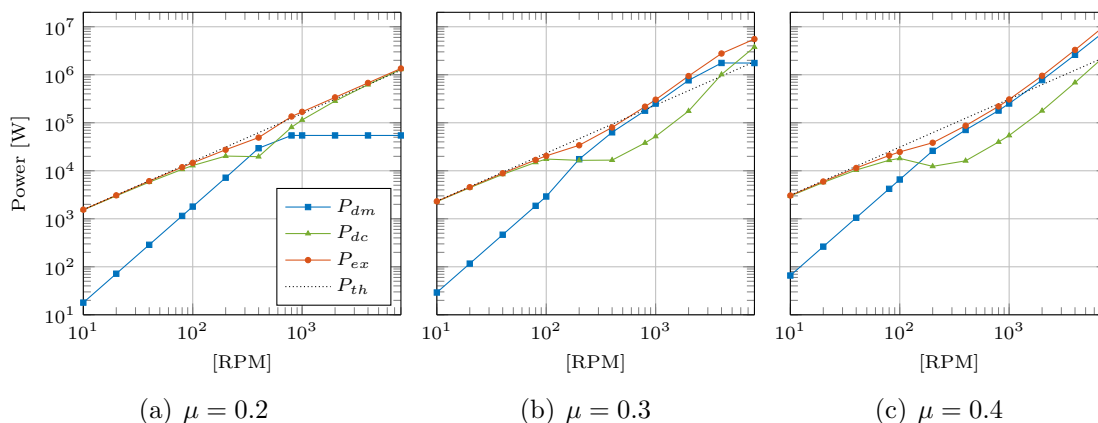
Figure 27: Scomposizione della potenza totale assorbita nei due termini dissipativi, per differenti velocità di rotazione della superificie rigida e diversi coefficienti di attrito.

attrito) potrebbe portare a degli errori significativi nella quantificazione dell'energia dissipata al contatto, e quindi dei fenomeni tribologici.

La caratterizzazione dinamica 2D e 3D del dispositivo sperimentale PhotoTrib ha permesso un confronto tra i risultati numerici del modello 2D semplificato e le misure sperimentali. Le misure sperimentali di squeal mostrano come gli stessi modi instabili siano riprodotti sia numericamente che sperimentalmente, ció permette di validare l'uso della simulazione 2D transitoria per l'analisi delle vibrazioni instabili indotte da attrito sul dispositivo sperimentale PhotoTrib.

I risultati di una campagna sperimentale preliminare permettono di distinguere tra i principali effetti della dissipazione locale dell'energia al contatto sulla risposta dinamica del sistema. Il riscaldamento, generato dall'energia dissipata al contatto è all'origine di una dilatazione termica reversibile che produce un'aumento della coppia resistente (Fig. 29). Inoltre, l'energia dissipata al livello del contatto è anche all'origine dell'usura e dei phonomeni fisico-chimici che portano alla generazione di uno strato di terzo corpo, che da luogo a una modificazione permanente delle superfici di contatto, i.e. la variazione permanente della coppia resistente (Fig. 30).

Un modello a parametri concentrati modulare e con dei contatti con attrito è stato sviluppato al fine di riprodurre le vibrazioni indotte da attrito (Fig. 23). L'uso di un modello ridotto, combinato ad una tecnica di soluzione lineare a tratti, permette una integrazione rapida della soluzione transitoria. Il modello, inoltre è stato concepito con una formulazione modulare, e ciascun modulo è caratterizzato da dei gradi li libertà sia in contatto che non in contatto con degli slider rigidi; lo scopo è il possibile incremento dei gradi di libertà del sistema e la presenza di gradi di libertà in grado di rappresentare sia l'interfaccia di contatto che il sistema.

L'equilibrio energetico precedentemente formulato è stato utilizzato sul modello a parametri concentrati, per affrontare il problema della sovra estimazione del numero di modi instabili, che è caratteristico di una analisi agli autovalori complessi.
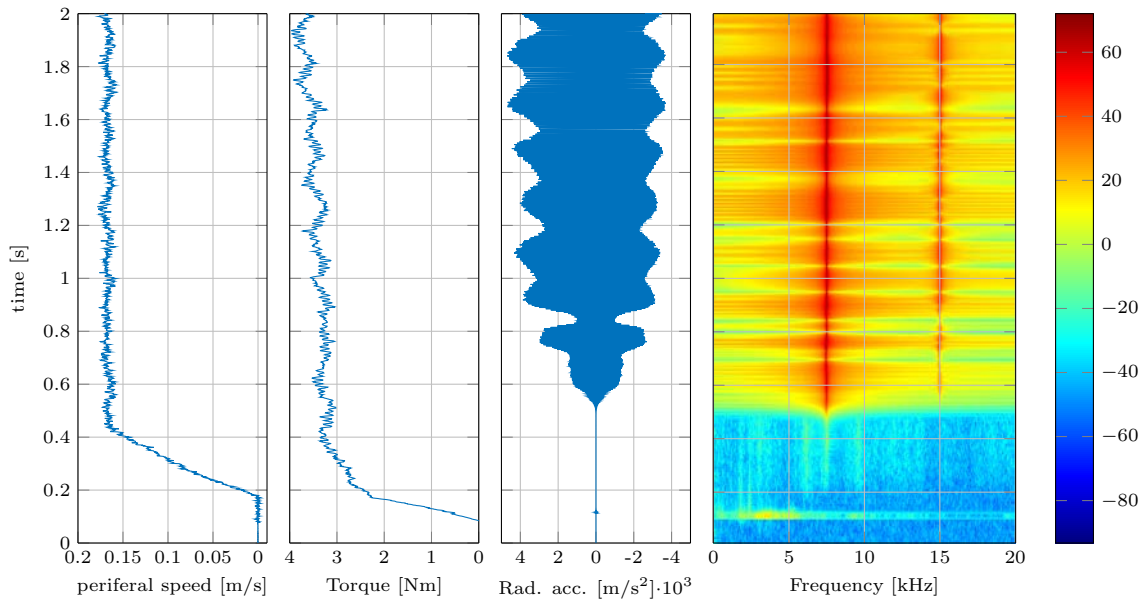
Figure 28: Risposta transitoria per una velocità di rotazione $\Omega = 80\,\mathrm{RPM}$ ed una espansione radiale $\Delta r = 10\,\mu\mathrm{m}$.
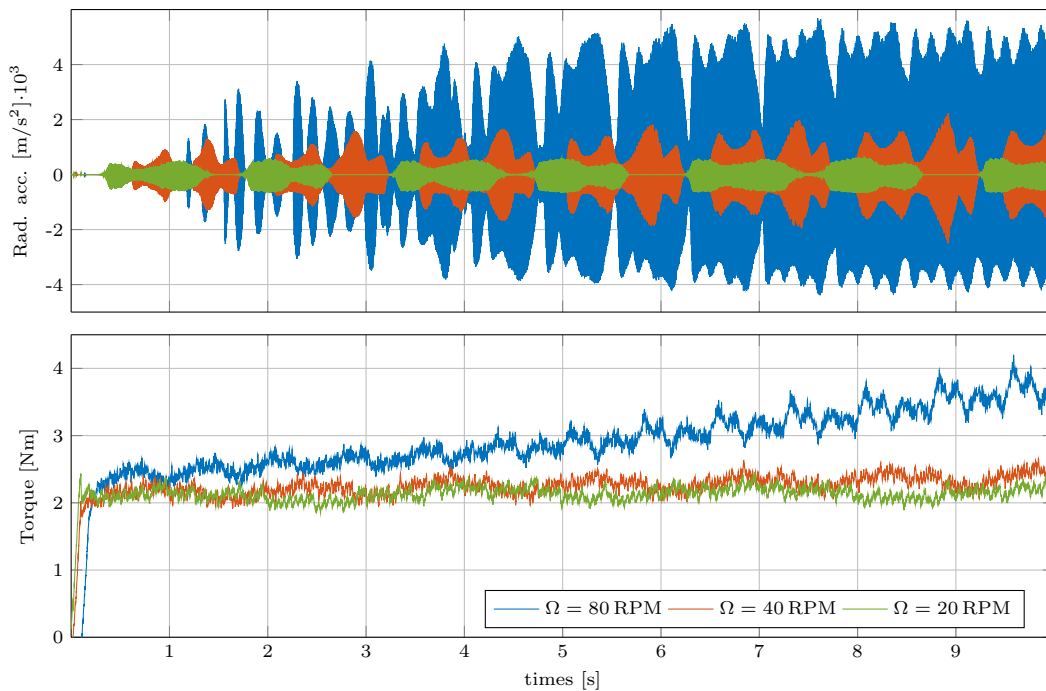
Figure 29: Risposta transitoria per diversi valori della velocità di rotazione ($\Omega = [20; 40; 80]\,\mathrm{RPM}$). Risposta dell'accelerazione in direzione radiale (in alto) e della coppia motore (in basso) in funzione del tempo.
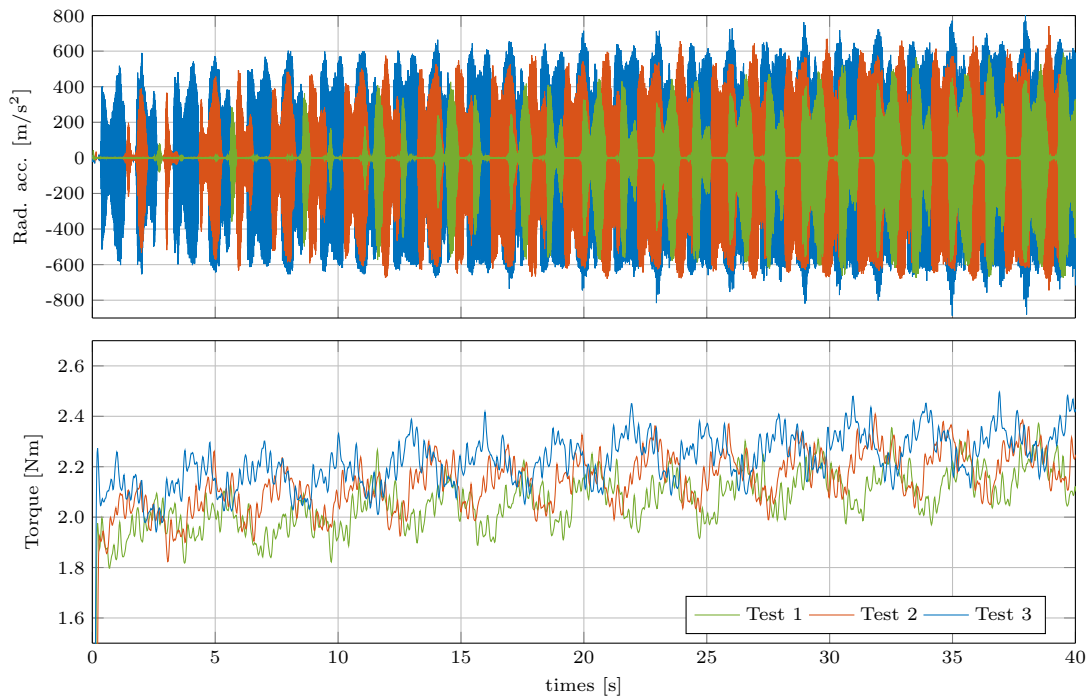
Figure 30: Risposta transitoria di tre misure consecutive con lo stesso valore di velocità di rotazione ($\Omega = 20\,\mathrm{RPM}$). Risposta dell'accelerazione in direzione radiale (in alto) e della coppia motore (in basso) in funzione del tempo.

Un nuovo indice d'instabilià (MAI) è stato definito, partendo da considerazioni energetiche, al fine di confrontare i differenti modi instabili e selezionare il modo che diventa effettivamente instabile durante la risposta transitoria (Table 2).

L'indice di assorbimento modale permette di quantificare la capacità di ciascun modo di scambiare energia con l'esterno. L'uso di questo nuovo indice energetico sul sistema a parametri concentrati mostra una buona corrispondenza tra il regime permanente (frequenza instabile) e il valore assunto dall'indice MAI, calcolato su tutti i modi instabili del sistema.

L'indice MAI permette quindi di definire una gerarchia tra i diversi modi instabili del sistema e di comprendere meglio l'evoluzione della risposta transitoria fino al ciclo limite del regime permanente. La coesistenza nella risposta in regime permanente di piú frequenze modali è stata associata a dei valori simili assunti dal MAI, i.e. la misura della capacità di ciascun modo ad assorbire energia.

È stato inoltre discusso il ruolo della perturbazione iniziale sulla selezione del modo instabile della risposta in regime permanente. In generale, si può supporre che l'eccitazione a banda larga all'interfaccia di contatto sia all'origine della perturbazione iniziale della dinamica del sistema. L'indice MAI tiene in conto della forma della perturbazione iniziale tramite una proiezione dell'equilibrio iniziale sugli autovettori del sistema.

		Friction coefficient μ						
		0.5	1.0	1.5	2.0	2.2	3.0	
Modes	1	$-1.36e-03$	$-1.43e-01$	$-6.87e-01$	$-1.72e+00$	$-2.30e+00$	$-5.67e+00$	χ_r [W]
	2	$-6.80e-14$	$-7.69e-12$	$-4.07e-11$	$-1.16e-10$	$-1.64e-10$	$-5.39e-10$	
	3	$-2.27e+00$	$-5.62e+00$	$-2.01e+01$	$-3.68e+02$	$-1.57e+02$	$-1.37e+02$	
	4	$-6.44e-03$	$-9.83e-01$	$-9.88e+00$	$-5.42e+01$	$+3.41e+01$	$+7.03e+01$	
	5	$-2.58e-10$	$-6.72e-10$	$-1.10e-09$	$-1.66e-09$	$-1.91e-09$	$-3.05e-09$	
	6	$-7.92e-12$	$-7.23e-11$	$+1.30e-10$	$+3.76e-10$	$+4.91e-10$	$+1.05e-09$	
$\mathrm{Re}(\lambda_4)$		-3.20	-3.11	-3.00	-1.03	$+1.29$	$+5.47$	Hz
$\mathrm{Re}(\lambda_6)$		-4.68	-0.91	$+1.24$	$+2.75$	$+3.32$	$+5.14$	
f_{lc}		$-$	$-$	219	$219-166$	166	166	Hz
mode_{lc}		$-$	$-$	6	$6-4$	4	4	

Table 2: Indice MAI χ_r confrontato alla parte reale degli autovalori per diversi valori del coefficiente di attrito. Le celle in grigio chiaro corrispondono ai modi accoppiati, le celle in grigio scuro corrispondono ai modi instabili. f_{lc} è la frequenza misurata nel ciclo limite e mode_{lc} è il modo corrispondente. I valori bordati indicano i modi previsti essere instabili dall'indice MAI χ ed i modi aventi la parte reale dell'autovalore più elevata

Prospettive

Questo lavoro è incentrato sullo studio dell'equilibrio dell'energia meccanica durante le vibrazioni indotte da attrito, prendendo in considerazione solo la deformazione elastica, la dissipazione per smorzamento e la dissipazione al contatto legata allo spostamento relativo. Diversi altri aspetti devono essere presi in considerazione, come gli effetti termici, le deformazioni plastiche locali e il loro effetto sulla distribuzione degli stress locali al contatto. La potenza dissipata al contatto potrebbe essere utilizzata per un accoppiamento con il metodo agli elementi discreti (DEM), al fine di distinguere la parte di potenza meccanica realmente dissipata in calore e la parte che produce delle modifiche permanenti delle superfici in contatto: come il distacco di materia e l'evoluzione del terzo corpo. Degli sviluppi ulteriori dell'equilibrio energetico potrebbero fornire delle informazioni importati verso una migliore modellazione del coefficiente di attrito locale, considerando l'effetto delle vibrazioni indotte da attrito sui fenomeni locali al contatto.

Un'analisi termomeccanica completa delle vibrazioni ad alta frequenza indotte da attrito sarebbe interessante, ma la differenza tra le scale temporali tra la dinamica del sistema (1ms) e i fenomeni termici globali (10 s) rende una integrazione diretta difficile da realizzare. Tuttavia, l'uso combinato di un'analisi termica quasi-statica con l'analisi modale complessa e l'analisi transitoria non lineare potrebbe portare ad una migliore comprensione dell'evoluzione dei fenomeni di squeal su un intervallo di tempo di più secondi, che generalmente caratterizza gli episodi di squeal.

La riproduzione sperimentale di vibrazioni indotte da attrito non è affatto semplice da gestire; infatti l'interazione reale di tutti i fenomeni multi-fisici implicati ne rende l'interpretazione piuttosto complessa. Lo studio numerico fornisce diversi ele-

menti utili per migliorare la comprensione del comportamento reale. L'osservazione diretta del comportamento locale al contatto è infatti impossibile senza introdurre delle modifiche rilevanti sul sistema meccanico. In questo contesto, la tribologia numerica, combinata a l'analisi di dettaglio della dinamica del contatto, fornisce delle informazioni utili sui fenomeni implicati nel contatto stesso.

Diversi aspetti devono essere ulteriormente studiati da un punto di vista sperimentale sul dispositivo PhotoTrib:

- delle ulteriori analisi parametriche devono essere effettuate per distinguere gli effetti termici e le differenti modifiche della superficie;

- delle osservazioni della superficie di contatto attraverso il materiale in policarbonato utilizzando una camera rapida possono fornire delle informazioni sull'evoluzione dello strato di terzo corpo;

- una misura locale della dinamica del contatto e dell'evoluzione della temperatura, per esempio tramite un vibrometro laser e delle termocoppie, fornirebbe una misura indiretta sperimentale dell'energia effettivamente introdotta nel disco di policarbonato sotto forma di vibrazioni, e dell'energia realmente dissipata al contatto;

- anche le vibrazioni fuori dal piano del disco dovranno essere misurate al fine di stimare la dissipazione di energia ad esse legata.

L'accoppiamento dell'analisi presentata con lo studio locale della generazione e della propagazione d'onde al contatto potrebbe fornire delle informazioni utili sul modo in cui il contenuto energetico ad alta frequenza al contatto (eccitazione ultrasonica legata alla propagazione delle onde di superficie nel volume) viene trasferito verso la gamma di frequenze di vibrazione del sistema (dinamica d'insieme del sistema). Dei test con una strumentazione acustica prossima al contatto potrebbero quindi validare questo approccio.

L'indice di assorbimento modale è stato applicato in questa tesi, con dei risultati molto promettenti, su un modello a parametri concentrati. Questo metodo è attualmente pronto per essere applicato a dei sistemi più realistici. Il prossimo passo sarà l'estrazione delle matrici degli autovettori dalla CEA, realizzata sul modello ad elementi finiti 2D del dispositivo PhotoTrib, al fine di calcolare il MAI e verificare che le frequenze di squeal ottenute tramite l'analisi transitoria e sperimentale corrispondano a quelle predette dal MAI. Una volta validato tramite le simulazioni agli elementi finiti e i test sperimentali, l'approccio presentato in questo lavoro sarà esteso ad un sistema di freno commerciale utilizzando la CEA, tramite un modello completo agli elementi finiti.

Abstract

Whenever relative motion between two system components occurs, through a dry contact interface, vibrations are induced by the frictional contact. The local dynamics at the contact (ruptures and wave generation) couples with the system dynamics, giving origin to vibrations and affecting the macroscopic frictional behavior of the system.

In this thesis, in order to develop an overall approach to the investigation of the multi-physic phenomenon, the energy has been pointed out as a coupling physical characteristic among the several phenomena at the different scales. The formulation of a mechanical energy balance is used for distinguishing between two different dissipative terms, i.e. the dissipation by material/system damping and the dissipation at the contact. The energy flows coming from the frictional surfaces, by friction induced vibrations, excites the dynamic response of the system, and vice versa the influence of the system dynamic response on the local energy dissipation at the contact interface affects the related tribological phenomena.

The friction-induced vibrations have been analyzed using three different approaches: the finite element approach, to investigate the coupling between the contact and system dynamics by the analysis of the energy flows; the experimental approach to validate the numerical results and observe the influence of phenomena not still included into the numerical model; a lumped parameter model approach to quickly investigate the effects of the system parameters.

The numerical analysis by the 2D finite element model allowed investigating the repartition of the energy introduced into the mechanical system between the two dissipative terms (material damping and contact) during both stable and unstable friction-induced vibrations. In particular, it has been shown how the friction-induced vibrations modify the overall capacity of the system to absorb and dissipate energy; an estimation of the power dissipated at the contact, without considering the dynamic behavior of the system (energy flows by friction induced vibrations) can lead to significant error in the quantification of the dissipated energy at the contact, which affects directly several tribological phenomena.

The experimental squeal measurements show how the same unstable modes are recovered both experimentally and numerically, validating the use of the 2D transient simulations for the reproduction of the unstable friction-induced vibrations.

Once the energy balance formulated, it has been used on the lumped model to approach the instability over-prediction issue characteristic of the complex eigen-

value analysis. By energy considerations, a newer instability index (MAI) has been defined to compare the different unstable modes and to select the mode that becomes effectively unstable during the transient response. The Modal Absorption Index allows quantifying the capability of each mode to exchange energy with the external environment.

Keywords: friction induced vibrations, energy balance, contact dynamics, mode coupling instabilities, instability index, dry friction

Contents

Contents

Contents

List of Figures

l

List of Tables

General introduction

Whenever relative motion between two system components occurs, through a dry contact interface, vibrations are induced by the frictional contact. The local dynamics at the contact (ruptures and wave generation) couple with the system dynamics, giving rise to vibrations and affecting the macroscopic frictional behavior of the system. The deformations due to the dynamic response of the system affect the local contact stress distribution; conversely the variation of the local contact stresses and status (sliding, sticking, detachment), the waves generated by the local ruptures, and the local contact characteristics (stiffness, damping, etc.) modify the dynamic response of the system.

The so called "friction-induced vibrations" can result in either a low amplitude acoustic noise characterized by a large frequency spectrum, which is a function of the surface characteristics (e.g. roughness) and the dynamics of the bodies in contact, or a high-amplitude acoustic signal characterized by either impulsive excitation or an harmonic spectrum. The last case is characteristic of dynamic system instabilities excited by contact forces. Contact dynamic instabilities have been the subject of several analyses focused on specific applications as joint squeak, squeaking of hip endoprostheses or brake noises. In particular, a large literature can be found on brake NVH (Noise, Vibration and Harshness) issues and more specifically on brake squeal.

Even if the dynamic behavior of mechanical system with frictional contact has been widely investigated in the literature in the last decades, a full comprehension of the issue is still missing. Friction-induced vibrations, in fact, cannot be "reduced" to a complex dynamic problem because they involve also other as complex phenomena related to the tribology of the contact. The unaccounted multi-physics nature, at the moment, leads one to consider most of the friction-induced vibrations related phenomena as "unpredictable", "tricky" or "fugitive".

To account for the real complexity of the issue is not a simple task, due to the spatial and temporal scale differences among the involved phenomena. In order to develop an overall approach to the investigation of the multi-physics phenomena, energy could be pointed out as a universal coupling physical characteristics. The study of the energy flows, in fact, could give new elements to the comprehension of the interaction between the system dynamic behavior, the local dynamic and the tribological behavior of the frictional interface.

This thesis focuses on the investigation of the mechanical energy flows involved

in friction-induced vibrations, in order to understand the influence of the contact dynamics on system response and vice versa. The energy flow, generated by friction-induced vibrations, comes from frictional surfaces, and excites the dynamic response of the system. Vice versa, the influence of the system dynamic response on the local energy dissipation at the contact interface affects the related tribology phenomena. The distinction between the different energy terms allows to identify two different dissipative terms, i.e. the dissipation by material/system damping and the dissipation at the contact. This work wants to introduce a new perspective in the study of friction induced vibrations, observing from an energy point of view the coupling between the local contact behavior and the global dynamics.

In this thesis, as a first step, the analysis of friction induced vibrations by an energy approach is mainly focused on the study of unstable vibrations, because of the high interaction between the local and contact dynamics. A first application of this general approach is proposed here to solve the problem of the selection of multiple unstable modes recovered by the complex eigenvalue analysis of a frictional system.

The work is organized as follow:

The first part provides an overview of the frictional contact dynamic issues in the literature (Chapter 1), including the research works focusing on the analysis of the energies involved in friction induced vibrations. Then, the models, the numerical tools, and the experimental equipment used for the numerical and experimental investigations presented in the thesis are introduced, and a mechanical energy balance has been formulated in Chapter 2.

Chapter 3 presents a numerical study on a 2D finite element model of an experimental setup. In a classical approach the stability of the system has been evaluated by a linear complex eigenvalue analysis as a function of the friction coefficient; then the steady state response of the system has been evaluated by a transient non linear analysis. The energy quantities involved in the friction induced vibrations are analyzed during the transient response to observe the effect of the local friction coefficient and the boundary conditions on the different terms of the energy balance.

In Chapter 4 a validation of the dynamic behavior of the 2D model is presented by the comparison of the 2D reduced model with a 3D finite element model which reproduce the whole setup. Moreover, the comparison of the squeal tests, performed on the experimental setup, with the numerical results allows to confirm that the 2D model is able to reproduce the dynamic instabilities of the real system.

In the last part of this work (Chapter 5) the energy balance is applied to address an open issue in friction dynamic instabilities, i.e. the actual predictability of the unstable steady state in case of a system characterized by several unstable modes. Here the energy approach is applied to a lumped parameter model. Starting from the results of the complex eigenvalue analysis, a newer instability index is defined by energy considerations. The new index allows the comparison of several unstable modes and gives a measure of the propensity of each mode to generate squeal and to dominate the transient response.

2

Chapter 1

From dry friction to body vibrations and vice-versa.

Contents

What happens when two bodies are rubbed against each other?

Since the antiquity, at the origin of scientific thought (Erone 70 A.D) scientists and engineers try to provide an answer to this question. At the end of the fifteenth century Leonardo Da Vinci introduced for the first time the concept of friction forces that arise at the contact interface when two bodies rub one each other (cf. Fig. 1.1(a)).

(a) Da Vinci's experiment.

(b) Coulomb's experiment to show the independence of the friction force from the contact area.

Figure 1.1: First experiments on friction.

Two centuries later, Amontons [AMO 99] and Coulomb [COU 21] provided a first relation stating that the friction force is proportional to the normal load and that is independent of the apparent contact area and sliding speed (cf. Fig. 1.1(b)). Furthermore, they introduced a dependency of the dry frictional behavior to the materials of the contacting pair. This first formulation of the friction problem is at the origin of the tribology, a complex and multidisciplinary research field that aims to understand the relationships between the surfaces, the material, the system parameters and the environmental conditions. One of the main interests in research about friction is the comprehension of the principles at the origin of friction forces, that are strictly related to the wear of contacting materials. An historical review and overview of the main results and understandings about the dry friction in the last centuries is presented in [BOW 50, BOW 64, TAB 81].

In this context, the introduction of the third body concept [GOD 84, GOD 90, BER 96] and of the tribological triplet includes into the study of the tribological problem both the influence of the mechanical system surrounding the contact and the effect of wear particles and its generation at the contact interface. The rheology of the contact and the energy balance within the system evolution become crucial in the analysis of contact issues.

Contact interfaces can have several functions in mechanical systems: in joints, they are optimized to minimize the dissipated energy to have a minimum impact on

4

the efficiency of the motion transmission; on the contrary, in brake systems they are optimized to maximize the conversion of the kinetic energy of the system into heat to improve the braking action; in the rolling contact between the tire and road the contact is optimized to assure the maximum of force transmission without relative sliding. The findings in tribology over these last decades drove the optimization process of all these systems.
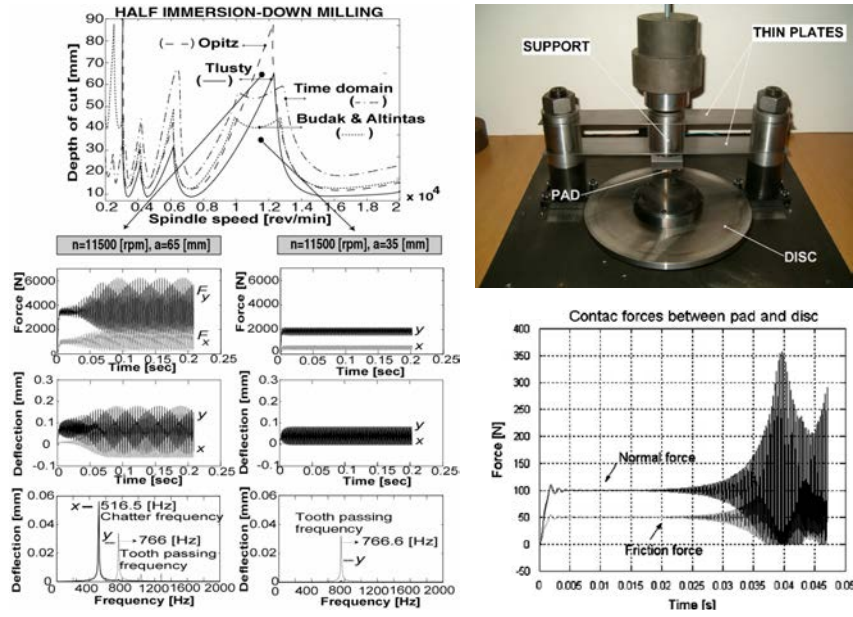
1.1 Friction-Induced Vibrations

In complex mechanical systems, the contact forces, which are generated by dry contact interaction between the components, produce waves that propagate on the surface and into the bulk, generating acoustic emission [AKA 02]. The system responds to the local acoustic excitation with its own dynamics. This phenomenon is known in literature as Friction-Induced Vibrations [IBR 94a, IBR 94b] and the study of these, not always predictable and often undesirable, dynamic behaviors has been the subject of a large amount of works in the last century. Vibrations causes are classified and named in the literature with different names (stick-slip, sprag-slip, chatter, squeal, squeaking, squeeze etc.) basing on the originating mechanism, on the frequency range and on the application that is mainly affected by such type of vibrations.

Unstable vibrations are of particular interest in several industrial field and applications because they can introduce an uncontrolled behavior, which is often associated to acoustic emission [AKA 02], into critical mechanical systems. Some examples of friction-induced vibrations are listed in the following of this section only to give an idea of the implications of such phenomena and of the amount of researches focusing on it (cf. Fig. 1.2).
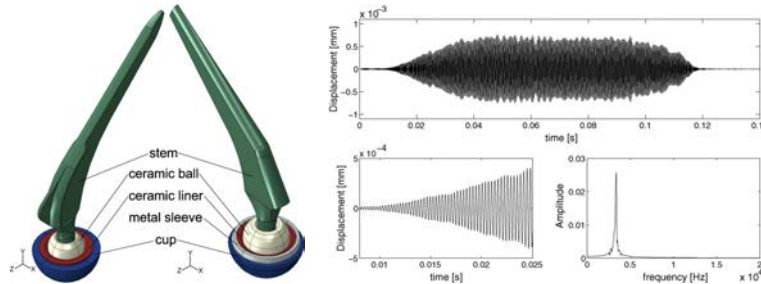
- The dynamic and frictional interaction of a cutting tool on a workpiece during a machining operation [HAN 12, ALT 04] can induce chatter vibrations that cause a poor surface quality and an excessive tool wear.

- Frictional contact between the disc and the lining pad can induce vibrations in the brake systems at high frequency; this phenomena is known in literature as brake squeal [KIN 03, OUY 05] and is a very prolific subject in research due to the high interest about this phenomena of the automotive, aircraft and train industry. In this case the high amplitude vibrations (usually above 1 kHz) produces an annoying noise emission (with a sound pressure level above 78 dB) that results to be very expensive to brake and automotive manufacturers in terms of warranty costs [CRO 91].

- The lateral contact between the railway and the wheel in narrow curves can give rise to high amplitude unstable vibrations, the curve squeal [RUD 76], that generate a sound emission with overall pressure level up to 120 dB [THO 00, BRU 06].

(a) Chatter study of the milling
process [ALT 04].

(b) Experimental setup for the
study of brake squeal and result
of a transient
simulation[MAS 07].

(c) Total hyp endoprosthesis and displacement of the ceramic
displacement measured in in vitro test [WEI 10].

Figure 1.2: Examples of friction induced vibrations.

- Friction interaction in the spherical joints of the artificial human prosthesis
  such as the hip replacement can generate unstable vibrations resulting in a
  sound, known in medical and engineering literature as squeaking [WEI 09,
  OUE 15, HOT 13, FAN 11].

- In the pantograph-catenary system of high-speed trains the friction couples
  the dynamic behavior of the pantograph with that of the catenary; this gives
  origin to vibrations that can affect the contact condition (the contact may
  even get lost) increasing wear and producing arc discharge [QIA 13].

- In cars with manual transmission the frictional interaction during the sliding

6

phase of clutch engagement can generate an audible disturbance known as automotive clutch squeal [HER 08].

- The tactile perception is a friction-induced vibration related phenomena; in fact, the scanning of a surface with the fingertip generates vibrations, that propagate in the finger skin activating the tactile receptors, allowing the brain to perceive information about surface properties [FAG 12].

The issues mentioned above are just some examples of research fields related to friction-induced vibrations, which are present whenever a frictional contact occurs. Another field of study related to friction-induced vibrations is the investigation about the early stages of sliding initiation [DIB 12] and the analysis of the waves propagation into the bulk, which excite the system dynamics. In these phenomena the local contact dynamic produces an excitation of the dynamic of the whole system. The study of the dynamic ruptures on the interface between different solids are of great interest for the study and prediction of the earthquake phenomena and more in general for investigating the origin of friction induced vibrations.

Recent works [TON 13] showed how the same mechanical system in the same operating conditions can switch between macroscopic stick-slip, modal instability or stable continuous sliding changing some system parameters or boundary conditions. In this case, the variation of the dynamic characteristics of the system produces a variation of the local contact dynamic and, consequently, the system response.

The observation of all these phenomena leads to the awareness of the importance of considering into the study of friction-induced vibrations the coupling of the global dynamic problem with the local dynamic contact problem. An approach that include the whole system [BER 96] in its complexity, considering the multi-physics and multi-scale nature of the phenomenon seems to be the key to clarify some of the still obscure aspects in friction-induced vibrations. In this context an energy approach to the issue could give new elements to clarify the interaction between the system dynamic behavior, the local dynamic and the tribological behavior of the contact interface during friction induced vibrations.

The contact interface, in fact, acts not only as a dissipative element of the mechanical system, producing a reduction of the energy content of the system (contact damper); the interface is also the place where the contact forces, that excite the system, act introducing energy into the mechanical system. Hence, there is a complex energetic exchange at the interface and a distinction has to be made between: *(i)* the energy that is actually dissipated at the contact and strongly linked to tribological aspects of the contact (heating, plastic deformation, wear, fractures, chemical reaction, etc.); *(ii)* the energy that flows from the surface to the bulk, producing the excitation of the system dynamics, and modifying its energy content.

The distinction of these two quantities results to be fundamental for a better comprehension of friction induced vibrations and the related tribological aspects. Therefore an energy approach, characterized by conservation laws at every scale and

on each physical domain could introduce new coupling terms among the analysis of the different scales and phenomena involved in friction induced vibrations.

Akay in [AKA 02] proposes a summary of the energy transformations involved during friction induced vibrations (cf. Fig. 1.3(a)) and the temporal and spatial scales of the phenomena involved in such vibrations (cf. Fig. 1.3(b)).

(a) A description of the energy path during friction [AKA 02].

(b) Length and time scales associated with friction and examples of different events that accompany each [AKA 02].
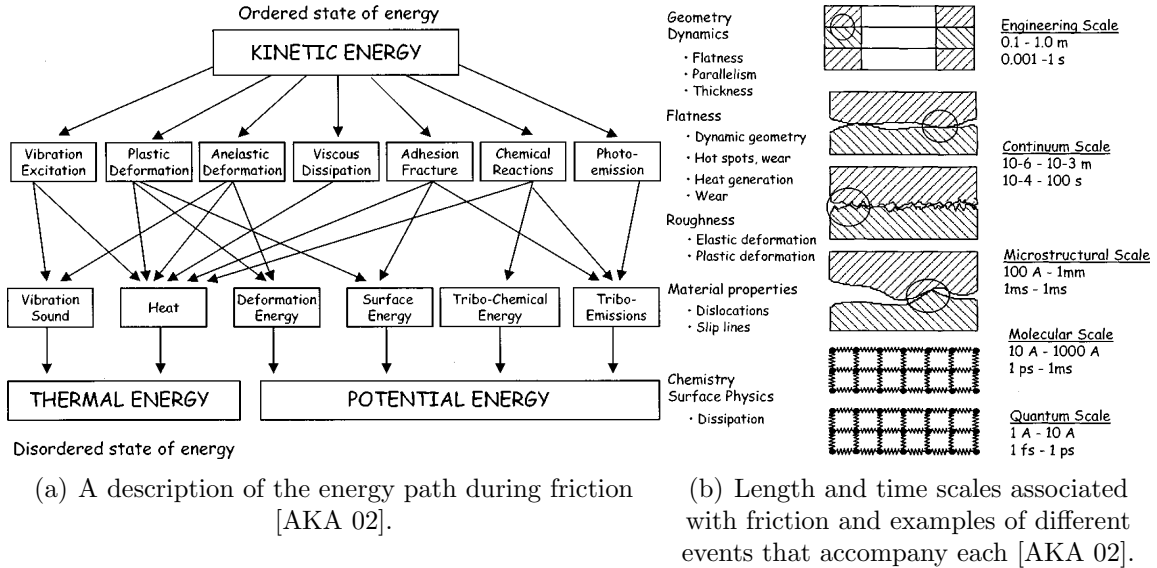
Figure 1.3: Energy transformations and scales of the involved phenomena.

1.2 Dynamic instabilities

In the study of friction-induced vibrations a fundamental distinction have to be introduced between stable and unstable vibrations.

In stable conditions the friction excitation is mainly characterized by the interaction between the asperities (roughness or textures) of the interfaces [OTH 90, STO 07] and the kinematics of the contacting interface. The system vibration in this case is strictly related both to the system dynamics, i.e. all the natural frequencies of the system that are excited by the wide band excitation at the contact, and eventually, to the spatial frequency of surface corrugations if there are any periodical pattern or texture [AKA 02, FAG 12]. Therefore, the waves that propagate from the interface excite the system vibrations but they are quickly damped by the system damping.

In unstable conditions the system dynamics results to be unstable and the contact forces produce a response of the system characterized by a very high amplitude of vibrations, associated with noise emission.

A general classification of dynamic instabilities with contact is extremely difficult, because of the different possible phenomena that can arise. A first distinction could
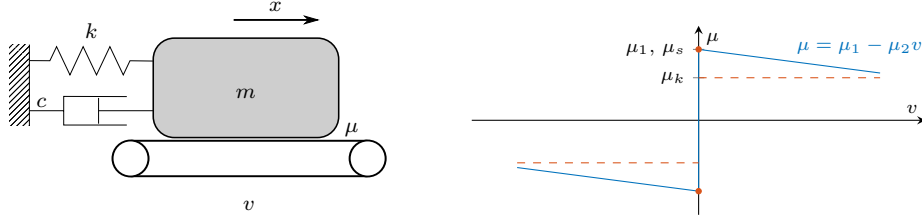
Figure 1.4: Spring (k) mass (m) damper (c) system on a moving (v) surface in frictional contact (μ).

be done between instabilities characterized by macroscopic stick-slip switches of the contact interface and instabilities characterized by harmonic system vibrations with a smother behavior at the interface. Nevertheless, this kind of classification, could be even scale dependent [TON 13] as a function of the relative dimensions between the system and the contact.

By another point of view the mechanisms at the origin of the unstable behavior have been widely studied in literature and are all based on considering friction forces as a cross coupling term between the global and local contact dynamic. An overview of the main mechanisms is reported below, while a more complete description of these mechanisms can be found in [KIN 03]:

Negative friction-velocity slope. After an analysis of different couples of drums and lining materials combinations characterized by a friction coefficient μ that was a decreasing function of the relative velocity, Mills [MIL 38] stated that a condition for a brake to squeal was $d\mu/dv < 0$. In fact, in case of a friction coefficient $\mu = \mu_1 - \mu_2 v$, the equation of motion of the oscillator in Fig. 1.4 becomes:

$$m\ddot{x} + (c - mg\mu_2)\dot{x} + kx = 0 \qquad (1.1)$$

If $\mu_2 > c/mg$ the global damping coefficient of the system becomes negative and it gives rise to self-excited vibrations.

These results led a school of thought up to the '60s, extending the negative velocity slope to the possibility to have a static friction coefficient μ_s higher than a dynamic friction coefficient μ_k as condition to have unstable vibrations [FOS 61] (cf. Fig. 1.4). This mechanism didn't receive much attention in recent years and Chen in 2003 [CHE 03] stated that: "Examination of the friction-velocity slope shows that there is no invariable correlation between the negative friction-velocity slope and occurrence of squeal. Squeal can occur in regions with both negative and positive friction-velocity slopes." demonstrating that the negative slope is not a necessary condition for squeal.

Sprag-slip. The sprag-slip theory was proposed by Spurr in 1961 [SPU 61] and applies even if the friction coefficient does not show any dependence to the sliding
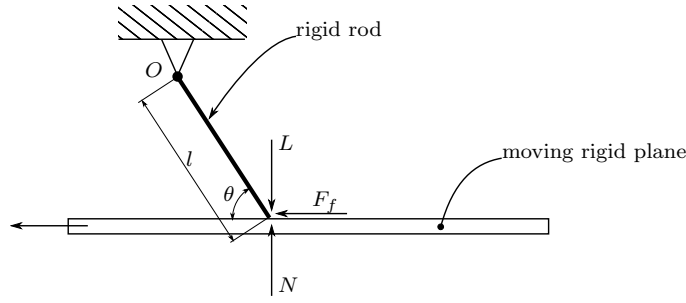
Figure 1.5: Rigid massless rod in frictional contact with a rigid plane to show the sprag-slip phenomena.

velocity. In the model proposed by Spurr (cf. Fig. 1.5) the variation of friction force is achieved by varying the normal force as result of a constrained interaction of various degrees of freedom of the system. In the model depicted in Fig. 1.5 the frictional torque $F_f l \sin\theta$ on the rigid rod pivoted at O causes the normal force N to increase. Hence, the contact forces can become unbounded. Assuming $F_f = \mu N$ Spurr showed that the equilibrium condition implies that:

$$ N = \frac{L}{1 - \mu \tan\theta} \qquad \text{and} \qquad F_f = \frac{\mu L}{1 - \mu \tan\theta} \tag{1.2} $$

and if $\theta \to \arctan(1/\mu)$ then $N, F_f \to \infty$. Spurr named this critical condition "spragging". Furthermore, including the flexibility of components, he showed that the deformation allows to free themselves from the spragging condition, leading to a sprag-slip limit cycle.

In recent years Sinou and coworkers [SIN 03a] adopted the sprag-slip model to study the heavy truck brake judder (low frequency instability that involves the dynamic of the whole front axle assembly) with a polynomial formulation of the contact nonlinearities and used the centre manifold approach in order to obtain an analytical expression of the limit cycle. They confirmed that the system instability can occur even with a constant friction coefficient and that changes in masses, stiffness, damping, friction coefficient and sprag-slip angle are significant on stability.

Hoffmann and Gaul in 2003 [HOF 04a] reexamined the issue, introducing as a sufficient condition for sprag-slip oscillation the lack of a steady sliding solution (the Painlevé paradox). Moreover, they observed how in that conditions the increasing of system damping does not produce the improvement of system vibration properties since there is no quiet static state to which the more damped system might tend to.

Mode Lock-in. North in 1972 [NOR 72] considered the self-excited vibration induced by a constant μ by incorporating, for the first time, the friction forces in the system dynamic equations as follower forces. Applying this approach, North developed a 2 DoFs model [NOR 76] to model a brake system (cf. Fig. 1.6). The contact forces $F_1 = \mu(k_1 y + N_0)$ and $F_2 = \mu(-k_1 y + N_0)$ introduce an asymmetric
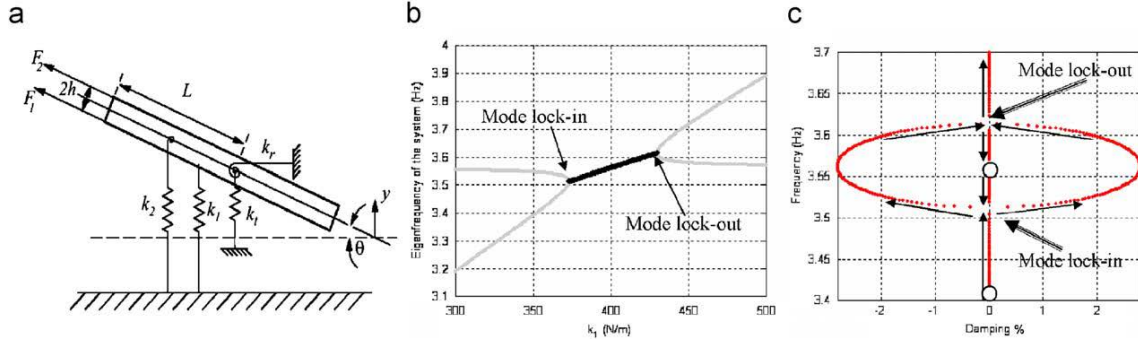
Figure 1.6: Complex eigenvalue analysis fo the North 2DoFs model. (a) Schematic of North's two-dof model, (b) lock-in plot, and (c) root behavior in the locus plot [AKA 09].

contributions to the stiffness matrix of the system $[K^\star]$.

$$[M]\{\ddot{x}\} + [K^\star]\{x\} = \{0\} \tag{1.3}$$

For this system the stability of the steady sliding condition can be evaluated by the sign of the eigenvalue real part. If the system is stable then the eigenvalues are complex and conjugate pure imaginary pairs. Varying the system parameter it is possible for the eigenvalue of the system to coalesce producing a split of real parts resulting in eigenvalues with positive real parts (negative apparent damping). In this case the sliding steady state of the system is unstable (flutter instability or supercritical Hopf bifurcation).

This coalescence was named by Akay [AKA 00] Lock-in and became one of the most accepted theory in the study friction induced instability such as brake squeal. Hence, the complex modal analysis on the linearized system, near the steady sliding equilibrium, became during the past years an universal tool to evaluate the stability of systems affected by friction-induced instabilities. This approach will be used also in this work and a more detailed description is presented in Section 2.1.

1.3   Energy and friction-induced vibrations.

Physical interpretation of friction-induced vibrations. Hoffmann and coworkers in 2002 [HOF 02], when studying a simple lumped model (cf. Fig. 1.7), observed how the follower nature of friction forces can transfer the energy from the contact to the vibrational system and vice-versa. The frictional contact ($F_F = \mu F_N$) gives rise to a non-symmetric stiffness matrix that produces a coupling between the motion in the out-of-plane direction (y in Fig. 1.7) and the motion in the in-plane direction (x).

Increasing the friction coefficient the frequencies coalesce and a critical value of the friction coefficient separates the stable and the unstable conditions. They gave in this work a physical interpretation to the mode coupling instabilities, showing
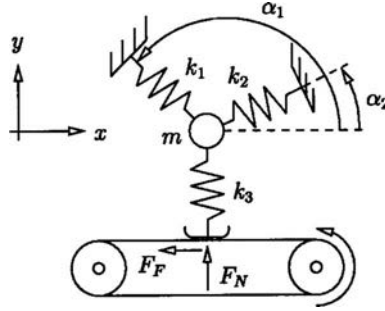
Figure 1.7: Minimal single mass two degree of freedom model [HOF 02].

how the out-of-plane oscillation, and thus the tangential force oscillation, is behind the tangential oscillation. This observation highlights that, in unstable conditions, the phase lag between these two quantities yields to an excitation with positive energy generation. They highlighted also the presence of beating cycle in case of stable condition next to the coalescing condition. The phase shift, between the in- and out-of-plane motion, changes during the beating cycle and it is correlated to the absorption and release of energy that produce the typical increase and decrease of beating oscillations. The beating conditions and the related energy exchanges were deeply investigated in a succeeding work [HOF 04b] to identify an optimal initial condition that gives rise to the maximum transient amplification, for a beating affected system due to frictional contact.

The "feed-in energy" method: Guan in 2003 [GUA 03] proposed the method of "feed-in energy" to evaluate the tendency of a brake system to squeal and used this approach to analyze the effect of structural modifications on the suppression of squeal noise. The method aims to evaluate the energy that excites the system from the friction coupling at the pad-disc interface.
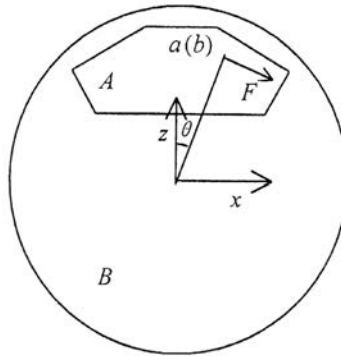
Figure 1.8: Schematic drawing for calculation of feed-in energy between pad A and brake disc B [GUA 03].

For an unstable mode, the relative displacement of the contacting points (at an

12

angular position θ), namely a for the disc and b for the pad, can be expressed as a function of the complex eigenvectors in both the tangential directions x and z and normal direction y. In the hypothesis of a penalty formulation of the normal contact condition with a normal contact stiffness k is:

$$x_a - x_b = A_{abx} \cos(\omega_i t + \theta_{abx}) \tag{1.4}$$

$$y_a - y_b = A_{aby} \cos(\omega_i t + \theta_{aby}) \tag{1.5}$$

$$z_a - z_b = A_{abz} \cos(\omega_i t + \theta_{abz}) \tag{1.6}$$

where A_{abx} represents the magnitude of the relative displacement in direction x and θ_{abx} is the corresponding phase, similarly for y an z direction. Hence, the tangential components of the contact forces, acting on the contacting points a and b, are a function of the normal relative displacement:

$$F_{xa} = -F_{xb} = \mu k(y_a - y_b)cos\theta \tag{1.7}$$

and similarly for the y component. Finally the nodal feed-in energy induced by the force in the x direction between nodes a and b during one cycle of vibrations can be expressed as:

$$E_{abx} = \int_0^T F_{xa}(\dot{x}_a - \dot{x}_b)dt \tag{1.8}$$

Extending this integration over each contact interface in both the tangential directions, the feed-in energy calculation of the unstable mode allows to find the effect of each substructure in term of energy transferred from one substructure to another through the frictional interfaces. Therefore, this method gives helpful elements to identify the structure modification target when attempting to reduce squeal.

The Energy Based stability Criterion (EBD): In 2004 Tarter [TAR 04] started from a similar formulation of harmonic contact forces and proposed a new energy-based stability criterion to identify the operating conditions that have the highest propensity for squeal vibrations. In the hypothesis of sliding contact of an oscillating block with respect to a fixed base (cf. Fig. 1.9) the tangential motion of the block and the tangential contact force can be expressed as harmonic function, with the same angular frequency ω and a phase angle θ, which is related to the phase lag between the in-plane x and out-of plane vibration z:

$$u_x = A_0 \cos(\omega t) \tag{1.9}$$

$$F_x = \mu \left[N_0 + N_1 \cos(\omega t + \theta) \right] \tag{1.10}$$

In this condition the work per vibration cycle can be expressed as:

$$E_0 = \int_0^{2\pi} F_x \Delta x \, d(\omega t) = \mu \pi N_1 A_0 \sin \theta \tag{1.11}$$
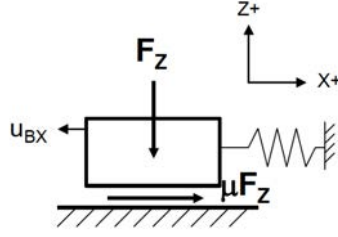
Figure 1.9: Oscillatory motion of a sliding block on a fixed base [TAR 04].

and both the amplitude and the direction (incoming or outgoing) of exchanged energy depends from the phase angle θ between the tangential force and the tangential displacement.

Afterwards, he used the same approach to define an Energy Based stability Criterion (EBC) on a beam on disc model. He normalized the different eigenvectors, which define the amplitude and relative phase between the vibration of the different points of the system, with respect to the amplitude of the disk normal displacement. By this way the EBC, which is calculated from the complex eigenvector solution, can be used to compare the generated energy of the different unstable modes of the pin on disc system and correlate this quantity to the vibrational propensity.
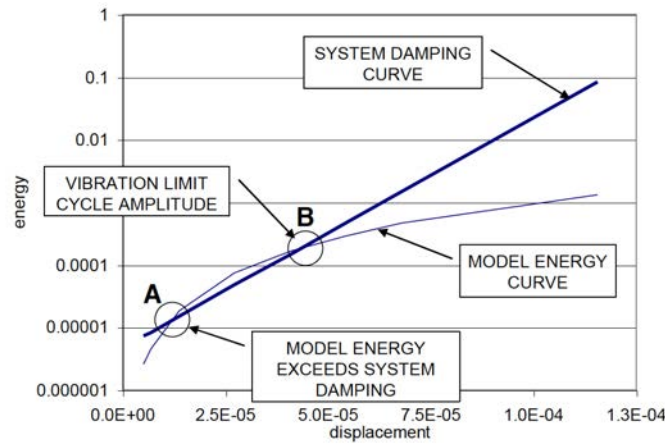
Figure 1.10: Comparing the system damping dissipated energy with predicted model vibration energy, to calculate unstable limit-cycle vibration amplitude [TAR 04].

Moreover, in this approach, the vibration amplitude of the unstable vibration (steady state limit cycle) can be estimated equating the generated energy at the contact with the dissipation of the system (cf.Fig. 1.10).

The works mentioned above are the more relevant contributions to the investigation of the energy flows during friction induced unstable vibrations. Nevertheless, works dealing with the mechanical energy balance of a frictional contact are not numerous. Starting from these contributions, it seem to be imperative the necessity

14

of extending the energy analysis of friction induced vibrations, in order to look for an energy understanding of the different phenomena.

1.4 Recent researches on friction-induced vibrations.

As sown in the previous sections, the friction-induced vibration is a multidisciplinary and complex problem. Researchers from the research community dealt with this topic for decades, focusing each time on a few of the many physical aspects that are involved and on a specific application (brake squeal, curve squeal, hip squeaking, ...).

A full review of all the scientific works on this topic would be very complex and it is not the purpose of this thesis. Several reviews have been proposed over the years trying to gather the most relevant results [ODE 85, FEE 98]. Ibrahim, in 1994 [IBR 94a, IBR 94b], made a fundamental work in reordering all the main results in the topic, highlighting its deep multidisciplinarity. An overview, which deals with the sound emissions that are generated by frictional contacts, was presented by Akay in 2002 [AKA 02].

Other review works focus a single application. Among them we can mention Thompson and Jones [THO 00] for a review of the theoretical models developed for the wheel/rail noise generation, Kinkaid et al. [KIN 03] for its complete review about the automotive disc brake squeal, Ouyang et al. [OUY 05] for a review on the numerical methods in the study of disc brake squeal and Altintas and Weck [ALT 04] for a review of the methods to model chatter vibrations in metal cutting and grinding. Oberst and Lai [OBE 11] collected data from precedent experimental and numerical works, for a study dealing with the chaos characteristics of friction induced vibrations; they provided an easy to use tabular classification of several numerical and experimental works on: lumped "oscillators", "pin-on-disc/plate systems", "beam-on-disc" systems, "laboratory brakes" and "tribo brakes".

To give a look to some of the recent findings, a first classification can be done on the approach used to analyze the phenomenon. In the following of this section a distinction is made between investigations conducted on extended systems and studies on lumped parameter models. While the former are generally analyzed either by finite element method and experimentally, the latter are analyzed with analytical approaches and are developed for theoretical purpose or as a simpler dynamic representation of more complex system.

1.4.1 Analytical studies on lumped models

In 2003 Sinou and coworkers [SIN 03a, SIN 03b, SIN 03c] used nonlinear methods on frictional lumped systems to study the non-linear stability behavior of the system and to find the equation for the limit cycle amplitude. Efficiency of these tech-

niques in the study of the stick-slip phenomena is also investigated in [HOF 04a]. A critical point in these methods remains the reduction of the degrees of freedom of the complex systems, including the simplification of contact nonlinearities, generally reduced to a polynomial form. Non-linear strategies to construct reduced order models, which are suitable for the adoption of such techniques, are illustrated in [SIN 04].

The role of non-proportional damping on modal coupling instabilities and the rise of "viscous instabilities" or "damping instabilities" in friction induced vibrations is investigated in [HOF 03]. Similar results in terms of system stability were obtained by Sinou in 2006 [SIN 06], which defined a robust damping factor in order to avoid design errors and to reduce flutter instability. Further analysis of the effect of damping on lumped system are in [SIN 07b, SIN 07a, CHE 08, SIN 08].

Another actual topic in the study of the friction-induced modal instabilities is the presence of multiple instabilities in the steady sliding equilibrium. The classical nonlinear methods [SIN 04] are not suitable to give the solution of the limit cycle shape and amplitude and the integration of the full set of nonlinear dynamic equations (or the transient nonlinear analysis in case of finite element models) is the only way to find the transient-state behavior of the system [CHE 09]. Numerical results presented in [CHE 09] show a switch between several unstable regimes, each one related to different of the system unstable modes, and an experimental evidence of this behavior can be found in [BRU 15b].

Coudeyras and coworkers in 2009 [COU 09] proposed a nonlinear method to deal with unstable system with multiple instabilities. It allows for computing the periodic or pseudo-periodic response (depending on the number of unstable frequencies) of the unstable frictional system. The spectrum of the dynamic response, in case of two unstable modes f_1 and f_2, includes peaks at the unstable frequencies and their respective harmonics (nf_1 and mf_2). Moreover, other frequencies are also found in the spectrum (modulation frequencies $nf_1 \pm mf_2$) due to the nonlinearities, which have a relevant contribution on the dynamic behavior and cannot be neglected.

1.4.2 Finite Element analyses and experimental investigations on extended systems

Over the last decades, with the improvement of the calculus capabilities and of the measurement and acquisition instrumentation, several studies have been performed on real extended system using either numerical techniques (e.g. the finite element method) or an experimental approach to the issue. The theoretical study of friction induced vibrations initially performed on lumped models (cf. Section 1.4.1) has been extended to experimental setup [TWO 99, AKA 00, CHE 03, GIA 06b, GIA 06a, MAS 06, CHE 07], which allows for a more simple control of the system parameters, up to real applications [CAO 04, OUY 05, BRU 04], in order to understand the origin of vibrations and find ad-hoc solutions to the problem.

Baillet, starting from 2003, developed the finite element code PLASTD [BAI 03,

16

BAI 05c]; it combines the Lagrange multiplier method at the contact with the explicit time integration, allowing for an efficient transient simulation of friction induced vibration phenomena on extended models. The use of this code, by means of the transient simulation, allows for the analysis of the arising of dynamic instabilities [BAI 05b], the occurrence of squealing noise [BAI 06] and for the observation of the actual contact dynamics during the unstable vibrations [LIN 06].

In 2007 Massi et al. [MAS 07], in the study of a beam on disc system, presented the combined use of the complex eigenvalue analysis approach with the transient nonlinear analysis (by PLASTD), showing a good agreement between the transient behavior of the system and the unstable modes predicted by the complex eigenvalue analysis. The presented results shows that the system presents harmonic vibrations at one of the unstable frequencies predicted by the complex eigenvalue analysis.

In the last decade of research on friction dynamic instability, the effects of damping has been widely investigated: findings on lumped systems [HOF 03, SIN 06] have been rapidly adopted in the analysis of complex systems. Fritz and coworkers [FRI 07b, FRI 07a, FRI 07c] observed the effects of damping distribution on the stability analysis of a finite element model of a brake system; they highlighted the relationship between the modal damping of the two modes involved in the coalescence and the stabilizing or destabilizing effect of added damping. Experimental evidence of the role played by the system damping on the stability behavior is presented by Massi and Giannini in [MAS 08]; in a following work [CAN 11] the results of a numerical model of the previously tested apparatus was proposed to clarify the experimental results.

Finite element models resulted in over-prediction of unstable modes by the complex eigenvalue analysis [OUY 05, MAS 07]. Sinou, in 2010 [SIN 10], studying an automotive disc brake system with the coexistence of unstable modes, confirmed the need for a complete non-linear analysis to fully predict the non-linear vibrations and the contribution of the several unstable modes on the system response. In this study Sinou indicates the change of the contact conditions, due to the high amplitude vibrations, as the cause of arising of new unstable modes that cannot be predicted by the complex eigenvalue analysis performed in the steady sliding equilibrium condition. The numerical results presented in his work showed that in case of multiple-instabilities, transient nonlinear vibrations are composed of a fundamental frequency of the unstable modes and its harmonic combinations; he obtained the same results given by the analysis proposed by [COU 09] using the non-linear method. An experimental proof of the possible simultaneous presence of several unstable modes is given in [SIN 13] in the numerical and experimental analysis of a railway brake system.

Recent and interesting studies on finite element modeling of brake squeal deal with the wear prediction during the transient unstable vibration [ABU 08] and the inclusion of gyroscopic term in the stability analysis of a rotating brake disc [KAN 09].

In the very recent years, numerical studies have been performed as well to es-

timate by finite element analyses, the sound radiation of brake system in squeal conditions [SOO 13, SOO 14, SOO 15].

1.5 Relevance of the presented work

This chapter gives a general, and of course non exhaustive, overview of the literature dealing with unstable friction induced vibrations, highlighting the main current research approaches in the study of this phenomena. The problem has been widely studied and modeled: by one side theoretical approaches on simple systems allowed for a simpler investigation on the effects of the system parameters; on the other hand, numerical and experimental approaches on continuous models and real systems allowed for ad hoc analyses of specific applications.

Although the enormous efforts of the scientific community, at present, a complete comprehension of the involved phenomena is still missing; this fact is reflected by the large amount of issues that can be encountered on industrial applications and which are related to friction-induced vibrations.

With respect to the different approaches reported in the literature, relatively few works dealt with the energy balance at the contact and the role played by the friction induced vibrations to exchange mechanical energy between surface and bulk, and vice-versa. An analysis of the mechanical energy flows involved in unstable friction induced vibrations can help to account for the different dynamic phenomena that happen at different scales (local contact dynamics, solid dynamics, system dynamics) and bring newer information on the frictional system behavior.

In this context, an energy investigation seems to be the key to better understanding the several involved phenomena.

The first part of this thesis presents an analysis of the mechanical energy, which is directly related to the induced vibrations, in order to identify the energy flows between the system and the contact interface and to give an estimation of the energy available for the physical phenomena. The energy balance has been formalized on a finite numerical model, able to reproduce dynamic instabilities recovered on an experimental set-up.

In the second part of the thesis, the developed energy balance approach has been applied to address another open issue in frictional dynamic instabilities, i.e. the actual predictability of the unstable steady state in case of a system characterized by several unstable modes. In fact, the prediction of the effective unstable mode is obtained into the literature by the full numerical analyses of the transient behavior which needs high computational efforts and time and are not suitable for the development of complex real systems in the industrial environment.

On the other hand the use of nonlinear methods to approximately determine the limit cycle amplitude and its harmonic content gives quite good results, but requires a large formal mathematical effort in order to reduce the system. Moreover, the reduction of complex systems to a few degree of freedoms is not an obvious task and

the approximations introduced in the simplification step can affect the reliability of the results.

Here, the energy approach is directly applied, allowing a physical interpretation of the unstable vibrations in order to define a new index, the Modal Absorption Index (MAI). Starting from the results of the complex eigenvalue analysis, which needs reasonable computational efforts even on models of real systems, the proposed index allows comparison of the several unstable modes: it gives a measure of the attitude of each mode to generate squeal and to dominate the transient response of the system in the steady state vibrations.

Models and numerical tools

Contents

This chapter introduces the numerical tools and the numerical and experimental models used in the following chapters for the study of friction-induced vibrations. Both a finite element model and a lumped model have been developed: the first one is aimed to reproduce and to analyze frictional instabilities on a real system; the second one is aimed to the investigation of key factors and descriptors.

For both numerical models, Complex Eigenvalue Analyses (CEA) transient analyses have been performed. The CEA is widely used in the study of frictional systems to evaluate the dynamic stability of the system when accounting for effects of contact forces. Nonlinear transient analyses are useful to investigate the response of systems with friction. The velocity of the phenomena that are involved in friction-induced vibrations, e.g. waves propagation and local switches of the contact status, leads to the use of explicit formulations to solve the transient problem on a finite element model. Moreover the simplicity of lumped component models allows for a less time consuming analytical formulation of the transient response, which permits an easier correlation between the system parameters and the dynamic behavior.

In the following sections the formulation for the CEA and transient analyses are presented for both the finite element and the lumped models.

In order to investigate the system stability from an energy point of view, the energy terms are formulated and given as output of the different models. The energy balance is then formulated taking into account the mechanical quantities involved in the phenomena. A particular focus is placed on the energy exchanges between surface and bulk by friction induced vibrations.

Finally, the experimental set-up "PhotoTrib", which is used in Chapter 4 to validate the numerical results in Chapter 3, is presented.

2.1 Complex Eigenvalue Analysis (CEA) for a non-self-adjoint system

One of the most accredited mechanisms at the origin of system instabilities due to frictional contact is the modal coupling or mode lock-in [AKA 02, SIN 07b, HOF 03]. Different numerical and experimental works [MAS 06, AKA 09, CAN 11], developed on complex systems with two or more deformable bodies in contact, highlighted that the unstable behavior arises when the frictional forces cause the coalescence between pairs of modes of the different system components.

By the Complex Eigenvalue Analysis (CEA) it is possible to find the complex eigenvalues and eigenvectors of the system by taking into account the contact forces. The CEA will be used in Chapters 3 and 5 to evaluate the dynamic stability of both the finite element model and the lumped model. A prestress quasi-static analysis is performed to apply the external load $\{F_e\}$ and the contact forces in uniform sliding condition $\{F_c\}$:

$$[K]\{x\} = \{F_c\} + \{F_e\}. \tag{2.1}$$

Frictional forces in sliding conditions can be expressed as a function of the system position $\{x\}$ and a friction coefficient μ. They are linearized by the introduction of a normal and a tangential stiffnesses at the contact element that result in an asymmetric contact stiffness matrix $[K_c(\mu)]$:

$$\{F_c\} = [K_c(\mu)]\{x\} \tag{2.2}$$

The prestress analysis leads to the definition of an asymmetric stiffness matrix $[K^\star]$, which includes the asymmetric contribution of the frictional contact interaction:

$$([K] - [K_c(\mu)])\{x\} = [K^\star]\{x\} = \{F_e\} \tag{2.3}$$

A proportional formulation of the system damping, also known as Rayleigh damping model, is adopted to account for the material dissipative effects:

$$[C] = \alpha_r[M] + \beta_r[K]. \tag{2.4}$$

The damping matrix $[C]$ can be expressed as the sum of a term that is proportional to the mass $[M]$ by means of the α_r coefficient, and a term that is proportional to the stiffness $[K]$ by means of the β_r coefficient. The asymmetries of the stiffness matrix $[K^\star]$ propagate to the damping matrix, which becomes asymmetric $[C^\star]$.

The equation of motion of the system becomes:

$$[M]\{\ddot{x}\} + [C^\star]\{\dot{x}\} + [K^\star]\{x\} = \{F_e\}. \tag{2.5}$$

The system, in the state space $\{y\} = \left\{\{x\}^T, \{\dot{x}\}^T\right\}^T$, can be expressed as:

$$[A]\{\dot{y}\} + [B]\{y\} = \{Q\} \tag{2.6}$$

where:

$$[A] = \begin{bmatrix} [C^\star] & [M] \\ [M] & [0] \end{bmatrix}, \quad [B] = \begin{bmatrix} [K^\star] & [0] \\ [0] & -[M] \end{bmatrix} \quad \text{and} \quad \{Q\} = \left\{ \begin{array}{c} \{F_e\} \\ \{0\} \end{array} \right\}. \tag{2.7}$$

The asymmetry of the system matrices $[A]$ and $[B]$, due to the presence of the nonconservative contact forces, leads to a non-self-adjoint system. In this case, two different eigen-problems can be defined to find the complex eigenvalues λ and both the left and right complex eigenvectors, respectively $\{v\}$ and $\{\xi\}$ as follows[1]:

$$\lambda_r\{v_r\}^T[A] = -\{v_r\}^T[B] \tag{2.8}$$

$$\lambda_r[A]\{\xi_r\} = -[B]\{\xi_r\} \tag{2.9}$$

Matrices of left and right complex eigenvectors, respectively $[\Upsilon]$ and $[\Xi]$, diagonalize the system matrices $[A]$ and $[B]$ in (2.6).

---

[1]Commercial finite element codes, by default, solve the right eigenvalue problem (2.9).

$$[\Upsilon]^T [A] [\Xi] \{\dot{z}\} + [\Upsilon]^T [B] [\Xi] \{z\} = [\Upsilon]^T \{Q\} \tag{2.10}$$

$$\left[\,`a_r` \, \right] \{\dot{z}\} + \left[\,`b_r` \, \right] \{z\} = \{p\} \,. \tag{2.11}$$

where $\{z\}$ is the vector of the complex modal coordinates. The right eigenvector matrix $[\Xi]$ allows the transformation between the state-space coordinates and the modal coordinates $\{Y\} = [\Xi]\{z\}$; $\{p\}$ is the projection on the modal base, by means of the left eigenvector matrix, $[\Upsilon]$, of the applied forces $\{Q\}$. Furthermore, a_r and b_r represent the diagonal terms after the modal transformation.

The resulting complex eigenvalues give information on the frequency (angular frequency ω) and on the modal damping (ζ) of the vibration modes:

$$\lambda = -\zeta\omega \pm i\omega\sqrt{1 - \zeta^2}. \tag{2.12}$$

Eigenvalues with positive real part (negative modal damping) correspond to unstable modes of the mechanical system. In fact, when expressing the system motion as a linear combination of all the system modes, the eigenvalues with positive real part introduce positive exponential terms that turn the system away from the equilibrium position. This results in unstable vibrations at the frequencies of the modes with positive real part.

Increasing the frictional forces (i.e. increasing the friction coefficient) affects the system by modifying the real parts of the coalescing modes, which depart from the original one due only to the material damping:

$$\zeta^\star = \frac{1}{2} \left(\frac{\alpha_R}{\omega} + \beta_R \cdot \omega \right). \tag{2.13}$$

One of the two coalescing eigenvalues moves toward the positive half space of the real part. When it becomes positive it causes the instability of the system. The system is characterized by super-critical Hopf bifurcations [HOP 42, MAR 76] as a function of the friction coefficient. The increase of the local friction coefficient μ increases the asymmetry introduced into the system matrices by the contact stiffness. The stable focus of the system, which corresponds to the equilibrium position in sliding condition, becomes unstable giveing rise to a stable orbit called limit cycle. This behavior and dependency from the friction coefficient will be observed both on the finite element model in Chapter 3 and on the lumped component model in Chapter 2.2.2.

2.2 Transient nonlinear contact analysis

This section shows the models and the numerical methods used in chapters 3 and 5 for the transient simulation of the system response. It is divided into two subsections: the first one shows the finite element model and its explicit formulation, which is

combined with the Lagrange multiplier method at the contact, for a reliable solution of the transient contact problem, the second one shows the lumped component model and the modal superposition approach adopted to obtain the transient solution.

2.2.1 Finite element model for explicit transient analysis

To simulate the dynamic behavior of the mechanical system in Section 2.4 the dynamic finite element code PLASTD is used. This code allows for a reliable simulation of the large deformation dynamic response of systems with nonlinear frictional contact.

The software PLASTD uses a forward Lagrange multiplier method to solve the dynamic contact problem, evaluating the normal and tangential contact stresses as well as the contact status (stick, slip or detachment), within an explicit formulation of the finite element method. The finite element model realized in this study and used for the transient simulations in Chapter 3 is composed by a deformable body Γ in frictional contact with a rigid body Σ_c (cf. Fig. 2.1).
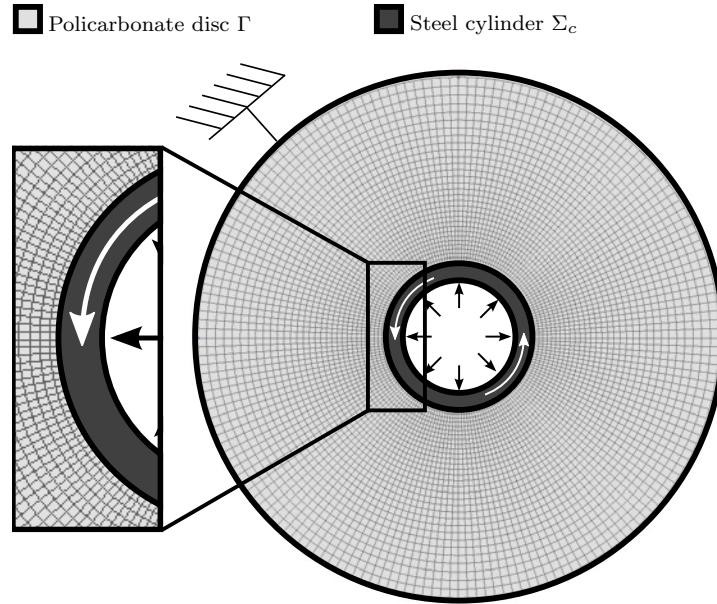
Figure 2.1: Finite element model for numerical simulations.

The 2D spatial discretization of the deformable body Γ is realized by 4 nodes quadrilateral elements with 2×2 Gauss quadrature rule. The contact algorithm uses contact (slave) nodes (placed on the contacting surface of the body Γ) and target (master) elements. In the model developed for this study the target elements have a rigid behavior, they have an arc shape and the totality of the target elements reproduces a rigid circumference.

The equations set of the forward incremental Lagrange multiplier method is constructed using the equations of motion developed via the principle of virtual

work at time step t_i augmented by displacement constraints acting on the contact nodes at time t_{i+1}:

$$\begin{cases} [M]\{\ddot{u}\}_i + [C]\{\dot{u}\}_i + [K]\{u\}_i + [G]_{i+1}^T \{\lambda\}_i = \{F\}_i^{ext} \\ [G]_{i+1}^T \left[\{X\}_i + \{u\}_{i+1} - \{u\}_i \right] \leq 0 \end{cases} \quad (2.14)$$

where:

$[M]$, $[K]$ are respectively the mass and stiffness matrices of the system;

$[C]$ is the Rayleigh's proportional damping matrix of the system (see (2.4));

$\{X\}_i$ is the coordinate vector at time i;

$\{X\}_{i+1} = \{X\}_i + \{u\}_{i+1} - \{u\}_i$ is the coordinate vector at time $i+1$;

$\{\lambda\} = \{\{\lambda_n\}^T \{\lambda_t\}^T\}^T$ are the contact forces acting on the contact nodes in normal and tangential direction, which are introduced as Lagrange multipliers;

$[G] = [[G_n][G_t]]$ is a collocation matrix of the displacement conditions (non-penetration) and the frictional contact forces, over the bodies in contact;

$\{u\}$, $\{\dot{u}\}$, $\{\ddot{u}\}$ are respectively the displacement, the velocity and the acceleration of the degrees of freedom of the system;

$\{F\}^{ext}$ is the vector of external nodal forces.

The code uses the explicit Newmark scheme [NEW 59] to discretize in time the transient problem in (2.14). The acceleration $\{\ddot{u}\}_i$ and the velocity $\{\dot{u}\}_i$ are expressed at each time step as follows:

$$\begin{cases} \{\ddot{u}\}_i = \dfrac{2}{\Delta t^2} \left(\{u\}_{i+1} - \{u\}_i - \Delta t \cdot \{\dot{u}\}_i \right) \\ \{\dot{u}\}_i = \dfrac{1}{1+2\beta_2} \left[\{\dot{u}\}_{i-1} + \Delta t \left(1-\beta_2\right)\{\ddot{u}\}_{i-1} + \dfrac{2\beta_2}{\Delta t} \left(\{u\}_{i+1} - \{u\}_i \right) \right] \end{cases} \quad (2.15)$$

In this formulation the coefficient $\beta_2 \in [0.5; 1)$ is related to the numerical damping. Values of $\beta_2 > 0.5$ correspond to the presence of numerical damping that has an effect which is similar to the effect of the material damping on the system dynamics [DIB 12]. When $\beta_2 = 0.5$ the method in (2.15) corresponds to the central differences method and does not introduce any numerical damping. For the analyses presented in Chapter 3 this choice ensures that no non-physical dissipation will be introduced, and the transient response respects the energy balance formulated in Section 2.3.

The nodal displacements $\{u_{i+1}^\star\}$ at time $t_{i+1}^\star$ are initially computed without contact interaction ($\lambda_i = 0$):

$$\{u_{i+1}^\star\} = \Delta t^2 [M]^{-1} \left(\{F_i\} - [K]\{u_i\} \right) + 2\{u_i\} - \{u_{i+1}\} \quad (2.16)$$

If the contact nodes result to be penetrated through the target element, the constraint matrix $[G_{i+1}]$ is updated and the calculation of contact forces λ_i and of the actual nodal displacement at time t_{i+1} is performed:

$$\begin{cases} \{\lambda_i\} = \left(\Delta t^2 \, [G_{i+1}] \, [M]^{-1} \, [G_{i+1}]^T\right)^{-1} [G_{i+1}] \left\{u_{i+1}^\star\right\} \\ \{u_{i+1}\} = \left\{u_{i+1}^\star\right\} - \left(\Delta t^2 \, [M]^{-1} \, [G_{i+1}]^T \{\lambda_i\}\right) \end{cases} \qquad (2.17)$$

Equations in (2.17) are solved using the Gauss-Seidel method [CAR 91].

During each iteration in (2.17) the following condition, which is applied to all the contact (slave) nodes k in normal direction n, allows to distinguish between nodes that are in contact and nodes that are in separation status:

$$\lambda_n^k \leq 0 \quad \rightarrow \quad \begin{cases} \lambda_n^k < 0 & \text{(contact)} \\ \lambda_n^k = 0 & \text{(separation)} \end{cases} \qquad (2.18)$$

Moreover, another condition in tangential direction is applied to the nodes that are detected to be in contact by (2.18) and allows to discriminate between the contact nodes in sliding and in sticking status, by using a classical Amontons-Coulomb friction law:

$$|\lambda_t^k| \leq \mu |\lambda_n^k| \quad \rightarrow \quad \begin{cases} \text{if } |\lambda_t^k| < \mu |\lambda_n^k| \;\; \rightarrow \; v_t^k = 0 & \text{(stick)} \\[2mm] \text{if } |\lambda_t^k| = \mu |\lambda_n^k| \;\; \rightarrow \; \lambda_t^k v_t^k \leq 0 & \text{(slip)}. \end{cases} \qquad (2.19)$$

The main advantage in using PLASTD for the solution of problems related to friction-induced vibrations is that the explicit Newmark integration scheme coupled with the forward Lagrange multiplier method allows for a more reliable solution of the dynamic contact problems. Lagrange multiplier method, in fact, avoids the use of artificial contact stiffnesses, which are introduced for example by penalty methods, that modify the mechanical model at the contact zone. Furthermore, the explicit method results to be particularly suitable for the solution of dynamic problem involving rapid dynamic phenomena such as local impact, wave and rupture propagation, which are typically present in contact problems.

2.2.2 Periodic modular model with lumped components

In this thesis, a lumped model (LM) composed of masses m connected by springs k and viscous dampers c has been developed to analyze the friction-induced vibrations on a simple mechanical system (cf. Fig. 2.2). The model is composed of both masses that are in frictional contact with rigid sliders and masses that are not in contact with the sliders, but linked to the adjacent masses. Furthermore, a static preload displacement δ can be applied at the upper end of the springs k_3^i, allowing for introducing the preload to the contact. The masses in contact with the sliders are able to switch among the different contact statuses (Sliding-Sticking-Detachment).
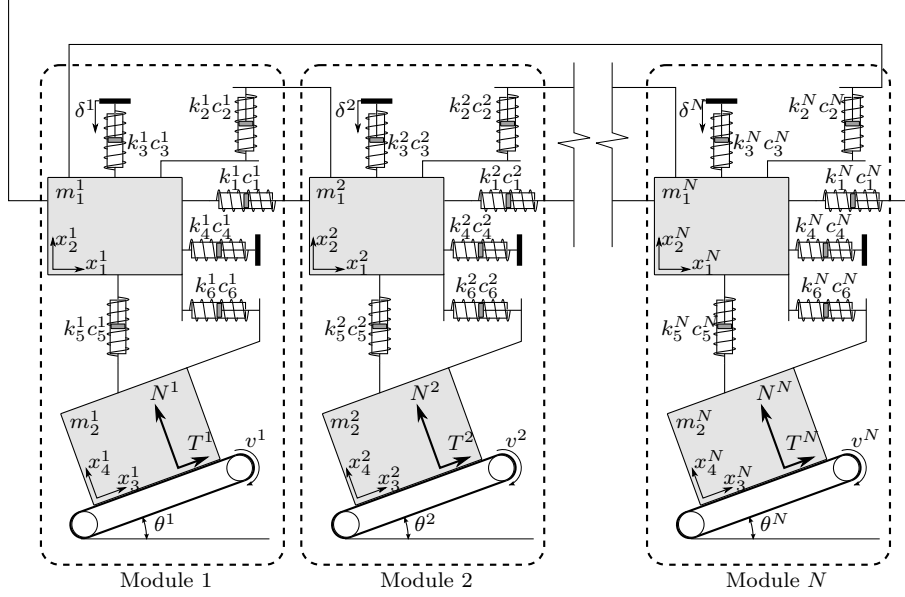
Figure 2.2: Periodic and N-modular lumped system

The presence of masses directly involved in the contact and masses that are not in contact allows consideration of both the bulk and the surface behavior of a system with frictional contacts. In fact, the strong coupling between the surface behavior and the dynamic response of the system is considered to be of main importance for friction induced vibration issues [ADA 98, ADA 95, BAI 05a, CHA 08, DIB 12, HOF 02, MAS 10, REN 11b, SIN 07b, TON 13]. Hence, by this LM, it is possible to model both the effects of system dynamics on the frictional forces exchanged at the contact interface and, vice-versa, the effects of the variation of the contact status on the system dynamic response.

The proposed LM is composed of single modules (i), each one composed of two masses (m_1^i and m_2^i in Fig. 2.2), the connecting stiffnesses and dampers ($k_{3:6}^i$ and $c_{3:6}^i$) and the respective boundary conditions (δ^i, v^i and θ^i). The module is repeated (N) times and the different modules are connected each other via stiffnesses and dampers ($k_{1:2}^i$ and $c_{1:2}^i$). Furthermore, a periodicity condition is imposed between the last (N) and the first (1) module.

The periodicity allows to account for the double modes, that are generally due to the symmetry of the system [BRU 15b]. On the other hand, the modularity permits a rapid variation of the number of degrees of freedom and consequently of the system complexity. Moreover, the presence of multiple contact points reproduces, even if in a discrete way, the distribution of the contact forces and tangential velocity over an extended contact surface, and their contribution to the exchange and dissipation of energy during friction induced vibrations [LIN 03].

Before the application of the contact constraints, in a general configuration, each

28

module is characterized by 4 degrees of freedom (DoF):

$$\{X\}^i = \left\{ \begin{array}{cccc} x_1^i & x_2^i & x_3^i & x_4^i \end{array} \right\}^T. \tag{2.20}$$

The mass sub-matrix of the single module is

$$[M]^i = \text{diag}(\begin{array}{cccc} m_1^i & m_1^i & m_2^i & m_2^i \end{array}) \tag{2.21}$$

The stiffness sub-matrix of the single module is:

$$[K]^i = \left[\begin{array}{ccc} k_1^i + k_4^i + k_6^i & 0 & -k_6^i \cos\theta^i \\ 0 & k_2^i + k_3^i + k_5^i & -k_5^i \sin\theta^i \\ -k_6^i \cos\theta^i & -k_5^i \sin\theta^i & k_5^i \sin^2\theta^i + k_6^i \cos^2\theta^i \\ k_6^i \sin\theta^i & -k_5^i \cos\theta^i & (k_5^i - k_6^i)\sin\theta^i \cos\theta^i \\ \hline -k_1^i & 0 & 0 \\ 0 & -k_2^i & 0 \end{array} \right.$$

$$\left. \begin{array}{c|cc} k_6^i \sin\theta^i & -k_1^i & 0 \\ -k_5^i \cos\theta^i & 0 & -k_2^i \\ (k_5^i - k_6^i)\sin\theta^i \cos\theta^i & 0 & 0 \\ k_5^i \cos^2\theta^i + k_6^i \sin^2\theta^i & 0 & 0 \\ \hline 0 & k_1^i & 0 \\ 0 & 0 & k_2^i \end{array} \right] \tag{2.22}$$

The elements of this matrix over the 4th line and columns represent the link between the module i and the module $i + 1$. To realize the periodicity condition the Nth module is linked with the 1st module. These sub-matrices, defined for each module, are assembled to obtain the full matrices $[M]$ and $[K]$ ($4N \times 4N$) of the mechanical system. The material damping is considered to be proportional to the mass and to the stiffness of the system, following the Rayleigh model (2.4).

The vector of the applied forces for the ith module is:

$$\{F\}^i = \left\{ \begin{array}{cccc} 0 & -k_3^i \delta^i & T^i & N^i \end{array} \right\}^T \tag{2.23}$$

Hence, the dynamic equation of motion can be written for the mechanical system:

$$[M]\left\{\ddot{X}\right\} + [C]\left\{\dot{X}\right\} + [K]\left\{X\right\} = \{F\} \tag{2.24}$$

The contact conditions

$$\begin{cases} x_4^i N^i = 0 \\ x_4^i \geq 0 \quad \text{and} \quad N^i \geq 0 \\ T^i = -\text{sign}(\dot{x}_3^i - v^i)\mu N^i \end{cases} \tag{2.25}$$

impose some constraints on the system, reducing the actual number of DoFs of each module. The contact between the mass m_2^i and the respective slider of each module i can assume four different statuses:

Sliding (SL): in this status the tangential speed of the contacting mass is lower than the slider speed ($\dot{x}_3^i < v^i$), the tangential force can be expressed as a function of the normal force by means of the friction coefficient μ ($T^i = \mu N^i$). Furthermore, the contact condition imposes that the position, velocity and acceleration in the direction x_4^i, that is normal to the contact, are nil ($x_4^i = \dot{x}_4^i = \ddot{x}_4^i = 0$). In these conditions the the local normal force, acting on the contact mass, is calculated as a function of the system state ($N^i = f(\{X\}, \{\dot{X}\})$);

Reverse-sliding (R-SL): in this status the tangential speed of the contacting mass is higher than the slider speed ($\dot{x}_3^i > v^i$). Concerning the direction normal to the contact, the same considerations for the SL status remains valid; nevertheless, in this case, the tangential force has a negative direction ($T^i = -\mu N^i$);

Sticking (ST): in this status the relative speed between the contacting mass and the slider is null ($\dot{x}_3^i = v^i$). Also in this case the mass m_2^i does not move in the direction normal to the contact and both the normal and tangential forces can be expressed as function of the system state $N^i = f_1(\{X\}, \{\dot{X}\})$ and $T^i = f_2(\{X\}, \{\dot{X}\})$. To remain in ST status the module of the tangential force must be $\|T^i\| < \mu N^i$. When $\|T^i\|$ reaches the limit value μN^i the system switch to the SL or R-SL status, as a function of the sign of the tangential force T^i;

Detachment (DT): when the normal force N^i reaches a nil value the unilateral contact constraint cannot apply a traction force on the mass ($N^i \geq 0$) and the mass detaches from the slider moving in both the normal ($x_4^i \geq 0$) and tangential direction. In this case the contact forces are nil $N^i = T^i = 0$ until the normal position $x_4^i > 0$. When the normal position reaches the nil value it means that the mass engages again the contact with the slider and the system switches to the SL or R-SL status, as a function of the sign of the relative tangential speed.

When at least one of the modules composing the system is in SL or R-SL status the tangential force has the following form:

$$T^i = -\text{sign}(x_3^i - v^i)\mu f\left(\{X\}, \left\{\dot{X}\right\}\right) \tag{2.26}$$

and introduces asymmetric terms on the stiffness and damping matrices.

Furthermore, when at least one of the contacting mass is in ST status with the slider that moves with a constant speed v^i, the position of the sticking mass is:

$$x_3^i(t) = \hat{x}^i + v^i(t - \hat{t}) \tag{2.27}$$

where $\hat{x}^i$ and $\hat{t}$ are respectively the tangential position of the sticking mass at the beginning of the ST status and the time of beginning of the ST status.

Hence, after the application of the contact constraints, in (2.26) and (2.27), the dynamic equation of the system, in (2.28), will be characterized by system matrices $[\widetilde{M}]$, $[\widetilde{C}]$ and $[\widetilde{K}]$ that are generally smaller than the matrices in (2.24) and they will be asymmetric if at least one of the contacting masses is in SL or R-SL status. Furthermore, the applied forces on the right side of (2.28) will be composed by constant terms $\{F_0\}$ if all the masses are in SL, R-SL or DT status. A time dependent linear term ($\{F_1\}t$) will appears if at least one of the contacting mass is in ST status. A general system of equation can be expressed as:

$$\left[\widetilde{M}\right]\left\{\ddot{\widetilde{X}}\right\} + \left[\widetilde{C}\right]\left\{\dot{\widetilde{X}}\right\} + \left[\widetilde{K}\right]\left\{\widetilde{X}\right\} = \{F_0\} + \{F_1\}\,t \qquad (2.28)$$

Time integration approach The defined mechanical system (cf. Fig. 2.2), due to its lumped nature, can reach a finite number of contact configurations (4^N). During the transient response, the system remains into the same contact configuration for a finite interval of time. The dynamic equations (2.28) can be assembled and calculated for each contact configuration and an analytical solution can be obtained. During each interval, the response of the system can be expressed with a modal decomposition approach [BRU 15a]. The mechanical system can be expressed in the state space coordinates $\{Y\}$ as previously shown in (2.7).

$$[A]\left\{\dot{Y}\right\} + [B]\{Y\} = \{Q_0\} + \{Q_1\}\,t \qquad (2.29)$$

The asymmetry of the stiffness and damping matrices, introduced by the friction law, leads to define the two eigen-problems in (2.8) and (2.9). The matrices of left and right eigenvectors, respectively $[\Upsilon]$ and $[\Xi]$, diagonalize the system in (2.29):

$$\left[\,\ddots a_r \ddots\,\right]\{\dot{z}\} + \left[\,\ddots b_r \ddots\,\right]\{z\} = \{p_0\} + \{p_1\}\,t. \qquad (2.30)$$

Each line of the system of equations in (2.30) is a first order linear differential equation with a constant and a linear excitation term and describes the motion along each of the modal coordinate z_r. The analytic solution is the sum of three terms: *(i)* the free response starting from the initial position $z_{r,0} = \{\xi_r\}^T\{Y_0\}$, *(ii)* the response to an Heaviside step function of amplitude $p_{r,0}$ and *(iii)* the response to a linear ramp with a slope coefficient $p_{r,1}$.

$$z_r(t) = e^{\lambda_r t}z_{r,0} + \frac{1}{b_r}\left(1 - e^{\lambda_r t}\right)p_{r,0} + \frac{1}{b_r}\left(\frac{1 - e^{\lambda_r t}}{\lambda_r} + t\right)p_{r,1} \qquad (2.31)$$

Finally, the response of the system in the state space coordinate, can be expressed as:

$$
\begin{aligned}
\{Y(t)\} \;&= [\Xi]\{z(t)\} \\
&= [\Xi]\left[\,\ddots e^{\lambda_r t} \ddots\,\right][\Xi]^{-1}\{Y_0\} + \\
&\quad + [\Xi]\left[\,\ddots b_r \ddots\,\right]^{-1}\left[\,\ddots 1 - e^{\lambda_r t} \ddots\,\right]\{p_0\} + \\
&\quad + [\Xi]\left[\,\ddots b_r \ddots\,\right]^{-1}\left[\,\ddots \tfrac{1-e^{\lambda_r t}}{\lambda_r} + t \ddots\,\right]\{p_1\}
\end{aligned}
\qquad (2.32)
$$

The solution in (2.32) is valid within a time interval, until one of the contact masses changes its contact status at time $t^\star$. The position and velocity of the system at this time $\{Y(t^\star)\}$ will be the initial condition $\{Y_0\}$ for the following time interval; the time response within the new time interval is still expressed by (2.32), but calculated starting from a set of system dynamic equations in (2.28) that account for the new contact configuration of the system. In such a way, the time response of the system is calculated analytically by successive time interval considering the set of dynamic equations appropriate to each contact configuration of the system.

2.3   Energy balance at the contact region

Once the transient response is known, using the techniques introduced in Sections 2.2.1 and 2.2.2, a general energy balance can be defined to determine the power flow between the contact surface and the bulk of the mechanical system. For the elastic body Γ (cf. Fig. 2.3) the potential elastic energy (total strain energy) E_e and the kinetic energy E_k composing the mechanical energy E_m can be defined as follows[2]:

$$E_e = \frac{1}{2} \{x\}^T [K] \{x\} \qquad \text{and} \qquad E_k = \frac{1}{2} \{\dot{x}\}^T [M] \{\dot{x}\} \tag{2.33}$$

The variation of the mechanical energy is equal to the difference between the work of external forces and the work of internal nonconservative forces, and is directly related to the amplitude of vibration.
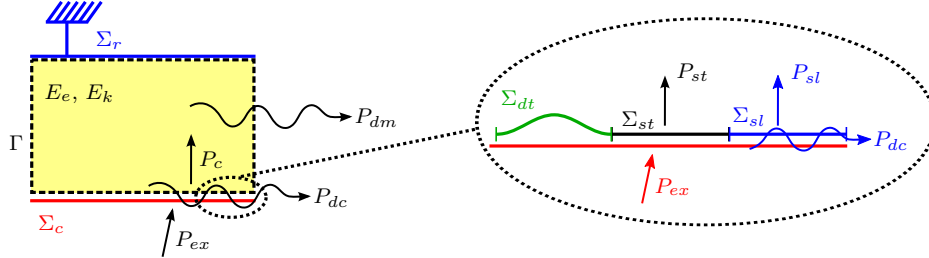
Figure 2.3: Energy balance scheme. E_e and E_k are respectively the elastic potential energy and the kinetic energy of the elastic body Γ, Σ_r is the portion of the edge where a rigid constraint is applied, Σ_c is the portion of the edge where the contact interaction is defined. P_c is the power totally exchanged at the contact, P_{ex} is the power globally absorbed by the system and P_{dm} is the power dissipated by the material damping. Σ_{dt}, Σ_{sl} and Σ_{st} represents respectively the portion of the contact surface Σ_c in detachment, sliding and sticking status. P_{sl} and P_{st} are respectively the powers exchanged in sliding and sticking. P_{dc} is the power dissipated at the contact.

---

[2]To calculate the potential term only the elastic force have to be considered; consequently to compute this quantity the matrix $[K]$ in (2.24) has to be considered, rather than the matrix $[\widetilde{K}]$ in (2.28), which includes also the non-conservative terms due to the contact forces.

In this case, the external forces are represented by the contact forces $\{F_c\}$ acting at the contact interface Σ_c, and the reaction forces $\{F_r\}$ at the fixed constraint Σ_r. The internal nonconservative forces are the material damping forces $\{F_d\} = [C]\{\dot{x}\}$ acting on the volume of the elastic media Γ. The variation of mechanical energy between time t_i and t_f can be expressed basing on the work-energy theorem as the work of nonconservative forces[3]:

$$E_m^f - E_m^i = \int_{t_i}^{t_f} \{\dot{x}\}^T \{F_c\} \, dt - \int_{t_i}^{t_f} \{\dot{x}\}^T \{F_d\} \, dt. \qquad (2.34)$$

Therefore, the derivative of the mechanical energy can be expressed as a function of the power exchange between the system and the external environment, in particular as the difference between the power P_c exchanged at the contact with the rigid surface and the power P_{dm} dissipated by the material damping:

$$\frac{dE_m}{dt} = \{\dot{x}\}^T \{F_c\} - \{\dot{x}\}^T \{F_d\} = P_c - P_{dm}. \qquad (2.35)$$

The dissipative term P_{dm} gives always a negative contribution to the variation of the mechanical energy E_m, due to the nature of the non-conservative damping forces that produce an action proportional to the velocity along the opposite direction with respect to the local velocity. On the other hand, the power exchanged at the contact P_c between the elastic system and the sliders can be either positive, increasing the energy content of the system E_m, or negative, subtracting energy from the system and acting as a damper with respect to the dynamic response of the system. In general, during friction-induced vibrations, a mutual exchange in the two directions is always present at the contact.

When the system is unstable, the phase combination between the tangential force and tangential speed produces a flow of energy at the contact toward the elastic body, increasing its total energy content (elastic and kinetic energy). The higher the energy content is, the higher the vibration amplitude will be and increases when instabilities occur.

During contact simulation, the contact interface Σ_c is composed of portions in sliding Σ_{sl}, sticking Σ_{st} and detachment Σ_{dt} (cf. Fig. 2.3). Portions of contact interface that are in detachment do not exchange any energy with the rigid surface. Portions that are in sticking move with the same velocity as the rigid surface v_r. On the contrary, the portions that are in sliding move with a tangential speed $\dot{x}_t$ that is different with respect to the tangential speed of the rigid surface.

Hence, due to the different contact status the external power P_{ex} in (2.36) can

---

[3]The work of reaction forces $\{F_r\}$ is nil if they act on a fixed constraint.

be decomposed into three terms:

$$P_{ex} = v_r \int_{\Sigma_c} \tau d\Sigma \qquad (2.36)$$

$$= v_r \int_{\Sigma_{st}} \tau_c d\Sigma + \int_{\Sigma_{sl}} \dot{x}_t \tau_c d\Sigma + \int_{\Sigma_{sl}} (v_r - \dot{x}_t)\tau_c d\Sigma \qquad (2.37)$$

$$= v_r \{F_{st}\} + \{\dot{x}_t\}^T \{F_{sl}\} + [v_r - \{\dot{x}_t\}]^T \{F_{sl}\} \qquad (2.38)$$

$$= P_{st} + P_{sl} + P_{dc} \qquad (2.39)$$

The three terms[4] have respectively the following meaning:

- P_{st} is the power exchanged by the sticking portions of the contact interface; it is defined as the product between the tangential speed of the rigid body (i.e. the local contact point) and the tangential contact forces;

- P_{sl} is the power exchanged by the sliding portions of the contact interface; it is defined as the product between the absolute tangential speed of the contact point and the tangential contact forces;

- P_{dc} is the power dissipated in the sliding portions of the contact interface; it is defined as the product between the relative (sliding) tangential speed at the contact and the tangential contact forces.

The power exchanged at the contact, P_c in (2.35), is the sum of the sliding P_{sl} and sticking P_{st} exchanged powers.

The sign of the contact exchanged power P_c indicates the direction of the energy flow at the contact and, for each term, it depends on the direction of the tangential speed ($\dot{x}_t$ in sliding and v_r in sticking) and of the tangential contact stress (τ_c)[5]. Each contacting point gives its positive or negative contribution over the simulation time.

Furthermore, it should be noticed that P_c is the energy exchanged and not the energy dissipated at the contact, even if it has a negative sign. In fact, a distinction must be done between the exchanged energy at the contact P_c and the energy dissipated at the contact P_{dc}, which is defined as the product of the relative speed ($v_r - \dot{x}_t$) and the tangential contact stress τ_c. This quantity is always negative because of the definition of the tangential force in (2.19).

During the limit cycle the system reaches a dynamic equilibrium condition, the energy dissipated by material damping and contact balances the energy introduced into the system:

$$P_{ex} = P_{dc} + P_{dm} \qquad (2.40)$$

---

[4]The integrals in (2.36) can easily be substituted by sums to apply these definitions to the lumped molde in Section 2.2.2.
[5]Contact forces T^i in case of lumped model in Section 2.2.2.

and in particular all the energy introduced by friction induced vibrations is dissipated by material damping:

$$P_c = P_{dm}. \tag{2.41}$$

The energy terms defined here have been employed in Chapters 3 and 5 for calculating the energy balance and the energy flows for respectively the finite element model and the lumped model. Moreover, the same energy quantities have been used in Chapter 5 to define the a stability index in order to define a hierarchy among the several unstable modes which can be predicted by the CEA.

2.4 Experimental setup (Phototrib)

The numerical analyses in Chapter 3 are performed on a finite element model of the "PhotoTrib" [SAU 13], an experimental setup developed at the LaMCoS Laboratory. It allows to reproduce experimentally friction induced vibrations on a polycarbonate disc and to observe the dynamic and the tribological effects of these vibrations on the system.

The system is composed of a deformable disc made of polycarbonate, which is constrained at its external circumference. A coaxial cylinder made of steel is put in rotation inside the polycarbonate one; a static radial expansion of the steel cylinder ensures the contact with the inner circumference of the polycarbonate disc, imposing the desired contact pressure. Radial forces (normal to the contact surface) and friction forces (along the tangential direction) at the contact interface induce vibrations on the system.
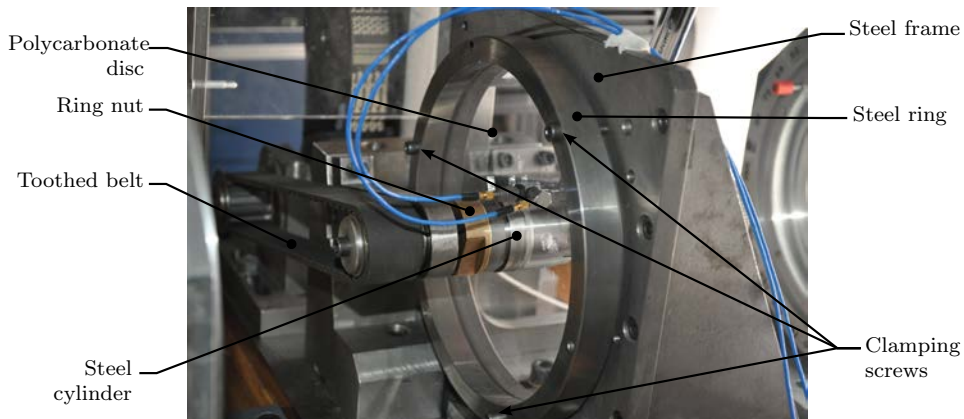
Figure 2.4: The experimental setup. PhotoTrib.

The polycarbonate disc (inner radius 20.5 mm, external radius 90.5 mm, thickness 9 mm) is clamped on a rigid frame, while the steel cylinder is linked by a transmission belt to the driving motor (cf. Fig. 2.4). Inside the steel cylinder a screw mechanism produces the axial compression of an elastic component (rubber cylinders placed inside the steel one) that generates the radial expansion of the outer

steel cylinder; the radial expansion is measured by an inductive proximity sensor and stopped when the desired contact pressure between the two bodies is reached. A full description of the expanding chuck and of the precautions adopted to minimize the axial asymmetry and conicity error are reported in [SAU 13, REN 11a]. The steel cylinder is maintained at constant rotational speed by a controller and the engine torque is measured during tests.

Experimental measurements of quantities at the contact interface are quite difficult: significant errors can arise due to the introduction of sensors and consequent modification of the contact pair. This is why numerical simulation is needed to investigate the issue. In this work the experimental set-up shown in Fig. 2.4 is used in Chapter 4 to validate the numerical analysis results in Chapter 3 by comparing with the macroscopic dynamic behavior of the system. To this aim, accelerometers have been placed on the free surface of the polycarbonate disc to measure the in-plane disc vibration during the frictional contact and compare the acceleration signals with the numerical ones (cf. Fig. 4.8). The polycarbonate material has been chosen for its photoelastic properties and transparency for the observation of shear stress distribution and third body analysis, reported in [SAU 13, REN 14].

Chapter 3

System stability and mechanical energy balance

Contents

This chapter presents a finite element analysis of a mechanical system to reproduce the vibrations that are induced by a frictional contact interface. Mode coupling instabilities of a single deformable body in frictional contact with a rigid one, are investigated. The mode coupling contact instability has been obtained by a such simple mechanical system, where the friction forces couple the tangential and normal deformations of the same body, allowing the generalization of phenomena addressed to specific systems, such as brakes.

The 2D finite element model is here developed to reproduce and analyze the energy flows occurring during the in-plain unstable vibrations of the PhotoTrib setup. A classical approach is used to investigate the dynamic behavior of the system. In the first phase, by means of the Complex Eigenvalue Analysis, the stability of the frictional mechanical system has been analyzed as a function of the friction coefficient. In the second phase, the transient simulation allows to observe the time response of the mechanical system in both stable and unstable conditions. The energy flows, related to the in-plane vibrations, are computed and analyzed for different operating conditions.

The analysis proposed in this chapter aims to investigate the influence of system vibrations on the repartition between the mechanical energy dissipated locally at the contact interface and the energy re-introduced into the bulk, by friction induced vibrations, and then dissipated by means of material damping. Quantify correctly the contact dissipated power is fundamental for numerous issues. It is the coupling physical quantity between the phenomena at the system scale, studied in this work, and the contact scale, where the dissipated energy is at the origin of the local heating, of local variation of the material properties and of wear phenomena.

3.1 Model description

The finite element model used for the following simulations is a 2D plane strain model (cf. Fig. 3.1) that reproduces the polycarbonate disc Γ of the PhotoTrib setup, described in Section 2.4.

The difference in stiffness between the materials of the two cylinders in contact (the polycarbonate Young's modulus is about $2.5\,\mathrm{GPa}$ while that of steel is about $210\,\mathrm{GPa}$) allows for considering only one deformable body Γ (the polycarbonate disc) in contact with a rigid one Σ_c (the steel cylinder). Moreover, because the elasticity of the whole steel frame is negligible, if compared to the polycarbonate disc, a rigid constraint is applied to the external circumference Σ_r of the disc in order to model the constrain with the fastening that fixes the disc in the real system.

Furthermore, the contact forces that give rise to the friction induced vibrations of the disc lie on the plane. Hence, the 2D plain-strain model can reproduce in a reliable way the response of the experimental set-up. These assumptions bring to a radical reduction of the model dimensions and of the computational efforts.

A dynamic analysis on a full 3D model, including the frame of the mechanical system and the axis, has been developed (cf. Chapter 4) and has highlighted that the
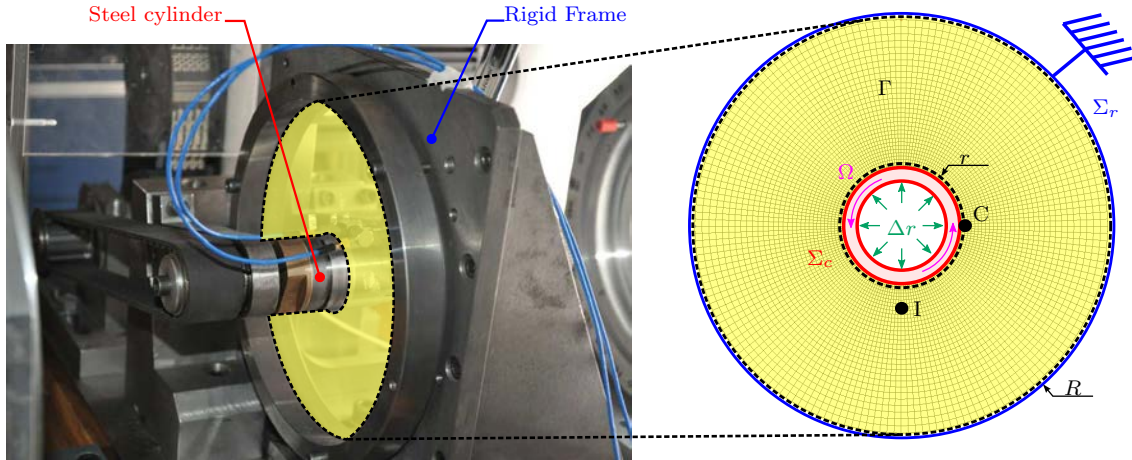
Figure 3.1: Experimental setup "PhotoTrib" used to validate the numerical results (left) and finite element model of the polycarbonate disc (right).

dynamic instabilities of interest are characterized by in-plane vibrations; they can be observed by the 2D model as well, with a substantial reduction of the computational time. A comparison between the in-plane mode frequencies calculated by the full 3D model and the simplified 2D model showed that frequencies of the simplified 2D model are higher than the frequencies of the full 3D model, but this frequency difference does not affect the modal shape that are very similar between the two models. The difference in frequency can be related to mainly three reasons: i) the introduction of a fixed boundary on the external edge of the 2D model, instead of the external frame, which increases the stiffness of the system; ii) the mass of the external frame is not taken into account in the 2D model, that results to be less massive than the 3D model and the real system; iii) the plane-strain formulation introduces an out of plane constraint that increases the global stiffness of the system.

Moreover, a further difference with the experiments is due to the connection between the polycarbonate disc and the frame: while the connection is bounded in the 3D numerical model, three screws and a steel annular frame are used to clamp the disc in the experiments. The rigidity of the experimental connection is lower, explaining the lower frequencies of the modes. The simplified boundary conditions and the 2D model produce an overestimation of the in-plane mode frequencies; nevertheless these considerations have to be accounted for when comparing the experimental and numerical results (see Section 4.1.2).

A linear finite element model has been developed with the commercial code ANSYS to perform a parametric prestressed Complex Eigenvalue Analysis (CEA) of the system (introduced in Section 2.1). A non-linear finite element model is developed with the code PLAST2 [BAI 03, BAI 02, BAI 05c] to perform a transient nonlinear analysis in explicit dynamic formulation (see Section 2.2.1). The use of these two numerical approaches allows, respectively, to analyze the stability of the system and to reproduce numerically the friction-induced vibrations observed

experimentally and predicted by the CEA.

The geometry of the 2D simplified model, used for numerical simulations, is reported in Fig. 3.1. The external circumference of polycarbonate disc is constrained to the fixed frame and the inner cylinder is in rotation with respect to the external one (see Section 2.4 for details).

Convergence analyses have been performed to find an optimal mesh size both for the linear model, in view of the complex modal analysis, and for the non-linear model, to perform the transient simulations. The finite element model adopted for the modal analysis is composed by 2 038 elements with a size of the contact elements of 0.859 mm. The model adopted for non linear transient analysis is composed by 6 300 elements with a size of the contact elements of 0.715 mm (cf. Fig. 3.1). Labeled dots indicate the position of the contact node C and of the internal node I considered in the following transient simulations.

A radial expansion $\Delta r = 25 \ \mu$m of the cylindrical rigid surface produces a normal contact stress between the two bodies $\widetilde{\sigma}_c = 2.812$ MPa. The rotation velocity Ω imposed on the cylindrical rigid surface generates frictional stresses τ_c, which excite the system dynamics.

In these analyses a Coulomb law with a constant value of the local friction coefficient has been adopted to solve the contact problem (see Section 2.2.1).

The material damping has been included, both in CEA and in transient non linear analysis, by means of the Rayleigh proportional model:

$$[C] = \alpha_R \, [M] + \beta_R \, [K] \tag{3.1}$$

where the damping matrix of the system $[C]$ can be expressed by the sum of two terms that are respectively proportional to the mass $[M]$ and to the stiffness matrix $[K]$. An experimental modal analysis on the polycarbonate disc has been performed to find the proportionality coefficients α_R and β_R in the frequency range of interest (see Section 4.1.3). Finally, table 3.1 lists the geometrical and material properties adopted in the following simulations.

3.2 System stability evaluation by Complex Eigenvalue Analysis

The Complex Eigenvalue Analysis (CEA) has been adopted as a standard tool in the study of the stability of nonlinear mechanical systems with contact interface. In this case, the stability of the equilibrium position can be evaluated by the analysis of the real part of the system eigenvalues calculated when the system is linearized in proximity of the equilibrium position. The equilibrium position corresponds to the uniform sliding state position. A pre-stress static analysis is performed, in the first step, to find the actual normal and tangential contact forces. The value of tangential forces affects the contribution of the asymmetric terms of the stiffness matrix to be accounted for the CEA.

40

Young modulus	E	2.5 GPa
Density	ρ	1202 kg/m^2
Poisson ratio	ν	0.38
Mass proportional Rayleigh damping coefficient	α_R	40 s^{-1}
Stiffness proportional Rayleigh damping coefficient	β_R	$4.5 \cdot 10^{-7}$s
Inner radius of the polycarbonate disc	r	20.5 mm
Outer radius of the polycarbonate disc	R	90 mm
Thickness of the polycarbonate disc	d	9 mm
Radial expansion of the rigid surface	Δr	25 μm
Static normal pressure	$\tilde{\sigma}_c$	2.812MPa
Element number		6300
Contact element size		0.715mm
Integration time step		$0.4e - 7$s

Table 3.1: Geometrical dimensions of the disc and material properties in nonlinear transient simulations and Complex Eigenvalue Analysis.

As highlighted in the previous chapter, the parameters that mainly affect the stability of the system are the material damping (the Rayleigh coefficients α and β) and the friction coefficient (local friction coefficient μ). Generally, the first has a stabilizing effect, when uniformly increased in the system [HOF 03, SIN 06, MAS 08], while the last has a destabilizing effect on the system behavior.

In this section the CEA has been used to evaluate the stability of the polycarbonate disc of the PhotoTrib setup in frictional contact with the inner steel cylinder, in order to study the squeal propensity of the system as a function of the friction coefficient and of the two damping coefficients. Even if these parameters are not directly or easily modifiable in real systems, they are characterized by large dispersion or variability. For instance, composite and plastic materials show a large dispersion of the damping characteristics, and friction coefficient depends on a large set of environmental and operating conditions; moreover, their values can also have significant variations during the single friction episode. Hence, the effect of these two antagonist quantities assume a particular interest in the study of the stability of frictional systems.

In the presented system the eigenmodes can be classified as radial (R), circumferential (C) and hybrid (H) modes, based on the displacement direction, that can be respectively in radial, circumferential or a combination of both.

Figure 3.2 shows the in-plane radial mode 9 (a) and the in-plane circumferential mode 24 (b). The modes are numbered in order of the natural frequency value. In this graphic representation of modal shape (eigenvector), the black arrows indicate the displacement direction and amplitude. The black dot-dashed lines in Fig. 3.2(b) represent the nodal lines of the mode, i.e. the locus of points with nil displacement.

Figure 3.3 shows three in-plane hybrid modes: in the order modes 4-5 (a), modes 9-10 (b) and modes 11-12 (c). Modes in Fig. 3.3(a) and (c) are characterized by an angular period $\theta = \pi$, while the double mode in Fig. 3.3(b) by an angular period $\theta = 2/3\pi$. Moreover, modes in (a) and (b) have $n = 4$ nodes while modes in (b)

(a) Radial Mode 9   (b) Circumferential Mode 24
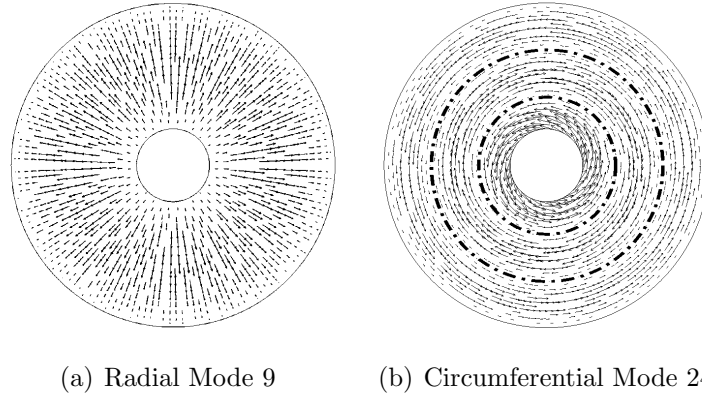
Figure 3.2: Radial and Circumferential mode shapes.

(a) Mode 4-5   (b) Mode 09-10   (c) Mode 11-12
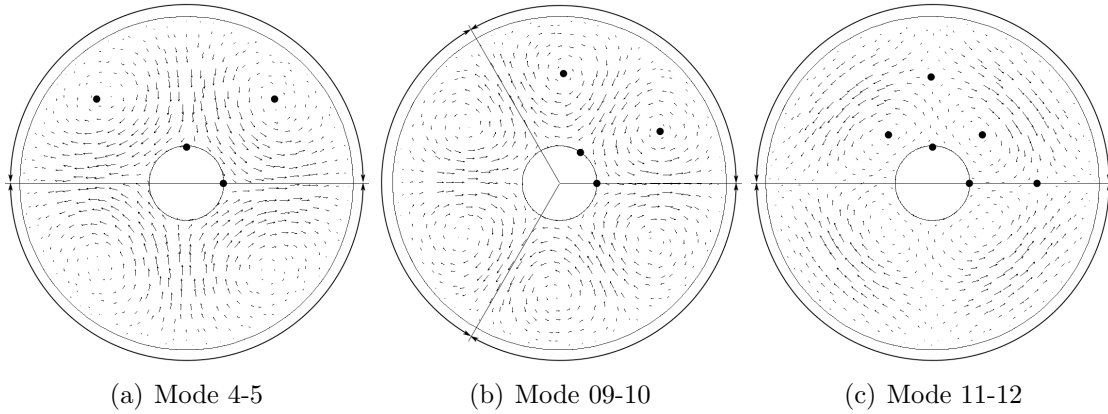
Figure 3.3: Hybrid mode shapes.

have $n = 6$ nodes on each angular period.

Table 3.2 shows the frequencies of the first eigenmodes of the system for a nil friction coefficient. A classification of modes is proposed in Table 3.2 based on the number of nodal lines for radial and circular modes, on the periodicity angle θ and the number of nodal points inside each period for the hybrid modes. Moreover, Table 3.2 highlights that hybrid modes are all double and their combination produces a deformation shape that can rotate, with respect to the geometrical center.

3.2.1 Effects of the local friction coefficient on the system dynamics

The asymmetry introduced by the friction forces on the system matrices ($[A]$ and $[B]$ in (2.6)) produces a variation of the eigenvalues and of the eigenvectors of the system.

Figure 3.4 shows the mode 7 for different values of the friction coefficient μ.

Mode	f [Hz]	Type	n	θ	Mode	f [Hz]	Type	n	θ
1	5857	C	0	-	17-18	14770	H	6	$2\pi/3$
2-3	7632	H	2	2π	19	14832	R	0	-
4-5	9837	H	4	π	20-21	16433	H	4	$\pi/3$
6-7	10500	H	4	2π	22-23	16437	H	6	2π
8	11077	C	1	-	24	16641	C	2	-
9-10	11237	H	4	$2\pi/3$	25-26	17144	H	10	π
11-12	11772	H	6	π	17-28	17434	H	8	$2\pi/3$
13-14	12909	H	4	$\pi/2$	29-30	17697	H	8	2π
15-16	14672	H	4	$2\pi/5$	31-32	18174	H	4	$\pi/4$

Table 3.2: Frequencies f of the eigenmodes of the system computed for a nil friction coefficient.

$\mu = 0$ $\mu = 0.3$ $\mu = 0.6$ $\mu = 0.9$
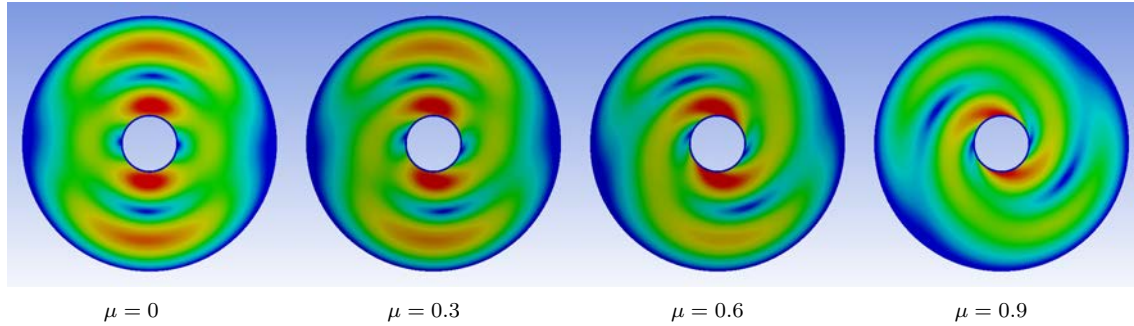
Figure 3.4: Effects of the friction coefficient on the 7th mode of the polycarbonate disc.

Increasing the friction forces the asymmetry on the system matrices modifies the modal shape with respect to the mode without friction. The higher the mode deformation at the contact is, the higher the modification effect of the friction forces on the modal shape will be.

Moreover, the real parts of both the complex eigenvalues of the double modes are negative for a nil friction coefficient. Increasing the effects of friction forces, the real parts of coalesced modes split from the initial value and one moves toward positive values, while the other moves toward negative ones. For a critical value of the friction coefficient $\mu^{\star}$ the real part moving in the positive direction becomes positive, i.e. negative modal damping ζ, and the equilibrium position becomes unstable (Hopf bifurcation point).

Figure 3.5 shows the behavior of the mode pairs 4-5 and 6-7, at about $9.85\,\text{kHz}$ and $10.5\,\text{kHz}$, in terms of frequency f and modal damping factor ζ ($\lambda = -\omega\zeta \pm \omega\sqrt{1-\zeta^2}$) with respect to the friction coefficient μ. Red points correspond to unstable modes (negative values of the modal damping). For the 7th mode the critical value of the friction coefficient is $\mu_{7c} = 0.14$, while for the 5th mode the critical value is $\mu_{5c} = 0.16$. In brake squeal literature, the coupling occurs between eigenfrequencies that coalesce with the increase of the friction coefficient, even when
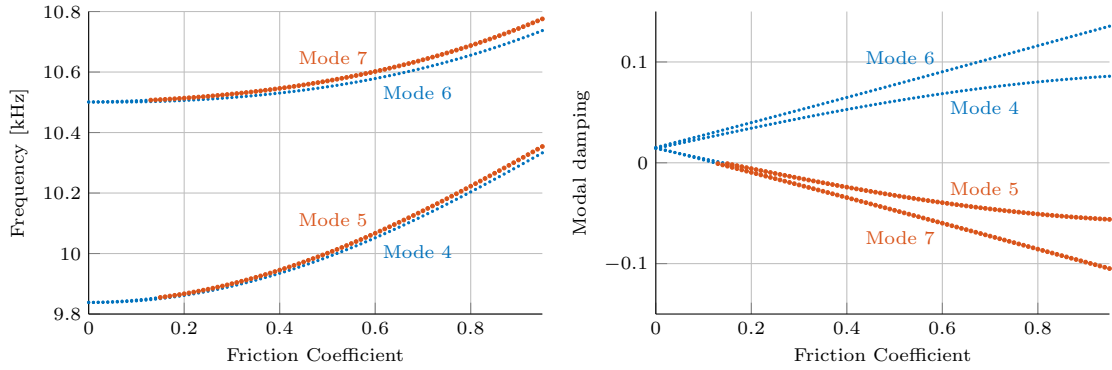
Figure 3.5: Frequency and modal damping of the first unstable modes for different friction coefficients.

they have different frequency for a nil friction coefficient [SIN 07b, MAS 07]. The system investigated here, modeled as a single deformable body, is completely axially-symmetric and the two coalescing modes have the same frequency, i.e. repeated frequency, when the friction coefficient is nil. The increase of friction coefficient causes a small shift between the mode frequencies (left plot in Fig. 3.5).

The modal dampings (right plot in Fig. 3.5) of the eigenvalue pair split toward the two opposite half spaces; the behavior, increasing the friction coefficient, is symmetric with respect to the starting value because the two modes have equal modal damping (they belong to the same body with the same material damping and similar natural frequency) and same deformed shape. It is worth noting that, between the two modes of the coalescing pair, the mode that becomes unstable is the higher frequency one, for all the coalescing pairs.

Figure 3.6 shows the first modes resulting from the CEA for a friction coefficient $\mu = 0.3$. Modal shapes are represented in color scale, red zones correspond to the zones of polycarbonate disc with highest displacement with respect to the equilibrium position.

In Fig. 3.7 are reported the system eigenvalues on the complex plane obtained by changing the friction coefficient μ in the range between 0 and 1.

The dashed curve in Fig. 3.7 represents the theoretical locus of the eigenvalues of the damped system. The two coalescing eigenvalues lie on this curve and are coincident for a nil friction coefficient. Increasing the friction coefficient they split in opposite directions and the real part of one mode of the pair can become positive, i.e. unstable (red points on the locus plot in Fig. 3.7). This phenomenon, known in brake squeal literature as lock-in or modal coupling, is here obtained for pairs of in-plane modes belonging to the same deformable body. The bar diagram on the right of Fig. 3.7 shows the instability intervals (red bars) of friction coefficient for coupled modes that become unstable.

Comparison between the modal shapes in Fig. 3.6 and the result of parametric stability analysis in Fig. 3.7 highlights that modes having large deformation at the
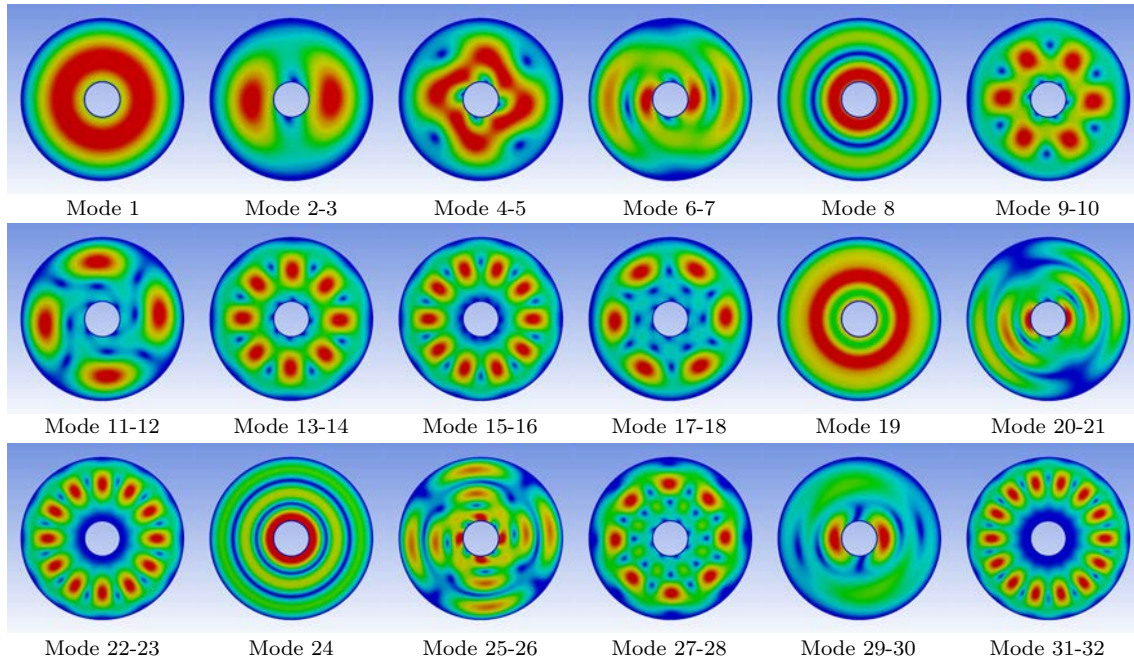
Figure 3.6: First modal shapes resulting from the CEA with a friction coefficient $\mu = 0.3$.
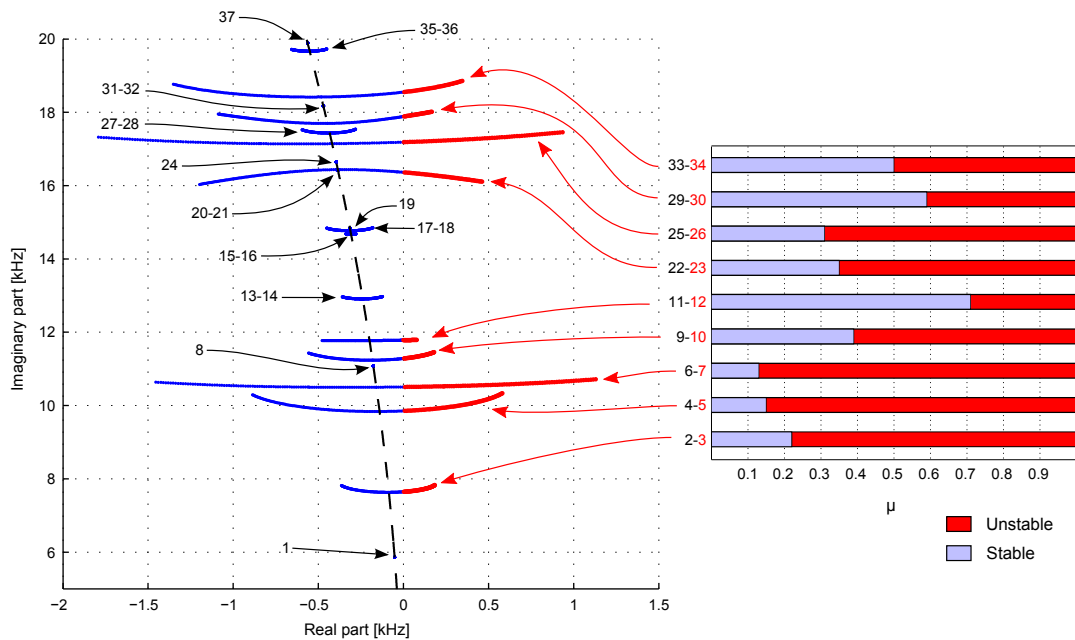
Figure 3.7: Locus plot of the system eigenvalues. For each eigenvalue that becomes unstable the critical value of the friction coefficient is reported in the Stability plot.

contact zone (modes 3, 5 and 7) become unstable; modes with small deformation at the contact zone (modes 14, 16 and 18) are only slightly affected by increasing the friction coefficient and remain stable. Mode 7 is the first mode that reaches the instability by increasing the friction coefficient and it is characterized by the highest displacement over the contact interface (length of the red zones over the contact interface in Fig. 3.6). It is worth noting that for large friction coefficients, even this simple system is characterized by a large number of predicted unstable modes, which, in general, will not be recovered in transient simulations.

3.2.2 Effects of the damping coefficients on the system stability

Figure 3.8 shows the effect of the variation of damping coefficient on the eigenvalue locus on the complex plane, for a damped mechanical system without friction (dot-dashed parabola in Fig. 3.7).

In particular, increasing the value of the mass matrix proportional coefficient α produces a shift of the curve in the negative real part direction. The effect of this variation becomes negligible for high frequencies. On the contrary, the stiffness matrix proportional coefficient β modifies the curvature of the locus curve. Higher values of β give rise to higher curvatures; hence, the higher the frequency of the mode is, the higher the effect of the variation of β on the stability margin will be.
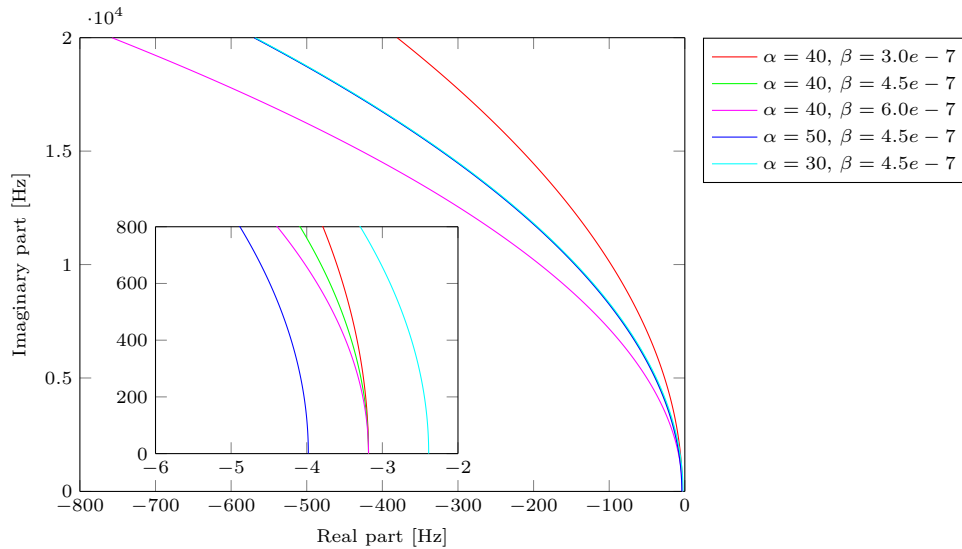
Figure 3.8: Effect of Rayleigh damping coefficient on the eigenvalues locus plot for a nil friction coefficient

Due to the high frequencies generally involved in squeal phenomena, slight variations of β coefficients can produce relevant changes in the system behavior, due to the strong influence of this parameter on the system stability. Figure 3.9 shows the

effect of $\pm 30\%$ variation of the stiffness proportional coefficient β on the stability of two coupled modes $4-5$ and $29-30$, respectively at frequency of 9.8kHz and 17.7kHz. More complex behavior are obtained when the damping increase is not homogeneous on the whole system [SIN 07a, MAS 08].
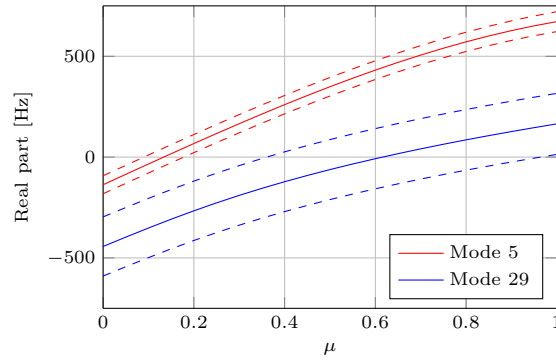
Figure 3.9: Effect of β coefficient on the critical friction coefficient $\mu^\star$ for mode 5 and 29.

3.3 Transient analysis and energy balance

The results shown in the previous section show that mechanical systems with frictional contact, even if constituted by a single deformable body, can be stable or unstable depending on the values assumed by the friction coefficient and the material damping coefficients. The transient behavior of the system is here analyzed, by means of the finite element code PLASTD2 (introduced in Section 2.2.1), for different operating conditions and different values of the system parameters. These analyses highlight the influences of the parameters on the friction-induced vibration phenomena and show some typical tendencies. Furthermore the energy flows involved in friction induced vibrations are shown both in stable and unstable conditions.

In the transient analyses presented in this section the external disc is rigidly fixed on the external circumference and the material damping coefficients are recovered by experimental modal analysis ($\alpha = 40[1/s]$ and $\beta = 4.5e - 7[s]$) [BRU 15b]. The inner rigid disc, reproducing the steel cylinder of the PhotoTrib set-up, rotates with a rotational speed Ω, which is kept constant over the whole simulation time. The local friction coefficient μ is considered to be constant, following the classical Coulomb law. The rigid surface is radially expanded in the first part of simulation ($\Delta r = 25\mu$m) to reproduce the radial expansion of the steel cylinder and to engage the contact with the polycarbonate disc.

3.3.1 Stable behavior

For a friction coefficient $\mu = 0.1$, as shown in Fig. 3.7 (where the lowest critical friction coefficient is 0.14), all the double modes are stable. When the system is stable, any perturbation from the static equilibrium position generates a damped vibrational response of the system. In fact, the amplitude of the initial vibration, which is excited by the radial expansion of the inner cylinder, decreases in time and the system comes back to its equilibrium position in uniform sliding.

(a) Velocity time response of the internal node I in circumferential and radial direction.

(b) Normal and tangential stresses measured on the contact node C.

(c) Exchanged and dissipated powers.
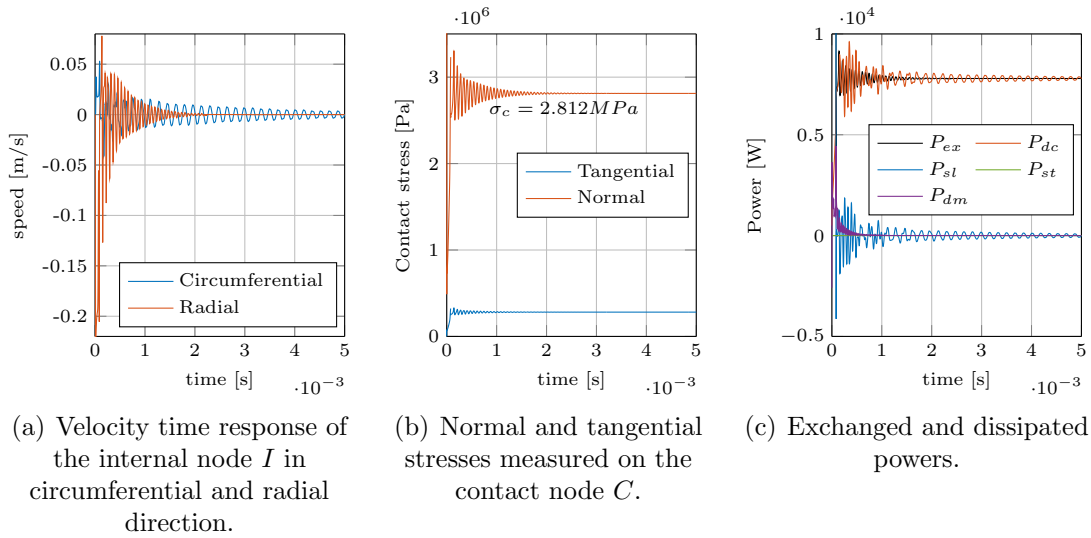
Figure 3.10: Response of the system in case of a friction coefficient $\mu = 0.1$ and a rotational speed $\Omega = 100$ RPM

Fig. 3.10(a) shows the time response, in the radial and circumferential direction, of the velocity of an internal node I, which is located at a radial distance of 13.66 mm from the contact surface Σ_c (cf. Fig. 3.1). Fig. 3.10(b) shows the normal and tangential stresses for a contact point during the transient response. Due to the axial-symmetry of the system this behavior is representative of the whole contact surface. Fig. 3.10(c) shows, for a stable case, the time evolution of the energy terms introduced in Section 2.3.

The initial vibration induced by the radial expansion is damped both by the frictional contact and by the material damping and the vibration amplitude decreases with exponential law towards the static equilibrium position, i.e. nil velocity (cf. Fig. 3.10(a)). The ratio between the normal and tangential contact stresses is equal to the imposed friction coefficient (cf. Fig. 3.10(b)). This implies that, in this numerical system, if there are no friction-induced vibrations (or if their amplitude is negligible), the calculation of global quantities, i.e. normal and tangential global forces, allows for a reliable estimation of the local friction coefficient.

Furthermore, the power terms (cf. Fig. 3.10(c)) show that during the vibration generated by the initial expansion Δr the external power P_{ex} is dissipated by both

the material damping P_{dm} and the contact P_{dc}. On the contrary, when the system reaches its stationary state ($t > 2\,\mathrm{ms}$), which in this case is again the static equilibrium position, the material damping dissipative terms P_{dm} is nil; as well, the two terms P_{sl} and P_{st} of the exchanged power at the contact P_c are nil, and all the external power P_{ex} is directly dissipated at the contact P_{dc}. Therefore, in case of stable systems with small amplitude of the friction-induced vibrations it is possible to estimate the power dissipated at the contact interface. Nevertheless, it should be kept in mind that, even when the system is stable, induced vibrations can be excited by surface roughness and a small quota part of the energy can be dissipated within the bulk.

3.3.2 Unstable behavior, energy balance and steady state limit cycle

For a friction coefficient $\mu = 0.3$ the equilibrium position in sliding condition becomes unstable because the coupled modes 2-3, 4-5 and 6-7 have positive real part (cf. Fig. 3.7).

Instability with local stick-slip-detachment. When the inner disc has an imposed rotational speed $\Omega = 800\mathrm{RPM}$ the analysis of the velocity response of the internal point I highlights four different stages identified in Fig. 3.11(a) by the letters from A to D. Furthermore, the comparison of the response with the status of contact nodes over the time in Fig. 3.11(b) shows the effect of the contact status variation on the transient behavior of the system.

(a) Velocity time response of the internal node I in circumferential and radial direction.

(b) Contact status evolution on the whole contact surface.
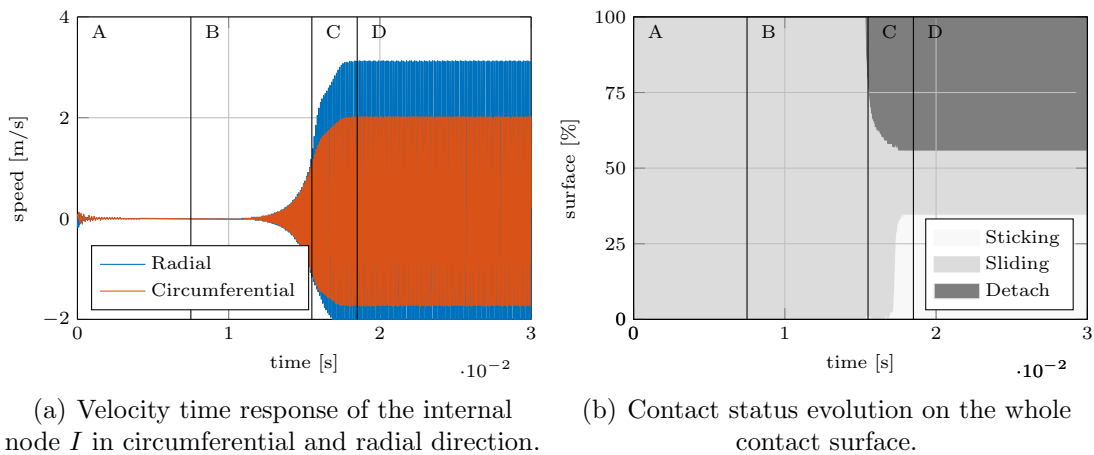
Figure 3.11: Unstable transient response for a friction coefficient $\mu = 0.3$ and a rotational speed $\Omega = 800\mathrm{RPM}$.

Figure Fig. 3.12(a) shows the Fast Fourier Transforms for different time intervals corresponding to the different stages of the simulation.

49

(a) Harmonic content of the transient response for different stages.

(b) Velocity field for stage B $t = 12$ms.

(c) Velocity field for stage D $t = 25$ms.
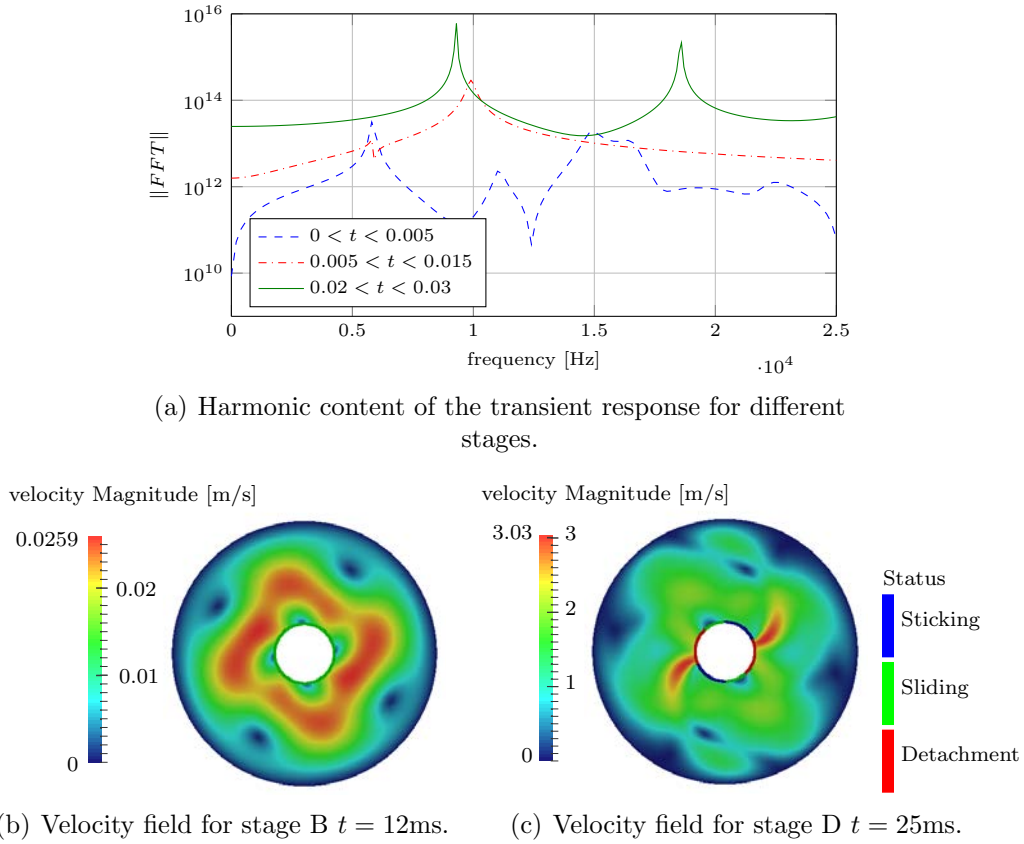
Figure 3.12: Harmonic content and velocity field at different times.

The first stage of the transient response (stage A in Fig. 3.11(a)) is characterized by a small amplitude of vibration excited by the rapid expansion of the rigid surface, which gives an impulsive radial and rotational excitation to the disc. The disc response, mainly at a frequency of 5.8 kHz (cf.Fig. 3.12(a)), corresponds to the first (circumferential) vibration mode of the system (see Table 3.2). The other contributions correspond to the other radial and circumferential in-plane modes (cf. Section 3.2). All the contact nodes are in sliding status and the vibration amplitude decreases according with the sign of the real part of the first eigenvalue.

Starting from time $t \simeq 0.01$ s (stage B in Fig. 3.11(a)) the main harmonic content is at an higher frequency of about 9.9 kHz that corresponds to the mode 5 (cf. Table 3.2), which is predicted to be unstable by the CEA (cf. Fig. 3.7). The vibration amplitude grows exponentially, which is typical of unstable systems. The exponential growth is consistent with the value of the real part of the eigenvalue calculated by the CEA with the linear model. The pattern of the velocity field shown in Fig. 3.12(b) is consistent with the deformed shape of the unstable mode 5 (cf. Fig. 3.6). At this stage all nodes are still in sliding and the contact nonlinearities, due to sticking and detachment, do not affect the system behavior.

The vibration amplitude increases progressively and, when the local tangential

50

speed of the contact nodes reaches the peripheral speed of the rotating surface, some of the nodes switch in sticking status (cf. Fig. 3.11(b)). Afterwards (stage C in Fig. 3.11(a)), increasing the vibration amplitude, the number of nodes in sticking and detachment condition increases and the system vibration reaches a limit cycle (stage D in Fig. 3.11(a)). The nonlinearities due to the contact become relevant during this transition and produce a slight decrease of the vibration frequency of the unstable mode, as shown by comparing the harmonic content in Fig. 3.12(a). In fact the appearance of zones of detachment, with respect to the linear behavior, introduces a less stiff constraint at the contact, causing the decrease of the vibration frequency. The velocity field of the disc vibration during the limit cycle (cf. Fig. 3.12(c)) is not exactly the same of the modal shape of the mode 5, because the presence of sliding and detachment conditions is not accounted for in the linearized model used for the CEA. Super-harmonics, which are due to the contact nonlinearities, appear at frequencies that are integer multiples of the original one.

(a) Displacement vs. Speed of the internal node I in x direction

(b) Trace of the contact node C.
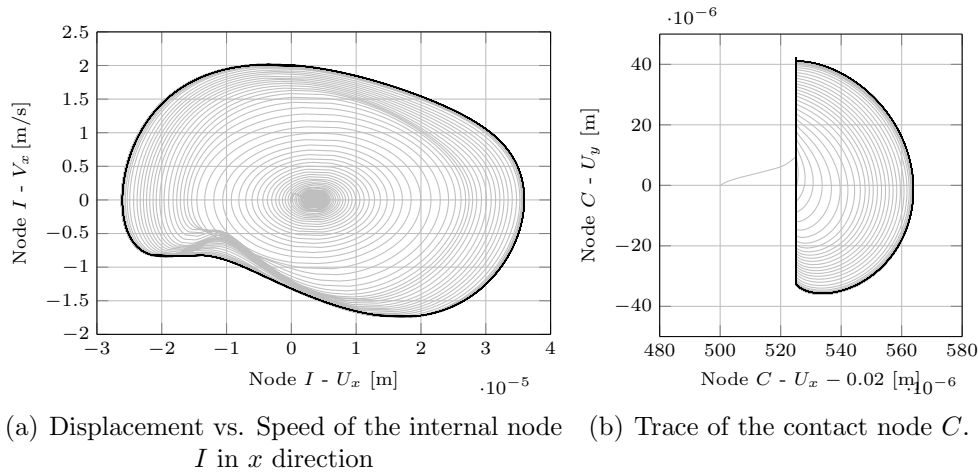
Figure 3.13: Limit cycles.

Figure 3.13(a) shows the phase plot (displacement, velocity) of the internal node I along the circumferential direction (cf. Fig. 3.1). The stage B of the transient simulation is characterized by an increasing spiral, while the stage D is characterized by the stationary limit cycle. Figure 3.13(b) presents the trace of the plane displacement of the contact node C (cf. Fig. 3.1), where the upper quasi-vertical line corresponds to the initial expansion of the inner rigid surface, the "horizontal" line corresponds to the stick-slip phases and the arcs on the bottom are due to the detachment of the node from the rotating surface. The amplitude increases until the system reaches the limit cycle.

Figure 3.14 shows the energy quantities presented in Section 2.3 and calculated during the simulation time. The different energy flows that constitute the external power P_{ex} are shown and can be correlated with the velocity response (cf. Fig. 3.11(a)) and to the status of contact nodes (cf. Fig. 3.11(b)).
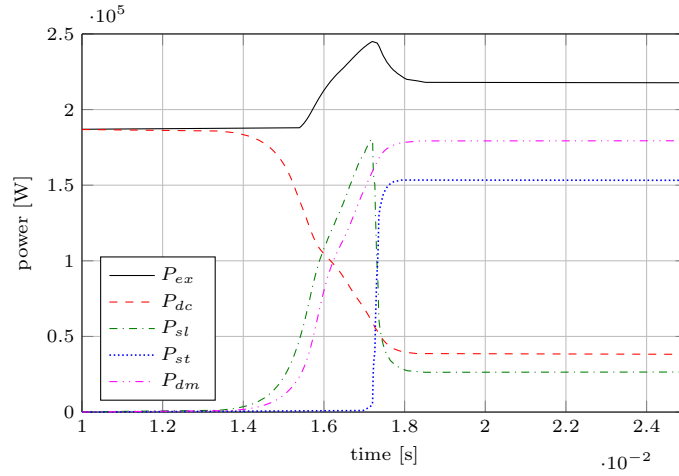
Figure 3.14: Energies involved in friction-induced vibrations and friction coefficient.

The external power P_{ex} starts from a value that corresponds to the product of the peripheral speed of the rigid surface by the tangential contact stress due to the radial expansion, in stable conditions. This represents a theoretical value of the power dissipated at the contact without friction-induced vibrations (cf. Section 3.3.1). Therefore, at the beginning of the simulation, when the system is near to its static equilibrium position, in overall sliding (negligible vibration amplitude), the external power P_{ex} is entirely dissipated at the contact P_{dc}, like in the stable case. In this condition, the energy reintroduced in the disc by friction-induced vibrations and the energy dissipated by material damping are negligible. When the unstable behavior appears (exponential growth of vibrations for $t > 13$ms) there is a progressive increase of the energy that is introduced into the system by friction-induced-vibrations by the oscillation of the portions of the contact surface that are in sliding P_{sl}. This produces a reduction of the energy dissipated at the contact P_{dc}. The sum of these terms (P_{ex}) is constant until $t = 15$ms when the first detachments appears (cf. Fig. 3.11(b)). While at the beginning of the unstable vibrations the energy is introduced only by sliding, when the sticking appears a drop of the sliding power curve can be noticed with a sharp increase of the sticking term contribution P_{st}. In the steady-state the energy is introduced both by sliding and by sticking zones.

Furthermore, when the unstable vibrations occur, the increase of vibration amplitude is associated with the increase of the energy content of the elastic media. In fact, during the transition between the equilibrium position and the steady-state limit cycle the power introduced by friction-induced vibrations in sliding conditions P_{sl} is always higher than the energy dissipated by material damping P_{dm}. This difference increases the mechanical energy content of the elastic media up the limit-cycle where the power introduced at the contact by friction-induced vibrations $P_c = P_{sl} + P_{st}$ equals the power dissipated by the material damping P_dm and the

system reaches a new energy equilibrium (steady state with limit cycle of vibrations).

The external power P_{ex} absorbed during the unstable vibration results in 16% higher power than the power absorbed during stable vibrations. This means that the mechanical system, in this case, is able to dissipate an higher amount of energy.

Moreover, it can be noticed that the energy dissipated by the friction forces P_{dc} during the unstable behavior is less than the energy dissipated during the stable behavior. During the limit cycle, the power dissipated at the contact (by frictional forces) is 18% of the external power. The remaining part is divided into the Sticking power (72%) and Sliding power (10%), which are powers re-introduced by the contact into the polycarbonate disc as friction-induced-vibrations and successively dissipated by material damping (82% of the total external power). From a tribological point of view, in contradiction with what could be expected, the system instability reduces the amount of energy that is dissipated at the contact by the frictional forces.

Instability with local stick-slip. For a lower angular speed of the inner surface, $\Omega = 100$RPM, the self-excited vibrations increase their amplitude up to a steady state limit cycle (cf. Fig. 3.15(a)) where the local contact zones switch between only sliding and sticking status (cf. the occurrence of sticking in Fig. 3.15(d)).

As in the previous case, with an higher rotational speed, the harmonic content of the transient response is shown in Fig. 3.16(a) at different stages of the response. Also in this case, a stage ($15 < t < 20$ms) where the amplitude of vibration increases with exponential trend can be found. In this stage the main contribution is at a frequency of about 9.9kHz, which corresponds to the mode 5 of the CEA (cf.Figures 3.7, 3.16(b) and 3.6). In this case, after the linear part of the transient response ($20 < t < 30$ms), two unstable modes coexist in the response (cf. Fig. 3.16(a)), which shows evident beats (cf. 3.15(a)).

During the steady-state limit cycle, due to the reduced rotational speed of the rigid surface, only sticking nonlinearities (no detachment) appear at the contact (cf. Fig. 3.15(d)). Furthermore, even if more than one unstable frequency was recovered in the saturation phase, the steady-state limit cycle ($t > 30$ms) is characterized by only one of the unstable frequencies of the mechanical system (cf. Fig. 3.12(a)). In this case the main frequency recovered in the steady-state is 10.5kHz and corresponds to the unstable mode 7 calculated by the CEA (cf. Fig. 3.7).

The velocity distribution in Fig. 3.16(c) is similar to the modal shape of mode 7 (cf. Fig. 3.6), confirming that at this rotational speed the system vibrates at another frequency due to the excitation by the contact nonlinearities of a different unstable system mode.

In the first phase of the simulation, when the system is in uniform sliding condition (cf. Fig. 3.15(a)), the ratio between the tangential and normal contact stresses (cf. Fig. 3.15(b)), integrated over the whole contact interface, is equal to the imposed local friction coefficient $\mu = 0.3$ (cf. Fig. 3.15(e)) and it confirms the assumptions done in the stable case. On the contrary, in the steady state, for each node of the contact surface there is a continuous switch between sliding and sticking phases (cf.

53

(a) Velocity time response of the internal node I in circumferential and radial direction.

(b) Normal and tangential stresses measured on a contact node.

(c) Exchanged and dissipated powers.

(d) Contact status evolution on the whole contact surface.

(e) Averaged local friction coefficient.

(f) Tangential forces and tangential velocity of a contact node. Gray parts represent the time intervals where the nodal power $\widetilde{P}_c < 0$.
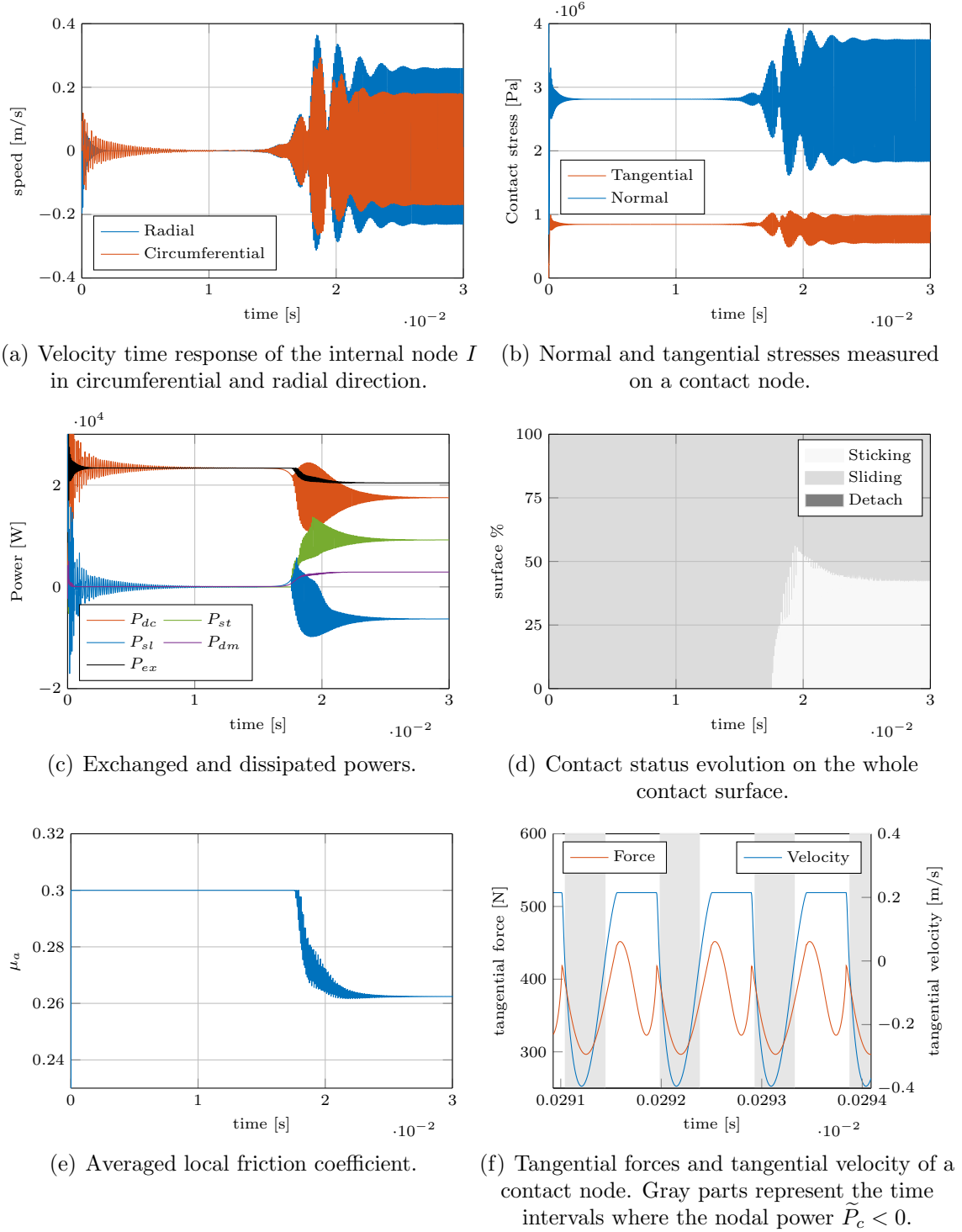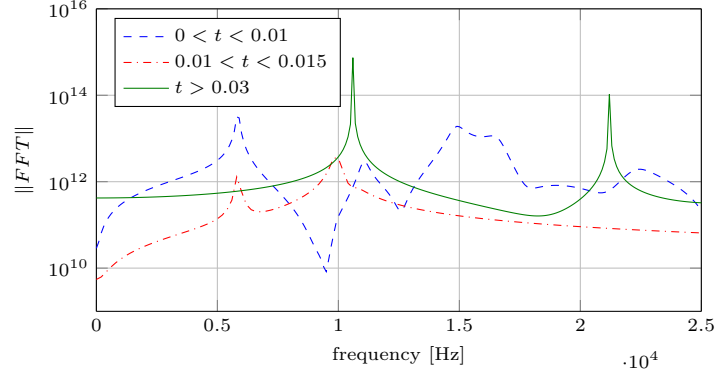
Figure 3.15: Response of the system in case of a friction coefficient $\mu = 0.3$ and a rotational speed $\Omega = 100$ RPM

(a) Harmonic content of the transient response for different stages.

(b) Velocity field in the linear phase $t = 16$ms.

(c) Velocity field in the steady-state $t = 30$ms.
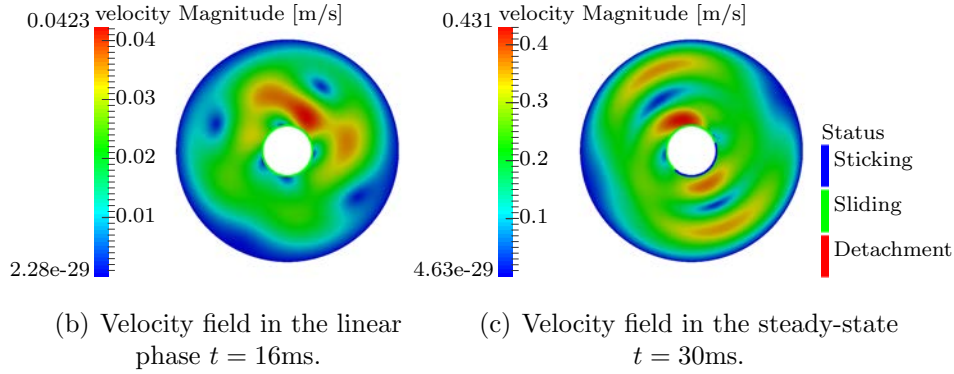
Figure 3.16: Harmonic content and velocity filed at different times for a rotational speed $\Omega = 100$RPM

the horizontal part of the tangential velocity in Fig. 3.15(f)), where the oscillation of the tangential pressure is bounded by the Coulomb law (see (2.19)). Hence, the friction coefficient decreases down to 0.262 (as showed in Fig. 3.15(e)). This means that the friction-induced vibrations modify the global frictional behavior of the mechanical system. In this case the global friction coefficient is less than the local one, and a measure of the global quantities, i.e. the global normal and tangential forces can lead to an erroneous estimation of the local friction.

Fig. 3.15(f) shows the two quantities that contribute to define the power exchanged by a single contact node $\widetilde{P}_c$: the nodal tangential force and the tangential velocity, which is bounded by the sticking condition ($r\Omega = 0.21\,\mathrm{m/s}$). During the sliding phase the change of sign of the tangential velocity produces a negative power flow (gray parts in Fig. 3.15(f)). Hence, in general, the sliding exchanged power P_{sl} can be negative (outgoing power) or positive (incoming power), while the sticking exchanged power P_{st} is always positive. The total exchanged power P_c between the rigid surface Σ_c and the elastic body Γ is composed by the sliding and by the sticking contribution. In this case, the negative contribution of the sliding exchanged power

55

P_{sl} reduces the total amount of power introduced into the polycarbonate disc by friction-induced vibrations P_c and dissipated by the material damping (cf. P_{dm} in 3.15(c)).

As a consequence, on the contrary of what was observed above, the rise of unstable vibrations produces a reduction of the power globally absorbed by the mechanical system P_{ex}, which passes form 23.3kW to 20.4kW with a percentage decrease of 12.5%. This is due to the fact that the induced vibrations, in this case, decrease the energy dissipated at the contact more than the increase of the energy dissipated by material damping. Moreover, the power that is actually dissipated at the contact P_{dc} passes from the totality of the energy introduced into the mechanical system without vibrations, to the 86.3% of the energy introduced into the mechanical system P_{ex} with vibrations. Only the remaining 13.7% is, in this case, dissipated in the bulk by material damping P_{dm}.

These results highlight how the friction-induced vibrations can modify the overall capacity of the system to absorb and dissipate energy, and that an estimation of the power dissipated at the contact without considering the dynamic behavior of the system can lead to significant errors in the quantification of contact energy dissipation and, consequently of the associated tribological phenomena.

3.4   Effect of damping on transient solution convergence

As showed in Section 2.1 and in Section 3.2 the damping parameters have a fundamental role in the system stability. Furthermore, the energy actually dissipated by the bulk P_{dm} is strictly related to these parameters (α_R and β_R); hence, even small variations can heavily change the response of the system. In fact, as introduced in Section 2.3, the steady-state behavior is driven by a dynamic energy equilibrium of the system; the introduced power at the contact interface P_c is equal to the power dissipated into the bulk by friction-induced vibrations P_{dm} and the change of the material dissipated power term leads to an equilibrium condition that can be extremely different, both in amplitude and shape.

A preliminary convergence analysis over space and time discretization, performed on the finite element model of the polycarbonate disc, showed the main role played by the damping coefficients to obtain the convergence of results in the transient numerical analysis.

Shear stress fields reported in Fig. 3.17 show that completely different transient behaviors can be obtained for different values of the material damping coefficients.

For low values of Rayleigh coefficients (cf. Fig. 3.17(a)), the system presents an unstable vibrational behavior, but no convergence in solution can be reached by increasing the number of elements or by reducing the time step for the calculation of the transient solution. In this case, the calculated response of the system is not harmonic and the in-plane vibration results to be different from any modal shape

(a) Hypo-damped system
$(\alpha_R = 10\,1/\mathrm{s};\ \beta_R = 1E - 9\,\mathrm{s})$

(b) Normo-damped system
$(\alpha_R = 40\,1/\mathrm{s};\ \beta_R = 4.5E - 7\,\mathrm{s})$

(c) Hyper-damped system
$(\alpha_R = 100\,1/\mathrm{s};\ \beta_R = 1.2E - 6\,\mathrm{s})$
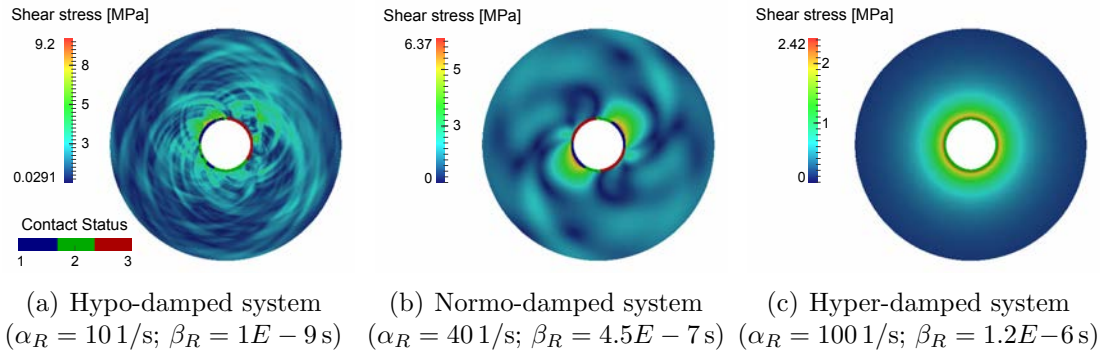
Figure 3.17: Different behavior (shear stress [MPa]) during the steady state of the system depending to the material damping coefficients.

found in the CEA (cf. Fig. 3.17(a) and Fig. 3.6).
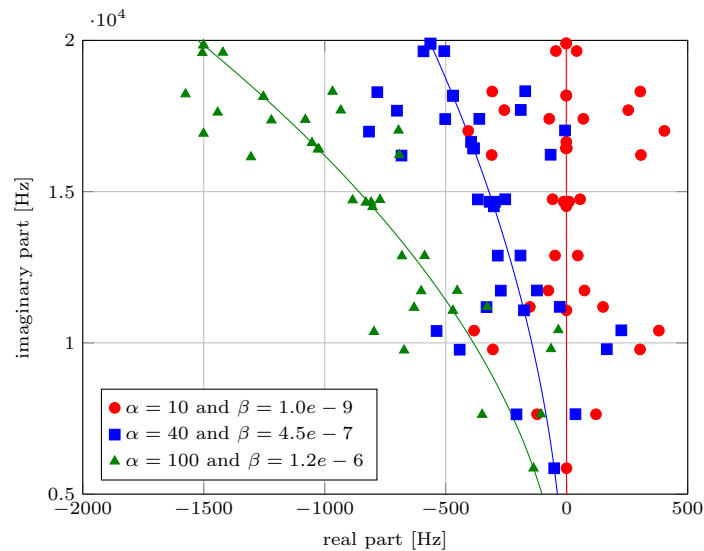
Figure 3.18: Complex eigenvalue on the complex plane for an hyper, hypo and normal-damped system.

Figure 3.18 shows the complex eigenvalues on the complex plane for the different sets of values of the damping coefficients α and β. Figure 3.19 shows the time response of an internal point of a system with a very small value of the damping coefficients.

With the coefficients adopted in Fig. 3.17(a), almost all the double modes in Table 3.2 are unstable (cf. Fig. 3.18) and the complexity of the response is due to the combination of several unstable modes of the system with the rise of high order sub-harmonics.

On the contrary, for high values of the damping coefficients α_R and β_R no convergence problems arise, and the system is always stable (cf. Fig. 3.18). In this case,

(a) Acceleration of the internal point I.
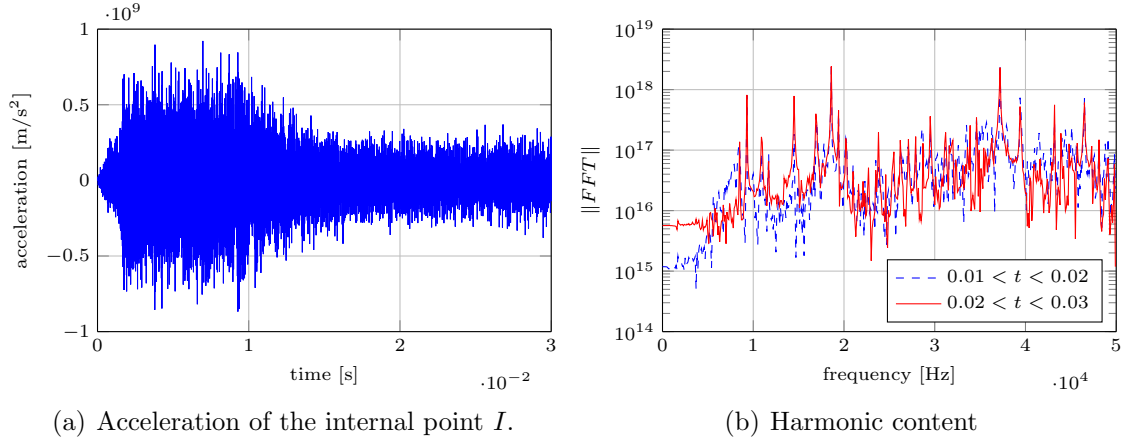
(b) Harmonic content

Figure 3.19: Time response and harmonic content of the steady state response for a hypo-damped system ($\alpha = 10[1/s]$ and $\beta = 1e - 9[s]$).

the system reaches a static equilibrium position with all the nodes over the contact interface in a uniform sliding status (cf. Fig. 3.17(c)).

When introducing realistic values of material damping coefficients (cf. Fig. 3.17(b)), obtained experimentally, the system vibrates at a frequency that is close to one of the unstable modes predicted by the CEA and the velocity field is similar to the modal shape of the unstable mode (as in the numerical analyses presented in Section 3.3.2).

Focusing on the energy flows, in the case of very low damping values, the energy introduced into the system by frictional forces cannot be dissipated correctly by the internal non conservative damping forces, so that the internal energy increases; the waves generated at the contact are continuously reflected at the boundaries (cf. Fig. 3.17(a)). This non-equilibrium can be considered at the origin of the non convergence of the solution. Increasing the damping coefficient values, the energy equilibrium can be reached and, for very high values of the damping coefficients, the system becomes artificially stable because the energy is rapidly dissipated by the damping forces.

This means that the material damping introduced into the system drastically affects the numerical solution that otherwise does not give reliable results or at worst does not converge. Because of its key role, the material damping of the polycarbonate disc has been estimated experimentally. An experimental modal analysis has been performed on the disc to estimate the modal damping factors by the half power method (see Section 4.1.3).

3.5 Effects of relative speed and local friction coefficient on local contact behavior and energy balance.

The results presented in Sections 3.3.2 and 3.4 highlight that, when nonlinearities arise in a mechanical system, its behavior is not easily predictable. In this section a full parametric analysis is presented to observe the effect on the transient response of the friction coefficient μ (in the range $0.2 \div 0.4$) and the rotational speed Ω (in the range $10 \div 8000$ RPM).

The variation of the friction coefficient μ affects the number of the unstable modes (cf. Fig. 3.7) of the system. The value of the real part of the eigenvalues affects the rate at which the vibration amplitude grows. Furthermore, the friction coefficient μ sets the limiting value of the friction force, while the rotational speed Ω sets the limiting value of the tangential velocity. Hence, these two parameters heavily affect the global transient response and the power flows at the interface.

3.5.1 Effects of relative speed and friction coefficient on contact status and system response

Figures 3.20 and 3.21 show the effects of these two parameters on the outputs that characterize the steady-state (limit cycle) of the unstable friction-induced vibrations.

(a) $\mu = 0.2$. (b) $\mu = 0.3$. (c) $\mu = 0.4$.
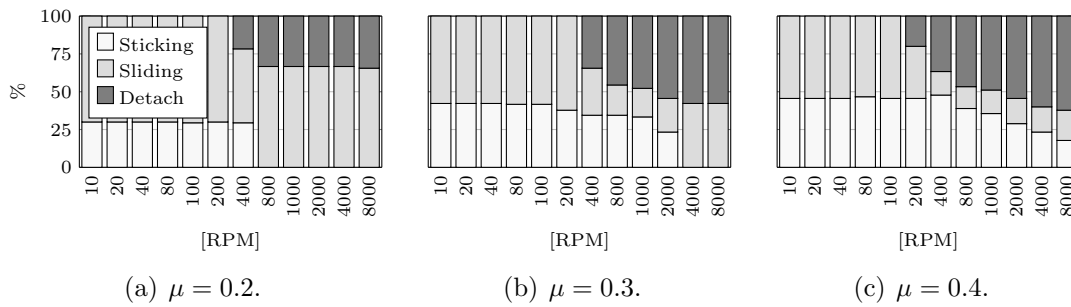
Figure 3.20: Effect of the rotational speed Ω (RPM) and of the friction coefficient μ on the contact status repartition for the whole contact surface Σ_c during the steady state.

Figure 3.20 shows the status of the contact interface during the limit cycle expressed as percentage of nodes in the different statuses. The results presented here highlight that, increasing the rotational speed Ω the contact nonlinearities that bound the amplitude of vibration change with a regular scheme. For low values of the rotational speed there is a continuous switch between local sticking and sliding; with increasing velocity, local detachments appear and the status of each contact node changes periodically among the three possible statuses. Finally, for extremely

high values of the rotational speed Ω, the sticking disappears and the contact status alternates between sliding and detachment. This behavior occurs for all the friction coefficients included in this parametric analysis[1].

Furthermore, it is worth noting that the higher is the friction coefficient, the lower is the speed at which the detachment appears; on the contrary, the higher the friction coefficient, the higher the speed at which the sticking disappears. In fact, when increasing the friction coefficient, the amplitude of vibration increases and the detachment can appear for lower values of the rotational speed. Moreover, the higher the amplitude of vibration, the higher is the percentage of nodes that are in sticking for low rotational speed and the higher the rotational speed for which the sticking status disappears.

Finally, for low values of the speed ($\Omega \leq 200\,\mathrm{RPM}$ in Fig. 3.20(a) and $\Omega \leq 100\,\mathrm{RPM}$ in Figures 3.20(b),(c)) and for high values of the speed ($\Omega \geq 800\,\mathrm{RPM}$ in Fig. 3.20(a) and $\Omega \geq 4000\,\mathrm{RPM}$ in Fig. 3.20(b)) there is no significant effect of speed on contact status repartition. Thus, a transition zone can be detected by the analysis of the percentages of the node statuses.

(a) Main frequency of vibrations measured during the limit clycle.

(b) Tangential amplitude of vibration of the contact node C during the limit cycle.

(c) Averaged local friction coefficient during the limit clycle.
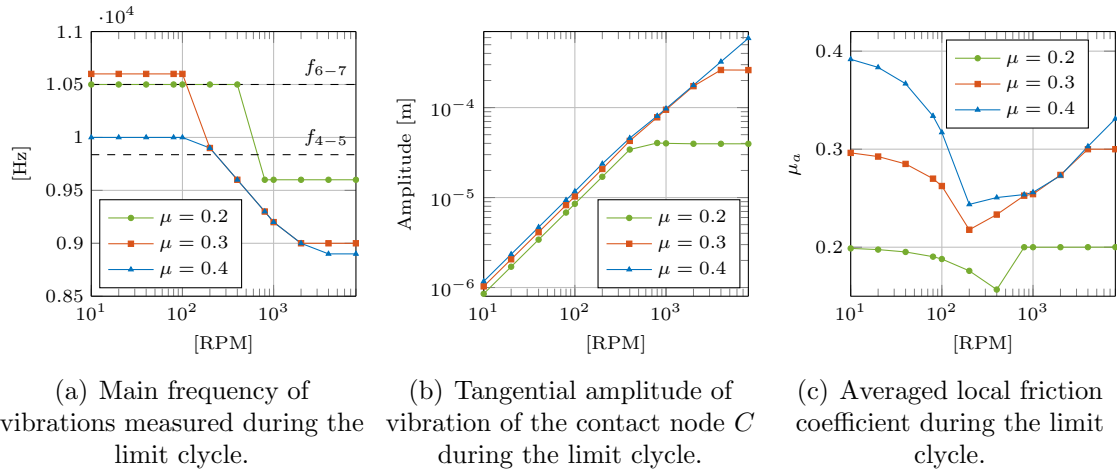
Figure 3.21: Global response of the system during the steady state for different value of friction coefficient and rotational speed of the inner rigid surface.

The same transition range of the rotational speed, which increases with the friction coefficient, can be observed by the macroscopic response of the system. Figure 3.21(a) highlights that the main frequencies measured during the steady state change as a function of the two parameters μ and Ω. The frequency of friction induced vibrations varies for two main reason: the first one is the variation of the unstable mode during the steady state of the response; the second one is the variation of the contact boundary conditions due to the contact nonlinearities. In fact

---

[1]For the highest value of the coefficient of friction (cf. Fig. 3.20(c)) the showed range of rotational speed ($\Omega = 10 \div 8000\,\mathrm{RPM}$) is not sufficient to describe the whole evolution of these variations.

contact nonlinearities change the global stiffness of the system and introduce boundary conditions that are softer, in case of detachment, and stiffer, in case of sticking, than the boundary conditions referred to the uniform sliding state. In this system a transition from the unstable mode 6-7 to the unstable mode 4-5 (cf. Table 3.2) can be noticed for a friction coefficient $\mu = 0.2$ at a rotational speed within the range $400 \div 800 \, \text{RPM}$ and for a friction coefficient $\mu = 0.3$ at a rotational speed within the range $100 \div 200 \, \text{RPM}$. For a friction coefficient $\mu = 0.4$ there is no variation of the excited mode, which is the mode 4-5 for every value of the rotational speed, within the range of this analysis. When the unstable mode is the same, the frequency measured during the steady state in condition of sticking-sliding ($\Omega \leq 100 \, \text{RPM}$ cf. Figures 3.21(a) and 3.20(c)) is higher than the frequency calculated in condition of uniform sliding. Moreover, the frequency shift (for $\mu = 0.2$ and 0.3) between the two unstable modes during the steady state is associated with a variation of the angular periodicity of both velocity distribution and contact status (cf. Table 3.2), which is not present for $\mu = 0.4$. The same transition zones observed in the contact status distribution (cf. Fig. 3.20) are reflected in the frequency shift of the main harmonics of vibration (cf. Fig. 3.21(a)).

For low values of Ω, the higher the percentage of sticking nodes (cf. Figures 3.20(a),(b)), the higher the main frequency recovered in the steady state is (cf. Fig. 3.21(a)). Conversely, for high values of the rotational speed, the higher the percentage of detachment nodes the lower is the frequency of the limit cycle. Moreover, when variation of the rotational speed does not produce a variation of the contact status distribution, there is no variation of the frequency recovered during the limit cycle.

Fig. 3.21(b) shows the effects in terms of amplitude of vibration on a contact node along the tangential direction. A general linear trend can be highlighted until the contact status is stabilized in a sliding detachment condition (cf. Fig. 3.20) and the amplitude of the limit cycle becomes independent from the variation of the rotational speed[2].

The saturation of the limit cycle amplitude with the relative speed at the contact, explained here by a stabilization of the contact status distribution, has been already observed experimentally [GIA 06a].

The averaged local friction coefficient μ_a (see Fig. 3.21(c)) can be defined as the ratio between tangential and normal stresses integrated over the whole contact interface. This quantity highlights the effects of the friction induced vibrations and of the local dynamic behavior at the contact on the macroscopic frictional behavior. It can be noted that when there are zones in stick conditions the averaged local friction coefficient μ_g is always less than the imposed local value μ, and this confirms what was stated in [ADA 98]. On the contrary, when the contact status is in sliding-detachment, the average local friction coefficient μ_a assumes exactly the same value

---

[2]For a friction coefficient $\mu = 0.4$, the system is still in sticking-sliding-detachment (cf. Fig. 3.20(c)) at the highest considered value of rotational speed ($\Omega = 8000\text{RPM}$) and the amplitude of the steady-state limit cycle is still dependent on the rotational speed (cf. Fig. 3.21(b)).

μ imposed locally at the contact (cf. $\Omega \geq 800\,\mathrm{RPM}$ for $\mu = 0.2$ in Fig. 3.20(a) and $\Omega \geq 4000\,\mathrm{RPM}$ for $\mu = 0.3$ in Fig. 3.20(b)).

3.5.2 Effects of relative speed and friction coefficient on the energy flows

(a) $\mu = 0.2$ (b) $\mu = 0.3$ (c) $\mu = 0.4$
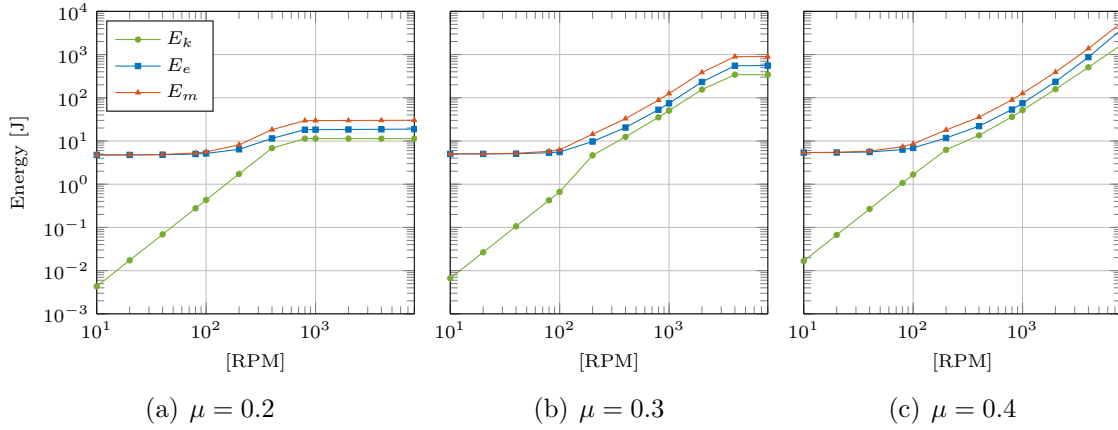
Figure 3.22: Mechanical energy repartition between the elastic and kinetic energy during the steady state limit cycle, for the different rotational speeds of the rigid surface.

Fig. 3.22 shows the effects of the parameters μ and Ω on the mechanical energy E_m and on its two components: the elastic potential energy E_e and the kinetic energy E_k of the system, introduced in (2.34). For low values of the rotational speed Ω the mechanical energy is composed mainly by the elastic potential energy due to the static equilibrium position. Increasing the rotational speed Ω there is an initial linear increase of the kinetic energy E_k up to a constant value corresponding to the configuration of maximal amplitude of the limit cycle reached by the system (cf. Fig. 3.21(b)). It is worth noting that the potential elastic energy E_e remains always higher than the kinetic energy E_k. Moreover, when the kinetic term reaches a value of comparable magnitude with the elastic potential term, the ratio between the two quantities remains almost constant for further increases of the rotational speed. The constant ratio depends on the ratio between the stiffness $[K]$ and mass matrix $[M]$ and on the ratio between the position and velocity distribution, which is constant and equal to the angular frequency of the unstable excited mode.

Fig. 3.23 shows the effects of the parameters μ and Ω on the power P_c exchanged at the contact, between the rigid surface Σ_c and the elastic body Γ, decomposed into the power exchanged by sliding P_{sl} and by sticking P_{st}. Positive values correspond to an incoming power into the system while negative values corresponds to an outgoing power flow. The absolute value $(-1 \cdot P_{sl})$ is considered in Fig. 3.23 to represent the outgoing power flows in the same logarithmic graph.

(a) $\mu = 0.2$ (b) $\mu = 0.3$ (c) $\mu = 0.4$
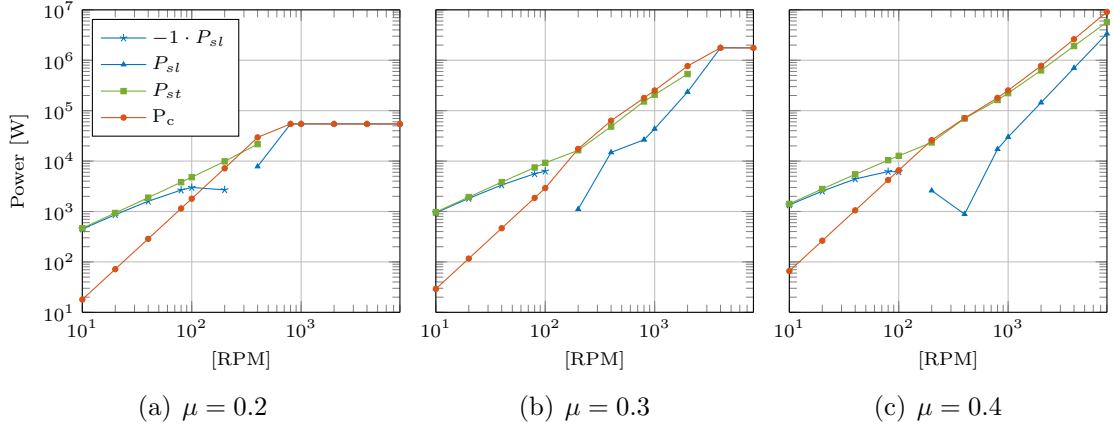
Figure 3.23: Contact exchanged power (P_c) during the steady state decomposed into power exchanged by sliding (P_{sl} incoming, $-1 \cdot P_{sl}$ outgoing) and power exchanged by sticking (P_{st}) versus Ω [RPM].

As highlighted previously (cf. Fig. 3.15(f)), the power P_{sl} exchanged by the sliding portions of the contact interface Σ_{sl} can be either positive or negative based on the combination of the sign of the local tangential velocities with the local tangential stresses. In these analyses, for low values of the rotational speed ($\Omega \leq 200\,\mathrm{RPM}$ for $\mu = 0.2$ in Fig. 3.23(a), and $\Omega \leq 100\,\mathrm{RPM}$ for $\mu = 0.3$ or $\mu = 0.4$ in Figures 3.23(b)(c)) the power exchanged by sliding is negative.

Furthermore, the absolute value of the sliding term is almost equal to the sticking term and, increasing the rotational speed Ω, these two quantities increase in amplitude. It is worth noting that, even if the system vibrates with a nonuniform distribution of the contact pressure and contact status [BRU 15b], from an energy point of view the equality between the incoming energy during the sticking and the outgoing energy during the sliding is comparable to the behavior recovered during the macroscopic stick slip behavior [CHA 08], where the material damping dissipation is negligible and almost the whole dissipation is due to the contact.

The power P_{st} exchanged by sticking is characterized by an almost linear increasing trend, until the sticking is present in the transient response (cf. Fig. 3.20). Figures 3.23(a)(b) highlight that the variation of the excited mode during the steady state (cf. Fig. 3.21(a)) corresponds to an increase of the power P_c exchanged at the contact. This behavior suggests that the amplitude and the shape of the limit cycle during the steady state are such as to ensure the maximum exchanged power P_c among the different configurations associated to the different unstable modes of the system. Moreover, the saturation of the vibration amplitude and stabilization of the contact status corresponds to a saturation in the energy flows that the unstable mode can absorb at the contact and dissipate by material damping.

Fig. 3.24 shows the evolution of the power globally absorbed by the system P_{ex} and its decomposition into the two dissipative terms P_{dc} and P_{dm} introduced

(a) $\mu = 0.2$ (b) $\mu = 0.3$ (c) $\mu = 0.4$
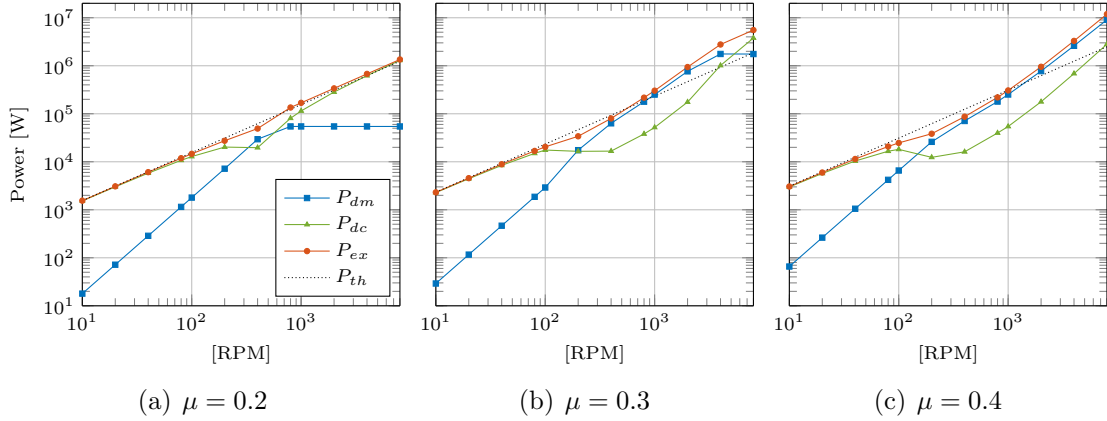
Figure 3.24: Decomposition of the total absorbed power into the two dissipative terms versus Ω (RPM).

in Section 2.3. The total power here is compared with the theoretical power P_{th} referred to the static equilibrium position in uniform sliding condition:

$$P_{th} = \widetilde{\sigma}_c \mu \, (2\pi r) \, r\Omega \tag{3.2}$$

(a) $\mu = 0.2$ (b) $\mu = 0.3$ (c) $\mu = 0.4$
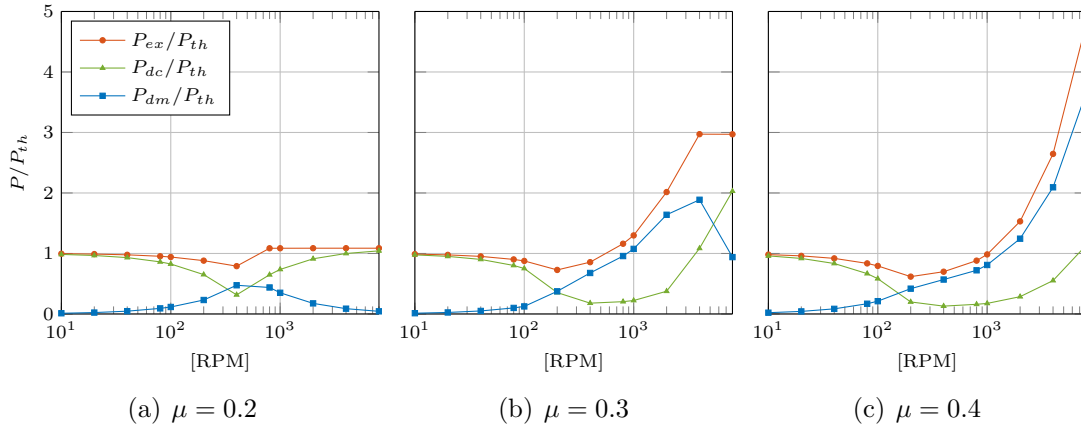
Figure 3.25: Total absorbed power and decomposition into the two dissipative terms normalized with respect to the theoretical power versus Ω (RPM).

Fig. 3.25 shows the same quantities reported in Fig. 3.24; in this case the powers are normalized with respect to the corresponding theoretical power P_{th}. The results showed in Figures 3.24 and 3.25 highlight that for low values of rotational speed Ω the absorbed power P_{ex} is almost entirely dissipated by the contact (P_{dc}) and, increasing the rotational speed Ω, the total absorbed power P_{ex} becomes lower than the theoretical one (P_{th}). This decrease of the external normalized power (P_{ex}/P_{th}) is related to a decrease of the normalized contact dissipated power (P_{dc}/P_{th}). On

the contrary, a further increase of the rotational speed Ω brings to a total power P_{ex} that is larger than the theoretical one P_{th} ($\Omega \geq 800\,\mathrm{RPM}$ for $\mu = 0.2$ or $\mu = 0.3$ and $\Omega \geq 2000\,\mathrm{RPM}$); it increases up to a constant ratio with the theoretical exchanged power ($P_{ex}/P_{th} = 1.09$ for $\mu = 0.2$ and $\Omega \geq 800\,\mathrm{RPM}$; $P_{ex}/P_{th} = 2.97$ for $\mu = 0.3$ and $\Omega \geq 4000\,\mathrm{RPM}$),when the saturation level is reached. The normalized contact dissipated power P_{dc}/P_{th} initially decreases with the rotational speed and then increases again, up to dissipate almost all the energy absorbed by the system (cf. Fig. 3.25(a)). On the contrary, the normalized power dissipated by material damping P_{dm}/P_{th} in Fig. 3.25(a),(b) highlights that a significant portion of the total energy is dissipated by material damping for the medium range of the velocity, in the transition range highlighted above[3]. In the steady state limit cycle, for the considered system, the damping dissipated power P_{dm} is higher than the contact dissipated power P_{dc} (cf. Fig. 3.25) when the contact status is characterized by alternating stick-slip-detachment conditions (cf Fig. 3.20), within the transition range of the rotational speed. All these results highlight the need to account for energy flows by friction induced vibrations to have a correct estimation of the energy really dissipated at the contact and the following tribological issues. During the transition zone the system seems to modify its vibrational response in order to be able to dissipate the larger amount of energy, up to a saturation value.

3.6 Concluding remarks

In this chapter the behavior of a simple model has been numerically analyzed to investigate the energy flows involved in in-plane contact dynamic instabilities. The model accounts for a single deformable body in frictional contact with a rigid surface. The modes that are coupled by the frictional forces are in-plane modes belonging to the same component, namely the disc.

The numerical analyses showed a good agreement between results from the linear CEA and the transient nonlinear analysis, allowing for a generalization of the mode lock-in theory, which is usually investigated in the literature for brake squeal. A convergence analysis highlighted the main role of the material damping; obtaining reliable values by an experimental estimation is necessary to avoid unrealistic numerical results.

The simplicity of the model allows as well to a detailed investigation of the energy flows involved in friction-induced vibrations in order to distinguish between the energy introduced by the contact into the system and the energy dissipated by the friction. The energy analysis allowed to quantify the part of the energy directly dissipated by the frictional forces at the contact, and the energy that is first introduced into the system as friction-induced vibrations and subsequently dissipated by the material damping into the bulk.

---

[3]For the highest value of the coefficient of friction (cf. Fig. 3.25(c)) the showed range of rotational speed ($\Omega = 10 \div 8000\,\mathrm{RPM}$) is not sufficient to describe the whole evolution of these variations.

Results of a parametric analysis show the effects of the friction coefficient and of the relative velocity on the transient response and on the energy flows involved in friction induced vibrations. The results of the parametric analysis highlighted the importance of the effects of the nonlinearities on the steady state response (limit cycle) and the link with the energy flows between contact surface and bulk.

Typical behaviors are highlighted for the mechanical energy and its two components (the elastic potential energy and the kinetic energy), such as for the contact exchanged power and the dissipative terms of the energy balance. The power globally absorbed and dissipated from the system can be higher or lower than the theoretical absorbed power in uniform sliding.

The energy balance of the system showed that during the limit cycle of the steady state vibrations a relevant part of the energy is dissipated by material damping. The energy dissipation at the contact during the contact dynamic instability is generally different from the dissipation during a stable sliding behavior. Without considering the system dynamic response, an erroneous estimation of the contact dissipation energy could lead to inconsistent tribological evaluations too.

In order to validate the 2D in-plane numerical model and the simulation results, an experimental campaign on the PhotoTrib set-up for squeal reproduction, together with a 3D dynamic analysis of the system, is presented in the next chapter.

Chapter 4

Experimental validation

Contents

This chapter shows a 3D numerical analysis and an experimental campaign on the PhotoTrib set-up to validate the results presented in Chapter 3. In fact the 2D model reproducing the disc in Chapter 3, even if it allows for a faster simulation of the transient response of the system, introduces a relevant reduction of the complexity of the system. The set-up, in fact, is a complex system with a complex dynamic behavior that involves not only the disc, but the whole assembly. Hence, even if the squeal phenomena for this system involve mainly the in-plane modes of the polycarbonate disc, the 3D geometry of the whole setup introduces a relevant axial component of displacement. Moreover, the elasticity of the frame and the joints significantly affects the system dynamics.

In this chapter a 3D finite element model is introduced in order to link the dynamics of the simplified 2D system with the dynamics of the real system. This step is needed to compare the experimental measurement performed on the PhotoTrib with the numerical results presented in Chapter 3.

Then, a preliminary experimental reproduction of the unstable induced vibrations on the PhotoTrib set-up is performed in order to validate the results from the 2D simulations and to investigate the transient response of the real system.

4.1 Setup Dynamics

This section presents a 3D finite element model of the PhotoTrib set-up, which has been developed by ANSYS in order to find the eigenmodes of the assembled system. This step is needed in order to identify the modes that involve mainly the in-plane dynamics of the disc, and to correlate the contact instabilities obtained experimentally with the ones obtained numerically by the 2D explicit transient analysis. This analysis, together with the 2D modal analysis performed in Chapter 3, allows to link the dynamics of the real (3D) system with the dynamics of the simplified (2D) system and for an estimation of the difference in frequency introduced by the simplification (3D/2D). This numerical comparison has been supported by experimental dynamic measurements of the whole setup, which allow the identification of the main natural frequencies of the disc. Moreover an experimental determination of the polycarbonate damping characteristics is here reported in order to find reliable values to be used for the numerical simulations.

4.1.1 3D modal analysis

The 3D finite element model (cf. Fig. 4.1) reproduces the whole steel frame, the polycarbonate disc, the fixing ring and the rotating axis of the experimental setup "Phototrib", introduced in Section 2.4. The finite element model counts overall 77,324 solid elements and 189,026 nodes with 3 DoFs for each node.

The supporting frame is modeled as a single component, even though the real system is composed of several components assembled by screws; hence, the contact interactions at the joints, which are far away from the disc-cylinder contact, are
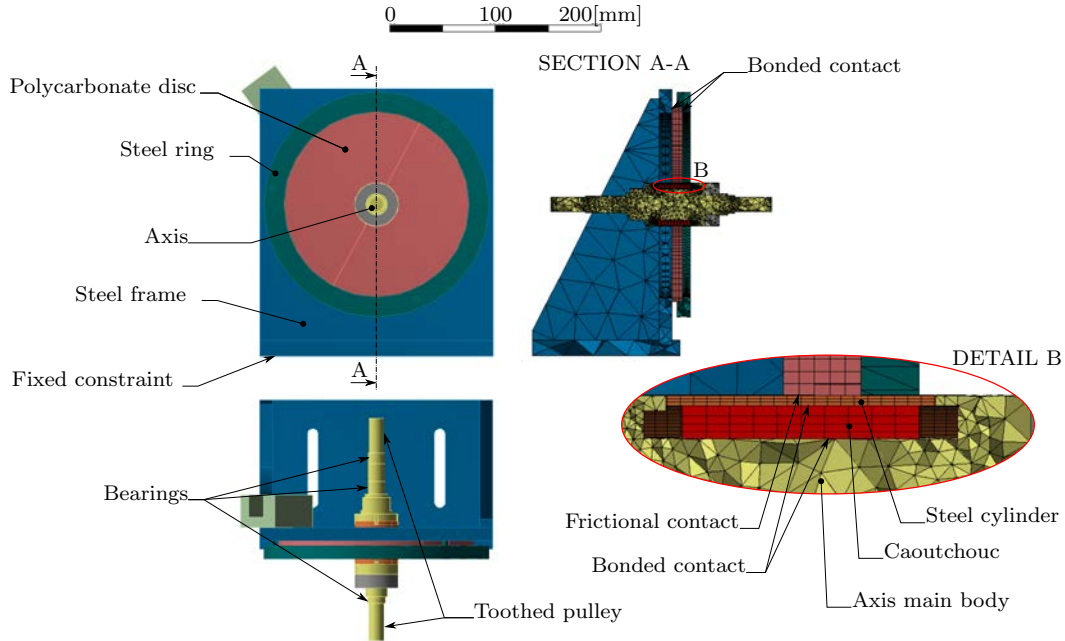
Figure 4.1: 3D finite element model, boundary conditions and contacts.

neglected in this model. The model of the axis includes the main body of the axis, the external steel cylinder and the internal rubber element, which produces the radial expansion. Bonded type contacts have been defined at the rubber element interface with the axis and the external cylinder (cf. detail view in Fig. 4.1).

The disc is fixed on the steel frame with the steel ring and a bonded type contact. A frictional contact, with a friction coefficient $\mu = 0.4$, is defined between the polycarbonate disc and the steel cylinder. All the contacts included in this model are defined with a penalty formulation. Table 4.1 summarizes the model properties and the material properties used for the 3D model.

Steel Young's modulus	E_s	$200\,\text{GPa}$
Steel density	ρ_s	$7850\,\text{kg/m}^3$
Steel Poisson's ratio	ν_s	0.3
Polycarbonate Young's modulus	E_p	$2.2\,\text{GPa}$
Polycarbonate density	ρ_p	$1200\,\text{kg/m}^3$
Polycarbonate Poisson's ratio	ν_p	0.37
Caoutchouc Young's modulus	E_c	$0.01\,\text{GPa}$
Caoutchouc density	ρ_c	$920\,\text{kg/m}^3$
Caoutchouc Poisson's ratio	ν_c	0.49
Caoutchouc coefficient of thermal expansion	α_L	$1 \cdot 66^{-6}\,^\circ\text{C}^{-1}$
Number of solid elements		77324
Number of nodes		189026
Number of nodes in frictional contact		935

Table 4.1: Material properties and characteristics of the 3D finite element model.

A fixed constraint acts on the lower face of the base of the steel frame. The axis is radially and axially supported by the surfaces corresponding to the three bearings. A rotation is imposed on the two cylindrical surfaces where the toothed pulleys are mounted.

A preliminary static analysis is made to establish the desired contact condition (sticking or sliding) at the disc cylinder interface. The static analysis is composed of two steps: 1. the radial expansion ($\Delta r = 0.25 \mu m$), which is obtained by imposing a dummy temperature variation ($\Delta T = 250°C$) to the rubber element, which produces a thermal expansion; 2. the axis rotation. The first step ensures a uniform sticking contact between the disc and the axis, while the rotation ensures the transition to the sliding condition. Therefore, the modal analysis can be performed at the end of each step, i.e. in both the equilibrium conditions (sticking or sliding).
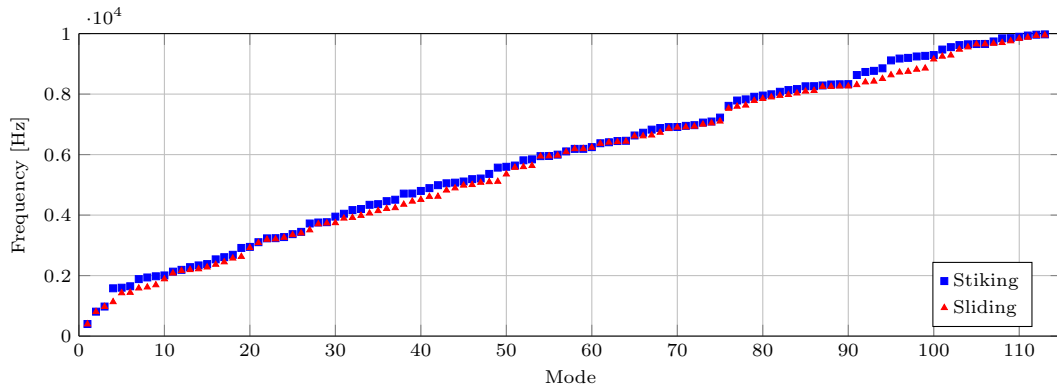
Figure 4.2: Global modal analysis results (eigenfrequencies) in sticking and sliding contact at the disc/cylinder interface.

Figure 4.2 shows the system eigenfrequencies in the range 0-10 kHz for both sliding and sticking contact status. The results in the plot highlight the high modal density of the system, due to the geometrical complexity of the system itself, and a general slight decrease of the eigenfrequencies due to the transition from the sticking condition to the sliding condition at the contact interface.

Among all the modes of the system, some of these are characterized by a prevalent displacement of the disc (disc modes, cf. modes 32 and 46 in Fig. 4.3), while the others are characterized by a displacement of the whole system (global modes, cf. modes 20 in Fig. 4.3). The frictional forces, which are at the origin of friction-induced vibrations, act at the disc-cylinder interface; hence the disc modes, which present large deformation at the interface, are mainly involved in the system response to the frictional excitation.

Figure 4.4 shows the displacement magnitude of the disc modes in the range 5-8 kHz, in order to characterize the response of the polycarbonate disc in the frequency range of interest. The disc, in fact, is the system element mainly involved in the friction-induced vibrations and the consequent acoustic emission. A fundamental distinction can be made between the disc modes that are characterized by a prevalent

70

Mode 20 (2918.5 Hz)   Mode 35 (4140.2 Hz)   Mode 32 (3916.1 Hz)   Mode 46 (5002.1 Hz)
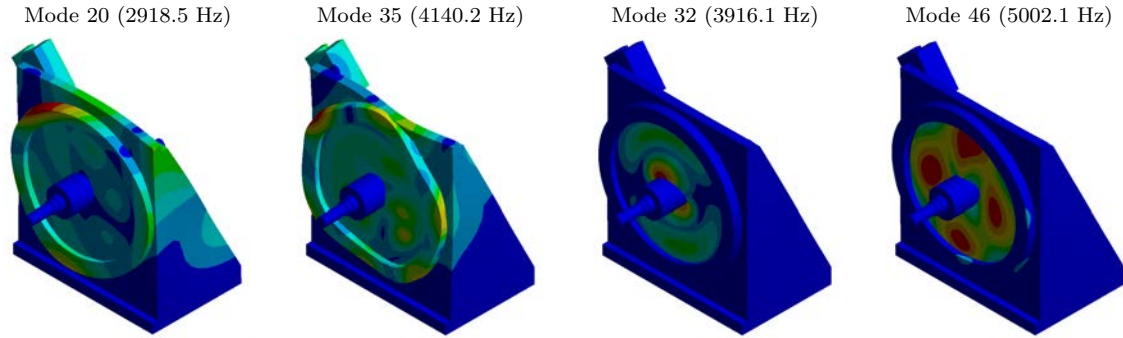
Figure 4.3: Displacement magnitude in color scale from blue (low) to red (high) of tow global system modes (25 and 35) and of two disc modes (32 and 46).

in-plane displacement (modes in the upper row of Fig. 4.4) and the disc modes that are characterized by a prevalent out-of-plane displacement (modes in the lower row of Fig. 4.4).

4.1.2 3D-2D modes comparison

The eigenmodes of the system computed with the 2D and 3D models differ in frequency, due to the different boundary conditions and to the plane strain constraint, which is only an approximation of the real strain distribution. Hence, in this section, a comparison is made between the in-plane eigenmodes obtained by the two models. Figure 4.5 shows the comparison between the modes 5 and 7 of the 2D model, which are the modes recovered in the numerical simulations (cf. Section 3.3.2), and the ones obtained by the 3D model, characterized by the same modal shape.

The comparison of the radial and the circumferential displacement of the 2D modes 5 and 7, shows a good correspondence with those of the 3D modes 46 and 74. The comparison highlights that the frequencies of the in-plane modes in the 3D model are considerably lower than the frequencies in the 2D model. In particular the mode 5 (at 9837 Hz) and the mode 7 (at 10500 Hz) of the 2D model correspond respectively to the mode 46 (at 5002 Hz) and to the mode 74 (at 7039 Hz) of the 3D model.

It is worth noting that the radial and the circumferential components of the modal shapes in proximity of the contact interface (cf. Fig. 4.5) present a phase shift corresponding to a quarter of the vibration period. This phase shift is at the origin of the power exchange at the contact.

Moreover the axial component of the displacement at the contact, for the two modes shown in Fig. 4.5, is characterized by a phased motion (or out-of-phase) with respect to the radial component. The axial component of vibration, which in this case is due to the proximity to other out-of-plane modes (cf. modes 47 and 69 in Fig. 4.4), introduces a dissipation into the system due to both the material damping and the contact. In the axial direction, in fact, the sign inversion of the tangential velocity produces a sign inversion of the tangential force too, which is always in the

71

Mode 46 (5002 Hz) Mode 64 (6435 Hz) Mode 74 (7039 Hz) Mode 82 (7978 Hz) Mode 85 (8091 Hz)

Mode 47 (5097 Hz) Mode 51 (5594 Hz) Mode 65 (6611 Hz) Mode 69 (6862 Hz) Mode 77 (7628 Hz)
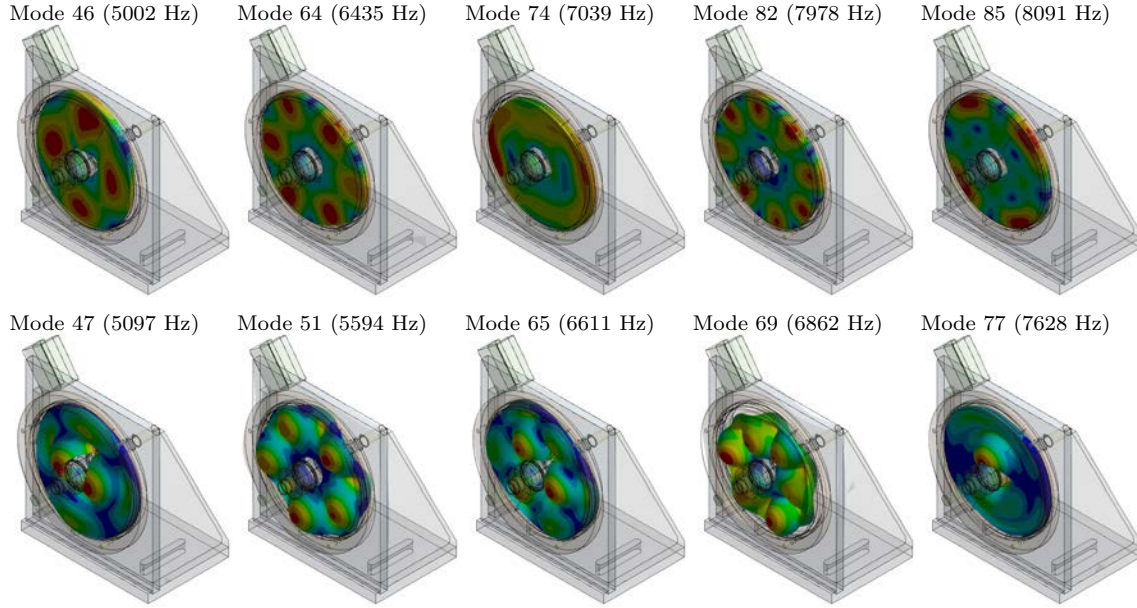
Figure 4.4: Displacement magnitude in color scale from blue (low) to red (high) of the in plane modes of the disc (first line) and of the out of plane mode of the disc (second line) in the range of frequency 5-8 kHz.

opposite direction with respect to the velocity. Hence, the axial contact interaction always produces a negative energy flow with respect to the system mechanical energy that does not depend on the phase shift between the normal and the tangential component of the vibration. The power dissipated at the contact by the out of plane vibrations can be estimated as:

$$P_c^o = - \int_{\Sigma_c} 4\mu\sigma_c X_o \tag{4.1}$$

where σ_c is the static component of the contact pressure, X_o is the amplitude of the disc vibration at the contact interface along the axial direction and Σ_c is the contact surface. For the 3D vibration of the system, the energy balance introduced in Eq. (2.35) should be reformulated considering the power dissipated by material damping (P_{dm}) and the power exchanged at the contact (P_c) due to both the out-of-plane (o superscript) and to the in-plane (i superscript) vibration:

$$\frac{dE_m}{dt} = P_c^o + P_c^i - P_{dm}^o - P_{dm}^i \tag{4.2}$$

For the modes shown in Fig. 4.5, the energy is introduced into the system by the in plane contact vibration ($P_c^i > 0$). It produces the increase of the energy content of the system, inducing vibrations with both in-plane and out of plane components (due to the modal shape). On the contrary, the contact due to the out of plane vibrations, subtracts energy to the system ($P_c^o < 0$), which results in a further contact dissipative contribution.

72

2D radial   2D circumferential   3D radial   3D circumferential   3D axial

2D mode 5 (9837 Hz)   3D mode 46 (5002 Hz)

2D mode 7 (10500 Hz)   3D mode 74 (7039 Hz)
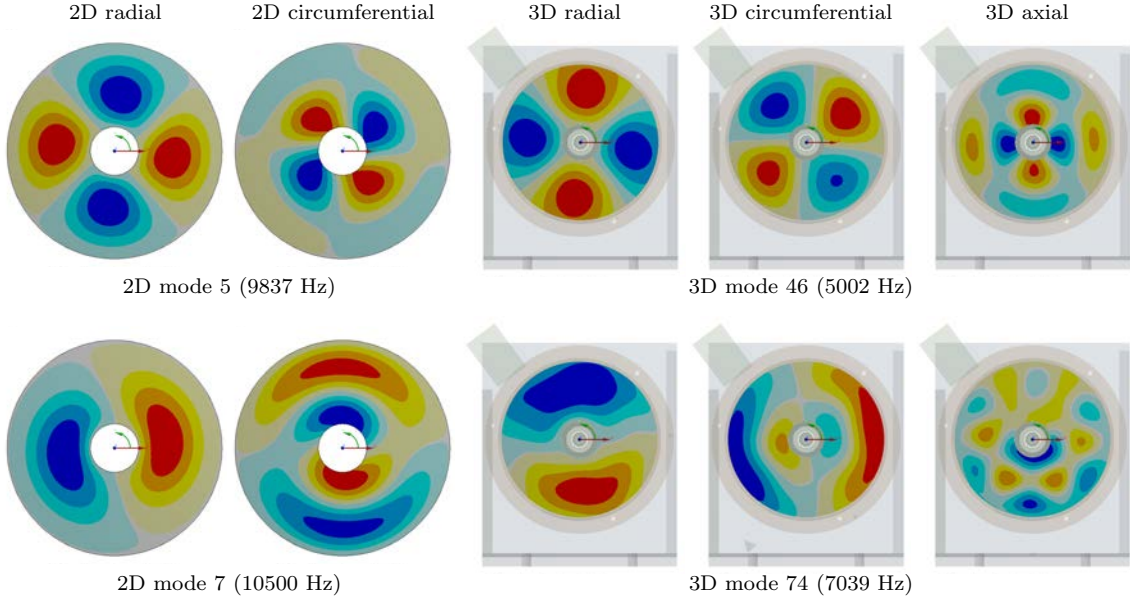
Figure 4.5: 3D and 2D mode comparison.

Finally, during the steady state ($dE_m/dt = 0$) 3D vibration, the external power introduced into the system P_{ex} is decomposed as shown in Eq. (2.39); the power exchanged at the contact ($P_c = P_{sl} + P_{St}$) is not entirely dissipated by material damping related to the in-plane vibrations, as shown in Eq. (2.40) for the 2D model, but also by the material damping and the contact effect along the axial direction. Hence the equation 2.41 becomes:

$$P_c^i = P_{dm}^o + P_{dm}^i + P_{dc}^o. \tag{4.3}$$

In order to verify the 3D modal analysis, Frequency Response Functions (FRF) have been obtained experimentally by exciting the system with an instrumented hammer, when the disc is in sticking contact with the steel cylinder, and measuring the response with accelerometers.

Figure 4.6 shows the magnitude of the driving point FRF measured at the polycarbonate disc along the out-of-plane direction. The marked peaks correspond to the frequencies of the out-of-plane modes of the disc.

Mode n.	Numerical f_n [Hz]	Experimental f_e [Hz] Hz	$|\Delta f\%|$	Nodes
9	1977	1963	0.71%	1 Diameter
15	2381	2397	0.67%	2 Diameters
23	3237	2984	7.82%	3 Diameters
32	4166	4165	0.02%	4 Diameters (with frame contribution)
37	4509	4583	1.64%	4 Diameters
46	5188	5214	0.50%	1 Diameter, 1 Circumference

Table 4.2: Numerical - Experimental frequency comparison of the out of plane modes of the disc and classification.
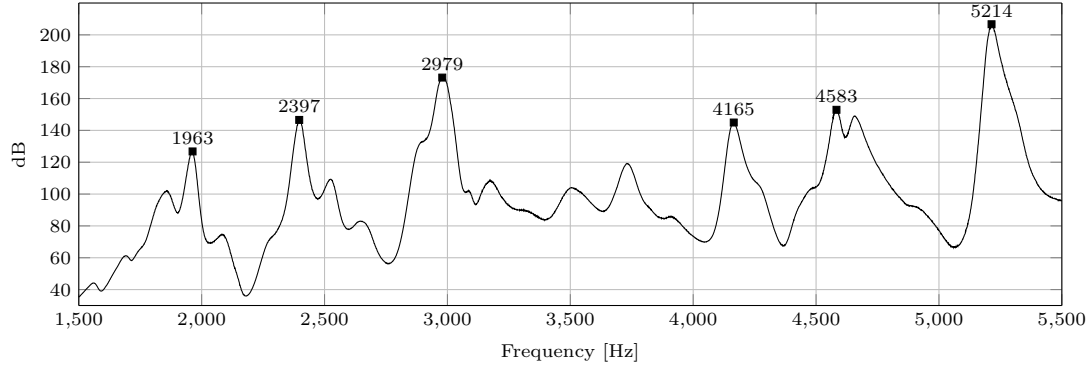
Figure 4.6: Drive point Frequency Response Function on the disc in the out of plane direction.

Table 4.2 compares the main peak frequencies recovered experimentally, with the eigenfrequencies of the out-of-plane modes resulting from the eigenvalue analysis performed on the 3D model (cf. Fig. 4.1), with the contact at the disc-cylinder interface in sticking condition. The numerical and experimental natural frequencies are in good agreement with a maximum relative error less than 2% in general and less than 8% for the mode 23. This experimental validation, with the established correspondence between the 2D and the 3D model results, allows for comparing the 2D numerical results in Chapter 3 with the experimental tests that are presented in the following of this chapter.

Due to the out-of-plane vibrations, the comparison will be performed only in terms of frequency, because the amplitude of vibration will be affected by the two further dissipative terms introduced by the out of plane vibrations.

4.1.3 Experimental Damping estimation

The power dissipated by material damping during friction-induced vibrations has a relevant effect on the system response. An experimental estimation of the Rayleigh coefficients has been performed for the polycarbonate disc, in order to find a couple of realistic values to be used in the numerical investigations of friction induced vibrations.

Figure 4.7(a) presents the Frequency Response Function (FRF) obtained by exciting the disc with an instrumented hammer in free-free conditions and measuring the response with an accelerometer. The half-power method has been used to calculate the modal damping factors for each mode in the frequency range 0–10000 Hz (black marks in Fig. 4.7(b)). By comparison between the experimental modal damping factors and the damping frequency behavior obtained with the proportional damping formulation (blue continuous line), the values of the Rayleigh coefficients are calculated. Figure 4.7(b) shows the contributions of the α_R Rayleigh coefficient (green dashed line) and the β_R coefficient (red dashed straight line) to the numerical material damping.

(a) Experimental FRF

(b) Modal Damping and damping coefficient identification
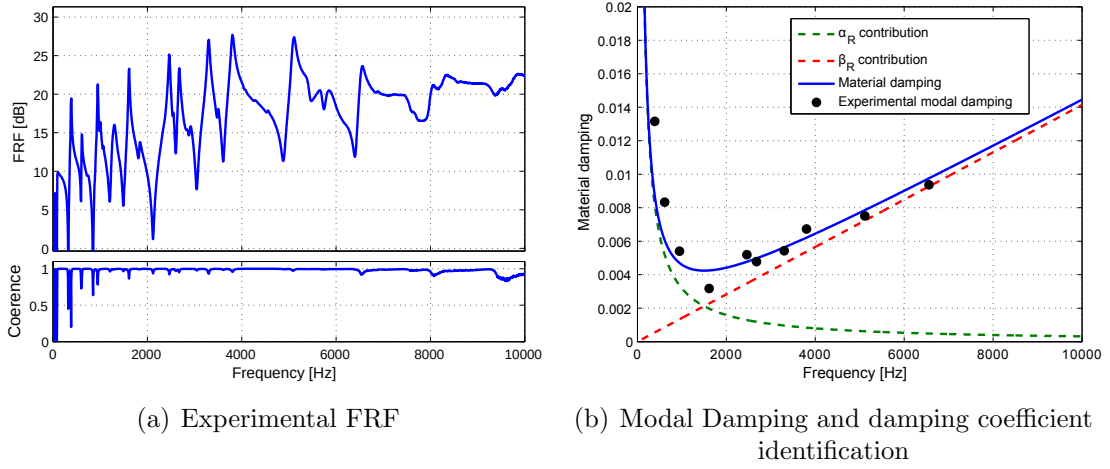
Figure 4.7: Experimental Rayleigh coefficient identification.

The Rayleigh coefficients obtained are $\alpha_R = 40\,1/\mathrm{s}$ and $\beta_R = 4.5E - 7\,\mathrm{s}$. With these values the convergence of the model is obtained and an unstable modal vibration of the system, corresponding to the experiments (see section 3.4) can be recovered by the numerical transient analysis.

4.2 Squeal reproduction

In this section experimental measurement of unstable vibrations are presented in order to validate the numerical transient results in Chapter 3 and to observe some effects of the real contact interaction on the system dynamic response.

4.2.1 Test conditions

The PhotoTrib set-up, used to reproduce the squeal vibrations, is presented in Section 2.4 and a detailed description of the system is provided in [REN 11a]. During the first phase of the test, the polycarbonate disc is put in contact with the steel cylinder by acting on the ring nut of the expansion mechanism of the axis (cf. Fig. 4.8). This produces a radial expansion ($\Delta r = 10 \div 30\,\mu\mathrm{m}$) of the cylinder in order to obtain a considerable contact pressure ($\sigma_c = 1.2 \div 3.7\,\mathrm{MPa}$, obtained from the numerical simulation). Afterward, a constant rotational speed ($\Omega = 4.5 \div 200\,\mathrm{RPM}$) is imposed on the axis, by the toothed belts, to bring the steel cylinder surface in relative motion with respect to the polycarbonate disc surface ($v_t = 10 \div 430\mathrm{mm/s}$).

During each test, the OROS acquisition system records with a sample frequency of 51.2 kHz the following signals:

- the engine torque, provided by the engine control system;

Figure 4.8: Acquisition sensor placement for squeal measurement.

- the engine rotational speed, provided by the engine control system;

- the dynamic response of the disc in radial, circumferential and axial direction, measured by a triaxial accelerometer on the disc surface (cf. Fig. 4.8);

- the radial dilatation of the steel cylinder, measured by an inductive proximity sensor (cf. Fig. 4.8).

The tests are developed in ambient temperature and humidity.

4.2.2 Squeal behavior

Several tests have been performed with different values of the radial expansion and different values of the rotational speed. During the rotation, the frictional contact can induce an unstable response of the system (exponential increase of vibrations), up the limit cycle of vibration (Fig. 4.9).

Figure 4.9 shows the transient response for an imposed rotational speed $\Omega = 80\,RPM$, which corresponds to a peripheral speed of the steel cylinder $v_t = 172\,\text{mm/s}$. The radial expansion imposed on the cylinder is $\Delta r = 10\,\mu\text{m}$. The Figure shows, from left to right, the plots of the torque signal, the peripheral velocity, and the acceleration of a point of the disc surface along the radial direction with its spectrogram. All the quantities are represented versus the time of simulation, in the vertical axis.

The plots show an initial elastic radial deformation of the system up to $t = 0.17\,\text{s}$, which corresponds to the linear increase of the couple signal and nil value of the velocity. Starting from $t = 0.17\,\text{s}$ the cylinder begins to slide and the peripheral speed reaches the imposed value $v_t = 172\text{mm/s}$. The system remains in this steady state sliding condition up to $t = 0.5\,\text{s}$ (acceleration signal shows a negligible vibration amplitude); after that the typical exponential increase of vibration amplitude appears and leads the system from the steady sliding equilibrium position to a steady state limit cycle. During the limit cycle the spectrogram of the radial acceleration shows a main harmonic peak of the response at a frequency $f = 7500\,\text{Hz}$. This frequency
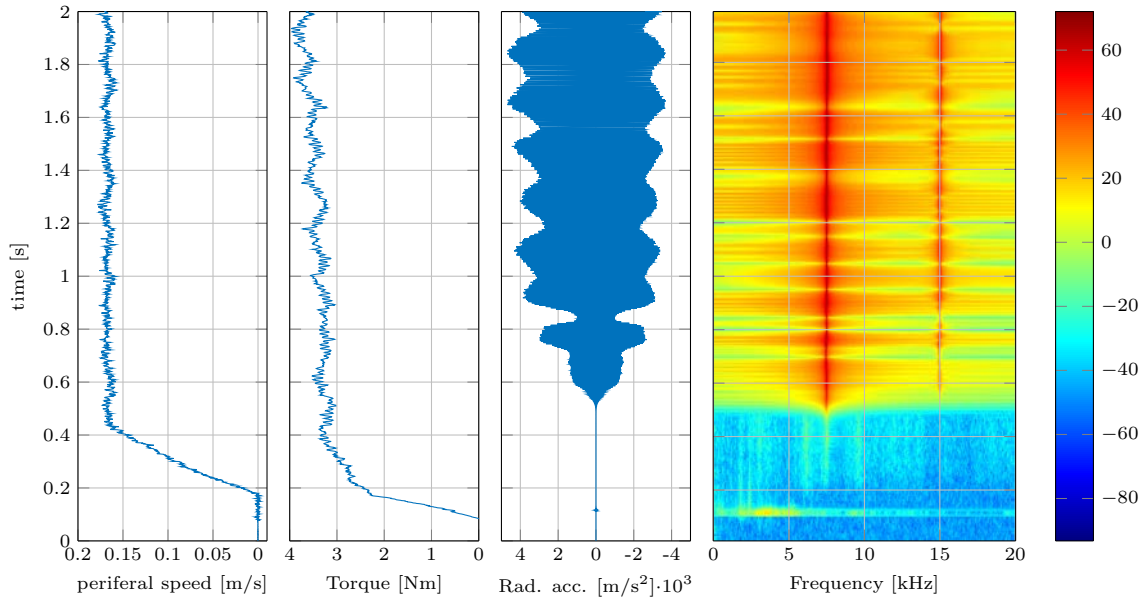
Figure 4.9: Transient response for a rotational speed $\Omega = 80\,\text{RPM}$ and a radial expansion $\Delta r = 10\,\mu\text{m}$.

corresponds to the mode 74 of the 3D model (cf. 4.5), i.e. the mode 7 of the 2D model. This mode is one of the two unstable modes recovered in the numerical simulations, in the Chapter 3.

Two different behaviors have been recovered during different tests: a continuous squeal and a discontinuous squeal. Several improvements have been adopted, in order to reduce the cylindrical error during the radial expansion and the concentricity error in the assembly phase. Despite that, unavoidable residual errors produce a variation of the contact condition (the contact pressure distribution) during the axis rotation. This is at the origin of the discontinuous squeal that arises with a periodicity that is strictly related to the rotation of the axis, hence to the geometrical errors. Figure 4.10 shows the response of the system for an imposed speed $\Omega = 24\,\text{RPM}$ and a radial expansion $\Delta r = 30\,\mu\text{m}$. The leftmost plot shows the radial displacement of the contact surface measured by the inductive proximity sensor; it shows a periodical oscillation having the same period of the axis rotation ($T = 2.52\,\text{s}$). The central plot shows the acceleration response in the radial direction and the rightmost plot shows the spectrogram of the acceleration response. The comparison of the radial position signal with the acceleration response, highlight that the intermittent squeal has the same periodicity. Furthermore, in this analysis, the main frequency recovered in the transient vibration is $f = 5450\,\text{Hz}$, which is the frequency of the mode 46 of the 3D model (cf. Fig. 4.5), i.e. the mode 5 of the 2D model.

It is worth noting that during the transient response the dissipated energy at the contact produces a heating of the contact resulting in a thermal dilatation of
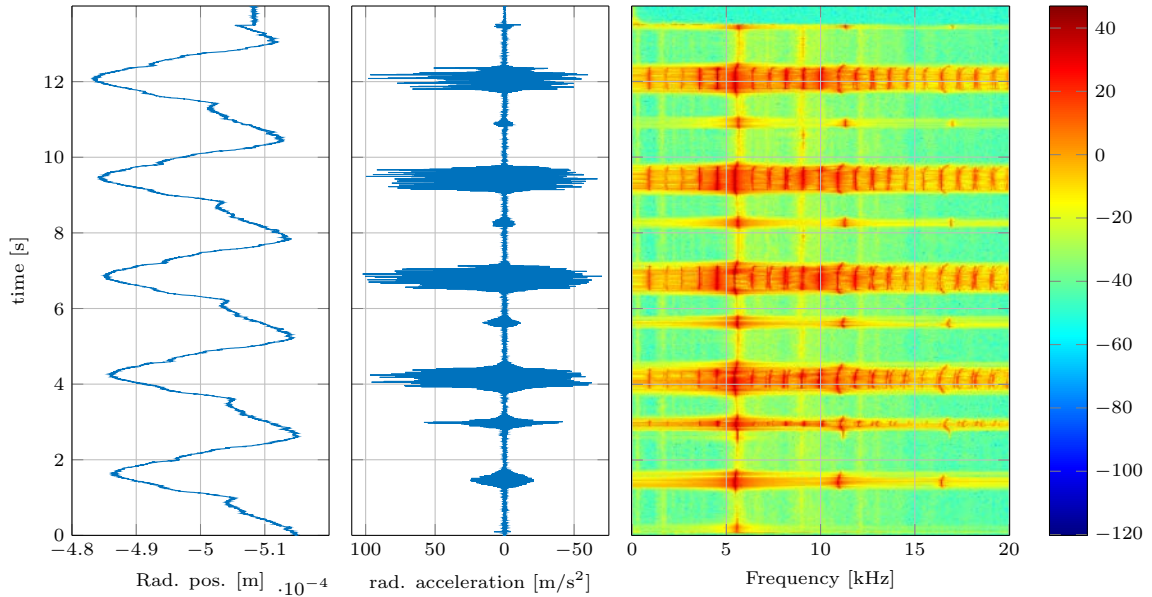
Figure 4.10: Transient response with intermittent squeal for a rotational speed $\Omega = 23.8\,\mathrm{RPM}$ and a radial expansion $\Delta r = 30\,\mu\mathrm{m}$. From left to right radial position, acceleration response in the radial direction and spectrogram of the acceleration response.

the steel cylinder. The radial dilatation generates the variation of the average value of the radial position (leftmost plot in Fig. 4.10), i.e. the average radius of the steel cylinder, that increases of about $2.5\,\mu\mathrm{m}$ over the simulation time.

Finally, whenever squeal occurs, during all the other tests performed on the set-up, the excitation of one of the two modes at about $7500\,\mathrm{Hz}$ and $5500\,\mathrm{Hz}$ is measured, which correspond to the modes 5 and 7 recovered also by the transient 2D simulations in Chapter 3. This confirms the attitude of the reduced model to reproduce the instabilities of the real system.

4.3 Other dynamic and tribological considerations

4.3.1 Effect of the relative speed on the squeal

Figure 4.11 shows the transient response of the system for three different values of the rotational speed $\Omega = [20; 40; 80]\,\mathrm{RPM}$, which correspond to the peripheral speeds $v_t = [43; 86; 172]$. The radial expansion is set at $\Delta r = 10\mu\mathrm{m}$ and the three tests have been performed consecutively, on the same specimen, with the purpose to maintain constant all the other system parameters.

Figure 4.11 shows the acceleration response measured in the radial direction and the engine torque evolution during the three tests. Results in the upper plot of

78
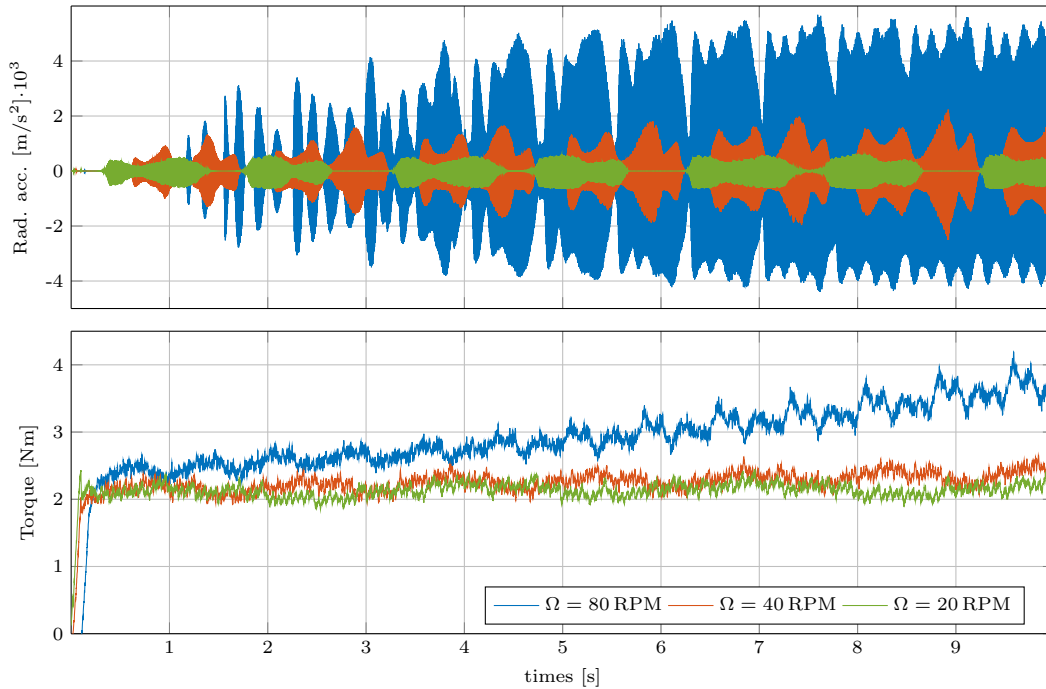
Figure 4.11: Transient response for different values of the rotational speed ($\Omega = [20; 40; 80]\,\mathrm{RPM}$). Acceleration response in the radial direction (top) and engine torque (bottom) versus time.

Fig. 4.11 highlight that the higher the rotational speed Ω is, the higher is the amplitude of friction induced vibrations; in particular for the three adopted velocity the amplitude of vibration reaches the maximum values of about $[600; 1800; 5500]\,\mathrm{m/s}^2$.

Results in the bottom plot shows that even if the torque has a similar value for the three tests in the first phase, before the arise of unstable vibrations, the torque increases over the time during the test. Furthermore, the higher the rotational speed is, the higher is the torque slope. The main contributions to this variation is the dissipated power at the contact, which produces a temperature increase; this can cause both a local thermal dilatation (cf. Fig. 4.10) of the contacting bodies (measured by the proximity sensor) and physicochemical phenomena that affect directly the frictional forces. Due to the thermal dilatation the contact pressure, as well as the friction forces, and the slope of the torque increase (cf. Fig. 4.11). The higher the rotational speed is, the higher the contact dissipated power and the higher the slope of the torque over the time is (cf. bottom plot of Fig. 4.11).

4.3.2 Squeal occurrence and torque variation

The tests presented in Fig. 4.11 show the high dependence of the torque with the energy dissipated at the contact. Moreover, the squeal tests performed on the set-up highlighted a direct correlation between the torque value and the arise of squeal
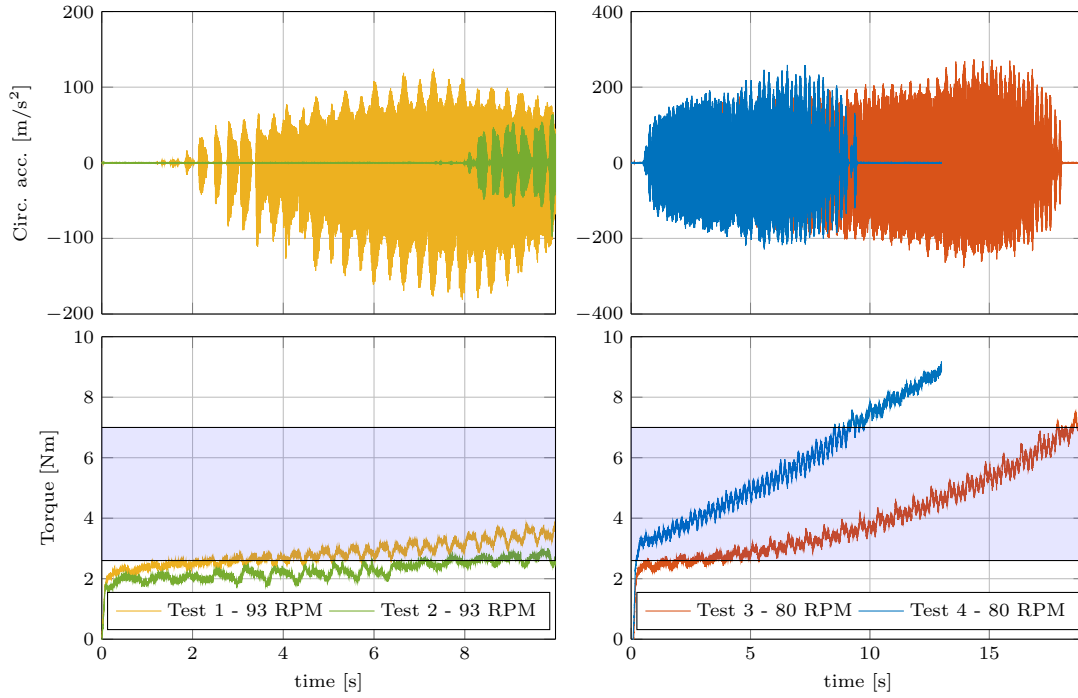
Figure 4.12: Transient responses of two couples of consecutive tests. Acceleration response in the radial direction (top) and engine torque (bottom) versus time. On the left responses for $\Omega = 93\,\mathrm{RPM}$, on the right responses for $\Omega = 80\,\mathrm{RPM}$.

vibrations. Figure 4.12 shows the measurements of the radial acceleration (top plots) and of the torque (bottom plots) for two couples of consecutive tests performed with an axial dilatation $\Delta r = 10\mu m$ and two different rotational speeds. The two plots on the left show the results for a rotational speed $\Omega = 93\,\mathrm{RPM}$, while the two on the right refer to a rotational speed $\Omega = 80\,\mathrm{RPM}$. The two couples of test have been performed on the same specimen but they are not consecutive one each other. The experimental results show a relationship between the arise of squeal and the measured torque. In the first couple of tests (left plots in Fig. 4.12) the unstable vibrations appear when the torque reaches the value 2.6 Nm. Similarly on the right, the tests show the rise of squeal when the torque is higher than 2.6 Nm. Moreover the disappear of squeal vibrations occurs for torque value higher than 7 Nm.

The rise of the squeal vibrations over 2.6 Nm could be linked to a critical value of the friction coefficient, as observed in the numerical stability analysis in Chapter 3; the frictional forces could increase with the mechanical energy dissipated at the contact and the consequent evolution of the tribological contact conditions (e.g. physicochemical properties of the material, detachment of wear particles, origin and evolution of the third body). The disappearance of vibrations for torques larger than 7 Nm could be related to a variation of the constraint conditions due to thermal dilatation of the cylinder, which correspond to an higher contact pressure and braking torque and to a modification of the system dynamics.

80

4.3.3 Effect of surface evolution
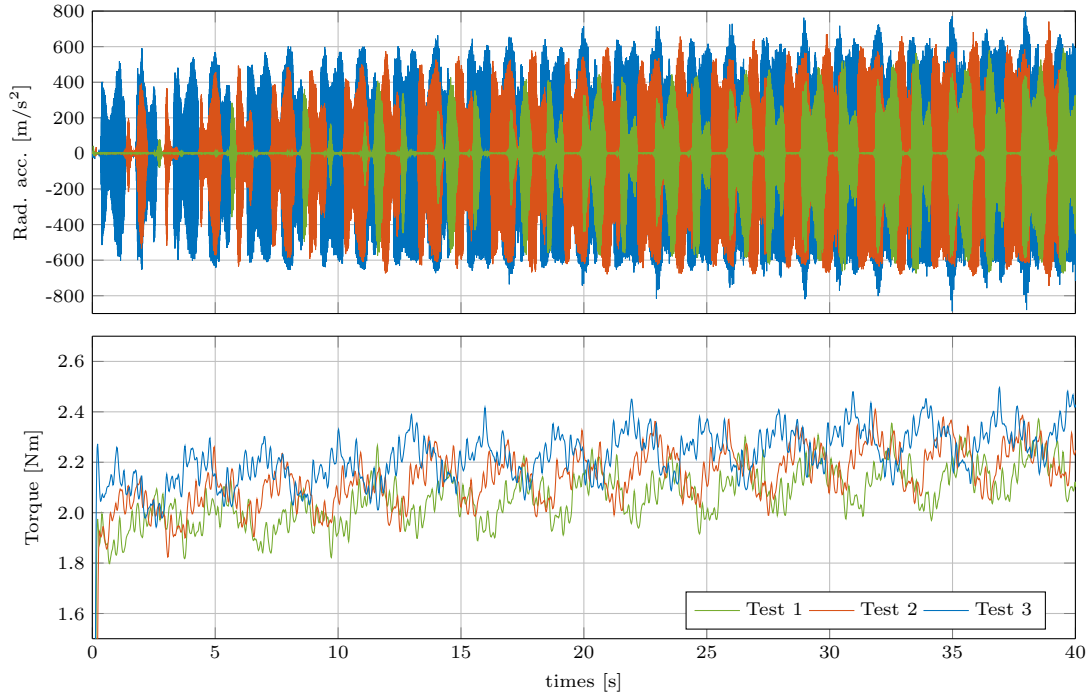
Figure 4.13: Transient responses of three consecutive tests with the same value of the rotational speed ($\Omega = 20\,\text{RPM}$). Acceleration response in the radial direction (top) and engine torque (bottom) versus time.

To investigate the effect of the surface evolution on the squeal behavior, a test composed by three consecutive measures have been performed on the same sample, maintaining constant all the other system parameters. The rotational speed is $\Omega = 20\,\text{RPM}$ while the radial dilatation is $\Delta r = 10\mu\text{m}$. Between one measure and the other an appropriate time interval allows for the system to cool down to avoid residual thermal dilatation from one measure to the other, monitored by the proximity sensor.

Figure Fig. 4.13 shows the acceleration in circumferential direction (top plot) and the torque measured during the three tests (bottom plot). The torque plot shows an increase of the measured value for each consecutive test. The same slope over the time is obtained for all the tests, as expected, being the relative velocity the same. Even if the system was cooled down between subsequent tests a slight increase of the initial value of the torque is noticed. This variation corresponds to a permanent variation of the contact interface, which in this case produces an increase of the macroscopic friction coefficient.

The variation of the friction coefficient affects the vibration amplitude of the system response (top plot in Fig. 4.13). In fact, the higher values of the friction coefficient correspond to more power introduced by friction induced vibrations, re-

sulting in higher vibration amplitude.

Summarizing, during the tests, the mechanical power dissipated at the contact produces three distinct phenomena with direct impact on the system dynamic response: *(i)* thermal dilatation due to the temperature increase; *(ii)* variation of material properties, due to temperature variation and the applied local stresses; *(iii)* wear, third-body evolution and permanent modification of the contacting surfaces. The first two effects are highlighted by the slope of the braking torque with the time; the last two are highlighted by an increase of the braking torque between successive tests.

Figure 4.14 shows the status of the contact surface of a polycarbonate disc used for the test. The observation of the specimen contact surface after the tests highlights the presence of a conspicuous third body layer.
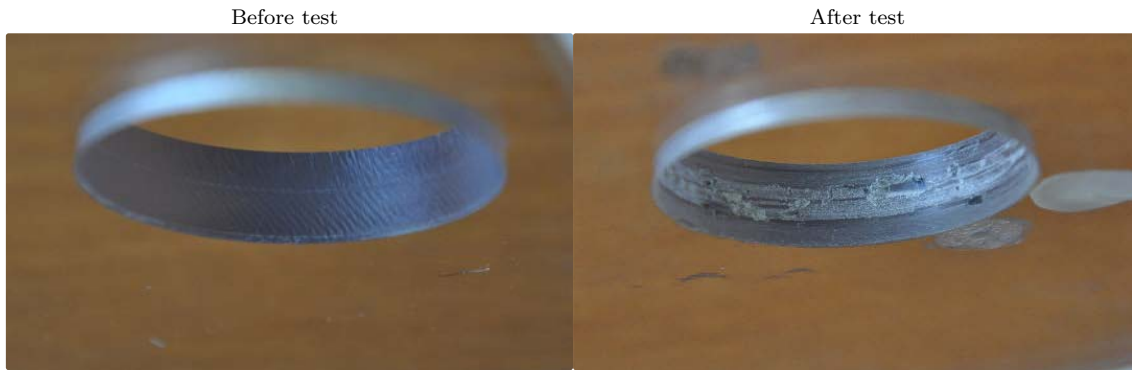
Figure 4.14: Surface status before and after tests of a specimens used in the tests for squeal reproduction, show a rich presence of third body.

4.4 Concluding remarks

In this chapter the analysis of the setup dynamics on the 3D finite element model, combined with the experimental observation of the squeal phenomena, confirmed the capability of the simplified 2D finite element model, adopted in the Chapter 3, to reproduce the in-plane unstable vibrations.

The modal analysis performed on a 3D finite element model, in fact, identified, among all the system modes, the ones which involve mainly the disc dynamics.

A detailed analysis of the deformation shapes in the radial, circumferential and axial direction allowed to associate the 3D modes with the modes recovered in the numerical study on the 2D model. The dynamic behavior of the 3D finite element model has been validated experimentally and the damping characteristics of the polycarbonate disc have been estimated by tests.

The squeal reproduction tests, performed on the PhotoTrib set-up, are presented in this chapter. They shows that the 2D model is able to predict the unstable vibra-

tions of the real system; the same 2 modes recovered numerically have been observed experimentally. Furthermore, this preliminary experimental campaign distinguishes among the main effects of the energy dissipated at the contact interface during the friction induced vibrations. The contact dissipated power, in fact, produces a local heating and a consequent reversible thermal dilatation (measured over the test time), which increases the braking measured torque. On the other hand, the physicochemical phenomena and the evolution of the third-body produce a permanent modification of the contact surface, which is at the origin of a non-reversible variation of the braking torque.

The numerical results in Chapter 3, together with the experimental ones reported in this chapter, show that in both cases the unstable response of the system is characterized by the presence of only two of the several unstable modes predicted by the complex eigenvalue analysis. In the next chapter the energy approach is applied, on a lumped parameter system, in order to investigate and predict this mode selection phenomena.

Chapter 5

Instability index on a lumped system

Contents

5.1   Introduction

The previous chapters showed that a frictional mechanical system is generally characterized by several unstable modes for the same system configuration. It has been also highlighted that the modes recovered during the limit cycle squeal vibrations, in transient numerical analysis and experiments, do not correspond to the ones with the larger real part of the eigenvalues calculated by CEA.

In this chapter the energy approach is used to define a new instability index, the Modal Absorption Index (MAI), by energy considerations; the main advantage of the new index is the possibility for comparing the capability of each unstable mode of the system to absorb energy from the contact interface. When a multi-instabilities configuration is predicted by the CEA, the new index allows for predicting the unstable mode selection occurring in the transient response of the mechanical system. The comparison between several modes was made possible by the use of the static equilibrium position projection on the complex modal base. By this way, it is possible to estimate the actual energy absorption due to the wide-band excitation generated at the frictional contacts. Similar approaches are used in the seismic analysis of civil structures to evaluate the significance of the vibration modes, i.e. the attitude of each mode to be excited by a base excitation [IRV 13].

In this chapter the modular lumped model (shown in Section 2.2.2) is used to reproduce the friction induced vibrations. The use of a lumped model allows for a fast integration of the transient solution. Using the lumped model, the performance of this new instability index has been verified for different system configurations and several operating conditions, showing a good agreement between the predicted (by the MAI index from CEA) and the simulated (by transient analysis) unstable behavior.

5.2   System response and energy analysis

In this section results by the transient analysis and CEA are presented to show the attitude of this system to reproduce friction-induced vibrations in unstable conditions. Moreover, the time evolution of the energy terms, detailed in Section 2.3, is analyzed.

The transient responses are presented for a system composed by two modules ($N = 2$ in Fig. 2.2 at page 28), where the masses m, the springs stiffness k, the inclination angle θ, the preload δ and the Rayleigh damping coefficients α and β, used to define the damping matrix $[C]$ in (2.4) are reported in Table 5.1.

Figure 5.1(a) shows the values of real and imaginary parts of the eigenvalues λ obtained by CEA and their dependence on the friction coefficient μ. Figure 5.1(b) shows the real mode shapes for a nil friction coefficient.

The friction coefficient μ, as well as the damping coefficients α and β, are considered to be key factors in the system stability [MAS 08, BRU 15b, SIN 07b, TON 13], because the two terms in (2.35) are strictly related to them.

(a) Real and Imaginary part of the complex eigenvalue λ as function of the friction coefficient μ

(b) Real mode shapes for $\mu = 0$
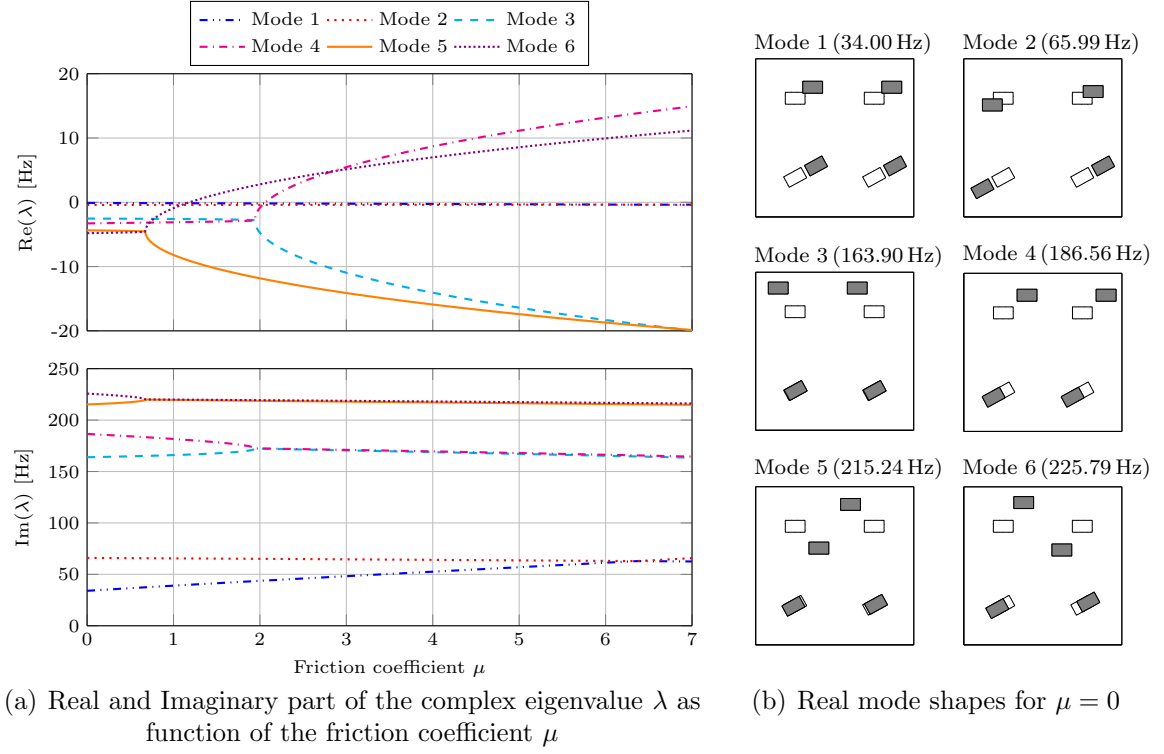
Figure 5.1: Complex Eigenvalues Analysis results and stability evaluation.

Parameter	Value	Unity
$m_{1:2}^i$	{ 0.3 0.7 }	kg
$k_{1:6}^i$	{ 5.5 6.0 2.2 6.0 30.0 25.0 }E + 4	N/m
θ^i	0.5	rad
δ^i	5.0E $-$ 3	m
α	0.0	s^{-1}
β	3.0E $-$ 5	s

Table 5.1: System parameters and boundary condition values

From a mathematical point of view the asymmetric contribution in $[\widetilde{K}]$ and $[\widetilde{C}]$ (2.28), due to the frictional contact interaction in SL or R-SL status (2.26), grows as a function of μ. This modifies the eigenvalues and eigenvectors of the system in (2.8) and (2.9) and, if the frequencies of two similar modes coalesce, it produces the lock-in phenomena with a consequent divergence of the real parts of the coalesced eigenvalues (cf. Fig. 5.1(a)). The system becomes unstable if one of the real parts reaches a positive value.

It is worth noting that the coalesced modes (cf. Fig. 5.1) are characterized by a displacement of the upper masses that is in phase, one each other, for modes $3 - 4$, and in phase opposition for modes $5 - 6$; the same observation can be done for the contact masses. Furthermore, observing each couple of coalesced modes, one of the two modes is characterized by displacements of the upper masses that

87

are quasi-perpendicular to the slider, while the other is quasi-parallel. When the modes couple to each other, the combination of these displacement directions (normal and tangential to the contact surface) generates a quasi-elliptic motion of the upper masses that is at the origin of the energy exchange between the mechanical system and the contact, i.e. of the stability or instability of the system [BRU 15a]. This quasi-elliptic motion is, in fact, at the origin of the phase difference between the tangential speed and the tangential force that produce the contact energy flow [BRU 15a, GUA 03, TAR 04].

On the contrary, the modes 1 and 2 are characterized by a quasi rigid motion of the modules along the direction of the sliders. Their deformation does not produce any variation of the normal contact force N; this is the reason why the two modes, even if they reach the same frequency for a friction coefficient $\mu \simeq 6.5$, don't coalesce and pass through each other (in frequency) without interacting. The presence of tangential and normal components of the coalescing modes at the contact interface has been found to be a necessary requirement in finite element models of continuous systems and experiments [MAS 07, MAS 06].

5.2.1 Stable behavior

The study of the eigenvalue real parts is a conventional tool to investigate the system stability. When all the eigenvalues real parts are negative, the system is stable and the transient response converges exponentially to the static equilibrium position. On the contrary, when at least one of the eigenvalues has a positive real part, the system is unstable and the response diverges.

Using this criterion, the system introduced in Section 5.2 is stable for a friction coefficient $\mu < 1.19$ (cf. Fig. 5.1(a)). In particular, for the friction coefficient $\mu = 1$, even if modes $5 - 6$ are already coalesced, all the real parts are still negative. The system response is reported in Fig. 5.2. In this case the initial condition is the static equilibrium position $\{X_0\}$ due to the application of the static preload $\delta^{1:2}$ (cf. Fig. 5.2(a)), with a perturbation applied on the velocity $\dot{x}_1^1(0) = \varepsilon = 1\text{mm/s}$ (cf. Fig. 5.2(b)).

The initial perturbation ε induces a vibration on the elastic system (cf. Fig. 5.2) that is progressively dissipated by the contact P_{dc} and by the material damping P_{dm}. In this case, due to the extremely low amplitude of the system vibrations Fig. 5.2(b), the contribution of the material dissipated power P_{dm} is negligible (cf. Fig. 5.3(a)) and almost all the external power P_{ex} (cf. Fig. 5.3(d)) is dissipated at the contact P_{dc} (cf. Fig. 5.3(b)). Furthermore, the energy exchanged at the contact P_c has a nil mean value and it tends to the nil value with the reduction of the vibration amplitude (cf. Fig. 5.3(c)). Hence, after the transient vibration generated by the initial perturbation ε all the external power P_{ex} is dissipated at the contact P_{dc} and the two quantities tend to the same value.

(a) Position response.

(b) Velocity response.
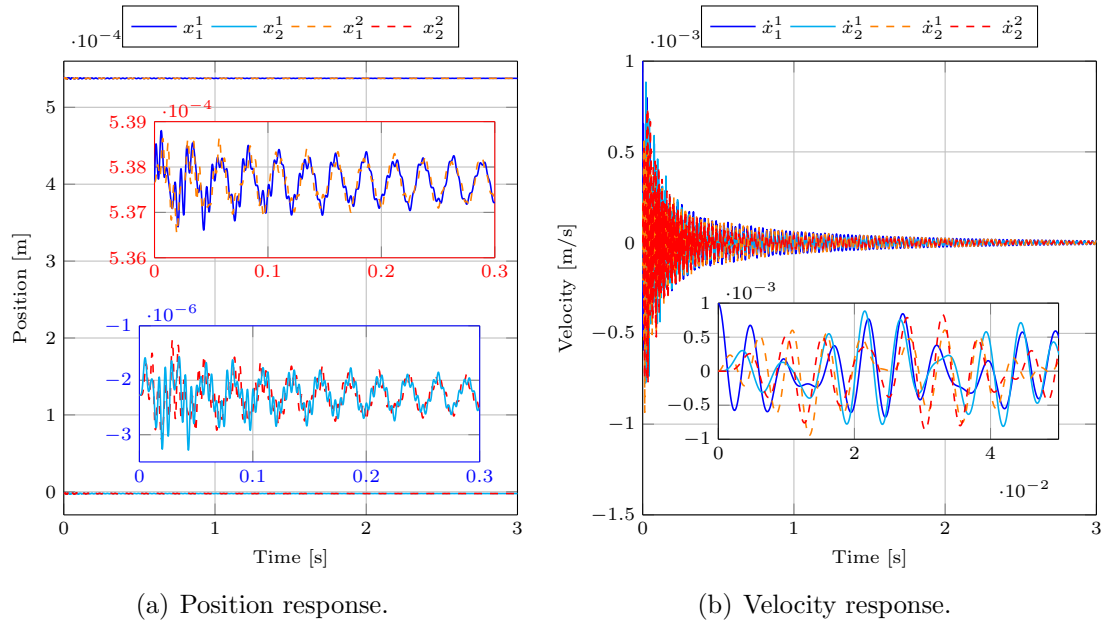
Figure 5.2: Stable response of the system composed by two modules $N = 2$ for a friction coefficient $\mu = 1$

(a) Material dissipated power

(b) Contact dissipated power

(c) Contact exchanged power

(d) External power
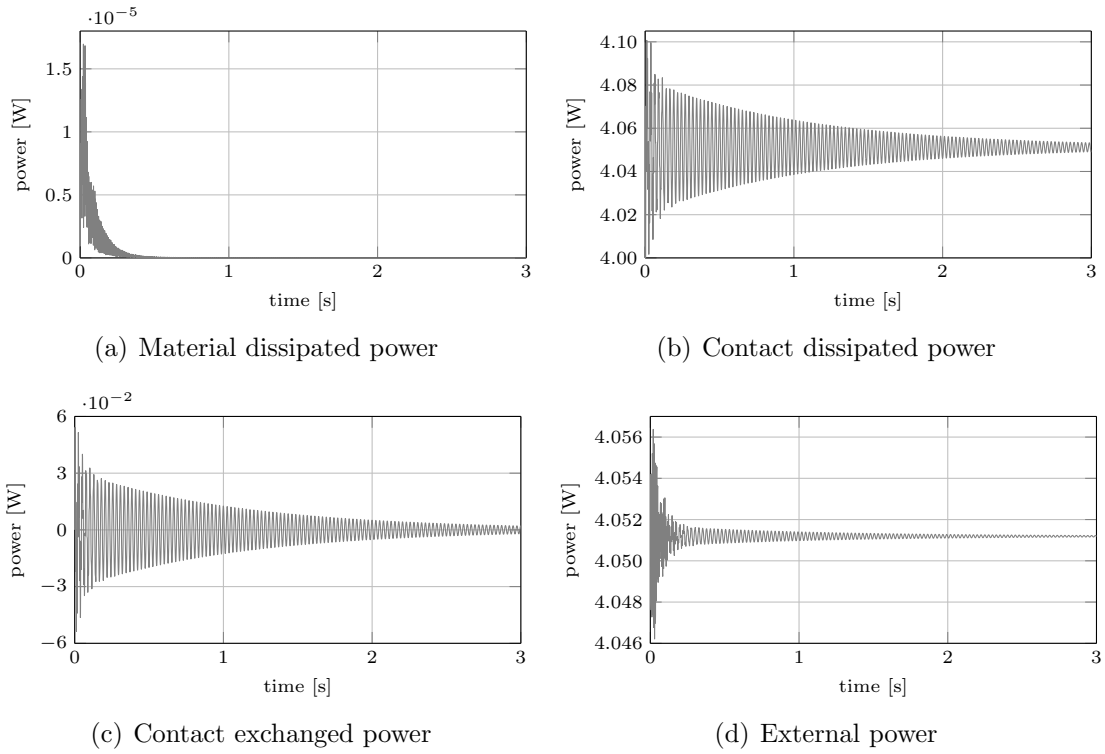
Figure 5.3: Energy terms for a stable response of a $N = 2$ system.

5.2.2 Unstable behavior

For the same model, in case of a friction coefficient $\mu = 2.2$ the system is unstable, the coalesced modes $3-4$ and $5-6$ have a positive real part (cf. Fig. 5.1(a)), and the same small perturbation ε generates a transient response with an amplitude that increases exponentially (cf.Fig. 5.4).

(a) Position response.   (b) Velocity response.
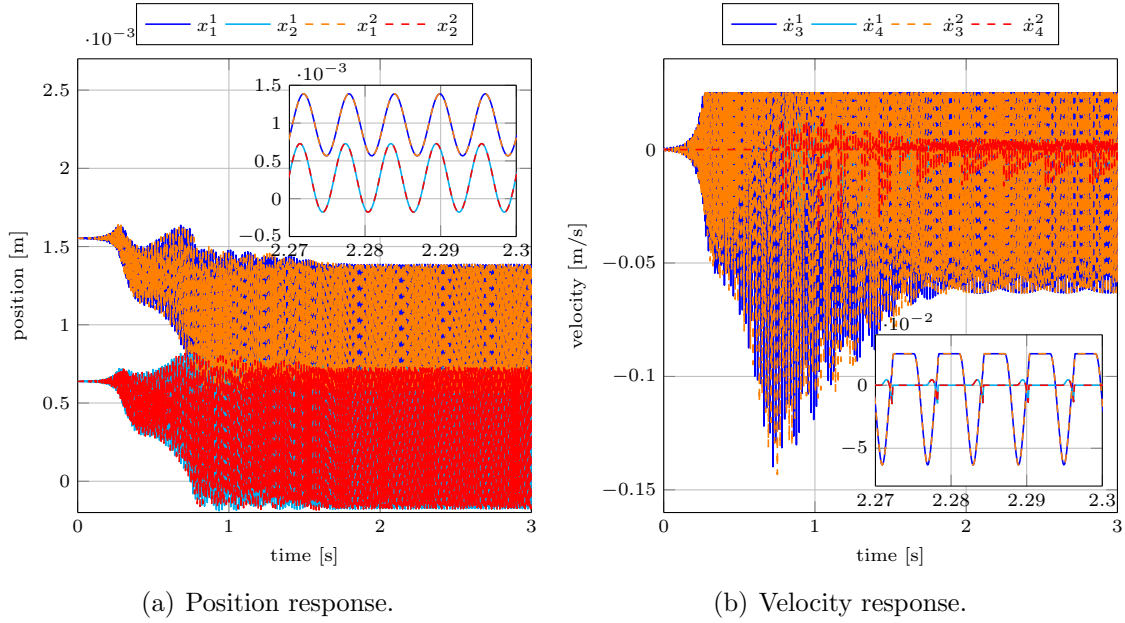
Figure 5.4: Unstable response of a system composed by two modules $N = 2$.

Figure 5.4 shows the transient response of the system when self-excited friction-induced vibrations arise. The amplitude of vibration increases with a complex behavior due to the presence of more than one unstable mode ($t < 1.5s$ in Fig. 5.4(a)). After an initial phase of increasing amplitude in overall sliding condition ($t < 0.4s$), an intermediate saturation phase occurs, where the contact nonlinearities (switches between different local contact status) heavily modify the linear behavior ($0.5 < t < 1.5s$); afterwards the system reaches a steady state behavior ($t > 2s$) characterized by the limit cycle.

The steady-state transient response is periodic (limit cycle) and the two subsystems are in phase, with each other (cf. magnified responses in Fig. 5.4(a) and Fig. 5.4(b)). During this steady state behavior the two contact masses switch between SL, ST (when the $\dot{x}_3^i = v^i = 2.5m/s$ in Fig. 5.4(b)) and DT (when $\dot{x}_4^i \neq 0$ in Fig. 5.4(b)).

When the system reaches a steady-state condition, the global amplitude of vibration remains constant, i.e. the integral of the power exchanged over a period of oscillation (2.34) is nil.

Analyzing the powers exchanged and dissipated (cf. Fig. 5.5), it is possible to highlight that during the transient response the external power P_{ex} is partially dis-

sipated at the contact P_{dc} (cf. Fig. 5.5(b)) and partially exchanged with the elastic system by P_c (cf. Fig. 5.5(c)), both during the SL phase and the ST phase. During the first interval ($t < 0.4s$) the energy is stored by the system, increasing the vibration amplitude; the equilibrium between the energy exchanged, from the contact to the system, and the energy dissipated by material damping is reached in the steady-state response, which is characterized by the limit cycle of the vibration. Hence, the energy introduced in the form of friction-induced vibrations is dissipated by material damping P_{dm} (cf. Fig. 5.5(a)). In general $dE_m(t)/dt$ in (2.35) is not nil $\forall t$ in the steady-state regime, but to have a constant internal energy content E_m, the condition is to have a nil contribution over the main period of oscillation $T^\star$:

$$\int_{t}^{t+T^\star} [P_c(t) - P_{dm}(t)]\, dt = 0 \qquad (5.1)$$

This condition is respected during the steady state and $P_c(t) - P_{dm}(t)$ has a periodic behavior with a nil mean value. In this conditions a large amount of energy is transferred from the contact to the bulk and subsequently dissipated by material damping [BRU 14].

(a) Material dissipated power

(b) Contact dissipated power

(c) Contact exchanged power

(d) External power
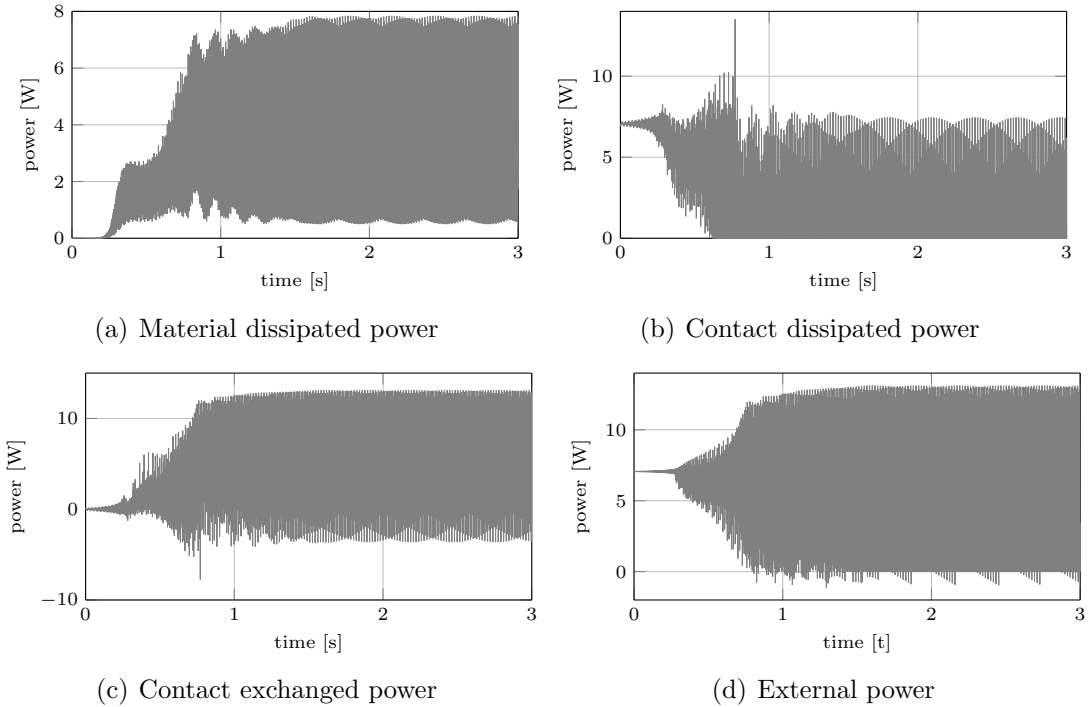
Figure 5.5: Energy terms for an unstable response of a $N = 2$ system.

5.2.3 Weakness of eigenvalue real part as unstable mode selector

It is known that one of the main drawbacks of CEA is the over-prediction of instabilities [MAS 07, OUY 05, BRU 15b, SIN 09]. The CEA parametric analysis gives as a result all the possible unstable system modes, with over-prediction of the unstable ranges and with the impossibility to predict which mode will be effectively unstable when several modes are predicted to have a positive real part of the eigenvalue. A higher value of a real part does not correspond to the probability of the mode to become unstable in the transient response, but only to the rate of growth of the vibrations in the initial linear phase before the nonlinear contact transitions. The previous simulations, reported in Section 5.2.1 and Section 5.2.2, show the reliability of the real part of the system eigenvalues to evaluate the stability of the system; on the contrary it is not possible, by the observation of real parts, to identify the "effectively unstable" mode in the case of system multi-instabilities (i.e. when more than one eigenvalues of the system have a positive real part) and to indicate the modal instability that would be recovered on the steady-state transient response. For example in the unstable response presented in Section 5.2.2 the modes $3-4$ and $5-6$ are in a lock-in status, their real parts (respectively $\mathrm{Re}(\lambda_{3-4}) = 1.292\mathrm{Hz}$ and $\mathrm{Re}(\lambda_{5-6}) = 3.317\mathrm{Hz}$), are positive and the system is unstable. During the initial part of the transient response ($t < 0.25\mathrm{s}$), when the system is in a uniform sliding state (cf. Fig. 5.4(b)), the frequency analysis in Fig. 5.6(b) shows the presence of the two unstable modes with an amplitude of their frequency peak that depends on the real part and on the particular perturbation chosen for this analysis. The resulting contact nonlinearities ($0.5\mathrm{s} < t < 1.5\mathrm{s}$) produces the increase of the contribution of modes $3-4$ on the system response. Finally, the frequency analysis of the unstable transient response in the time interval $2\mathrm{s} < t < 3\mathrm{s}$ shows a single peak in the spectrum (with some small super-harmonic contributions) corresponding to the frequency $f \simeq 166\mathrm{Hz}$ of the coalesced mode $3-4$, which is the one with the lower value of the real part.

Furthermore, an analysis of the transient responses (cf. Fig. 5.4) shows that the two modules move perfectly in phase one each other, confirming the deformation of the corresponding $3-4$ coalesced real modes (cf. Fig. 5.1(b)), which is characterized by the same motion of the two subsystems.

5.3 A new instability index for mode selection based on energy considerations

As highlighted in 5.2.3, the real part of the unstable eigenvalues is not able to predict the real propensity of each unstable mode to promote squeal. In this section a new index is defined based on the observation that the unstable modes are the ones with a more relevant deformation at the contact [BRU 15b], which increases the energy

(a) Velocity response along x_1^1

(b) Discrete Fourier Transform
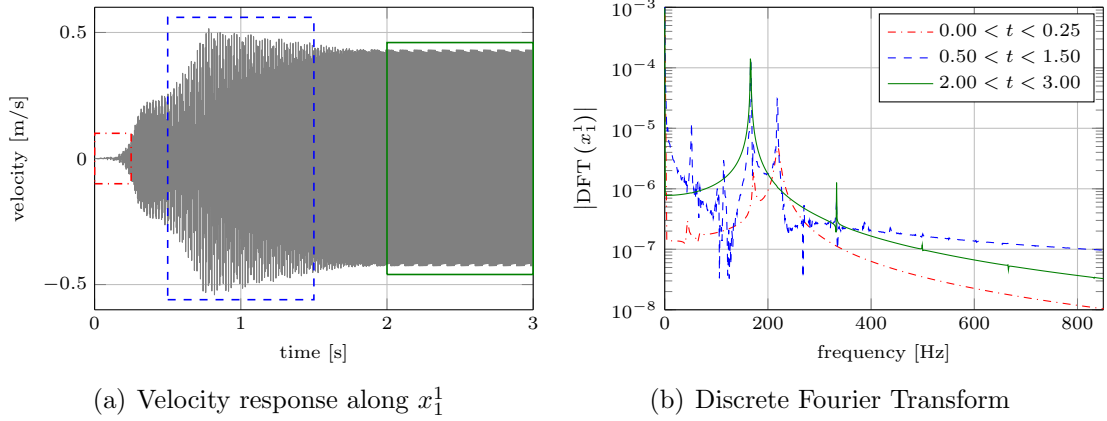
Figure 5.6: Frequency analysis of the unstable transient response of a $N = 2$ system with a friction coefficient $\mu = 2.2$.

flow at the contact. The idea is to compute, for each eigenvector of the system, the variation of the total energy E_t due to the power introduced by the contact during friction induced vibrations P_c, as in [TAR 04, GUA 03], and the power dissipated by material damping P_m, evaluated as mean values over an oscillation period. In this way, it is possible to have a comparison between different modes, not only based on the information coming from the eigenvalue (eigenfrequency and modal damping) but also on the eigenvectors (modal shapes), which contain important information about the energy distribution over the system, and on the attitude of each mode to absorb and dissipate energy from both the contact and the bulk.

The distribution of stresses in combination with the local tangential velocity at the contact interface is related to the attitude of each mode to introduce energy into the system. These considerations can be done referring to each complex eigenvector (complex modal shape) resulting from the CEA; nevertheless each mode contribution is defined as proportional to an arbitrary constant that is complex and generally different for left and right modes in case of non self-adjoint system (cf. (2.8) and (2.9)).

To account for the contribution of each mode, a decomposition on the modal base, by means of the left and right eigenvectors ([Υ] and [Ξ]), of the static equilibrium position $\{\widetilde{X}_0\}$ is proposed here. By this way, also the contact forces in the static equilibrium position (overall sliding) are projected over the modal base. In fact, the static equilibrium position is the actual deformation of the system in the steady-state condition (braking phase) without instabilities induced by the contact; the friction-induced vibrations produce an oscillation of the system around this position. Assuming that a large band excitation is provided at the contact interface, the contribution of such excitation on each system mode can be approximated by the modal projection of the static equilibrium position on the complex modal base. By this way, the projection of the equilibrium position on the system modes allows for

comparing the energy amount absorbed by each mode during the vibration around the equilibrium position (steady-state deformation), that are generated by a wide-band perturbation with the same geometrical distribution fo the static contact force.

$$\left[\widetilde{K} \right] \left\{ \widetilde{X}_0 \right\} = \{ F_0 \} \tag{5.2}$$

$$[B] \{ Y_0 \} = \{ Q_0 \} \tag{5.3}$$

where $[B]$ is the system matrix in the state coordinates defined in (2.7) and $\{Y_0\}$ and $\{Q_0\}$ are respectively the static equilibrium state of the system and the corresponding external forces defined in the state coordinates (cf. (2.7)). Eq. (5.3) can be diagonalized by means of the system eigenvectors:

$$[\Upsilon]^T [B] [\Xi] \{ z_0 \} = [\Upsilon]^T \{ Q_0 \} \tag{5.4}$$

The complex eigenvalues are 2×2 complex and conjugate ($\lambda_r^\star = \lambda_{r+1}$ where * indicates the complex and conjugate operation), the elements on the even columns of the complex eigenvectors matrices are the complex and conjugate of the previous odd columns ($\{v_r\}^\star = \{v_{r+1}\}$ and $\{\xi_r\}^\star = \{\xi_{r+1}\}$). Hence, the modal contributions $\{z_0\}$ are 2×2 complex and conjugates ($z_r^\star = z_{r+1}$) and the sum of a couple of them gives a real contribution on the state plane. Finally, it is possible to consider the contribution on the system position of each complex and conjugate couple of modes as follows:

$$\{ Y_r \} = \frac{1}{b_r} \{ \xi_r \} \{ v_r \}^T \{ Q_0 \} \tag{5.5}$$

$$\{ Y_{r+1} \} = \{ Y_r \}^\star = \frac{1}{b_{r+1}} \{ \xi_{r+1} \} \{ v_{r+1} \}^T \{ Q_0 \} \tag{5.6}$$

and, being these contributions complex and conjugates, their sum is real too.

Quantities in (5.5) and (5.6) contain information about both the position $\{ \widetilde{X}_r \}$ and the velocity $\{ \dot{\widetilde{X}}_r \}$ for each couple of complex and conjugated modes; hence, the corresponding contact forces $\{N_r\}$ and $\{T_r\}$ can be calculated.

The damping forces $\{F_d\}$ are expressed as the product of the damping matrix $[\widetilde{C}]$ times the speed vector $\{ \dot{\widetilde{X}} \}$; it is possible as well to calculate the damping forces $\{F_{d,r}\}$ generated by each modal contribution $\{ \dot{\widetilde{X}}_r \}$.

$$\{ F_{d,r} \} = \left[\widetilde{C} \right] \left\{ \dot{\widetilde{X}}_r \right\} \tag{5.7}$$

The modal contribution of the system speed $\{ \dot{\widetilde{X}}_r \}$ and the modal contribution of the damping forces $\{F_{d,r}\}$, are complex quantities, and for both of them it is possible to define a modulus (indicated respectively by $\{\Lambda_r\}$ and $\{\Gamma_r\}$) and phase

94

(indicated respectively by $\{\Phi_r\}$ and $\{\Psi_r\}$). The mean power dissipated by material damping for each mode during a period of oscillation is:

$$\widehat{P}_{dm,r} = 2\{\Lambda_r\}^T [\{\Gamma_r\} \odot \cos(\{\Phi_r\} - \{\Psi_r\})] \tag{5.8}$$

where $\odot$ indicates the Hadamard product (element by element product) of the two vectors.

The mean power introduced into the system by the frictional contact $\widehat{P}_{c,r}$ can be expressed, for each mode, during a period of oscillation, as the sum of the power exchanged on each contact mass. Each contribution can be expressed as the product of the modulus τ_r^i of tangential force T_r^i and the modulus ρ_r^i of the tangential speed $\dot{x}_{3,r}^i$, times the cosine of the difference of phases, respectively ψ_r^i and ϕ_r^i:

$$\widehat{P}_{c,r} = 2\sum_{i=1}^{N} \tau_r^i \rho_r^i \cos\left(\psi_r^i - \phi_r^i\right). \tag{5.9}$$

The Modal Absorption Index (MAI) is defined, for each mode r, as the ratio between the total energy variation $\Delta E_{m,r}$, over a period of oscillation Δt_r, and the period of oscillation itself. It is given by the sum of the mean contribution of the contact exchanged power and the material dissipated power for each couple of complex and conjugate modes:

$$\chi_r = \frac{\Delta E_{m,r}}{\Delta t_r} = \widehat{P}_{c,r} + \widehat{P}_{c,r+1} - \widehat{P}_{dm,r} - \widehat{P}_{dm,r+1}. \tag{5.10}$$

The MAI allows for comparison of the different system modes, by describing their respective capability to absorb energy by the environment and to generate squeal. The information coming from this quantity results to be particularly interesting in case of systems characterized by multi-instabilities highlighted by CEA, where the standard approach does not gives further information about the steady-state behavior.

The use of the static position decomposition allows to compare the different unstable modes by taking into account the "shape" of the excitation at the contact zone. In the numerical model, during the first part of the response, in uniform sliding condition, the energy is introduced into the system at the contact interface by the frictional forces; the contribution of each mode on the transient behavior is strictly related to the initial external perturbation and to the modal damping factor (real part of the corresponding eigenvalue). During the relative motion, both random excitation from the sliding surface and local variations of contact status (local sticking and/or detachment) generate a uniform wide-band excitation that involves all the system modes; the mode with a higher attitude to introduce energy into the mechanical system is the one that will overcome in the steady-state response.

5.4 Application of the instability index to the lumped model

5.4.1 Application to the 2-module system

Using the quantities introduced in Section 5.3 for the model analyzed in Section 5.2, it is possible to highlight that the MAI, thanks to the further information provided by the complex eigenvalues, is able to predict the transient behavior of the unstable system. Several transient analyses have been performed to highlight the different behaviors of the unstable system for several values of the friction coefficient (cf. Fig. 5.1). This table is a more synthetic representation of Fig. 5.1, for the values of the friction coefficient used in the transient simulations.

Table 5.2 shows the 12 complex and conjugated eigenvalues of the system composed by 2 modules and characterized by 6 DoFs. The modal coupling locks the frequencies of a couple of modes at about the same value (light gray highlighted cells in Table 5.2) and the real parts of the coalesced modes diverge towards opposite direction and one of the two becomes positive, i.e. unstable (dark gray highlighted cells).

		Friction coefficient μ											
		0.5		1.0		1.5		2.0		2.2		3.0	
Modes	1	-0.12	$\pm i 36.55$	-0.14	$\pm i 39.01$	-0.16	$\pm i 41.39$	-0.18	$\pm i 43.66$	-0.19	$\pm i 44.62$	-0.22	$\pm i 48.21$
	2	-0.41	$\pm i 65.76$	-0.40	$\pm i 65.54$	-0.40	$\pm i 65.31$	-0.40	$\pm i 65.08$	-0.40	$\pm i 64.98$	-0.39	$\pm i 64.60$
	3	-2.56	$\pm i 164.77$	-2.59	$\pm i 165.94$	-2.65	$\pm i 167.70$	-4.57	$\pm i 172.27$	-6.87	$\pm i 171.88$	-10.96	$\pm i 170.52$
	4	-3.20	$\pm i 184.23$	-3.11	$\pm i 181.62$	-3.00	$\pm i 178.25$	-1.03	$\pm i 172.38$	1.29	$\pm i 172.14$	5.47	$\pm i 171.05$
	5	-4.46	$\pm i 217.44$	-8.19	$\pm i 219.61$	-10.32	$\pm i 219.15$	-11.80	$\pm i 218.76$	-12.34	$\pm i 218.59$	-14.11	$\pm i 217.95$
	6	-4.68	$\pm i 222.79$	-0.91	$\pm i 219.91$	1.24	$\pm i 219.63$	2.75	$\pm i 219.36$	3.32	$\pm i 219.24$	5.14	$\pm i 218.74$

Table 5.2: Real and imaginary part of the eigenvalues for several values of the friction coefficient, for the 2 module system. Dark-gray highlighted cell correspond to unstable modes while light-gray highlighted cells correspond to the coalesced modes.

Using the relations expressed in (5.5) and (5.6), it is possible to calculate $\widehat{P}_{dm,r}$, the material dissipated power (5.8) associated to each modal contribution at the static equilibrium position. Table 5.3 shows this quantity calculated for each mode, for several values of the friction coefficient, in both stable and unstable conditions with one or more than one unstable modes. It is worth noting that when two modes are coupled the power dissipated by material damping on each mode is the same. This power can assume only positive values due to its nature of dissipative power (cf. (5.10)). Modes 3 and 4 show the highest values and the order of magnitude of the energy dissipated by these modes is several order of magnitude higher than the others, except that for the first mode.

The power exchanged at the contact $\widehat{P}_{c,r}$ expressed in (5.9), for the same set of values of the friction coefficient is reported in Table 5.4. In this case the sign

				Friction coefficient μ				
		0.5	1.0	1.5	2.0	2.2	3.0	
	1	4.54e + 00	1.28e − 01	5.91e − 01	1.44e + 00	1.90e + 00	4.54e + 00	
	2	5.51e − 10	7.74e − 12	4.12e − 11	1.17e − 10	1.66e − 10	5.51e − 10	
Modes	3	3.41e + 01	5.67e + 00	2.05e + 01	2.18e + 02	6.33e + 01	3.41e + 01	$\widehat{P}_{dm,r}$ [W]
	4	3.41e + 01	1.01e + 00	1.02e + 01	2.18e + 02	6.33e + 01	3.41e + 01	
	5	9.77e − 10	3.74e − 10	4.84e − 10	6.35e − 10	7.00e − 10	9.77e − 10	
	6	9.77e − 10	3.74e − 10	4.84e − 10	6.35e − 10	7.00e − 10	9.77e − 10	

Table 5.3: Material dissipated power $\widehat{P}_{dm,r}$ for several values of the friction coefficient. Highlighted cells corresponds to material dissipated power for coupled modes.

of the power contribution depends to the phase difference between the tangential contact velocity and the tangential contact force on the different contact points. It is positive if the power produces an increase of the mechanical energy of the system and it is negative otherwise. In this case, for the pair of coupled modes, the contact exchanged power assumes values with the same order of magnitude but opposite sign.

				Friction coefficient μ				
		0.5	1.0	1.5	2.0	2.2	3.0	
	1	−8.57e − 05	−1.53e − 02	−9.56e − 02	−2.82e − 01	−3.95e − 01	−1.12e + 00	
	2	+2.31e − 16	+5.33e − 14	+4.30e − 13	+1.66e − 12	+2.60e − 12	+1.20e − 11	
Modes	3	−1.21e − 03	+4.76e − 02	+4.08e − 01	−1.50e + 02	−9.35e + 01	−1.03e + 02	$\widehat{P}_{c,r}$ [W]
	4	+7.51e − 05	+2.25e − 02	+3.23e − 01	+1.64e + 02	+9.74e + 01	+1.04e + 02	
	5	−3.91e − 13	−2.98e − 10	−6.16e − 10	−1.02e − 09	−1,21e − 09	−2.07e − 09	
	6	+7.38e − 14	+3.02e − 10	+6.13e − 10	+1.01e − 09	+1,19e − 09	+2.03e − 09	

Table 5.4: Contact exchanged power $\widehat{P}_{c,r}$ for several values of the friction coefficient for a 2 modules system. Highlighted cells correspond to contact exchanged power for coupled modes, while, dark-gray highlighted cells correspond to unstable modes.

Finally the MAI can be computed for each mode and its values are reported in the first part of Table 5.5 for the same set of values of the friction coefficient. The cells on Table 5.5 are light gray if the corresponding modes are coalesced, while they are dark gray highlighted if the corresponding mode is unstable. The bordered cells indicate the mode that is predicted to be unstable by the MAI.

The second part of Table 5.5 shows the values assumed by the eigenvalues real parts of the modes 4 and 6, which become unstable increasing the friction coefficient. Again, highlighted cells correspond to unstable modes, while bordered cells indicate the unstable mode with the highest value of the eigenvalue real part. Finally, the last part of the table shows the frequency actually recovered in the steady-state regime (limit-cycle) of the transient response f_{lc}, and the corresponding excited unstable mode.

The sign of the MAI results to be strictly related to the sign of the real part of the corresponding eigenvalues. Nevertheless, the respective value of MAI for the

different unstable modes is not in agreement with the amplitude of the real part of the eigenvalues. In fact, being the magnitude of the powers that are involved in modes $3 - 4$ several order of magnitude higher than the ones of modes $5 - 6$ (cf. Table 5.4 and Table 5.3), when mode 4 becomes unstable ($\mathrm{Re}(\lambda_4) > 0$, for $\mu \geq 2.07$) the corresponding MAI value immediately overcomes the value of mode 6; i.e. the power absorption corresponding to the unstable pair of modes $3 - 4$ is larger.

In fact, this is in agreement with the actual unstable behavior of the system (cf. third part of Table 5.5) simulated by the transient analysis for the same values of the friction coefficient; as soon as the mode 4 is unstable ($\mathrm{Re}(\lambda_4) > 0$, for $\mu \geq 2.07$), the only frequency measured over the stationary limit cycle is 166Hz, which corresponds to the unstable mode 4.

On the contrary, the eigenvalues of the coalesced modes $5 - 6$ show an higher real part with respect to the modes $3 - 4$, for the same interval of the friction coefficient, which is not in agreement with the transient response of the system. The MAI index is able to predict the mode that is at the origin of squeal vibrations in the transient behavior, when several modes are predicted to be unstable by CEA.

| | | Friction coefficient μ | |
		0.5	1.0	1.5	2.0	2.2	3.0	
Modes	1	$-1.36\mathrm{e}-03$	$-1.43\mathrm{e}-01$	$-6.87\mathrm{e}-01$	$-1.72\mathrm{e}+00$	$-2.30\mathrm{e}+00$	$-5.67\mathrm{e}+00$	χ_r [W]
	2	$-6.80\mathrm{e}-14$	$-7.69\mathrm{e}-12$	$-4.07\mathrm{e}-11$	$-1.16\mathrm{e}-10$	$-1.64\mathrm{e}-10$	$-5.39\mathrm{e}-10$	
	3	$-2.27\mathrm{e}+00$	$-5.62\mathrm{e}+00$	$-2.01\mathrm{e}+01$	$-3.68\mathrm{e}+02$	$-1.57\mathrm{e}+02$	$-1.37\mathrm{e}+02$	
	4	$-6.44\mathrm{e}-03$	$-9.83\mathrm{e}-01$	$-9.88\mathrm{e}+00$	$-5.42\mathrm{e}+01$	$+3.41\mathrm{e}+01$	$+7.03\mathrm{e}+01$	
	5	$-2.58\mathrm{e}-10$	$-6.72\mathrm{e}-10$	$-1.10\mathrm{e}-09$	$-1.66\mathrm{e}-09$	$-1.91\mathrm{e}-09$	$-3.05\mathrm{e}-09$	
	6	$-7.92\mathrm{e}-12$	$-7.23\mathrm{e}-11$	$+1.30\mathrm{e}-10$	$+3.76\mathrm{e}-10$	$+4.91\mathrm{e}-10$	$+1.05\mathrm{e}-09$	
$\mathrm{Re}(\lambda_4)$		-3.20	-3.11	-3.00	-1.03	$+1.29$	$+5.47$	Hz
$\mathrm{Re}(\lambda_6)$		-4.68	-0.91	$+1.24$	$+2.75$	$+3.32$	$+5.14$	
f_{lc}		–	–	219	$219 - 166$	166	166	Hz
mode_{lc}		–	–	6	$6 - 4$	4	4	

Table 5.5: MAI index χ_r compared with the real part of complex eigenvalues for several values of the friction coefficient. Light-gray highlighted cells correspond coupled modes, while dark-gray highlighted cells correspond to the unstable modes. f_{lc} is the frequency recovered in the stationary limit cycle and mode_{lc} is the corresponding mode. Bordered values indicate both the modes predicted to be unstable by the MAI index χ and the modes having larger real part of the eigenvalues.

Figure 5.7(a) shows the transient response for a 2-modules sytem for a friction coefficient $\mu = 1.5$. For this value of the friction coefficient only the modes $5 - 6$ are coalesced and unstable. The mode predicted to be unstable both by the eigenvalue real part and by the Modal Absorption Index is the 6th mode at a frequency of about $219\,\mathrm{Hz}$ (cf. Fig. 5.1). The frequency analysis (cf. Fig. 5.7(b)) of the response shows that during the linear phase, before the arising of contact status transitions ($0 < t < 0.7\mathrm{s}$), during the saturation phase ($0.7 < t < 1.2\mathrm{s}$) and during the steady-

98

(a) Velocity response along x_1^1.

(b) Discrete Fourier Transform
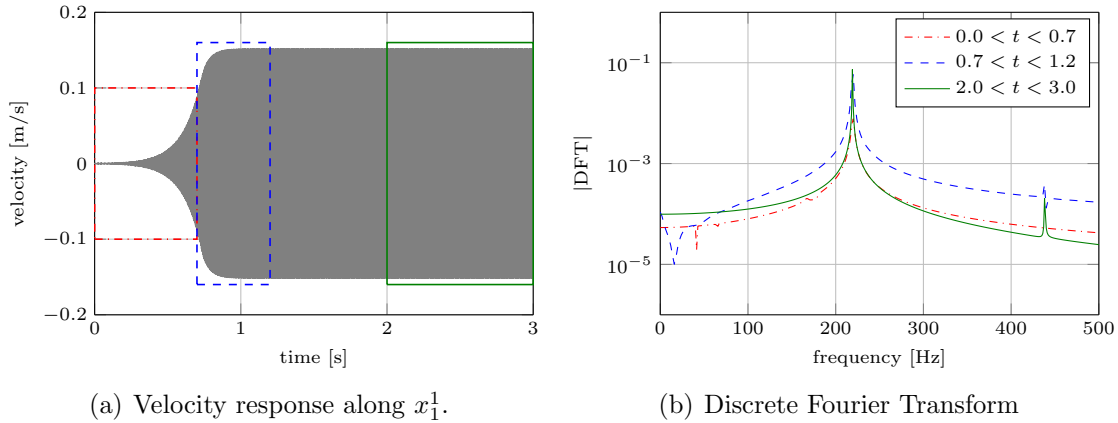
Figure 5.7: Unstable transient response of a $N = 2$ system with friction coefficient $\mu = 1.5$.

state regime ($2 < t < 3$s), the main frequency recovered is in agreement with the mode predicted to be unstable by both the eigenvalue real part and by the MAI.

For a friction coefficient $\mu = 2.2$ (cf. Table 5.5) the mode predicted to be unstable by the MAI is the 4th mode, while by the analysis of the real parts and larger value is obtained for the 6th mode. The comparison of these results with the transient response in Fig. 5.6(a) and its frequency analysis in Fig. 5.6(b), shows that the linear phase of the respose ($0 < t < 0.25$s) and the saturation phase ($0.5 < t < 1.5$s) are characterized by the presence of both the unstable modes ($3 - 4$ and $5 - 6$ respectively at the frequency of $166\,\mathrm{Hz}$ and $219\,\mathrm{Hz}$). In particular the amplitude of each mode contribution in the spectral analysis results to be strictly related to the shape of initial perturbation ε and to the value of the eigenvalue real parts (growth of vibration in linear phase). On the contrary, during the steady-state regime ($2 < t < 3$s) the only frequency detected is the one corresponding to the 4th mode, as correctly predicted by the MAI (cf Table 5.5). While the transient linear increase of vibration is mainly affected by the different growth rate of the mode instabilities, when the nonlinearities excite the system at the contact interface, the MAI index indicates which mode will absorb more energy, i.e. will dominate the limit cycle vibration.

5.4.2 Extension of the mode selection approach to more complex systems

In this section the analysis is extended to a system composed by 4 modules to confirm the reliability of the approach showed in the previous section.

Figure 5.8(a) shows the real and imaginary part of complex eigenvalue as a function of the friction coefficient. In this case the system has 12 DoFs and the complex modal analysis shows 24 complex and conjugated modes (cf. Fig. 5.8(a)).

Due to the symmetry of the system there are double modes such as the modes

(a) Real and Imaginary part of the complex eigenvalue λ as function of the friction coefficient μ.

(b) Coalescing modes.
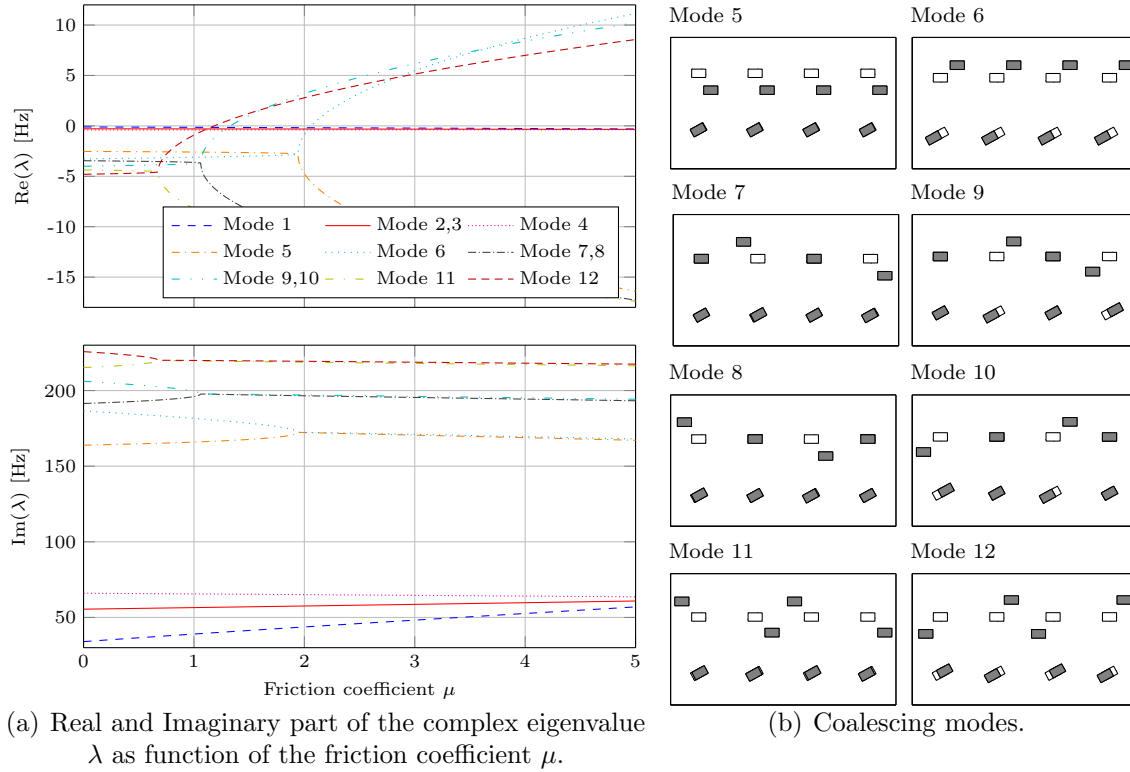
Figure 5.8: Complex Eigenvalue Analysis results and stability evaluation for a system composed by 4 modules ($N = 4$)

$2, 3$ (at $f_{2,3} = 55$Hz for a nil friction coefficient), modes $7, 8$ and $9, 10$ (respectively at $f_{7,8} = 191$Hz and $f_{9,10} = 206$Hz). Increasing the friction coefficient modes $5 - 6$, double modes $7, 8 - 9, 10$ and modes $11 - 12$ coalesce one each other and become unstable. The first coalescing modes are modes $11 - 12$ for a friction coefficient $\mu > 1.2$, and the system is unstable.

Figure 5.8(b) shows the modal shapes of the coalescing modes. The empty rectangles represent the equilibrium position and the filled rectangles represent the position that is reached by each mass during the modal oscillation. Coalescing modes $5 - 6$ are characterized by an in-phase motion of all the component modules. Coalescing modes $7 - 9$ and $8 - 10$, on the contrary, are characterized by a motion, respectively, of the even and the odd modules, that is in-phase opposition one each other. Finally, coalescing modes $11 - 12$ are characterized by a phase opposition motion of the even modules with respect to the odd modules.

Similarly to the 2 modules system, the MAI has been calculated for each mode and its values are shown in the first part of Table 5.6 for different values of the friction coefficient. Light gray highlighted cells indicate that modes are coalesced while dark gray highlighted cells indicate that the corresponding modes are unstable. Bordered cells indicate the unstable modes with the highest value of the MAI index, which are predicted to be the effectively squeal mode during the steady-state squeal

100

vibrations.

The second part of Table 5.6 shows the values of eigenvalue real parts of the unstable modes of the 4 module system. Also in this case dark gray highlighted cell indicate that the corresponding modes are unstable. Bordered cells in this case indicate the mode with the highest value of the eigenvalue real part, for each value of the friction coefficient.

Finally, the third part of Table 5.6 shows the main frequency f_{lc} recovered during the steady-state regime (limit cycle) of the unstable response, and the corresponding unstable mode.

			Friction coefficient μ				
		0.6	1.3	1.4	1.8	2.2	4.0	
Modes	1	$-3.73e-03$	$-8.31e-01$	$-1.08e+00$	$-2.49e+00$	$-4.59e+00$	$-2.58e+01$	
	2,3	$-5.52e-13$	$-1.51e-10$	$-2.04e-10$	$-5.43e-10$	$-1.19e-09$	$-2.00e-08$	
	4	$-1.89e-13$	$-4.72e-11$	$-6.29e-11$	$-1.59e-10$	$-3.27e-10$	$-4.19e-09$	
	5	$-5.26e+00$	$-2.28e+01$	$-2.98e+01$	$-1.60e+02$	$-3.14e+02$	$-3.86e+02$	χ_r[W]
	6	$-1.87e-02$	$-8.24e+00$	$-1.27e+01$	$-1.15e+02$	$+6.82e+01$	$+2.39e+02$	
	7,8	$-3.87e-09$	$-3.96e-08$	$-3.77e-08$	$-4.27e-08$	$-5.30e-08$	$-1.21e-07$	
	9,10	$-4.94e-11$	$-5.38e-10$	$+2.73e-09$	$+1.09e-08$	$+1.86e-08$	$+6.37e-08$	
	11	$-1.04e-09$	$-1.82e-09$	$-2.00e-09$	$-2.84e-09$	$-3.81e-09$	$-9.53e-09$	
	12	$-5.77e-11$	$+9.37e-11$	$+1.75e-10$	$+5.40e-10$	$+9.82e-10$	$+3.92e-09$	
Re(λ_6)		-20.00	-19.15	-19.01	-18.27	$+8.12$	$+54.61$	
Re($\lambda_{9,10}$)		-24.42	-1.29	$+2.87$	$+15.23$	$+24.44$	$+52.76$	Hz
Re(λ_{12})		-29.14	$+3.10$	$+5.55$	$+13.91$	$+20.84$	$+43.94$	
f_{lc}		–	220	$195-219$	$168-195-219$	166	166	Hz
mode$_{lc}$		–	12	$9,10-12$	$6-9,10-12$	6	6	

Table 5.6: MAI index χ_r compared with the real part of complex eigenvalues for several values of the friction coefficient. Light-gray highlighted cells correspond coalesced modes, while dark-gray highlighted cells correspond to the unstable modes. f_{cl} is the frequency recovered in the stationary limit cycle and mode$_{cl}$ is the corresponding mode. Bordered values correspond to the modes with highest value of the index χ and the eigenvalue real part.

Also in this case the values assumed by the MAI highlight that there are some modes (1, 5 and 6 in Table 5.6) that, due to the decomposition of the static position on the modal base, are able to exchange an amount of energy that is several order of magnitude higher that the energy exchanged by the other modes. While the mode with an higher real part of the eigenvalue is not the mode recovered in the steady state response of the system, the new index shows correspondence between the modes with highest MAI and the frequency recovered on the limit cycle of the transient analysis (cf Table 5.6 and Fig. 5.9).

Furthermore, the analysis of the power flows around the equilibrium steady-state position, allows to better understand the presence of several frequencies in the steady state response, observed sometime in the literature [SIN 09, CHE 09, COU 09]. In fact, for specific values of the friction coefficient several mode frequencies are de-

tected in the limit cycle response; e.g. for a friction coefficient $\mu = 1.4$ there are two main peaks on the Discrete Fourier Transform of the steady state response that correspond to modes $9 - 10$ and 12. The presence of several unstable mode in the steady-state response corresponds to values of the energy index of the same order of magnitude. This means that two unstable modes have similar attitude to absorb energy from the contact and both of them are present in the transient response. When friction coefficient increases, the mode 6 becomes unstable and the steady state is characterized by an harmonic behavior with only its frequency at $f = 166$Hz; this is due to the value of the energy index MAI, which is several order of magnitude greater than the others.
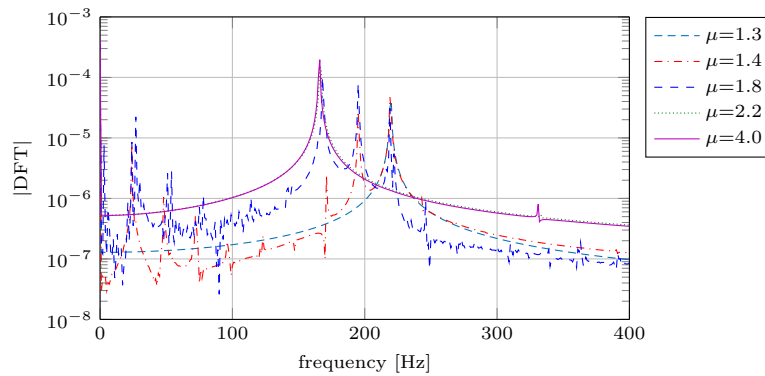
Figure 5.9: Discrete Fourier Transform of the steady state limit cycle for different values of friction coefficient.

Figure 5.9 shows the harmonic content of the steady state transient response, for each value of the friction coefficient reported in Table 5.6. The MAI prediction is in very good agreement with the actual unstable transient response of the system, by predicting the mode that will effectively dominate the steady state vibration limit cycle and by predicting possible multi-frequency vibrations due to similar magnitude of the MAI index for the corresponding unstable modes.

5.5 Modal Absorption Index and unstable mode transition

It is worth noting that the coalesced modes with an higher capability to exchange energy at the contact, i.e. with a significantly higher value of the Modal Absorption Index, can affect the transient response even if it is not still unstable. For instance, coalesced modes $3 - 4$ of the 2 modules system (cf. Section 5.4.1), due to the higher energy exchange with the contact (cf. Table 5.4), affect the transient response of the system also when they are coalesced but they are not unstable yet. In fact, even if for a friction coefficient $\mu = 2.0$ the real parts of this couple of modes are still negative, a contribution of these modes can be recovered by the spectrum (cf. Fig. 5.10(b))

in the first part of the transient response ($t < 0.25\,$s). Indeed, when modes $3 - 4$ are coupled there is already a consistent positive power introduced into the system by the contact (cf. Table 5.4), that is dissipated during the system vibration by the material damping; nevertheless the energy that is dissipated by material damping is still higher than the one introduced by the contact for this value of the friction coefficient (cf. Table 5.3). Hence, even if the total amount of the energy introduced by the unstable mode 4 is negative, the high amount of energy exchanged by this mode, produces an excitation of the system at its frequency; the energy is introduced locally at the frictional interface, but is then dissipated into the bulk by material damping during the vibration (deformation) of the whole system.

(a) Velocity response along x_1^1.

(b) Discrete Fourier Transform
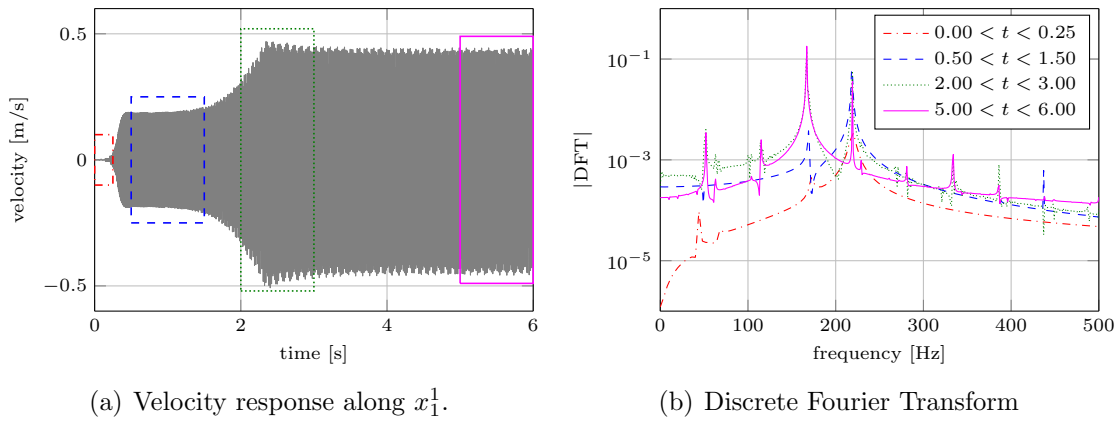
Figure 5.10: Unstable transient response of a $N = 2$ system with a friction coefficient $\mu = 2.0$.

Figure 5.10 shows, for the 2 module system introduced in Section 5.4.1, the transient velocity response (a) and its harmonic content (b) in case of a friction coefficient $\mu = 2.0$. After an initial exponential increase of the vibration amplitude ($0 < t < 0.5$) the system reaches a first orbit. In the time interval $0.5 < t < 1.5$ the system response is dominated by mode 6 at 219Hz (cf. Table 5.5 and Fig. 5.10(b)) with the masses m_1 that move in phase opposition one each other according to the corresponding real mode shape in Fig. 5.1(b). In this time interval the system reaches the ST status alternatively on the two contact points and in these conditions a mode at a frequency 167.80Hz with a modal shape characterized by a phased motion of the two masses m_1 (similar to mode 4 in Fig. 5.1(b)) is unstable. This mode is characterized by an high capability to exchange energy at the contact (cf. Table 5.4). Hence, this orbit results to be unstable and a progressive excitation of the phased mode that is similar both in frequency and in shape to mode 4 in Fig. 5.1(b) leads to a new orbit characterized by the co-presence of two main frequencies with an higher contribution at the frequency of mode 4 and their super-harmonics and sub-harmonics.

The behavior in this transition zone shows that the mode 4, which has an high capability to transfer energy at the contact, also in case of reduced stability margin,

due in this case to the modal coupling in uniform sliding condition, can heavily affect the stationary response. In fact, the variation of the contact condition due to the other unstable mode can drive the system to a new configuration where this mode becomes unstable and starts to influence the transient response.

A similar behavior can be observed for the 4 modules system in Section 5.4.2. In fact, for a friction coefficient $\mu = 1.8$ mode 6, that has the highest attitude to exchange energy, is yet stable but has a reduced margin of stability. Hence, the variation of the contact boundary conditions can lead the system to a configuration where this mode becomes unstable and a relevant contribution of this mode can be found on the steady-state limit cycle. The same order of magnitude of the energy absorbed by these modes from the contact favorites the presence of several harmonics in the system vibration spectrum.

5.6   Effect of the initial perturbation

Transient results showed in Section 5.4.1 and Section 5.4.2 are all obtained considering a small velocity perturbation ϵ in the x_1^1 direction. Therefore, the first part of the transient response is strictly related to the initial perturbation as well as to the eigenvalue real part.

Experimental observations and numerical analyses on extended mechanical system show that the main frequency recovered during the linear phase of the response is generally characterized by the same modal frequency of the steady-state [BRU 15b, TON 13, MAS 05, MAS 06]. This is due to the fact that, for real frictional systems, the perturbation come from the contact interface and is generally related to the surface roughness and the local switches between contact statuses. Consequently, the initial perturbation is in this case a wide-band excitation acting at the contact interface. In order to reproduce this behavior the same Heaviside variation of the speed was applied to all the contact masses in the direction tangential to the contact. This produces a wide-band excitation that is geometrically distributed on the overall contact interface.

Figure 5.11 shows the harmonic content of the 4 modules system introduced in Section 5.4.2. In Fig. 5.11(a) the response is generated by a velocity perturbation ($\varepsilon = 1e - 3 \text{m/s}$) on the direction x_1^1, while, in Fig. 5.11(b) the response is generated by a perturbation applied on all the DoFs of the masses in contact along the direction parallel to the contact sliders x_3^i (cf. Fig. 2.2). The harmonic content of the initial phase ($0 < t < 0.5$), of the saturation phase ($0.5 < t < 1.0$) and of the steady state limit cycle ($2 < t < 3$) are shown. The comparison of these results highlight that while the initial response is affected by the initial perturbation the steady-state limit cycle is not.

The distribution of the numerical perturbation at the contact interface is more representative of real perturbations on frictional systems; in these conditions, also in the first phase of the simulation, the mode that is excited is the mode predicted by the MAI, as recovered generally in real systems. In fact, the predicted mode has

104

(a) Perturbation on x_1^1 direction.

(b) Perturbation on x_3^i directions.
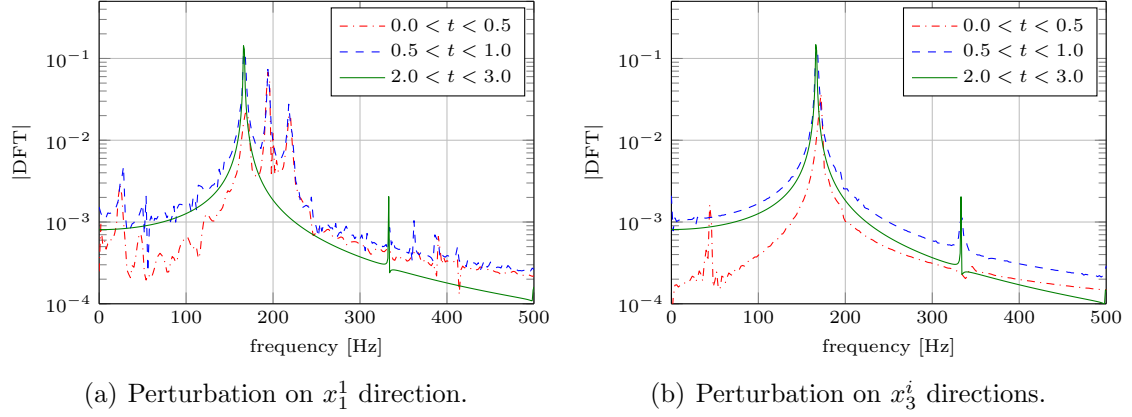
Figure 5.11: Effect of the initial perturbation for a $N = 4$ system with a friction coefficient $\mu = 2.2$.

the highest capability to inject energy into the system from the contact interface, where the perturbation occurs.

5.7 Concluding remarks

In this chapter a new instability index has been proposed to compare the different unstable modes recovered by CEA and to select the mode expected to become effectively unstable during the transient response of the system.

In order to test the index, a lumped model has been developed to reproduce the unstable friction induced vibrations in a more efficient way. The stability of the system, as a function of the friction coefficient, has been presented both from a mathematical point of view, by the analysis of the eigenvalues, and from a physical point of view, analyzing the power flows that the system exchanges with the environment during the friction-induced vibrations.

The new stability index has been introduced by quantifying the attitude of each mode to exchange energy with the external environment. The index is based on the projection of the static equilibrium position on the modal base, allowing to account for not only the sign of the energy content variation but also for the shape of the excitation source located at the contact. The broadband excitation coming from the frictional interface is more effective on the modes that have the highest level of local displacement and stresses at the contact. The projection on the initial condition allows for comparing the instability propensity of the modes obtained by the CEA, which are defined with an arbitrary constant.

The analysis of the new energy index on the lumped system shows a good agreement between the steady state response (unstable frequency) and the values of the MAI index, compared between all the unstable system modes. Even when the magnitude of the real part of the eigenvalue is not in agreement with the transient

unstable frequency, the mode predicted to absorb more energy by the MAI index corresponds to the effective unstable frequency. The MAI index allows one to define a hierarchy among the different system modes to better understand the evolution of the transient response up to the steady state limit cycle.

The energy analysis permits as well to explain the possible coexistence of several harmonics in the steady state limit cycle of vibration: modes with same order of magnitude of the absorbed energy (comparable values of the MAI) can coexist in the steady state response. Moreover, the nature of the perturbation, coming from the broadband excitation from the contact, is shown to be at the origin of the selection mode since the first linear phase of the system response. Future work will be addressed to extend the calculation of the MAI index from CEA on finite element models in order to validate it on continuous systems and by experiments.

Chapter 6

Conclusions and outlines

Contents

The present thesis shows an analysis of the mechanical energy flows involved in frictional contacts. Looking at the friction induced vibrations from an energy point of view allows for a physical interpretation of the issue. The analysis of the energies exchanged at the contact interface, in fact, highlights the strong energy coupling between the surface behavior and the bulk/system dynamic response.

To this aim, after an overview of the analysis tools that are available into the literature to study the friction induced vibration phenomena, a general energy balance has been formulated in order to distinguish among the involved mechanical energy terms. A distinction has been made between the energy dissipated at the contact and the energy reintroduced into the system by the friction induced vibrations. The two main dissipative terms have been formulated to account for: the energy dissipated by the material damping during the bulk vibration and the energy dissipated by the contact due to the local sliding velocity at the contact interface.

In this thesis, the friction-induced vibrations have been analyzed using three common approaches: the finite element approach to investigate the coupling between the contact and system dynamics by the analysis of the energy flows; the experimental approach to validate the numerical results and observe the influence of phenomena not still included into the numerical models; a lumped parameter model approach to quickly investigate the effects of the system parameters. By applying the formulated energy balance, a new instability index has been developed, and validated on the lumped model, to investigate the multi-instability issue. The main contribution of this work are summarized in the following section.

6.1 Original contributions

- The friction induced vibrations have been numerically analyzed on a 2D system, composed by an elastic body in frictional contact with a rigid surface, which reproduces the PhotoTrib setup, developed at the LaMCoS laboratory. The results of the transient non linear analysis confirmed the results of the complex eigenvalue analysis about the system stability. The transient response is characterized by a harmonic response at the frequency of one of the unstable in-plane modes predicted by the complex eigenvalue analysis. The results highlight how even a simple system constituted by one single deformable body in frictional contact can be unstable. The obtained instabilities are due to in-plane unstable modes of the system.

- An energy balance formulation has been developed and analyzed during the transient response with both stable and unstable friction induced vibrations. It shows that during frictional contact in stable conditions the largest part of the energy is actually dissipated at the contact, while a small amount of energy introduced into the bulk produces a vibration that is dissipated by the material damping. On the contrary, in case of unstable vibrations, the initial exponential increase of the vibration amplitude is related to a difference

108

between the energy introduced by the friction-induced vibrations and the dissipative terms; the steady state limit cycle is characterized by an equilibrium between the energy introduced into the system by the contact and the dissipative terms of vibrations. This equilibrium allows for a repartition of the energy introduced into the mechanical system between the two dissipative terms.

- A parametric analysis has been developed to investigate the effects, on the transient response, of changes in the friction coefficient and in the relative velocity between the rigid surface and the elastic body. The results highlighted the influence of the contact nonlinearity distribution on the excitation of the effective unstable mode, among the several unstable modes resulting from the complex eigenvalue analysis.

- The friction-induced vibrations and the local dynamic behavior affect the averaged local friction coefficient, which shows a maximum value equal to the imposed friction coefficient. Moreover, specific behaviors have been highlighted for the mechanical energy and its two components (the elastic potential energy and the kinetic energy), as well as for the contact exchanged power and the dissipative terms of the energy balance. Transition ranges of the energy flows have been recovered for specific ranges of the parameters, corresponding to the transition of the local contact behavior.

- The power globally absorbed and dissipated from the system in the steady state limit cycle is generally different from the theoretical power absorbed during the steady state in uniform sliding condition. The amount of the energy absorbed by the system during the limit cycle, as well as the repartition among the different dissipative terms, depends on the actual contact behavior reached during the unstable vibrations. In particular, the friction induced vibrations modify the overall capacity of the system to absorb and dissipate energy; an estimation of the power dissipated at the contact, without considering the dynamic behavior of the system (energy flows by friction induced vibrations) can lead to significant error in the quantification of the dissipated energy at the contact, which affects directly several tribological phenomena.

- The 2D and 3D dynamic characterization of the PhotoTrib allowed for a comparison between the numerical results of the 2D simplified model and the experimental measurements. The experimental squeal measurements show how the same unstable modes are recovered both experimentally and numerically, validating the use of the 2D transient simulations for the reproduction of the unstable friction-induced vibrations on the PhotoTrib setup.

- The results of a preliminary experimental campaign allow to distinguish among the main effects of the local contact energy dissipation on the system dynamic response. The heating, due to the dissipated energy at the contact produces a reversible thermal dilatation resulting in an increase of the braking torque.

Furthermore, the energy dissipated at the contact is also at the origin of wear and physicochemical phenomena, with the rise of a third-body layer, which produce a permanent modification of the contacting surfaces, i.e. permanent modification of the braking torque.

- A modular lumped model with frictional contact has been developed to reproduce the friction induced vibrations. The use of a lumped model, combined with a piece-wise linear solution technique, allows for a fast integration of the transient solution. The model has been conceived with a modular formulation and each modulus has degrees of freedom either in contact and in non contact with the sliders; the aim is the possible extension of the system degree of freedom and the presence of degree of freedom representing either the contact interface and the bulk.

- Once the energy balance formulated, it has been used on the lumped model to approach the instability over-prediction issue characteristic of the complex eigenvalue analysis. By energy considerations, a newer instability index (MAI) has been defined to compare the different unstable modes and to select the mode expected to become effectively unstable during the transient response.

- The Modal Absorption Index allows one to quantify the attitude of each mode to exchange energy with the external environment. The use of the new energy index on the lumped system showed a good agreement between the steady state response (unstable frequency) and the value of the MAI index compared between all the unstable modes of the system. The MAI index defines a hierarchy among the several unstable system modes to better understand the evolution of the transient response up to the steady state limit cycle. the coexistence of several modal frequencies in the transient response has been associated to similar values of the MAI, i.e. similar attitude of the modes to absorb energy.

- The role of the initial perturbation on the selection of the unstable mode into the transient response has been highlighted. In general, the broadband excitation at the contact interface can be assumed to be at the origin of the initial perturbation of the system dynamics. The MAI index account for the form of the initial perturbation by the projection of the eigenvectors on the initial equilibrium position.

6.2 Outlines

This thesis presents a preliminary work dealing with the analysis of the energy flows in the study of friction induced vibrations. This work is focused on the mechanical energy balance during squeal vibrations, considering only the elastic deformation,

the damping dissipation and the contact dissipation related to the relative displacement.

- Several other aspect are needed to be accounted for, such as the thermal effects, local plastic deformations and their effects on the stress distribution at the contact. The power dissipated at the contact could be used for a coupling with the Discrete Element Method (DEM) formulations, in order to distinguish between the portion of the mechanical power actually dissipated by heating and the portion that produces local surface modifications such as the detachment of material and evolution of the third-body. The further development of the energy balance could provide important information toward a better modeling of the local friction coefficient, accounting for the effect of friction induced vibrations on the heating phenomena and third-body evolution.

- A full thermo-mechanical analysis of high frequency friction induced vibrations would be interesting, but the relevant difference in temporal scales between the system dynamic (ms) and global thermal phenomena (10 s) makes a direct full integration hard to be implemented. Nevertheless, a combined use of quasi-static thermo-mechanical analysis with the complex eigenvalue analysis and the nonlinear transient analysis could lead to a better comprehension of the evolution of the squeal phenomena over a time interval of several seconds, that usually characterize the squeal episodes.

The experimental reproduction of friction induced vibrations is not always easy to manage; in fact, the real interaction of all the included multi-physic phenomena make their interpretation not at all obvious. The numerical investigation gives several useful elements to improve the comprehension of the real behavior. The direct observation of the local contact behavior, in fact, is impossible without substantial modifications of the mechanical system itself. In this context the numerical tribology, combined with the detailed analysis of the contact dynamics, gives meaningful tips on the phenomena involved at the contact.

- Several aspects should be further investigated from an experimental point of view on the PhotoTrib setup: *(i)* a further parametric analysis should be performed to distinguish between thermal and different surface modification effects; *(ii)* observations of the contact surface toward the polycarbonate material, with a fast camera, could give information about the evolution of the third body layer; *(iii)* a local measurement of the contact dynamics and temperature evolution, e.g. by means of a laser vibrometer and thermocouples, would provide an experimental indirect measurement of the energy actually introduced in the polycarbonate disc, and the energy actually dissipated at the contact; *(iv)* out-of-plane vibrations should be as well measured in order to estimate the energy dissipation due to the out-of-plane component of vibration.

- The coupling of the present analysis with local wave generation and propagation analysis at the contact could give meaningful information on how the high frequency energy content at the contact (ultrasonic excitation due to the wave propagation though the surface and the bulk) is transferred to the system vibration frequency range (overall dynamics of the system). Experiments with acoustical instrumentation close to the contact could as well validate this approach.

- The Modal Absorption Index has been applied in this thesis, with very promising results, on a lumped parameter model. This method is now ready to be applied to a more realistic system. The next step will be the extraction of the eigenvector matrices from the CEA, performed on the 2D finite element model of the PhotoTrib, in order to calculate the MAI and verify that the squeal frequencies obtained by transient analysis and experiments correspond to the one predicted by the MAI. Once validated by the finite element simulations and the experiments, the presented approach will be extended to commercial brake system using the CEA by full finite element models.

Bibliography

[ABU 08] AbuBakar A. R., Ouyang H.
Wear prediction of friction material and brake squeal using the finite element method. *Wear*, vol. 264, nº 11-12, 2008, p. 1069 - 1076.

[ADA 95] Adams G. G.
Self-Excited Oscillations of Two Elastic Half-Spaces Sliding With a Constant Coefficient of Friction. *Journal of Applied Mechanics*, vol. 62, nº 4, 1995, p. 867–872.

[ADA 98] Adams G. G.
Steady Sliding of Two Elastic Half-Spaces With Friction Reduction due to Interface Stick-Slip. *Journal of Applied Mechanics*, vol. 65, nº 2, 1998, p. 470–475.

[AKA 00] Akay A., Wickert J., Xu Z.
Final Report: Investigation of mode lock-in and friction interface. report, 2000, Department of Mechanical Engineering, Carnegie Mellon University.

[AKA 02] Akay A.
Acoustics of friction. *The Journal of the Acoustical Society of America*, vol. 111, nº 4, 2002, p. 1525-1548, ASA.

[AKA 09] Akay A., Giannini O., Massi F., Sestieri A.
Disc brake squeal characterization through simplified test rigs. *Mechanical Systems and Signal Processing*, vol. 23, nº 8, 2009, p. 2590 - 2607.

[ALT 04] Altintas Y., Weck M.
Chatter Stability of Metal Cutting and Grinding. {*CIRP*} *Annals - Manufacturing Technology*, vol. 53, nº 2, 2004, p. 619 - 642.

[AMO 99] Amontons G.
De la résistance causée dans les machines, tant par le frottement des parties qui les composent que par la roideur des corps qu'on y employe, et la manière de calculer l'un et l'autre. *Compte rendu de l'Académie des Sciences*, , 1699, p. 206–227.

[BAI 02] Baillet L., Sassi T.
Méthode d'éléments finis avec hybridisation frontière pour les problèmes de con-

tact avec frottement. *Comptes Rendus Mathematique*, vol. 334, nᵒ 10, 2002, p. 917 - 922.

[BAI 03] Baillet L., Sassi T.
Simulations numériques de différentes méthodes d'éléments finis pour les problèmes de contact avec frottement. *Comptes Rendus Mécanique*, vol. 331, nᵒ 11, 2003, p. 789 - 796.

[BAI 05a] Baillet L., D'Errico S., Berthier Y.
Influence of sliding contact local dynamics on macroscopic friction coefficient variation. *Revue Européenne des Éléments finis*, vol. 14, nᵒ 2-3, 2005, p. 305-321.

[BAI 05b] Baillet L., Linck V., D'Errico S., Laulagnet B., Berthier Y.
Finite Element Simulation of Dynamic Instabilities in Frictional Sliding Contact. *Journal of Tribology*, vol. 127, nᵒ 3, 2005, p. 652–657, American Society of Mechanical Engineers.

[BAI 05c] Baillet L., Sassi T.
Mixed finite element formulation in large deformation frictional contact problem. *Revue Européenne des Éléments finis*, vol. 14, nᵒ 2-3, 2005, p. 287-304.

[BAI 06] Baillet L., D'Errico S., Laulagnet B.
Understanding the occurrence of squealing noise using the temporal finite element method. *Journal of Sound and Vibration*, vol. 292, nᵒ 3-5, 2006, p. 443 - 460.

[BER 96] Berthier Y.
Maurice Godet's Third Body. Dowson D., Taylor C. M., Childs T. H. C., Dalmaz G., Berthier Y., Flamand L., Georges J. M., Lubrecht A. A., Eds., *The Third Body Concept Interpretation of Tribological Phenomena*, vol. 31 of *Tribology Series*, p. 21 - 30 Elsevier, 1996.

[BOW 50] Bowden F. P., Tabor D.
The Friction and Lubrication of Solids - Part I. Clarendon Press, Oxford, 1950.

[BOW 64] Bowden F. P., Tabor D.
The Friction and Lubrication of Solids - Part II. Clarendon Press, Oxford, 1964.

[BRU 04] Brunel J., Dufrénoy P., Demilly F.
Modelling of squeal noise attenuation of ring damped wheels. *Applied Acoustics*, vol. 65, nᵒ 5, 2004, p. 457 - 471.

[BRU 06] Brunel J., Dufrénoy P., Naït M., noz J. M., Demilly F.
Transient models for curve squeal noise. *Journal of Sound and Vibration*, vol. 293, nᵒ 3-5, 2006, p. 758 - 765. Proceedings of the Eigth International Workshop on Railway NoiseProceedings of the Eighth International Workshop on Railway Noise.

[BRU 14] BRUNETTI J., MASSI F., D'AMBROGIO W., BAILLET L.
Steady state of modal coupling instabilities as a dynamic energy equilibrium. *Proceeding of ISMA2014 including USD2014*, 2014.

[BRU 15a] BRUNETTI J., MASSI F., D'AMBROGIO W., BERTHIER Y.
Dynamic and energy analysis of frictional contact instabilities on a lumped system. *Meccanica*, vol. 50, n° 3, 2015, p. 633-647, Springer Netherlands.

[BRU 15b] BRUNETTI J., MASSI F., SAULOT A., RENOUF M., D'AMBROGIO W.
System dynamic instabilities induced by sliding contact: A numerical analysis with experimental validation. *Mechanical Systems and Signal Processings*, vol. 58-59, 2015, p. 70-86.

[CAN 11] CANTONE F., MASSI F.
A numerical investigation into the squeal instability: Effect of damping. *Mechanical Systems and Signal Processing*, vol. 25, n° 5, 2011, p. 1727 - 1737.

[CAO 04] CAO Q., OUYANG H., FRISWELL M. I., MOTTERSHEAD J. E.
Linear eigenvalue analysis of the disc-brake squeal problem. *International Journal for Numerical Methods in Engineering*, vol. 61, n° 9, 2004, p. 1546–1563, John Wiley & Sons, Ltd.

[CAR 91] CARPENTER N. J., TAYLOR R. L., KATONA M. G.
Lagrange constraints for transient finite element surface contact. *International Journal for Numerical Methods in Engineering*, vol. 32, n° 1, 1991, p. 103–128, John Wiley & Sons, Ltd.

[CHA 08] CHATELET E., MICHON G., MANIN L., JACQUET G.
Stick/slip phenomena in dynamics: Choice of contact model. Numerical predictions & experiments. *Mechanism and Machine Theory*, vol. 43, n° 10, 2008, p. 1211 - 1224.

[CHE 03] CHEN G., ZHOU Z., KAPSA P., VINCENT L.
Experimental investigation into squeal under reciprocating sliding. *Tribology International*, vol. 36, n° 12, 2003, p. 961 - 971.

[CHE 07] CHEN G., ZHOU Z.
Time-frequency analysis of friction-induced vibration under reciprocating sliding conditions. *Wear*, vol. 262, 2007, p. 1 - 10.

[CHE 08] CHEVILLOT F., SINOU J.-J., MAZET G.-B., HARDOUIN N., JÉZÉQUEL L.
The destabilization paradox applied to friction-induced vibrations in an aircraft braking system. *Archive of Applied Mechanics*, vol. 78, n° 12, 2008, p. 949-963, Springer-Verlag.

[CHE 09] CHEVILLOT F., SINOU J.-J., HARDOUIN N.
Nonlinear transient vibrations and coexistences of multi-instabilities induced by friction in an aircraft braking system. *Journal of Sound and Vibration*, vol. 328, 2009, p. 555 - 574.

[COU 21] COULOMB C. A.
Theorie des machines simples: en ayant egard au frottement de leurs parties et a la roideur des cordages. Bachelier, 1821.

[COU 09] COUDEYRAS N., NACIVET S., SINOU J.-J.
Periodic and quasi-periodic solutions for multi-instabilities involved in brake squeal. *Journal of Sound and Vibration*, vol. 328, n° 4-5, 2009, p. 520-540.

[CRO 91] CROLLA D., LANG A.
Paper {VII} (i) Brake Noise and Vibration - The State of the Art. D. DOWSON C. T., GODET M., Eds., *Vehicle Tribology*, vol. 18 of *Tribology Series*, p. 165 - 174 Elsevier, 1991.

[DIB 12] DI BARTOLOMEO M., MASSI F., BAILLET L., CULLA A., FREGOLENT A., BERTHIER Y.
Wave and rupture propagation at frictional bimaterial sliding interfaces: From local to global dynamics, from stick-slip to continuous sliding. *Tribology International*, vol. 52, n° 0, 2012, p. 117 - 131.

[FAG 12] FAGIANI R., MASSI F., CHATELET E., COSTES J., BERTHIER Y.
Contact of a Finger on Rigid Surfaces and Textiles: Friction Coefficient and Induced Vibrations. *Tribology Letters*, vol. 48, n° 2, 2012, p. 145-158, Springer US.

[FAN 11] FAN N., CHEN G., QIAN L.
Analysis of squeaking on ceramic hip endoprosthesis using the complex eigenvalue method. *Wear*, vol. 271, n° 9‚Äì10, 2011, p. 2305 - 2312. 18th International Conference on Wear of Materials.

[FEE 98] FEENY B., GURAN A., HINRICHS N., POPP K.
A Historical Review on Dry Friction and Stick-Slip Phenomena. *Applied Mechanics Reviews*, vol. 51, n° 5, 1998, p. 321–341, ASME.

[FOS 61] FOSBERRY R., HOLUBECKI Z.
Disc Brake Squeal: Its Mechanism and Suppression. Report: Motor Industry Research Association Motor Industry Research Association, 1961.

[FRI 07a] FRITZ G., SINOU J.-J., DUFFAL J.-M., JÉZÉQUEL L.
Effects of damping on brake squeal coalescence patterns - application on a finite element model. *Mechanics Research Communications*, vol. 34, n° 2, 2007, p. 181 - 190.

116

[FRI 07b] Fritz G., Sinou J.-J., Duffal J.-M., Jézéquel L.
Investigation of the relationship between damping and mode-coupling patterns in case of brake squeal. *Journal of Sound and Vibration*, vol. 307, nᵒ 3-5, 2007, p. 591 - 609.

[FRI 07c] Fritz G., Sinou J.-J., Duffal J.-M., Jézéquel L.
Parameter analysis of brake squeal using finite element method. *European Journal of Computational Mechanics*, vol. 16, nᵒ 1, 2007, p. 11-32.

[GIA 06a] Giannini O., Akay A., Massi F.
Experimental analysis of brake squeal noise on a laboratory brake setup. *Journal of Sound and Vibration*, vol. 292, nᵒ 1,Äì2, 2006, p. 1 - 20.

[GIA 06b] Giannini O., Sestieri A.
Predictive model of squeal noise occurring on a laboratory brake. *Journal of Sound and Vibration*, vol. 296, nᵒ 3, 2006, p. 583 - 601.

[GOD 84] Godet M.
The third-body approach: A mechanical view of wear. *Wear*, vol. 100, nᵒ 1-3, 1984, p. 437 - 452.

[GOD 90] Godet M.
Third-bodies in tribology. *Wear*, vol. 136, nᵒ 1, 1990, p. 29 - 45.

[GUA 03] Guan D., Huang J.
The method of feed-in energy on disc brake squeal. *Journal of Sound and Vibration*, vol. 261, nᵒ 2, 2003, p. 297 - 307.

[HAN 12] Han X., Ouyang H., Wang M., Hassan N., Mao Y.
Self-excited vibration of workpieces in a turning process. *Proceedings of the Institution of Mechanical Engineers, Part C: Journal of Mechanical Engineering Science*, vol. 226, nᵒ 8, 2012, p. 1958-1970.

[HER 08] Hervé B., Sinou J., Mahé H., Jézéquel L.
Analysis of friction-induced self-generated vibrations originated from mode-coupling in clutches. *International Journal of Pure and Applied Mathematics*, vol. 42, nᵒ 3, 2008, Page 369, Academic Publications.

[HOF 02] Hoffmann N., Fischer M., Allgaier R., Gaul L.
A minimal model for studying properties of the mode-coupling type instability in friction induced oscillations. *Mechanics Research Communications*, vol. 29, nᵒ 4, 2002, p. 197 - 205.

[HOF 03] Hoffmann N., Gaul L.
Effects of damping on mode-coupling instability in friction induced oscillations. *ZAMM - Journal of Applied Mathematics and Mechanics*, vol. 83, nᵒ 8, 2003, p. 524–534, WILEY-VCH Verlag.

[HOF 04a] Hoffmann N., Gaul L.
A sufficient criterion for the onset of sprag-slip oscillations. *Archive of Applied Mechanics*, vol. 73, n° 9-10, 2004, p. 650-660, Springer-Verlag.

[HOF 04b] Hoffmann N., Gaul L.
Non-conservative beating in sliding friction affected systems: transient amplification of vibrational energy and a technique to determine optimal initial conditions. *Mechanical Systems and Signal Processing*, vol. 18, n° 3, 2004, p. 611 - 623.

[HOP 42] Hopf E.
Abzweigung einer periodischen Lösung von einer stationären Lösung eines Differentialsystems. *Ber. Math.-Phys. Kl Sächs. Akad. Wiss. Leipzig*, vol. 94, 1942, p. 1–22.

[HOT 13] Hothan A., Lewerenz K., Weiss C., Hoffmann N., Morlock M., Huber G.
Vibration transfer in the ball-stem contact interface of artificial hips. *Medical Engineering & Physics*, vol. 35, n° 10, 2013, p. 1513 - 1517.

[IBR 94a] Ibrahim R. A.
Friction-Induced Vibration, Chatter, Squeal, and Chaos - Part I: Mechanics of Contact and Friction. *Applied Mechanics Reviews*, vol. 47, n° 7, 1994, p. 209–226.

[IBR 94b] Ibrahim R. A.
Friction-Induced Vibration, Chatter, Squeal, and Chaos - Part II: Dynamics and Modeling. *Applied Mechanics Reviews*, vol. 47, n° 7, 1994, p. 227–253.

[IRV 13] Irvine T.
Effective Modal Mass and Modal Participation Factors. *Available on the web on site: http://www. vibrationdata. com/tutorials2/ModalMass. pdf.(last access on march 7 2007)*, , 2013.

[KAN 09] Kang J.
Squeal analysis of gyroscopic disc brake system based on finite element method. *International Journal of Mechanical Sciences*, vol. 51, n° 4, 2009, p. 284 - 294.

[KIN 03] Kinkaid N., O'Reilly O., Papadopoulos P.
Automotive disc brake squeal. *Journal of Sound and Vibration*, vol. 267, n° 1, 2003, p. 105 - 166.

[LIN 03] Linck V., Baillet L., Berthier Y.
Dry friction: influence of local dynamic aspect on contact pressure, kinematics and friction. G. Dalmaz A.A. Lubrecht D. D., Priest M., Eds., *Transient Processes in Tribology Proceedings of the 30th Leeds-Lyon Symposium on Tribology*, vol. 43 of *Tribology Series*, p. 545 - 552 Elsevier, 2003.

118

[LIN 06] LINCK V., SAULOT A., BAILLET L.
Consequence of contact local kinematics of sliding bodies on the surface temperatures generated. *Tribology International*, vol. 39, nº 12, 2006, p. 1664 - 1673.

[MAR 76] MARSDEN J. E., MCCRACKEN M.
The Hopf bifurcation and its applications, vol. 19. Springer-Verlag, 1976.

[MAS 05] MASSI F., GIANNINI O. et al.
Extension of a modal instability theory to real brake systems. *Proc. International Modal Analysis Conference-IMAC-XXIII, Orlando, Florida*, 2005.

[MAS 06] MASSI F., GIANNINI O., BAILLET L.
Brake squeal as dynamic instability: An experimental investigation. *The Journal of the Acoustical Society of America*, vol. 120, nº 3, 2006, p. 1388-1398, ASA.

[MAS 07] MASSI F., BAILLET L., GIANNINI O., SESTIERI A.
Brake squeal: Linear and nonlinear numerical approaches. *Mechanical Systems and Signal Processing*, vol. 21, nº 6, 2007, p. 2374 - 2393.

[MAS 08] MASSI F., GIANNINI O.
Effect of damping on the propensity of squeal instability: An experimental investigation. *The Journal of the Acoustical Society of America*, vol. 123, nº 4, 2008, p. 2017-2023, ASA.

[MAS 10] MASSI F., ROCCHI J., CULLA A., BERTHIER Y.
Coupling system dynamics and contact behaviour: Modelling bearings subjected to environmental induced vibrations and "false brinelling" degradation. *Mechanical Systems and Signal Processing*, vol. 24, nº 4, 2010, p. 1068 - 1080.

[MIL 38] MILLS H.
Brake squeal, Technical Report 9000 B. report, 1938, Institution of Automobile Engineers.

[NEW 59] NEWMARK N. M.
A method of computation for structural dynamics. *Journal of the engineering mechanics division*, vol. 85, 1959, p. 67-94.

[NOR 72] NORTH M.
Disc brake squeal: a theoretical model. Hillington Press, 1972.

[NOR 76] NORTH M.
Disc brake squeal. *proc. conf. on braking of road vehicles-proceedings of a conference-institution of mechanical engineers, automobile division-institute of road transport engineers (Loughborough)*, 1976, p. 169-176.

[OBE 11] Oberst S., Lai J.
Chaos in brake squeal noise. *Journal of Sound and Vibration*, vol. 330, n° 5, 2011, p. 955 - 975.

[ODE 85] Oden J., Martins J.
Models and computational methods for dynamic friction phenomena. *Computer Methods in Applied Mechanics and Engineering*, vol. 52, n° 1, 1985, p. 527 - 634.

[OTH 90] Othman M., Elkholy A., Seireg A.
Experimental investigation of frictional noise and surface-roughness characteristics. *Experimental Mechanics*, vol. 30, n° 4, 1990, p. 328-331, Kluwer Academic Publishers.

[OUE 15] Ouenzerfi G., Massi F., Renault E., Berthier Y.
Squeaking friction phenomena in ceramic hip endoprosthesis: Modeling and experimental validation. *Mechanical Systems and Signal Processing*, vol. 58 - ??59, n° 0, 2015, p. 87 - 100.

[OUY 05] Ouyang H., Nack W., Yuan Y., Chen F.
Numerical analysis of automotive disc brake squeal: a review. *International Journal of Vehicle Noise and Vibration*, vol. 1, n° 3-1, 2005, p. 207-231.

[QIA 13] Qian W. J., Chen G. X., Zhang W. H., Ouyang H., Zhou Z. R.
Friction-Induced, Self-Excited Vibration of a Pantograph-Catenary System. *Journal of Vibration and Acoustics*, vol. 135, n° 5, 2013, p. 051021–051021, ASME.

[REN 11a] Renouf M., Massi F., Saulot A., Fillot N.
Dialogues Numériques Entre Echelles Tribologiques. report, 2011, INSA Lyon. 106 pages.

[REN 11b] Renouf M., Massi F., Saulot A., Fillot N.
Numerical Tribology of Dry Contact. *Tribology International*, vol. 44, n° 7-8, 2011, p. 834-844.

[REN 14] Renouf M., Nhu V.-H., Saulot A., Massi F.
First-Body Versus Third-Body: Dialogue Between an Experiment and a Combined Discrete and Finite Element Approach. *Journal of Tribology*, vol. 136, n° 2, 2014, p. 021104-1/9.

[RUD 76] Rudd M.
Wheel/rail noise–Part II: Wheel squeal. *Journal of Sound and Vibration*, vol. 46, n° 3, 1976, p. 381 - 394.

[SAU 13] Saulot A., Massi F., Renouf M., Berthier Y.
Competition between 3rd body flows and local contact dynamics. *Proceedings of the 5th World Tribology Congress (WTC-2013)*, 2013.

[SIN 03a] Sinou J.-J., Thouverez F., Jézéquel L.
Analysis of friction and instability by the centre manifold theory for a non-linear sprag-slip model. *Journal of Sound and Vibration*, vol. 265, nº 3, 2003, p. 527 - 559.

[SIN 03b] Sinou J.-J., Thouverez F., Jézéquel L.
Center manifold and multivariable approximants applied to non-linear stability analysis. *International Journal of Non-Linear Mechanics*, vol. 38, nº 9, 2003, p. 1421 - 1442.

[SIN 03c] Sinou J.-J., Thouverez F., Jézéquel L.
Extension of the Center Manifold Approach, Using Rational Fractional Approximants, Applied to Non-Linear Stability Analysis. *Nonlinear Dynamics*, vol. 33, nº 3, 2003, p. 267-282, Kluwer Academic Publishers.

[SIN 04] Sinou J.-J., Thouverez F., Jézéquel L.
Methods to reduce non-linear mechanical systems for instability computation. *Archives of Computational Methods in Engineering*, vol. 11, nº 3, 2004, p. 257-344, Springer Netherlands.

[SIN 06] Sinou J.-J., Fritz G., Jézéquel L.
The Role of Damping and Definition of the Robust Damping Factor for a Self-Exciting Mechanism With Constant Friction. *Journal of Vibration and Acoustics*, vol. 129, nº 3, 2006, p. 297–306, ASME.

[SIN 07a] Sinou J.-J., Jézéquel L.
The influence of damping on the limit cycles for a self-exciting mechanism. *Journal of Sound and Vibration*, vol. 304, nº 3-5, 2007, p. 875 - 893.

[SIN 07b] Sinou J.-J., Jézéquel L.
Mode coupling instability in friction-induced vibrations and its dependency on system parameters including damping. *European Journal of Mechanics - A/Solids*, vol. 26, nº 1, 2007, p. 106 - 122.

[SIN 08] Sinou J.-J., Jézéquel L.
On the stabilizing and destabilizing effects of damping in a non-conservative pin-disc system. *Acta Mechanica*, vol. 199, nº 1-4, 2008, p. 43-52, Springer-Verlag.

[SIN 09] Sinou J.-J., Coudeyras N., Nacivet S.
Study of the nonlinear stationary dynamic of single and multi-instabilities for disk brake squeal. *International Journal of Vehicle Design*, vol. 51, nº 1-2, 2009, p. 207–222, Inderscience Publishers.

[SIN 10] Sinou J.-J.
Transient non-linear dynamic analysis of automotive disc brake squeal ‚Äì On the need to consider both stability and non-linear analysis. *Mechanics Research Communications*, vol. 37, nº 1, 2010, p. 96 - 105.

[SIN 13] Sinou J.-J., Loyer A., Chiello O., Mogenier G., Lorang X., Cocheteux F., Bellaj S.
A global strategy based on experiments and simulations for squeal prediction on industrial railway brakes. *Journal of Sound and Vibration*, vol. 332, n° 20, 2013, p. 5068 - 5085.

[SOO 13] Soobbarayen K., Besset S., Sinou J.-J.
Noise and vibration for a self-excited mechanical system with friction. *Applied Acoustics*, vol. 74, n° 10, 2013, p. 1191 - 1204.

[SOO 14] Soobbarayen K., Sinou J.-J., Besset S.
Numerical study of friction-induced instability and acoustic radiation - Effect of ramp loading on the squeal propensity for a simplified brake model. *Journal of Sound and Vibration*, vol. 333, n° 21, 2014, p. 5475 - 5493.

[SOO 15] Soobbarayen K., Besset S., Sinou J.-J.
A simplified approach for the calculation of acoustic emission in the case of friction-induced noise and vibration. *Mechanical Systems and Signal Processing*, vol. 50-51, 2015, p. 732 - 756.

[SPU 61] Spurr R. T.
A theory of brake squeal. *Proceedings of the Institution of Mechanical Engineers: Automobile Division*, vol. 15, n° 1, 1961, p. 33–52, SAGE Publications.

[STO 07] Stoimenov B. L., Maruyama S., Adachi K., Kato K.
The roughness effect on the frequency of frictional sound. *Tribology International*, vol. 40, n° 4, 2007, p. 659 - 664. {NORDTRIB} 2004.

[TAB 81] Tabor D.
Friction—The Present State of Our Understanding. *Journal of Lubrication Technology*, vol. 103, n° 2, 1981, p. 169–179, ASME.

[TAR 04] Tarter J. F.
Prediction of unstable friction-induced vibrations using an energy criterion. ThËse de doctorat, Carnegie Mellon University, 2004.

[THO 00] THOMPSON D., JONES C.
A review of the modelling of wheel/rail noise generation. *Journal of Sound and Vibration*, vol. 231, n° 3, 2000, p. 519 - 536.

[TON 13] Tonazzi D., Massi F., Culla A., Baillet L., Fregolent A., Berthier Y.
Instability scenarios between elastic media under frictional contact. *Mechanical Systems and Signal Processing*, vol. 40, n° 2, 2013, p. 754 - 766.

[TWO 99] Tworzydlo W., Hamzeh O. N., Zaton W., Judek T. J.
Friction-induced oscillations of a pin-on-disk slider: analytical and experimental studies. *Wear*, vol. 236, nᵒ 1‚Äì2, 1999, p. 9 - 23.

[WEI 09] Weiss C., Hothan A., Morlock M., Hoffmann N.
Friction-Induced Vibration of Artificial Hip Joints. *GAMM-Mitteilungen*, vol. 32, nᵒ 2, 2009, p. 193–204, WILEY-VCH Verlag.

[WEI 10] Weiss C., Gdaniec P., Hoffmann N. P., Hothan A., Huber G., Morlock M. M.
Squeak in hip endoprosthesis systems: An experimental study and a numerical technique to analyze design variants. *Medical Engineering & Physics*, vol. 32, nᵒ 6, 2010, p. 604 - 609.

FOLIO ADMINISTRATIF

THÈSE SOUTENUE DEVANT L'INSTITUT NATIONAL DES SCIENCES APPLIQUÉES DE LYON

ABSTRACT:
Whenever relative motion between two system components occurs, through a dry contact interface, vibrations are induced by the frictional contact. The local dynamics at the contact (ruptures and wave generation) couples with the system dynamics, giving origin to vibrations and affecting the macroscopic frictional behavior of the system.
In this thesis, in order to develop an overall approach to the investigation of the multi-physic phenomenon, the energy has been pointed out as a coupling physical characteristic among the several phenomena at the different scales. The formulation of a mechanical energy balance is used for distinguishing between two different dissipative terms, i.e. the dissipation by material/system damping and the dissipation at the contact. The energy flows coming from the frictional surfaces, by friction induced vibrations, excites the dynamic response of the system, and vice versa the influence of the system dynamic response on the local energy dissipation at the contact interface affects the related tribological phenomena.
The friction-induced vibrations have been analyzed using three different approaches: the finite element approach, to investigate the coupling between the contact and system dynamics by the analysis of the energy flows; the experimental approach to validate the numerical results and observe the influence of phenomena not still included into the numerical model; a lumped parameter model approach to quickly investigate the effects of the system parameters.
The numerical analysis by the 2D finite element model allowed investigating the repartition of the energy introduced into the mechanical system between the two dissipative terms (material damping and contact) during both stable and unstable friction-induced vibrations. In particular, it has been shown how the friction-induced vibrations modify the overall capacity of the system to absorb and dissipate energy; an estimation of the power dissipated at the contact, without considering the dynamic behavior of the system (energy flows by friction induced vibrations) can lead to significant error in the quantification of the dissipated energy at the contact, which affects directly several tribological phenomena.
The experimental squeal measurements show how the same unstable modes are recovered both experimentally and numerically, validating the use of the 2D transient simulations for the reproduction of the unstable friction-induced vibrations.
Once the energy balance formulated, it has been used on the lumped model to approach the instability over-prediction issue characteristic of the complex eigenvalue analysis. By energy considerations, a newer instability index (MAI) has been defined to compare the different unstable modes and to select the mode that becomes effectively unstable during the transient response. The Modal Absorption Index allows quantifying the capability of each mode to exchange energy with the external environment.
KEYWORDS: friction-induced vibrations; energy balance; contact dynamics; mode coupling instabilities; instability index; dry friction; squeal